

SMART SYSTEMS

THEORY AND ADVANCES

ORGANIZER

GLAUCO FONTGALLAND





2022 - Editora Ampla
Copyright © Editora Ampla
Editor in Chief: Leonardo Tavares
Cover: Editora Ampla
Layout: João Trajano



Smart Systems: Theory and Advances is licensed under CC BY 4.0.

This license requires that reusers give credit to the creator. It allows reusers to distribute, remix, adapt, and build upon the material in any medium or format, even for commercial purposes.

The content of the work and its data in its form, correctness and reliability are the sole responsibility of the authors, and do not represent the official position of Ampla Publishing. Downloading and sharing of the work is permitted as long as credit is given to the authors. All rights to this edition were ceded to Editora Ampla.

ISBN: 978-65-5381-063-1

DOI: 10.51859/ampla.sst631.1122-0

Editora Ampla
Campina Grande – Brazil
contato@amplaeditora.com.br
www.amplaeditora.com.br



2022

EDITORIAL BOARD

Andréa Cátia Leal Badaró – Universidade Tecnológica Federal do Paraná
Andréia Monique Lermen – Universidade Federal do Rio Grande do Sul
Antoniele Silvana de Melo Souza – Universidade Estadual do Ceará
Aryane de Azevedo Pinheiro – Universidade Federal do Ceará
Bergson Rodrigo Siqueira de Melo – Universidade Estadual do Ceará
Bruna Beatriz da Rocha – Instituto Federal do Sudeste de Minas Gerais
Bruno Ferreira – Universidade Federal da Bahia
Caio Augusto Martins Aires – Universidade Federal Rural do Semi-Árido
Caio César Costa Santos – Universidade Federal de Sergipe
Carina Alexandra Rondini – Universidade Estadual Paulista
Carla Caroline Alves Carvalho – Universidade Federal de Campina Grande
Carlos Augusto Trojaner – Prefeitura de Venâncio Aires
Carolina Carbonell Demori – Universidade Federal de Pelotas
Cícero Batista do Nascimento Filho – Universidade Federal do Ceará
Clécio Danilo Dias da Silva – Universidade Federal do Rio Grande do Norte
Dandara Scarlet Sousa Gomes Bacelar – Universidade Federal do Piauí
Daniela de Freitas Lima – Universidade Federal de Campina Grande
Darlei Gutierrez Dantas Bernardo Oliveira – Universidade Estadual da Paraíba
Denise Barguil Nepomuceno – Universidade Federal de Minas Gerais
Diogo Lopes de Oliveira – Universidade Federal de Campina Grande
Dylan Ávila Alves – Instituto Federal Goiano
Edson Lourenço da Silva – Instituto Federal de Educação, Ciência e Tecnologia do Piauí
Elane da Silva Barbosa – Universidade Estadual do Ceará
Érica Rios de Carvalho – Universidade Católica do Salvador
Fernanda Beatriz Pereira Cavalcanti – Universidade Estadual Paulista “Júlio de Mesquita Filho”
Fredson Pereira da Silva – Universidade Estadual do Ceará
Gabriel Gomes de Oliveira – Universidade Estadual de Campinas
Gilberto de Melo Junior – Instituto Federal do Pará
Givanildo de Oliveira Santos – Instituto Brasileiro de Educação e Cultura
Higor Costa de Brito – Universidade Federal de Campina Grande
Isabel Fontgalland – Universidade Federal de Campina Grande
Isane Vera Karsburg – Universidade do Estado de Mato Grosso
Israel Gondres Torné – Universidade do Estado do Amazonas
Ivo Batista Conde – Universidade Estadual do Ceará
Jaqueline Rocha Borges dos Santos – Universidade Federal Rural do Rio de Janeiro
Jessica Wanderley Souza do Nascimento – Instituto de Especialização do Amazonas
João Henriques de Sousa Júnior – Universidade Federal de Santa Catarina
João Manoel Da Silva – Universidade Federal de Alagoas
João Vitor Andrade – Universidade de São Paulo
Joilson Silva de Sousa – Instituto Federal do Rio Grande do Norte
José Cândido Rodrigues Neto – Universidade Estadual da Paraíba
Jose Henrique de Lacerda Furtado – Instituto Federal do Rio de Janeiro
Josenita Luiz da Silva – Faculdade Frassinetti do Recife
Josiney Farias de Araújo – Universidade Federal do Pará
Karina de Araújo Dias – SME/Prefeitura Municipal de Florianópolis
Katia Fernanda Alves Moreira – Universidade Federal de Rondônia
Laís Portugal Rios da Costa Pereira – Universidade Federal de São Carlos
Laíze Lantyer Luz – Universidade Católica do Salvador
Lindon Johnson Pontes Portela – Universidade Federal do Oeste do Pará
Luana Maria Rosário Martins – Universidade Federal da Bahia
Lucas Araújo Ferreira – Universidade Federal do Pará
Lucas Capita Quarto – Universidade Federal do Oeste do Pará
Lúcia Magnólia Albuquerque Soares de Camargo – Unifacisa Centro Universitário
Luciana de Jesus Botelho Sodrê dos Santos – Universidade Estadual do Maranhão
Luís Paulo Souza e Souza – Universidade Federal do Amazonas



Luiza Catarina Sobreira de Souza – Faculdade de Ciências Humanas do Sertão Central
Manoel Mariano Neto da Silva – Universidade Federal de Campina Grande
Marcelo Alves Pereira Eufrazio – Centro Universitário Unifacisa
Marcelo Williams Oliveira de Souza – Universidade Federal do Pará
Marcos Pereira dos Santos – Faculdade Rachel de Queiroz
Marcus Vinicius Peralva Santos – Universidade Federal da Bahia
Maria Carolina da Silva Costa – Universidade Federal do Piauí
Marina Magalhães de Moraes – Universidade Federal do Amazonas
Mário César de Oliveira – Universidade Federal de Uberlândia
Michele Antunes – Universidade Feevale
Milena Roberta Freire da Silva – Universidade Federal de Pernambuco
Nadja Maria Mourão – Universidade do Estado de Minas Gerais
Natan Galves Santana – Universidade Paranaense
Nathalia Bezerra da Silva Ferreira – Universidade do Estado do Rio Grande do Norte
Neide Kazue Sakugawa Shinohara – Universidade Federal Rural de Pernambuco
Neudson Johnson Martinho – Faculdade de Medicina da Universidade Federal de Mato Grosso
Patrícia Appelt – Universidade Tecnológica Federal do Paraná
Paula Milena Melo Casais – Universidade Federal da Bahia
Paulo Henrique Matos de Jesus – Universidade Federal do Maranhão
Rafael Rodrigues Gomides – Faculdade de Quatro Marcos
Reângela Cíntia Rodrigues de Oliveira Lima – Universidade Federal do Ceará
Rebeca Freitas Ivanicska – Universidade Federal de Lavras
Renan Gustavo Pacheco Soares – Autarquia do Ensino Superior de Garanhuns
Renan Monteiro do Nascimento – Universidade de Brasília
Ricardo Leoni Gonçalves Bastos – Universidade Federal do Ceará
Rodrigo da Rosa Pereira – Universidade Federal do Rio Grande
Rubia Katia Azevedo Montenegro – Universidade Estadual Vale do Acaraú
Sabryna Brito Oliveira – Universidade Federal de Minas Gerais
Samuel Miranda Mattos – Universidade Estadual do Ceará
Shirley Santos Nascimento – Universidade Estadual Do Sudoeste Da Bahia
Silvana Carloto Andres – Universidade Federal de Santa Maria
Silvio de Almeida Junior – Universidade de Franca
Tatiana Pascholette R. Bachur – Universidade Estadual do Ceará | Centro Universitário Christus
Telma Regina Stroparo – Universidade Estadual do Centro-Oeste
Thayla Amorim Santino – Universidade Federal do Rio Grande do Norte
Thiago Sebastião Reis Contarato – Universidade Federal do Rio de Janeiro
Virgínia Maia de Araújo Oliveira – Instituto Federal da Paraíba
Virginia Tomaz Machado – Faculdade Santa Maria de Cajazeiras
Walmir Fernandes Pereira – Miami University of Science and Technology
Wanessa Dunga de Assis – Universidade Federal de Campina Grande
Wellington Alves Silva – Universidade Estadual de Roraima
Yáscara Maia Araújo de Brito – Universidade Federal de Campina Grande
Yasmin da Silva Santos – Fundação Oswaldo Cruz
Yuciara Barbosa Costa Ferreira – Universidade Federal de Campina Grande





2022 - Editora Amplla
Copyright © Editora Amplla
Editor in Chief: Leonardo Tavares
Cover: Editora Amplla
Layout: João Trajano

Cataloging in Publication Program (CIP)

Smart systems [e-book]: theory and advances /
organization Glauco Fontgalland. -- Campina
Grande : Editora Amplla, 2022.
254 p.

Format: PDF
ISBN: 978-65-5381-063-1

1. Smart Systems. 2. Data Communication.
3. Antennas 4. Microwave. 5. Optoelectronics. I.
Fontgalland, Glauco. II. Title.

CDD-006.3

Sueli Costa - Librarian - CRB-8/5213 (SC
Assessoria Editorial, SP, Brazil)

Indexes for systematic catalog:

1. Smart Systems 006.3



2022



PREFACE

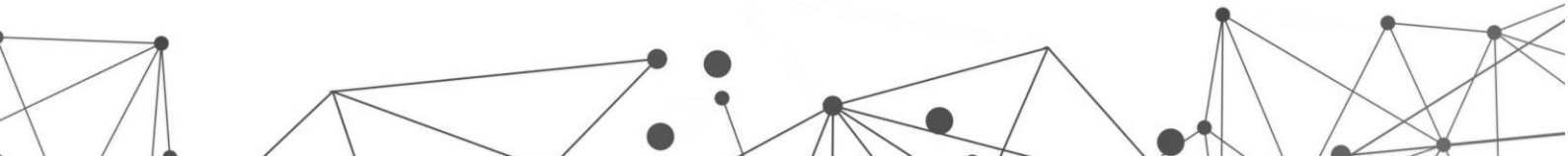
Along with technology advances, which includes but not limited to electronics, microelectronics, optoelectronics, photonics, signal processing, and programming has come the interest on fast, multifunction, lightweight, and low power consumption communication devices. Such high demanded and sometimes conflicting features have greatly increased interest worldwide in wireless and optical technologies for building applications of intelligent systems. It is paramount necessary to study how these applications are being developed and what are the challenges that must be overcome for successful deployments of this technology. Under this scenario, the sector where the development of this technology is most expected is undoubtedly in the telecommunication sector. The gains with the implementation of this technology go far beyond to just replace the existing ones to provide tools that possess decision-making capability and to fulfill the society needs.


There are several competing technologies in the market and as this market grows, the number of technological options to embed in a device will only increase. Within this vision, a plethora of projects are being developed in recent years on techniques and methods from RF and microwaves to Terahertz, optics, and photonics.

This book aims to highlight the strength and state-of-art of some techniques and methods applied to intelligent systems. Rather to cover the variety of techniques and methods available in the literature, which is out of scope of this book, it focuses on those consolidated and applied and on those with high potential of implementation to smart systems.

This book has fourteen chapters covering a broad range of topics in communications. The first three chapters are devoted to state-of-art and review papers on planar filters, unmanned aerial vehicles (UAV), negative group delay, nanoclusters, and tunable lights, while the remain chapters cover specific topics such as smart monitoring, V2I, high-speed links, RF and Optical sensors, composite material, metamaterial, energy harvesting, radar, SWIPT, and electromagnetic sources.

The opportunity to organize a book of this magnitude, whose content inspires the continuous search for knowledge and pursue research, brings encouragement

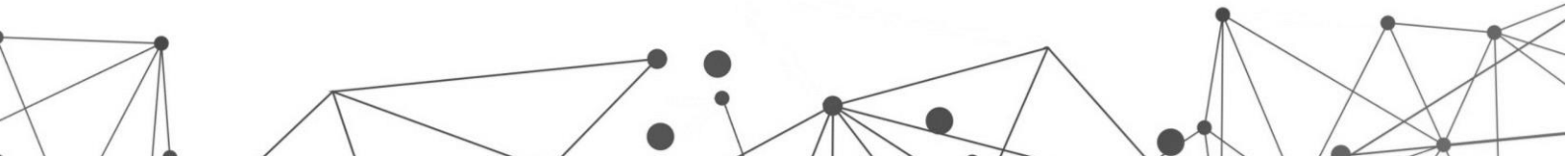




and great pleasure to this researcher. It is not by chance that I had the opportunity to meet most of the authors, regularly attempting international events, invited talks, invited lectures, organizing sessions, workshops, and events and project partnerships abroad. More than ever, the academia and the industry believe in the power of multidisciplinary approach and sympathizes with the most rigorous scientific criteria. The authors, each in their own way, made a remarkable contribution to microwaves and optoelectronics topics to compile this first edition and provide necessary fundamental resources to the readers. The reader will be impressed by its content and each chapter is a unique journey!

Enjoy reading!

Glauco Fontgalland



SUMMARY

CHAPTER I - LITERATURE REVIEW ON RF AND MICROWAVE DESIGN OF PASSIVE MICROSTRIP CIRCUIT WITH BANDPASS TYPE NGD BEHAVIOR	9
CHAPTER II - OVERVIEW ON BANDPASS NGD BASED SIGNAL PROPAGATION DELAY SUPPRESSION FOR UAV BASE STATION CELLULAR NETWORK	37
CHAPTER III - A REVIEW OF RECENT RESULTS OF WHITE LIGHT GENERATION AND TUNABLE VISIBLE LIGHT EMISSION BY AG NANOCLOUDS: UNDOPED AND DOPED Tm^{3+} /Yb^{3+} DOPED GeO_2-PBO GLASSES	57
CHAPTER IV - SMART MONITORING SYSTEM BY OPTICAL DEVICE FOR VEHICLE TRAJECTORY PREDICTION	74
CHAPTER V - HIGH SENSITIVITY ENVELOPE DETECTOR ASSISTED BY MICROWAVE PHOTONICS	91
CHAPTER VI - INVESTIGATION OF ELECTROMAGNETIC AND ABSORBER PROPERTIES OF DOUBLE-LAYER SYSTEM USING IRON CARBONYL AND FERRITE COMPOSITES	107
CHAPTER VII - OPTICAL MULTIMODE INTERFERENCE WAVEGUIDES AS SENSING DEVICES	118
CHAPTER VIII - DEVELOPMENT OF METAMATERIAL-BASED MICROWAVE DIELECTRIC SENSORS	139
CHAPTER IX - MONITORING BIOMETRIC PARAMETERS AND PREDICTION PRODUCTIVITY IN SUGARCANE CROPS USING DRONE-BORNE SYNTHETIC APERTURE RADAR	153
CHAPTER X - APPLICATION OF MULTICOMMODITY FLOW OPTIMIZATION FOR PROPAGATION LOSS MODEL FOR INDOOR ENVIRONMENTS	178
CAPÍTULO XI - MOBILE CHANNEL CHARACTERIZATION IN V2I SYSTEM INSIDE A TUNNEL IN 5.8 GHZ	195
CHAPTER XII - NEW ANALYTICAL APPROACH TO ESTIMATE THE ELECTROMAGNETIC SPECTRUM FROM DEVICES SUBMITTED TO HIGH VOLTAGES	207
CHAPTER XIII - PROPOSAL FOR MATCHING THE IMPEDANCE OF A BROADBAND AND HIGH BAND RF RECTIFIER EFFICIENCY FOR ENERGY HARVESTING	224
CHAPTER XIV - TECHNIQUES TO OPTIMIZE RETURN LOSS OF HIGH-SPEED SERIAL LINKS ON A MULTILAYER PCB	238

LITERATURE REVIEW ON RF AND MICROWAVE DESIGN OF PASSIVE MICROSTRIP CIRCUIT WITH BANDPASS TYPE NGD BEHAVIOR

DOI: 10.51859/amplla.sst631.1122-1

Eric Sambatra¹
Samuel Ngoho²
Frank Elliot Saha³
Glauco Fontgalland⁴
Vladimir Mordachev⁵
Nour Mohammad Murad⁶
Fayu Wan⁷
Blaise Ravelo⁷

¹ Institut Supérieur de Technologie D'Antsiranana (IST-D), BP 509, Antsiranana 201, Madagascar

² Association Française de Science des Systèmes (AFSCET), Paris 75013, France

³ Laboratoire de Physique Nucléaire et Physique de l'Environnement (LPNPE), Université d'Antananarivo, Antananarivo 101, Madagascar

⁴ Federal University of Campina Grande, Applied Electromagnetic and Microwave Lab., Campina Grande/PB, 58429, Brazil

⁵ EMC R&D Laboratory, Belarusian State University of Informatics and Radioelectronics (BSUIR), vulica Pietrusia Brouki 6, Minsk 220013, Belarus

⁶ PIMENT, Institut Universitaire de Technologie, University of La Reunion, Saint Pierre 97410, France

⁷ NUIST, School of Electronic & Information Engineering Nanjing, Jiangsu, China 210044

ABSTRACT

Due to its counterintuitive aspects, the negative group delay (NGD) circuits remain an unfamiliar electronic function to majority of radio frequency (RF) and microwave design engineers. The present book chapter provides a literature review for non-initiated graduate students and non-specialist engineers to afford an overview about the recent research progress about the NGD microwave circuit design and the main roadmap on NGD future applications. A simple and fundamental NGD theory inspired from filter analogy was initiated. The types of low-pass (LP), high-pass (HP), bandpass (BP) and stop-band (SB) NGD specifications were defined. The NGD microwave passive circuit applications are still not widely developed because of their attenuation and reflection loss critical performances. Progressive research work was made the three-last decades to improve the RF and microwave NGD performances. One of the main challenges is the low attenuation loss NGD microstrip design susceptible to operate in the GHz range as L- and S-bands. This chapter reviews different designs of BP-NGD microstrip passive circuits. The BP-NGD specifications as NGD value, center frequency, bandwidth, attenuation and reflection losses are defined. The BP-NGD microstrip passive circuit design method in function of expected specifications is described. The BP-NGD performances of diverse topologies are compared.

Key words: Negative group delay (NGD), microstrip circuit, bandpass (BP) NGD specifications, BP-NGD design method, literature review.

1. INTRODUCTION

Some decades ago, particular engineering and scientific work efforts were paid on the development of the negative group delay (NGD) electronic circuit design with remarkable research results [1-79]. Indeed, it was outstandingly theoretically and experimentally demonstrated that the NGD circuits present a strange property of generating outputs in advance of its input [1-17]. Some of curious interpretations want to state that the NGD effect is like an impossible phenomenon or also classified as anomalous physical phenomenon. So, it is somehow hard for many engineers and researchers to believe the existence of such counterintuitive property. This finding is susceptible to limit also the development of NGD RF and microwave electronic and communication applications for many non-specialist engineering. So, many curious questions are still open about the understanding of assumed as mysterious NGD circuit engineering.

1.1. FUNDAMENTAL DEFINITIONS AND TYPES OF NGD CIRCUITS

Remarkable and outstanding research works need to be done about the understanding and interpretation of NGD circuit responses. Because of infinite diversity of NGD electronic circuit topologies, the simplest and fundament NGD circuit theory from similitude with the filter one was initiated [1-4]. In difference with the filter theory which is based on the magnitude frequency response, the NGD theory depends on the group delay (GD) diagram [1-4]. The types of low-pass (LP) [5-17], high-pass (HP) [18-23], bandpass (BP) [24-27], stop-band (SB) [28-29] and all-pass (AP) [30] NGD circuit topologies were introduced with R, L and C lumped components. Somehow, one may confuse NGD and filter behaviors. Table 1 indicates the main differences between these two electronic functions.

Table 1 – Technical notable differences between filter and NGD circuit behaviors [1-2]

Characteristics	Filter	NGD
Cut-off frequencies	Root(s) of transmission coefficient magnitude equation	Root(s) of GD equation
Operation frequency bands	Transmission coefficient magnitude higher than -3 dB	GD is negative
Center frequency	Harmonic average of filter operation frequency band	Harmonic average of NGD frequency band

1.2. STATE OF THE ART ON LP-NGD ELECTRONIC CIRCUITS

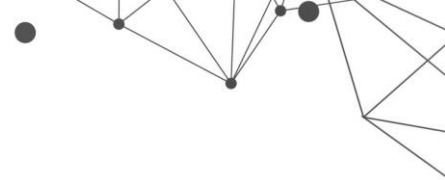
Like all electronic basic topologies, it is capital for the circuit design researchers to identify the simplest topologies satisfying the required specifications. To design LP-NGD circuit, the main specifications are the NGD value, NGD cut-off frequency and transmittance magnitude at very low frequencies [5-17]. All electronic circuit engineering design leads to the identification of elementary NGD circuit based on first order RC or RL network-based topologies [5-6]. Feedback network-based topologies operating with LP-NGD effect were also identified [7-8]. Miniature LP-NGD integrated circuits in CMOS technology was recently designed [9-10]. By playing on the circuit equivalent theory, some innovative LP-NGD circuit as via-hole based lumped circuit was designed [11]. It is noteworthy that the LP-NGD circuits are expected to operate with baseband signals [12-17].

1.3. STATE OF THE ART ON BP-NGD LUMPED CIRCUITS

The basic understanding of BP-NGD behavior can be theoretically, numerically and experimentally investigated with lumped circuits [1-4, 24-27]. The initial validation of NGD behavior was performed with RLC-network based topologies as reported in [1-4, 24]. But thanks to the knowledge of LP- [5-17] and HP- [18-23] NGD behaviors, it was inspired from filter responses that BP-NGD circuit can be designed without use of inductance component [25]. Some unexpected innovative topologies of RC-network based bridged-T network were recently proposed [26-27]. However, because of attenuation loss and lumped component, research works have been made by RF and microwave engineers to develop microstrip topologies as introduced in the following paragraph.

1.4. STATE OF THE ART ON BP-NGD MICROSTRIP CIRCUITS

The main challenge of BP-NGD RF and microwave circuit design [31-70] was the feasibility of topologies susceptible to operate with low-attenuation loss and also miniaturized sizes. The less expensive, theoretically, numerically and experimentally affordable solutions lead to the deployment of microstrip topologies [31-70]. Outstanding diversity of microstrip circuit topologies as based-on structures as stub terminated [31-32] and parallel interconnect line [33-39] was found. But the most significant NGD research work on microstrip circuit design is based on coupled interconnected line [40-54]. In order to optimize certain BP-NGD



performances as bandwidth, some mixed topologies as proposed in [55-56] were also designed. To compensate losses, BP-NGD active circuits using transistors or low-noise amplifier were introduced [59-64]. It was also investigated that there are possibilities to design multi-band BP-NGD circuits [64-66].

1.5. STATE OF THE ART ON BP-NGD TIME-DOMAIN MEASUREMENTS

The NGD behavior interpretation is hardly understandable in the frequency domain. Therefore, time-domain investigation seems needed to answer to some curious questions. One of the most challenging tasks about the BP-NGD investigation are the time-domain measurements [67-70]. Modulated signals with BP-NGD center frequency as carrier is necessary to perform such experimentations. The final results should be the comparison of signal envelopes [67-70]. The main limit of current research results on the BP-NGD time-domain experimentation is on the consideration of high-speed signals used in 5G- and 6G-technologies.

1.6. STATE OF THE ART ON MULTI-PORT NGD CIRCUITS

At the beginning, all the research work on LP-, HP- and BP-NGD circuit design was focused on two-port topologies [1-70]. In the past two year, more general topologies of NGD circuit with multi-port accesses were performed [71-78]. The design feasibility was verified with three-port topologies as Y- or T-shape circuits [71-74]. The BP-NGD function was also verified with Δ -shape lumped circuit [75]. More complex topologies as H-shape circuits were proposed [76-77]. Compared to filter, power combiner and power divider, the multi-port NGD design remains a non-explored field. A lot of research work are expected in the future to the design and experimentation techniques of NGD multi-port circuits. But before this challenging study, the present chapter is devoted on the illustrative literature review of BP-NGD circuit design.

1.7. OUTLINE OF THE CHAPTER

The present chapter is focused on the literature review of BP-NGD microstrip circuit design. For the basic understanding of counterintuitive circuits, we propose three different sections:

- Section 2 describes the S-parameter modelling approach and design methodology of BP-NGD microstrip circuit. The proposed approach permits to guide the beginners to identify the NGD RF and microwave circuit topologies.

The fundamental knowledge for RF and microwave engineering graduate students, engineers and researchers is dedicated.

- Once the NGD circuit topologies are correctly identified, the verification of NGD effect is always a critical task for the NGD circuit design researchers. Section 3 introduces different RF and microwave validation results of different microstrip circuit topologies. Various microstrip circuit proofs of concept (POC) are described. The validations are based on comparison between simulated and measured GDs. For the better comprehension, the chapter section is only focused on the passive microstrip circuit.
- Against the signal time-delay issues in printed circuit boards (PCBs) [78-79], Section 4 presents some tentative potential applications of NGD circuits [80-113] especially in electronic and communication engineering.
- Last section 5 is the conclusion of the chapter.

2. DESIGN METHODOLOGY OF BP-NGD MICROSTRIP CIRCUIT

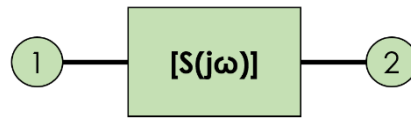
The design method of BP-NGD microstrip circuit must be performed with good knowledge of S-parameter analysis. Somehow, the analytical modelling is quite complex. However, there are still possibilities to perform simulations especially with 2-D or 3-D structures. The measurements must be performed with vector network analyzer (VNA).

2.1. S-PARAMETERS AND GD MODELLING

The S-parameter analyses are traditionally performed in the frequency domain. High level mathematic skills associated to circuit and system (CAS) fundamental knowledge, are needed to develop RF and microwave NGD circuit theory and analytical modelling. Doing this, let us denote ω the angular frequency variable. For the two-port RF and microwave circuits as represented by the black box of Fig. 1, the S-parameter model can be represented by 2-D matrix:

$$[S(j\omega)] = \begin{bmatrix} S_{11}(j\omega) & S_{12}(j\omega) \\ S_{21}(j\omega) & S_{22}(j\omega) \end{bmatrix} \quad (1)$$

Figure 1 – Two-port S-parameter black block [31-58]



For the case of symmetrical circuit, we have reflection and transmission coefficients as complex number:

$$S_{11}(j\omega) = S_{22}(j\omega) = \text{Re}[S_{11}(j\omega)] + j \cdot \text{Im}[S_{11}(j\omega)] \quad (2)$$

$$S_{12}(j\omega) = S_{21}(j\omega) = \text{Re}[S_{21}(j\omega)] + j \cdot \text{Im}[S_{21}(j\omega)] \quad (3)$$

To characterize the NGD RF and microwave circuit, we need:

- the traditional reflection and transmission coefficient magnitudes:

$$|S_{11}(j\omega)| = \sqrt{\text{Re}[S_{11}(j\omega)]^2 + \text{Im}[S_{11}(j\omega)]^2} \quad (4)$$

$$|S_{21}(j\omega)| = \sqrt{\text{Re}[S_{21}(j\omega)]^2 + \text{Im}[S_{21}(j\omega)]^2} \quad (5)$$

- The transmission phase associated to expression (3) is defined as:

$$\varphi(\omega) = \arg[S_{21}(j\omega)] \quad (6)$$

- But the capital analysis should be performed with the less familiar expression of GD defined by:

$$GD(\omega) = -\partial\varphi(\omega) / \partial\omega \quad (7)$$

These basic definitions enable to explore the microstrip circuit NGD specifications as described in the following paragraph.

2.2. NGD SPECIFICATION DIAGRAM

In addition to the Bode diagrams, we should consider the GD frequency domain diagram to practice NGD RF and microwave electronic engineering. Figs. 2 depict all the essential parameters constituting the unfamiliar BP-NGD specifications.

Figure 2 – BP-NGD (a) GD, (b) reflection and (c) transmission parameter specifications [2-58]

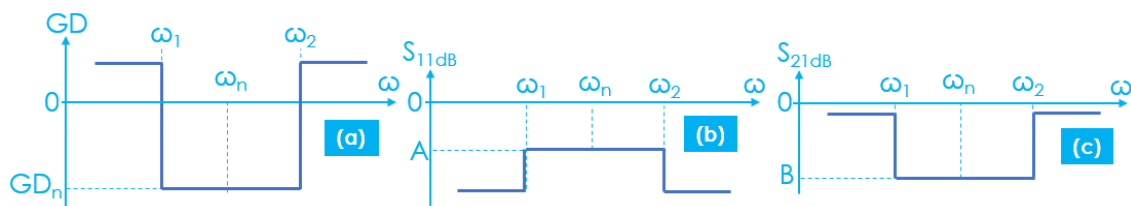


Fig. 2(a) shows the ideal GD diagram of BP-NGD ideal RF and microwave circuit. The diagram of Fig. 2(c) indicates the main NGD specifications as GD center frequency $f_n = \omega_n / (2\pi)$, NGD value GD_n and NGD frequency bandwidth $[\omega_1, \omega_2]$ which are analytically given by:

- where we have the GD value:

$$GD_n = GD(\omega_n) < 0 \quad (8)$$

- The NGD cut-off frequencies ω_1 and ω_2 are the root of equation:

$$GD(\omega) = 0 \quad (9)$$

- The NGD cut-off frequencies ω_1 and ω_2 are the root of equation:

$$GD(\omega) = 0 \quad (10)$$

In the given NGD frequency band $[\omega_1, \omega_2]$, the BP-NGD circuit should operate with respect to all classical RF and microwave device requirements. For example, the reflection and transmission coefficients can be ideally represented as shown in Fig. 2(b) and in Fig. 2(c), respectively. Given the specifications denoted A for the matching condition (which is generally equal to -10 dB), we should verify:

$$|S_{11}(j\omega)| < A \quad (11)$$

Given the maximal attenuation loss, we should verify:

$$|S_{21}(j\omega)| > B \quad (12)$$

2.3. NGD DESIGN ROUTINE METHODOLOGY

Like all classical electronic circuits, the BP-NGD circuits can be designed with a relevant method. The design methodology of BP-NGD microstrip circuit can be started from the required specifications. In the present chapter, we are focusing only to the case of two-port microwave circuits. It means that the simulations and measurements should generate the S-matrix introduced in equation (1). To start, it is particularly important for the NGD design engineers to have a good knowledge of microstrip technology of the microstrip transmission line (TL) structure displayed in Fig. 3. Then, the NGD circuit (NGDC) design engineer must choose the topology corresponding to the application requirements. The different stages of analysis from ideal to realistic situations must be investigated. Mathematical analyses are one of the most critical tasks in this stage. However, S-parameter simulations of the microstrip structures can also be performed with commercial software tools as ADS® from Keysight Technologies or HFSS® from ANSYS® or CST MWS from

DASSAULT SYSTEM®. The specifications indicated in Figs. 2 must be extracted after simulations. The main task behind is to determine the good geometrical parameters and physical shape of the structure allowing to get the optimal results in the expected operating frequency band.

Figure 3 – 3-D design of microstrip transmission line with physical length d and width w having substrate thickness h under metallization thickness t [31-58]

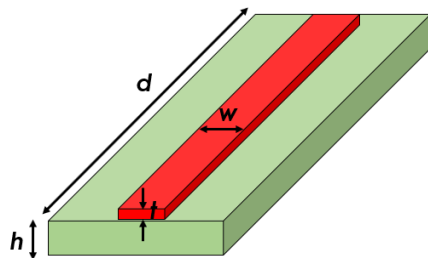
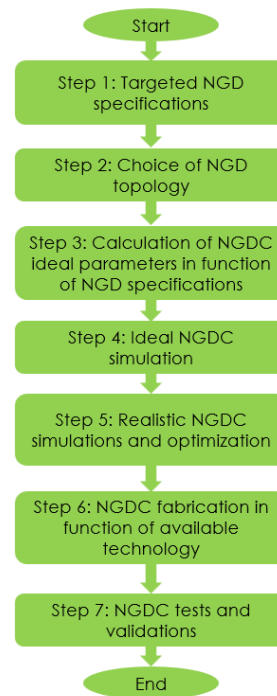


Figure 4 – Design flow of BP-NGD microstrip circuit [31-58]



To summarize the different tasks of the BP-NGD design, we proposed the design flow shown in Fig. 4. For further understanding on the application results of this design flow, simulation and experimental results of different BP-NGD microstrip circuits from literature are described in the following section.

3. SIMULATION AND EXPERIMENTATION OF BP-NGD MICROSTRIP CIRCUITS

The present section describes examples of BP-NGD validation results from literature review. Different microstrip structures designed following the routing methodology of Fig. 4 are considered.

3.1. RLC-NETWORK PASSIVE CIRCUIT-BASED BP-NGD DESIGN

The BP-NGD behaviors were investigated with resonant RLC-networks composed of R, L and C lumped components [1-4]. For the fundamental understanding and to develop solid skills, it is worth to recommend NGD design

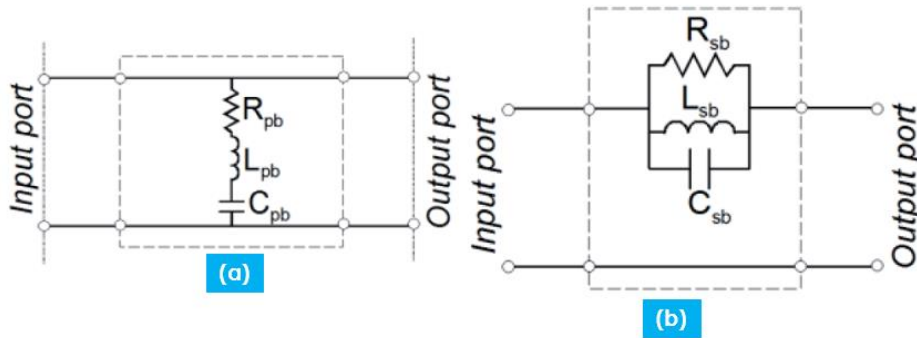
engineer beginners to start to elaborate the NGD model of these RLC-network topologies.

3.1.1. NGD THEORETICAL APPROACH

The simplest topologies of that circuits with RLC-series and RLC-parallel networks are displayed in Fig. 5(a) and Fig. 5(b), respectively. For both topologies, we can assume that the NGD center frequency as:

$$\omega_n = 1 / \sqrt{LC} \quad (13)$$

Figure 5 – BP-NGD RLC (a) series and (b) parallel network topologies [2]



At this frequency, it was theoretically demonstrated that [2]:

- For the BP-NGD RLC topology shown in Fig. 5(a), the reflection, transmission coefficients and GD become:

$$|S_{11}(j\omega_n)| = R_0 / (R_0 + 2R_{pb}) \quad (14)$$

$$|S_{21}(j\omega_n)| = 2R_{pb} / (R_0 + 2R_{pb}) \quad (15)$$

$$GD(\omega_n) = -2R_0L_{pb} / [R_{pb}(R_0 + 2R_{pb})] \quad (16)$$

- For the BP-NGD RLC topology shown in Fig. 5(b), the reflection, transmission coefficients and GD become:

$$|S_{11}(j\omega_n)| = R_{sb} / (2R_0 + R_{sb}) \quad (17)$$

$$|S_{21}(j\omega_n)| = 2R_0 / (2R_0 + R_{sb}) \quad (18)$$

$$GD(\omega_n) = -4R_{sb}C_{sb} / (2R_0 + R_{sb}) \quad (19)$$

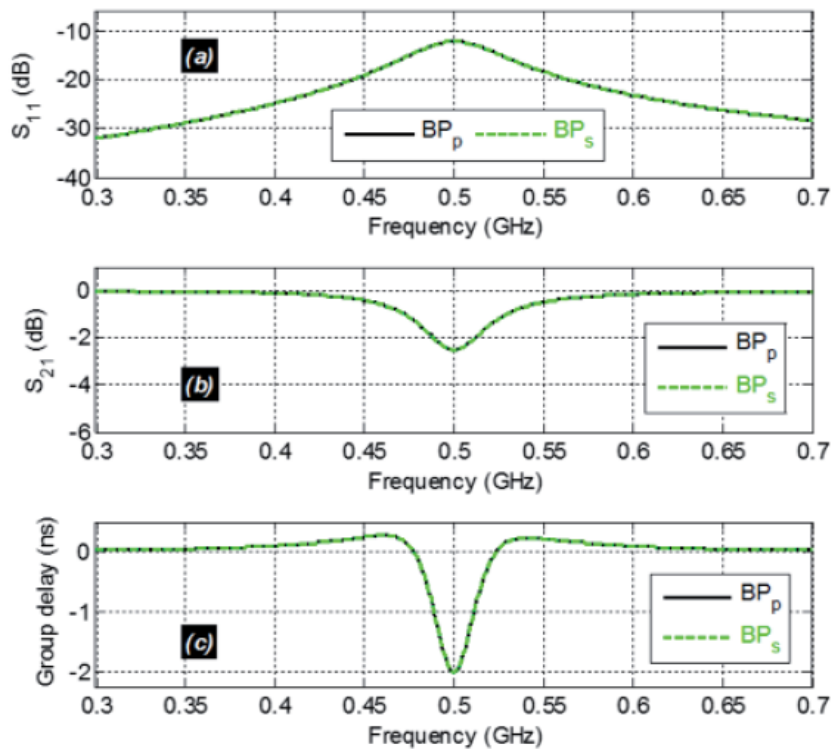
We can underline that the GDs are always negative for both RLC-resonant topologies. This finding simplifies the design feasibility during the circuit study.

3.1.2. NGD VALIDATION

Following the synthesis formulas of each constituting components by taking $f_n=0.5$ GHz, $GD_n=-2$ ns and $S_{21}(f_n)=-3$ dB, we can design a proof-of-concept. Figs. 6(a) show the GD responses from 0.3 GHz to 0.7 GHz.

As expected, we can emphasize here that we have $GD(f)<0$ around f_n . This means that the considered circuit behaves as a BP-NGD function. Moreover, we can see also that the transmission coefficient presents an attenuation exactly equal to the expected requirement. Then, the reflection coefficients in the NGD frequency are lower than -10 dB. It is interesting to get the BP-NGD designability with such topologies but they are not always working for certain cases above GHz frequency range because of the reactive component manufacturing. As solution against such technological limitations, we can use distributed circuits as based on microstrip technologies.

Figure 6 – BP-NGD responses from topologies shown in Fig. 5 [2]

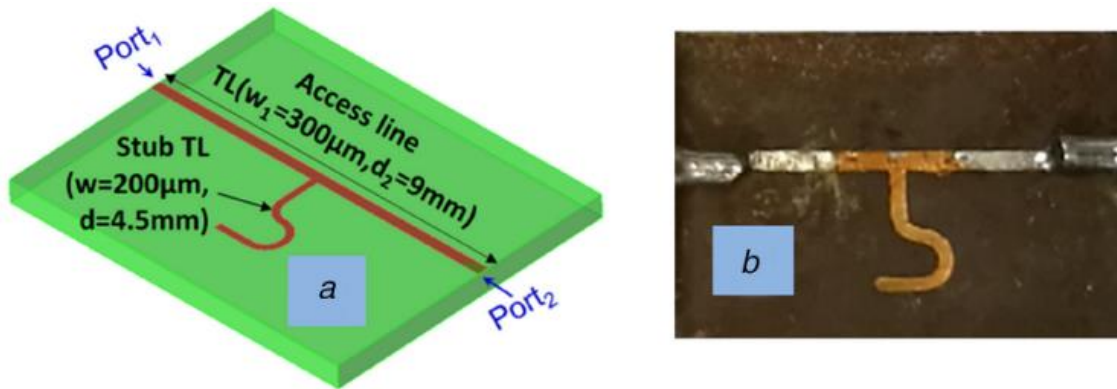


3.1.3. BP-NGD OPEN STUB CIRCUIT-BASED DESIGN [31]

Based on the TL theory, we have an equivalent between RLC-series network and open-ended stub. This is one main idea allowing to design microstrip circuits

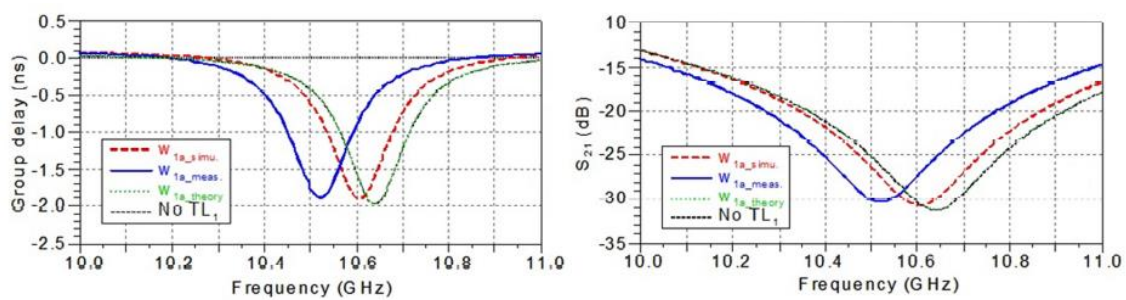
equivalent to the RLC topology introduced in Fig. 5(a). The 3-D design solution and the prototype photograph are presented in Fig. 7(a) and Fig. 7(b), respectively.

Figure 7 – Open-stub BP-NGD microstrip circuit: (a) 3-D design and (b) prototype photo [31]



This microstrip circuit was implemented on Kapton substrate with copper metallization. The validation study of the open-ended stub circuit was performed from 10 GHz to 11 GHz. In left of Fig. 8, we have the GD diagram of the compared simulation and measurement. In right of Fig. 8, we have the transmission coefficient magnitude. We emphasize that the open-ended circuit is significantly lossy up to more than 30 dB attenuation around the NGD center frequency. To limit the attenuation loss, different other microstrip topologies were explored with results presented in the following subsections.

Figure 8 – Compared simulated and measured (in left) GD and S_{21} (in right) of open-stub circuit shown in Fig. 7 [32]

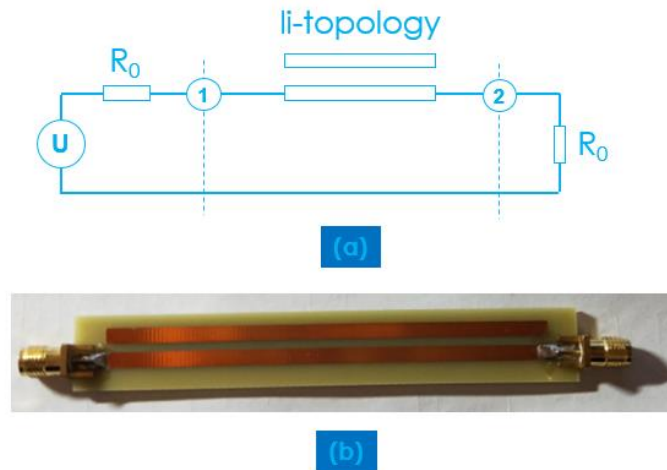


3.1.4. BP-NGD “LI” MICROSTRIP CIRCUIT DESIGN [40]

The li-topology is a distributed circuit constituted by coupled line (CL) as displayed by Fig. 9(a). To study the design feasibility and the BP-NGD behavior, a POC is needed. Accordingly, a prototype of the fabricated li-microstrip circuit is presented by the photograph of Fig. 9(b). It acts as two pieces of straight microstrip lines placed in proximity. Before early 2020, this simple TL based distributed

topology was quite familiar and well-known by RF and microwave design engineers. But we should emphasize that by curiosity, few of them were aware of its BP-NGD responses.

Figure 9 – (a) topology and (b) photograph of microstrip circuit prototype [40]



This prototype was designed and implemented on FR4 substrate under copper strip metallization. Because of the EM coupling between them we have again the BP-NGD effect.

Figure 10 – Mapping's of (a) GD, (b) S_{21} and (c) S_{11} of the li-circuit shown in Fig. 9 [40]

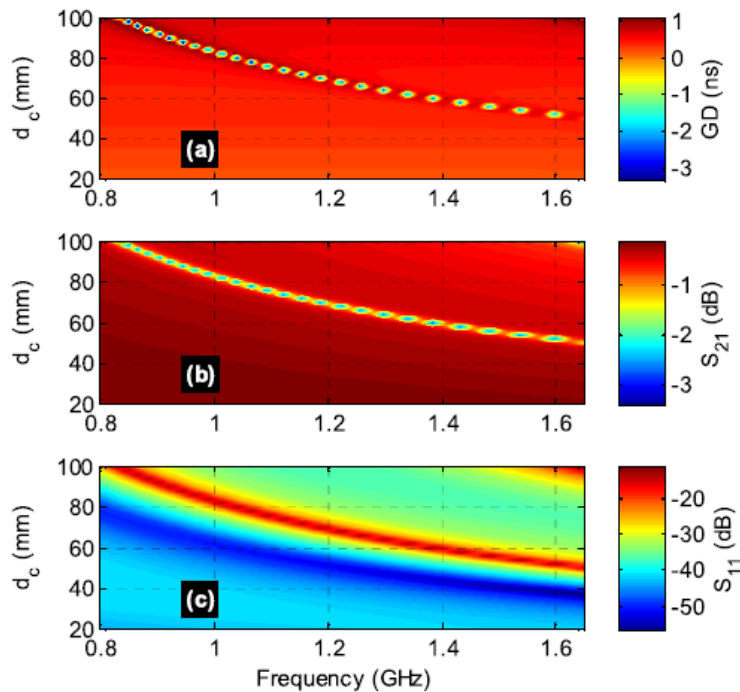
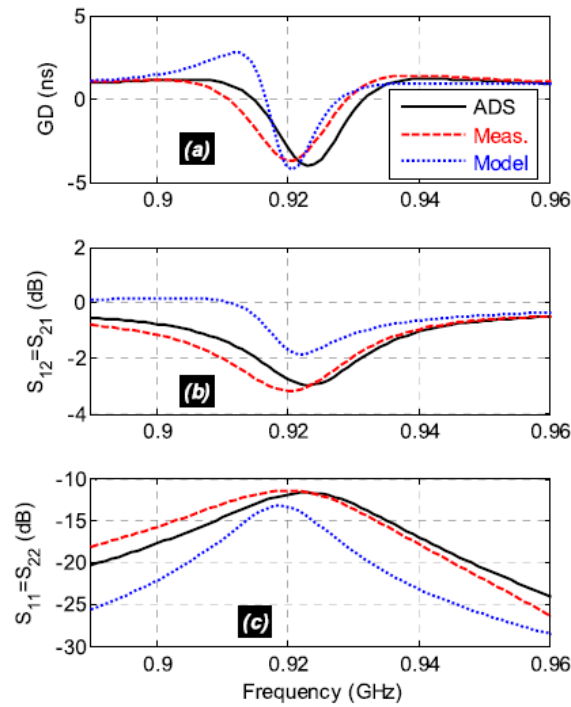


Figure 11 – Calculated, simulated and measured (a) GD, (b) S_{21} and (c) S_{11} of the li-circuit shown in Fig. 9 [40]



To understand the effect of the length (d_c) on the NGD responses, parametric S-parameter analyses were performed. Fig. 10 presents the obtained results in the operating frequency chosen from 0.8 GHz to 1.62 GHz. It can be seen that the NGD center frequency is inversely proportional to d_c . The comparison of simulated and experimented results shown in Figs. 11 confirms that we have again the BP-NGD behavior with center frequency around 0.92 GHz.

3.1.5. BP-NGD “10” MICROSTRIP CIRCUIT DESIGN

Substituting the “i”-shape element of previously described “li” structure by “0”-shape element, we have a “10” microstrip topology presented in Fig. 12(a). The two-cell design of such topology is displayed in Fig. 12(b). We can see in Fig. 12(c) the photograph of the experimental setup using a VNA. Fig. 13(a) depicts that the 10 circuit behaves also as a BP-NGD function. The NGD absolute value is increasing with the number of cells. In this case of study, the attenuation loss around the NGD center frequency is around 4 dB.

Figure 12 – (a) Single and (b) double cell “10”-microstrip circuits, and (c) Experimental setup [44]

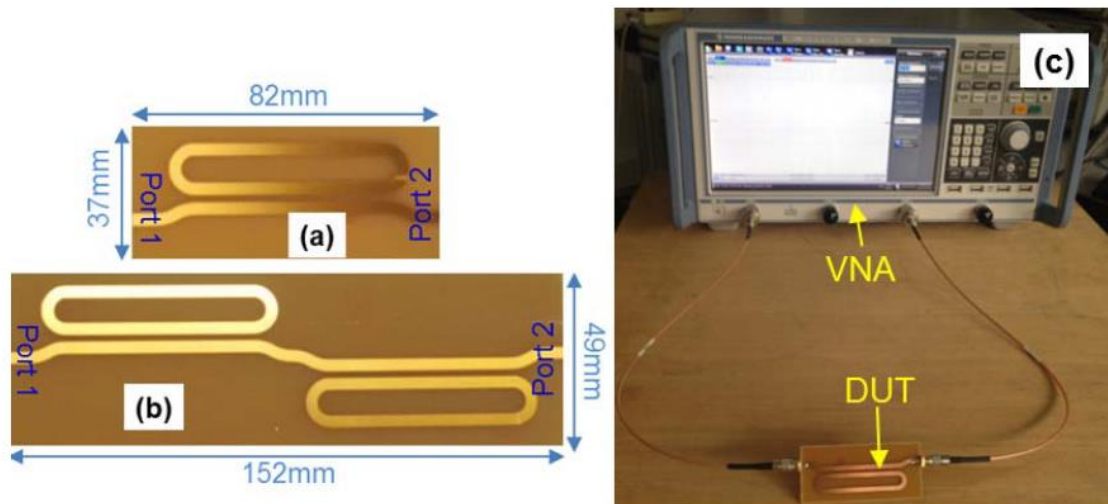
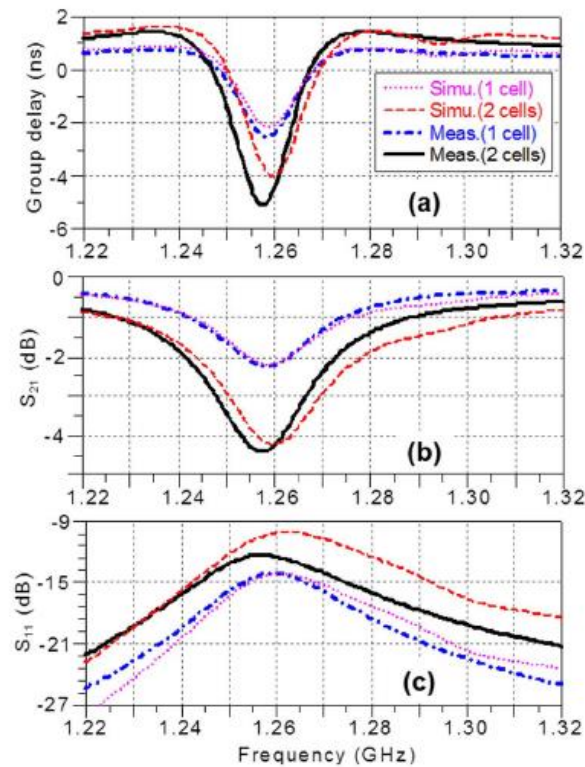


Figure 13 – Simulated and measured (a) GD, (b) S_{21} and (c) S_{11} of the “10”-circuit shown in Fig. 12 [44]

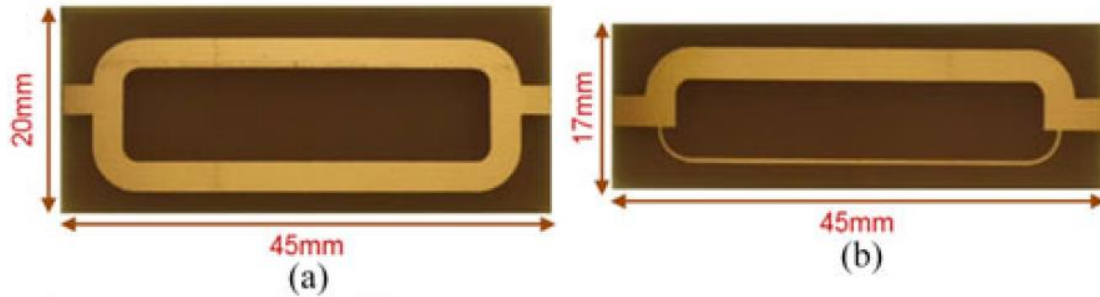


3.1.6. BP-NGD PARALLEL INTERCONNECT LINE (PIL) MICROSTRIP CIRCUIT DESIGN

The most fundamental distributed topology of BP-NGD circuit is the PIL structure. This topology is composed of two different interconnect lines connected in parallel. Figs. 14 show two different cases of PIL microstrip circuits. Fig. 14(a) is an example of structure with constituting TLs same characteristic impedance but

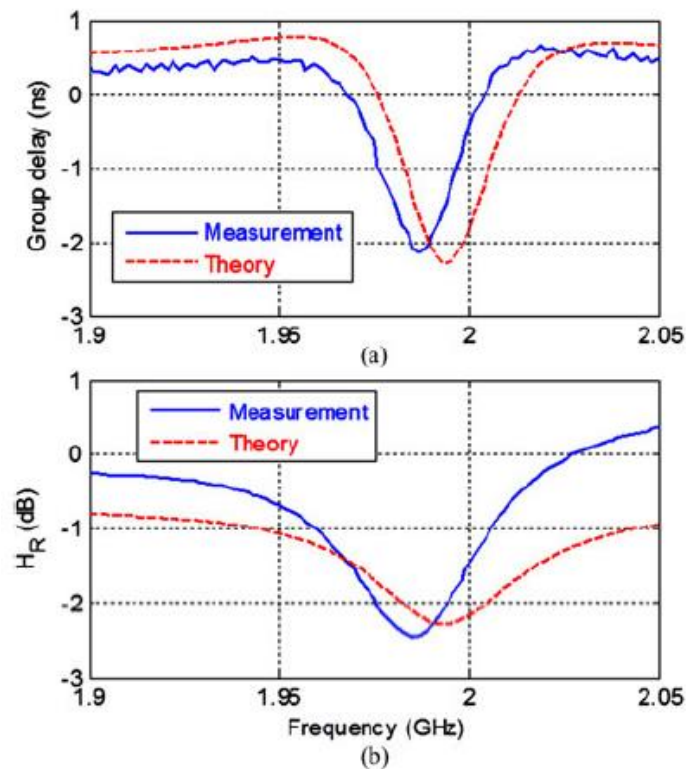
different physical lengths. However, Fig. 14(b) presents another example with different characteristic impedance but the same physical lengths.

Figure 14 – BP-NGD PIL microstrip circuit with different (a) length and (b) impedance arms [33]



Similar to the previous case, Figs. 15 show that we have BP-NGD behaviors with both circuits with NGD center frequency slightly below 2 GHz.

Figure 15 – Simulated and measured (a) GD, (b) S_{21} and (c) S_{11} of the PIL-circuit shown in Fig. 14 [33]



3.2. BP-NGD LADDER-SHAPE MICROSTRIP CIRCUIT DESIGN

Figs. 16 present the design and photograph of two-cell based ladder microstrip circuit. The S-parameter simulations from 3.8 GHz to 4 GHz were performed to study the BP-NGD behavior of this structure.

Figure 16 – (a) HFSS® design and (b) photo of BP-NGD ladder-shape microstrip circuit [38]

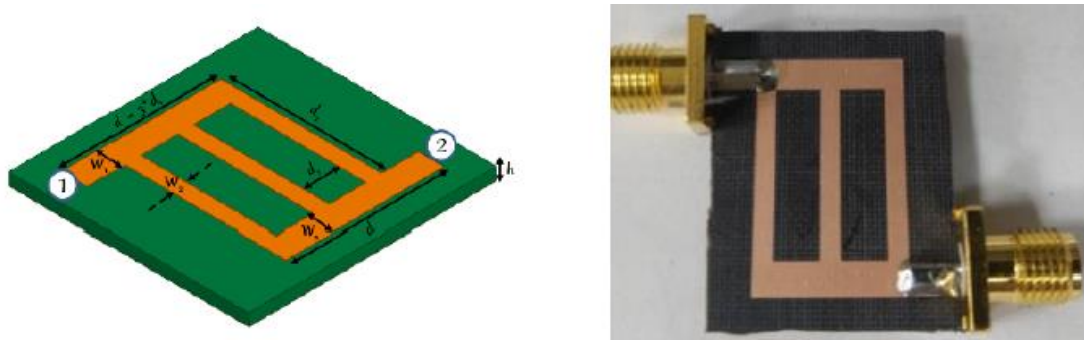


Figure 17 – Cartographies of (a) GD, (b) S_{21} and (c) S_{11} vs (f , w_1), and (d) $\min(\text{GD})$, (e) $\min(S_{21})$, and (f) $\min(S_{11})$ [38].

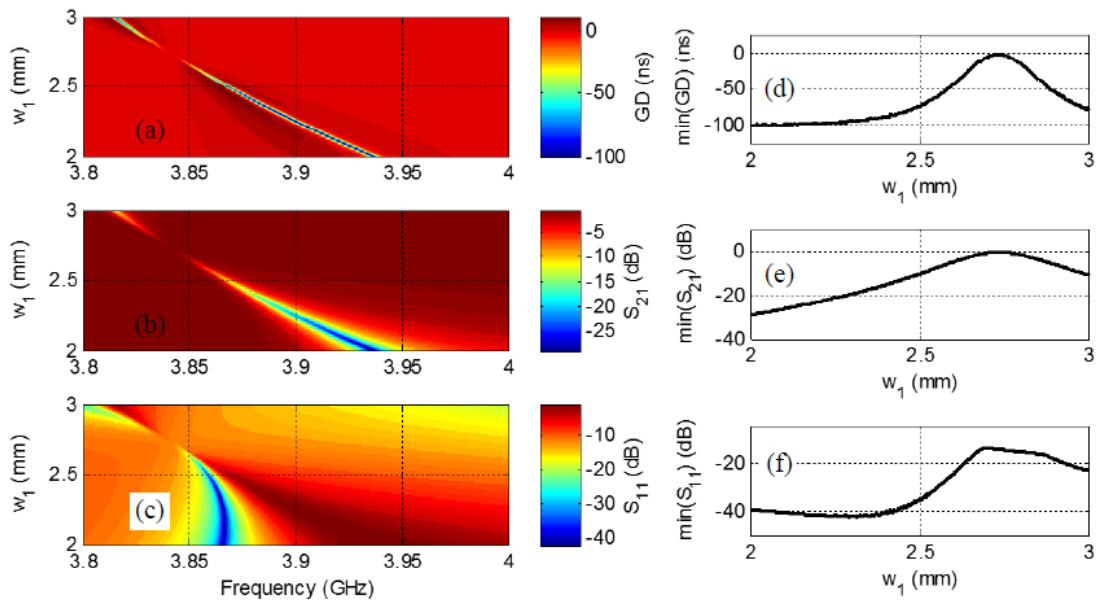
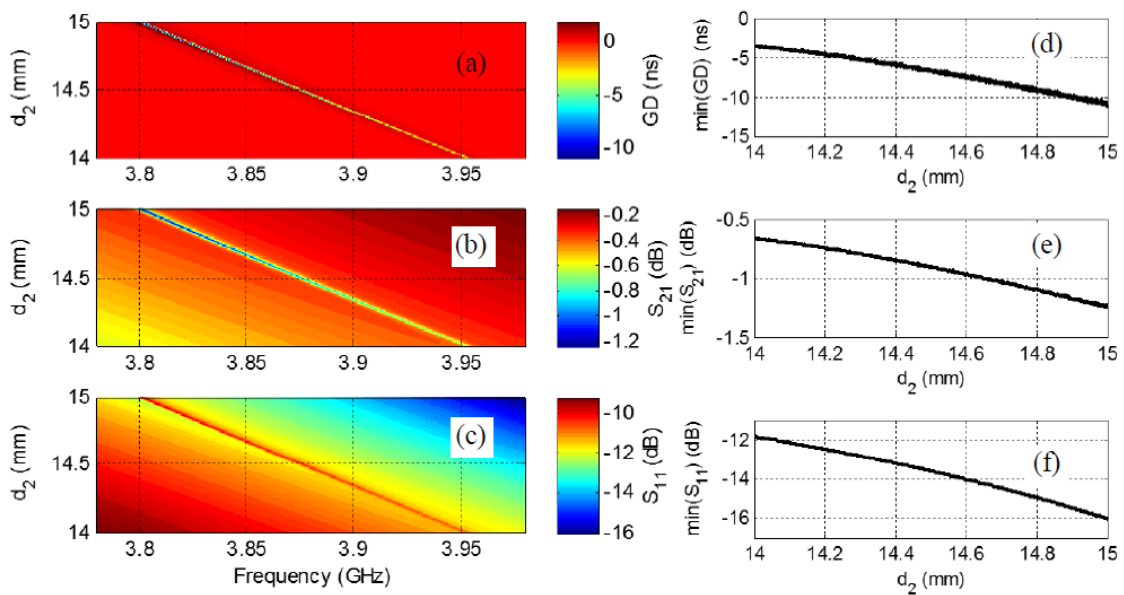
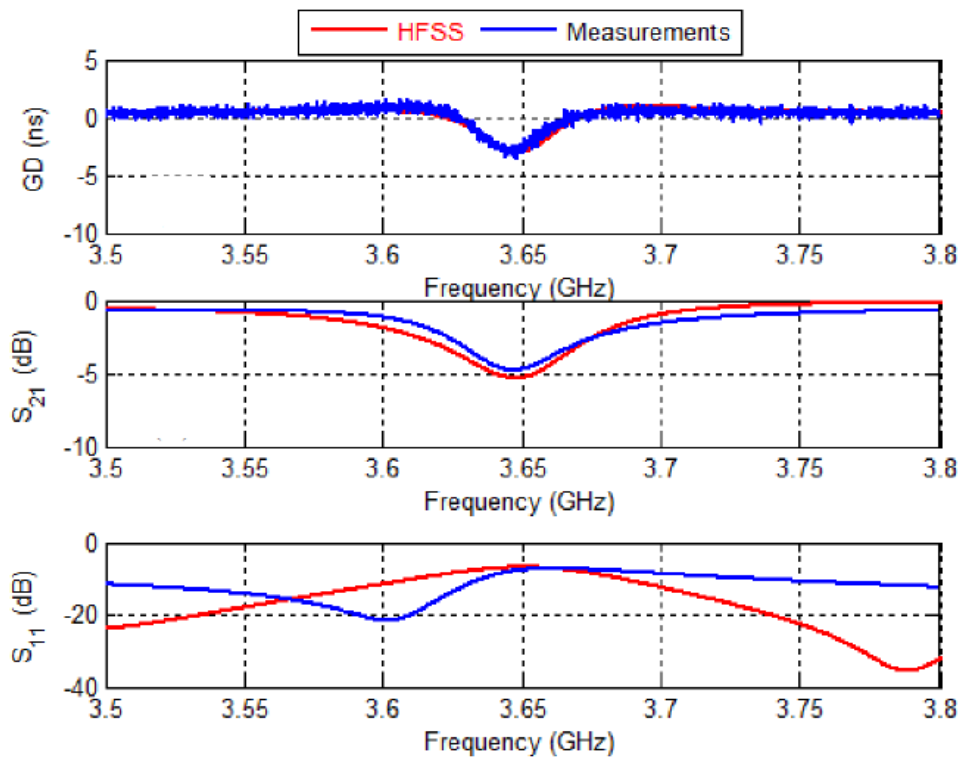


Figure 18 – Cartographies of (a) GD, (b) S_{21} and (c) S_{11} vs (f , d_2), and (d) $\min(\text{GD})$, (e) $\min(S_{21})$, and (f) $\min(S_{11})$ [37].



The sweep of the geometrical width w_1 and length d_2 enables to understand how they can influence the BP-NGD performances as seen in Figs. 17 and in Figs. 18. The BP-NGD behavior validity is verified with the results of Figs. 19. We have NGD center frequency around 3.65 GHz.

Figure 19 – Simulated and measured (a) GD, (b) S_{21} and (c) S_{11} of the ladder-circuit shown in Fig. 16 [37]



Owing to the hopeful research progress about the BP-NGD microstrip circuit design, all engineers and scientists are today wondering about the NGD RF and microwave electronic engineering application.

4. BRIEF DISCUSSION ON RF AND MICROWAVE ELECTRONIC ENGINEERING APPLICATIONS OF NGD CIRCUIT

The present chapter section is dedicated to brief discussion about the NGD circuit original and innovative applications. The NGD solutions introduced herein may revolutionize the future RF and microwave communication engineering. These applications are nowadays the NGD RF and microwave electronic circuit design future research work with industrial companies.

4.1. NGD CIRCUIT DESIGN APPLICATION CONTEXT

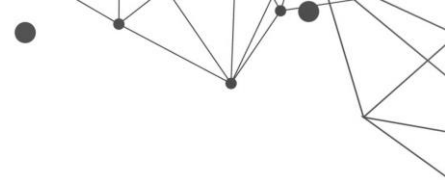
So far despite the progress of RF and microwave electronic engineering, the communication circuits and systems suffer from signal time delay as the electric interconnection effects in PCBs [78-79]. The NGD RF and microwave electronic engineering is the most promising solution against the time-delay problem in the communication systems and all electronic circuits. Since the late of 2000s, some potential tentative applications [80-113] were proposed in the literature. The present section describes basically some of them. But in few near future years, industrial funding's from small, medium and large RF and microwave communication engineering companies are expected to develop those potential applications.

4.2. DELAY COMPENSATION, CANCELLATION AND REDUCTION WITH NGD CIRCUITS [80-83]

With the increase of design complexity, the delay influences of electrical interconnection structures as PCB traces [78-79] and also transmission cables on the performance of electronic circuits and communication systems cannot be neglected. The natural applications of the NGD circuits are the possibility to compensate, cancel out and reduce the positive delay. The feasibility of this idea was theoretically and experimentally proved in different frequency bands as reported in [80-83]. These innovative applications are currently under exploitation for the design of new generation RF and microwave electronic PCBs in terms of signal integrity, electromagnetic compatibility (EMC) and electromagnetic interference (EMI) engineering.

4.3. ELECTRIC INTERCONNECT EQUALIZATION AND SIGNAL INTEGRITY (SI) IMPROVEMENT [84-93]

Because of the possibility to investigate the NGD circuits with S-parameter approach including the transmission and reflection coefficients, the NGD solution for the signal integrity improvement is expected to be the biggest application. By means of RC-, RLC- and RLCG- interconnect equivalent circuit models, different preliminary studies [84-93] are performed to verify the feasibility of this innovative idea. So far, the NGD circuit equalizer was experimented only with large size PCBs.



The industrial solutions in real-system as communication transceiver can be expected with integrated circuits in CMOS and MMIC technologies.

4.4. PULSE COMPRESSION WITH BP-NGD RF AND MICROWAVE CIRCUIT [94-95]

The RF and microwave pulse signals are used in many areas as radar, satellite, aeronautics and space engineering. One of issues limiting the performances of radar and space communication system is the pulse signal spreading. The compression technique with BP-NGD circuits are expected to be a potential candidate against this technical limitation. The feasibility of the pulse compression NGD technique was proposed in [94-95].

4.5. NGD TECHNIQUE OF RLC RESONANCE EFFECT REDUCTION FOR RF AND MICROWAVE EMC APPLICATION [96-98]

The resonance effects are very expensive for EMC and EMI engineers. By means of NGD equalization technique, it was analytically demonstrated with RLC-network based POC circuits that the BP-NGD circuits are capable to reduce cheaply the RLC resonance effect [96-98]. The possibility to solve this EMC and EMI issues was also verified by 3-D electromagnetic full wave simulations for example with different commercial tools as HFSS®, CST MWS® and FeKo®.

4.6. NGD SYNCHRONIZATION OF MULTI-BAND WIRELESS COMMUNICATION WITH 5G POTENTIAL APPLICATIONS [99-100]

The challenge of anywhere and anytime applications of 5G technology requires a challenge in term of delay synchronization of RF and microwave signal transmission. A preliminary study with multi-band BP-NGD circuit is promising for the feasibility of propagation delay effect reduction [99-100]. The GD spectral analyses allow to state the possibility to solve the problem related to the multi-band desynchronization.

4.7. RF AND MICROWAVE PHASE SHIFTER (PS) WITH NEGLECTED DELAY [101-106]

Most of classical RF and microwave PS suffers from delay effect which may induce some phase noise in the communication system. The NGD circuits constitutes a potential candidate as solution against such issues. Under a very good matching condition, by cascading a positive GD and NGD circuits, we can obtain a PS with delay theoretically equal to zero. This NGD PS RF and microwave design represents many promising solutions for the future 5G and 6G transceiver systems.

4.8. IMPROVEMENT OF RF AND MICROWAVE DEVICES PERFORMANCES WITH BP-NGD CIRCUITS FOR TRANSCEIVER COMMUNICATION SYSTEM APPLICATIONS [107-108]

Several concepts and applications of BP-NGD circuits for transceiver communication system and their constituting devices are suggested in [107]. The concept was extended to microwave broadband Balun in [108]. The development of power divider and combiner with operating under independent frequency is currently in progress. The NGD design solution is expected to improve the performances of wireless communication receiver as introduced in [109-110].

4.9. SOME LP-NGD CIRCUIT DESIGN POTENTIAL APPLICATIONS FOR LOW-FREQUENCY SENSORS AND ACTUATORS [111-113]

In addition to RF and microwave communication system, innovative ideas of LP-NGD application were also initiated. For example, it was experimentally demonstrated that the LP-NGD circuit permits:

- To reconstruct with very high correlation distorted arbitrary signals [111],
- To anticipate signals provided by industrial actuators [112],
- To pre-detect sensed signals with possibility to increase time-advance with multi-stage LP-NGD circuits [113].

5. CONCLUSIONS

The NGD is one of the most fascinating and counterintuitive electronic functions ever being investigated. A lot of questions about the methodology to design, implemented and test the BP-NGD circuits have been wondered by students, scientists, physicists, and even non-specialist RF and microwave design, fabrication, test and commercial engineers. As answer, a literature review on the BP-NGD microstrip circuit design is presented in this chapter. A non-exhaustive state of art on the generality about the NGD circuit, theory, design and engineering is introduced. Moreover, different types of NGD topologies inspired from filter theory are defined. The main focus on the design method and the analysis of different microstrip circuits is presented.

The future research works on the NGD engineering in the next two decades will be massively on the development of applications notably for the RF and microwave devices to improve front- and back-end communication system architecture. Nevertheless, many questions about the BP-NGD circuit integrability

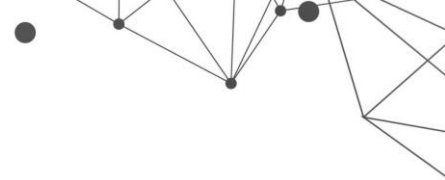
and testability are still open. Following the roadmap about the NGD electronic circuit utility, brief discussion on the NGD circuit potential applications are opened at the end of chapter.

ACKNOWLEDGEMENTS

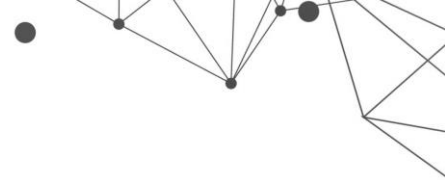
This research work was supported in part by FCT/MCTES through national funds and, when applicable, co-funded by the EU funds under the project UIDB/50008/2020-UIDP/50008/2020. This research work was also supported in part by NSFC under Grant 61971230, and in part by the Jiangsu Specially Appointed Professor program and Six Major Talents Summit of Jiangsu Province (2019-DZXX-022), and in part by the Startup Foundation for Introducing Talent of NUIST.

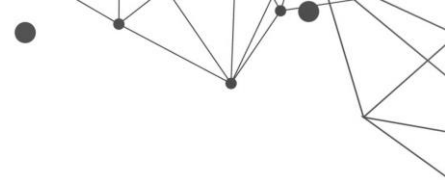
REFERENCES

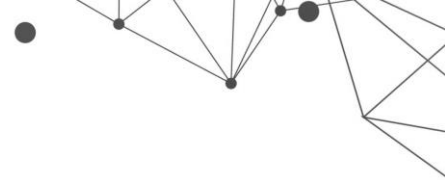
- [1] B. Ravelo, "Similitude between the NGD function and filter gain behaviours," *Int. J. Circ. Theor. Appl.*, vol. 42, no. 10, Oct. 2014, pp. 1016–1032.
- [2] B. Ravelo, "On the low-pass, high-pass, bandpass and stop-band NGD RF passive circuits", *URSI Radio Science Bulletin*, Vol. 2017, No. 363, Dec. 2017, pp. 10-27.
- [3] B. Ravelo, *Étude des circuits analogiques numériques NGD et leurs applications : Théorie fondamentale et expérimentations des circuits analogiques et numériques à temps négatif et leurs applications* (in French), Éditions Universitaires Européennes (EUE), Ed. by M. Fabre, 432 Pages, 13 Jan. 2012.
- [4] B. Ravelo, *Theory and Design of Analogue and Numerical Elementary NGD Circuits: Theoretical Characterization of Analogue and Numerical NGD Circuits*, LAP Lambert Academic Publishing, Germany, 352 pages, ISBN-13: 978-8484-1558-8, 14 Mar. 2012.
- [5] B. Ravelo, "First-order low-pass negative group delay passive topology," *Electronics Letters*, vol. 52, no. 2, Jan. 2016, pp. 124–126.
- [6] B. Ravelo, "Methodology of elementary negative group delay active topologies identification", *IET Circuits Devices Syst. (CDS)*, Vol. 7, No. 3, May 2013, pp. 105-113.
- [7] B. Ravelo, "Theory on negative time delay looped system", *IET Circuits, Devices & Systems*, Vol. 12, No. 2, Mar. 2018, pp. 175–181.
- [8] B. Ravelo, "Unity direct chain with feedback series impedance based innovative negative group delay circuit", *Int. J. Electron. Commun.*, Vol. 91, July 2018, pp. 11-17.
- [9] B. Ravelo, W. Rahajandraibe, M. Guerin, B. Agnus, P. Thakur and A. Thakur, "130-nm BiCMOS design of low-pass negative group delay integrated RL-circuit", *Int. J. Circ. Theor. Appl.*, Feb. 2022, pp. 1-17.
- [10] F. Wan, T. Gu, B. Li, B. Li, W. Rahajandraibe, M. Guerin, S. Lalléchère, and B. Ravelo, "Design and Experimentation of Inductorless Low-Pass NGD Integrated Circuit in 180-nm CMOS Technology", *IEEE Tran. CADICS*, Early Access, Dec. 2021, pp. 1-10.

- 
- [11] B. Ravelo, F. Wan, S. Lalléchére, W. Rahajandraibe, P. Thakur, and A. Thakur, "Innovative Theory of Low-Pass NGD Via-Hole-Ground Circuit," *IEEE Access*, Vol. 8, No. 1, Jul. 2020, pp. 130172-130182.
- [12] B. Ravelo, "Baseband NGD circuit with RF amplifier", *Electronic Letters*, Vol. 47, No. 13, June 2011, pp. 752-754.
- [13] R. Randriatsiferana, Y. Gan, F. Wan, W. Rahajandraibe, R. Vauché, N. M. Murad and B. Ravelo, "Study and Experimentation of a 6-dB Attenuation Low-Pass NGD Circuit," *Analog. Integr. Circ. Sig. Process.*, pp. 1-14, Apr. 2021.
- [14] F. Wan, Z. Yuan, B. Ravelo, J. Ge, and W. Rahajandraibe, "Low-Pass NGD Voice Signal Sensoring with Passive Circuit," *IEEE Sensors Journal*, Vol. 20, No. 12, June 2020, pp. 6762-6775.
- [15] B. Ravelo, "Demonstration of negative signal delay with short-duration transient pulse", *Eur. Phys. J. Appl. Phys. (EPJAP)*, Vol. 55 (10103), 2011, pp. 1-8.
- [16] F. Wan, T. Gu, B. Ravelo, B. Li, J. Cheng, Q. Yuan, and J. Ge, "Negative Group Delay Theory of a Four-Port RC-Network Feedback Operational Amplifier," *IEEE Access*, Vol. 7, No. 1, Dec. 2019, pp. 75708 - 75720.
- [17] F. Wan, J. Wang, B. Ravelo, J. Ge, and B. Li, "Time-Domain Experimentation of NGD Active RC-Network Cell", *IEEE Tran. CAS II: Express Briefs*, Vol. 66, No. 4, Apr. 2019, pp. 562-566.
- [18] B. Ravelo, "High-Pass Negative Group Delay RC-Network Impedance", *IEEE Tran. CAS II: Express Briefs*, Vol. 64, No. 9, Sept. 2017, pp. 1052-1056.
- [19] F. Wan, X. Huang, K. Gorshkov, B. Tishchuk, X. Hu, G. Chan, F. E. Sahoo, S. Baccar, M. Guerin, W. Rahajandraibe and B. Ravelo, "High-pass NGD characterization of resistive-inductive network based low-frequency circuit," *COMPEL - The International Journal for Computation and Mathematics in Electrical and Electronic Engineering*, Vol. 40, No. 5, pp. 1032-1049, 2021.
- [20] F. Wan, X. Huang, K. Gorshkov, B. Tishchuk, X. Hu, G. Chan, F. E. Sahoo, S. Baccar, M. Guerin, W. Rahajandraibe and B. Ravelo, "High-pass NGD characterization of resistive-inductive network based low-frequency circuit," *COMPEL - The International Journal for Computation and Mathematics in Electrical and Electronic Engineering*, Vol. 40, No. 5, pp. 1032-1049, 2021.
- [21] R. Yang, X. Zhou, S. Yazdani, E. Sambatra, F. Wan, S. Lalléchére and B. Ravelo, "Analysis, design and experimentation of high-pass negative group delay lumped circuit", *Circuit World*, Aug. 2021, pp. 1-25.
- [22] S. Fenni, F. Haddad, A. Jaomiary, S. S. Yazdani, F. E. Sahoo, L. Ramifidisoa, M. Guerin, W. Rahajandraibe, and B. Ravelo, "Investigation on four-port mono-capacitor circuit with high-pass negative group delay behavior", *Int. J. Circ. Theor. Appl.*, Vol. 50, No. 2, Feb. 2022, pp. 478-495.
- [23] M. Guerin, W. Rahajandraibe, G. Fontgalland, H. S. Silva, G. Chan, F. Wan, P. Thakur, A. Thakur, J. Frnda and B. Ravelo, "Theory and Original Design of Resistive-Inductive Network High-Pass Negative Group Delay Integrated Circuit in 130-nm CMOS Technology," *IEEE Access*, Vol. 10, No. 1, Mar. 2022, pp. 27147 - 27161.
- [24] F. Wan, L. Wang, Q. Ji and B. Ravelo, "Canonical transfer function of band-pass NGD circuit", *IET Circuits, Devices & Systems*, Vol. 13, No. 2, Mar. 2019, pp. 125-130.
- [25] B. Ravelo, S. Ngoho, G. Fontgalland, L. Rajaoarisoa, W. Rahajandraibe, R. Vauché, Z. Xu, F. Wan, J. Ge, and S. Lalléchére, "Original Theory of NGD Low Pass-High

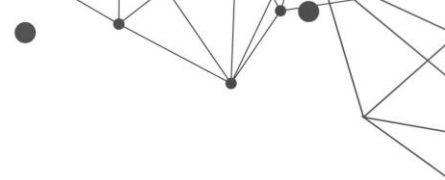
- Pass Composite Function for Designing Inductorless BP NGD Lumped Circuit,” *IEEE Access*, Vol. 8, No. 1, Oct. 2020, pp. 192951-192964.
- [26] Z. Xu, J. Nebhen, G. Chan, W. Rahajandraibe and B. Ravelo, “Innovative study of resistor shunt-based bridged-T topology with bandpass negative group delay behavior,” *Radio Science*, Vol. 56, No. 7, pp. 1-12, July 2021
- [27] S. Lalléchère, J. Nebhen, Y. Liu, G. Chan, G. Fontgalland, W. Rahajandraibe, F. Wan and B. Ravelo, “Suitability of passive RC-network-based inductorless bridged-T as a bandpass NGD circuit”, *Circuit World*, Nov. 2021, pp. 1-15.
- [28] M. Guerin, Y. Liu, A. Douyère, G. Chan, F. Wan, S. Lalléchère, W. Rahajandraibe, and B. Ravelo, “Design and Synthesis of Inductorless Passive Cell Operating as Stop-Band Negative Group Delay Function,” *IEEE Access*, Vol. 9, No. 1, July 2021, pp. 100141–100153.
- [29] S. Fenni, F. Haddad, K. Gorshkov, B. Tishchuk, A. Jaomiary, F. Marty, G. Chan, M. Guerin, W. Rahajandraibe and B. Ravelo, “AC low-frequency characterization of stop-band negative group delay circuit,” *Progress In Electromagnetics Research (PIER) C*, Vol. 115, pp. 261-276, 2021.
- [30] B. Ravelo, N. Li, F. Wan and J. Feng, “All-Pass Negative Group Delay Function with Transmission Line Feedback Topology,” *IEEE Access*, Vol. 7, No. 1, Dec. 2019, pp. 155711-155723.
- [31] B. Ravelo, “X-band negative group-delay lossy stub line”, *IET Microwaves, Antennas & Propagation*, Vol. 12, No. 1, Jan. 2018, pp. 137–143.
- [32] F. Wan, Y. Xu, and B. Ravelo, “Radial Stub Based-Negative Group Delay Circuit Theory”, *IET Microwaves, Antennas & Propagation*, Vol. 14, No. 6, May 2020, pp. 515-521.
- [33] B. Ravelo, “Negative Group-Delay Phenomenon Analysis with Distributed Parallel Interconnect Line”, *IEEE Tran. EMC*, Vol. 58, No. 2, Apr. 2016, pp. 573-580.
- [34] B. Ravelo, “Tee power divider and combiner based negative group delay topology”, *Int. J. RF and Microwave Computer-Aided Engineering*, Vol. 28, No. 9, Nov. 2018, pp. 1-9.
- [35] F. Wan, X. Huangi, P. Thakur, A. Thakur, S. Lalléchère, and B. Ravelo, “Negative group delay experimentation with tee connector and cable structures,” *Eur. Phys. J. Appl. Phys. (EPJAP)*, Vol. 91, No. 1 (10903), July 2020, pp. 1-11.
- [36] S. Ngoho, M. D. Camara, Y. Dong, A. Douyère, N. M. Murad, P. Thakur, A. Thakur, R. Randriatsiferana and B. Ravelo, “S-matrix based bandpass negative group delay innovative model of inverted parallel arm distributed topology,” *Journal of Electromagnetic Waves and Applications*, pp. 1-20, 2022.
- [37] S. Ngoho, Y. C. Mombo Boussougou, S. S. Yazdani, Y. Dong, N. M. Murad, S. Lalléchère, W. Rahajandraibe and B. Ravelo, “Design and modelling of ladder-shape topology generating bandpass NGD function,” *Progress In Electromagnetics Research (PIER) C*, Vol. 115, pp. 145-160, 2021.
- [38] T. Gu, F. Wan, J. Nebhen, N. M. Murad, J. Rossignol, S. Lallechere and B. Ravelo, “Bandpass NGD investigation of O-shape fully distributed structure with S-matrix modelling,” *COMPEL - The International Journal for Computation and Mathematics in Electrical and Electronic Engineering*, Vol. 40, No. 3, pp. 640-659, 2021.
- [39] F. Wan, N. Li, B. Ravelo, Q. Ji and J. Ge, “S-Parameter Model of Three Parallel Interconnect Lines Generating Negative Group-Delay Effect,” *IEEE Access*, Vol. 6, No. 1, Dec. 2018, pp. 57152-57159.

- 
- [40] B. Ravelo, L. Wu, F. Wan, W. Rahajandraibe and N. M. Murad, "Negative Group Delay Theory on li Topology," *IEEE Access*, Vol. 8, No. 1, Mar. 2020, pp. 47596-47606.
- [41] B. Ravelo, F. Wan and J. Feng, "Design, Modelling and Synthesis of Negative Group Delay IL-Shape Topology," *IEEE Access*, Vol. 7, No. 1, Dec. 2019, pp. 153900-153909.
- [42] X. Zhou, T. Gu, L. Wu, F. Wan, B. Li, N. M. Murad, S. Lalléchère, and B. Ravelo, "S-Matrix and Bandpass Negative Group Delay Innovative Theory of Ti-Geometrical Shape Microstrip Structure," *IEEE Access*, Vol. 8, No. 1, 2020, pp. 160363-160373.
- [43] F. Wan, B. Ravelo, N. Li, W. Rahajandraibe, and S. Lalléchère, "Design of \perp -Shape Stub Based Negative Group Delay Circuit," *IEEE Design & Test*, Vol. 38, No. 2, Apr. 2021, pp. 78-88.
- [44] B. Ravelo, "Theory on Coupled Line Coupler-Based Negative Group Delay Microwave Circuit," *IEEE Tran. MTT*, Vol. 64, No. 11, Nov. 2016, pp. 3604-3611.
- [45] F. Wan, L. Wu, B. Ravelo, and J. Ge, "Analysis of Interconnect Line Coupled with a Radial-Stub Terminated Negative Group Delay Circuit," *IEEE Tran. EMC*, Vol. 62, No. 5, Oct. 2020, pp. 1813-1821.
- [46] F. Wan, T. Gu, S. Lalléchère, J. Nebhen, and B. Ravelo, "NGD investigation on medusa-shape interconnect structure", *Int. J. RFMICAE*, Vol. 31, No. 10, Oct. 2021, pp. 1-22.
- [47] B. Ravelo, F. Wan, N. Li, Z. Xu, P. Thakur, and A. Thakur, "Diakoptics Modelling Applied to Flying Bird-Shape NGD Microstrip Circuit", *IEEE Tran. CAS II: Express Briefs*, Vol. 68, No. 2, Feb. 2021, pp. 637-641.
- [48] T. Gu, F. Wan, J. Nebhen, S. Lallechère and B. Ravelo, "Design engineering of tri-band Ulu-shape NGD circuit," *Radio Science*, Vol. 56, No. 7, pp. 1-16, July 2021.
- [49] F. Wan, N. Li, B. Ravelo, N. M. Murad and W. Rahajandraibe, "NGD Analysis of Turtle-Shape Microstrip Circuit", *IEEE Tran. CAS II: Express Briefs*, Vol. 67, No. 11, Nov. 2020, pp. 2477-2481.
- [50] F. Wan, T. Gu, B. Ravelo, and S. Lalléchère, "S-Parameter Model of IB-Shape Interconnect Lines Including Crosstalk Perturbation," *IEEE Tran. EMC*, Vol. 62, No. 6, Dec. 2020, pp. 2567 - 2575.
- [51] F. Wan, B. Liu, P. Thakur, A. Thakur, S. Lalléchère, W. Rahajandraibe, and B. Ravelo, "OIO-Shape PCB Trace Negative Group-Delay Analysis," *IEEE Access*, Vol. 8, No. 1, Dec. 2020, pp. 2169-3536.
- [52] B. Ravelo, F. Wan, S. Lalléchère, G. Fontgalland, and W. Rahajandraibe, "Design and Test of Crab-Shape Negative Group Delay Circuit," *IEEE Design & Test*, Vol. 39, No. 1, Feb. 2022, pp. 67-76.
- [53] F. Wan, T. Gu, S. Lalléchère, P. Thakur, A. Thakur, W. Rahajandraibe, and B. Ravelo, "Design and Test of Innovative Three Couplers-Based Bandpass Negative Group Delay Active Circuit," *IEEE Design & Test*, Vol. 39, No. 1, Feb. 2022, pp. 57-66.
- [54] H. Du, F. Wan, S. Lalléchère, W. Rahajandraibe and B. Ravelo, "Robustness Study of Bandpass NGD Behavior of Ring-Stub Microstrip Circuit Under Temperature Variation", *International Journal of Microwave and Wireless Technologies*, First View, Oct. 2021, pp. 1-9.
- [55] F. Wan, N. Li and B. Ravelo, "O=O Shape Low-Loss Negative Group Delay Microstrip Circuit", *IEEE Tran. CAS II: Express Briefs*, Vol. 67, No. 10, Oct. 2020, pp. 1795-1799.

- 
- [56] R. Yang, F. Wan and B. Ravelo, "Parametric geometrical study of 000-microstrip circuit with dual-band bandpass NGD behavior", *Radioengineering*, Vol. 30, No. 2, June 2021, pp. 1-10.
- [57] T. Gu, F. Wan, P. Thakur, A. Thakur, S. Lalléchère, W. Rahajandraibe and B. Ravelo, "Dielectric Resonator Negative Group Delay Circuit," *Radio Science*, Vol. 56, No. 4, pp. 1-13, Apr. 2021.
- [58] L. Wu, F. Wan, W. Rahajandraibe, S. Lalléchère and B. Ravelo, "On the investigation of contactless bandpass NGD control with microstrip patch-based circuit," *Journal of Electromagnetic Waves and Applications*, Vol. 34, No. 14, Aug. 2020, pp. 1849-1857.
- [59] B. Ravelo, "Investigation on microwave negative group delay circuit", *Electromagnetics*, Vol. 31, No. 8, Nov. 2011, pp. 537-549.
- [60] B. Ravelo, A. Perennec, M. Le Roy and Y. Boucher, "Active Microwave Circuit with Negative Group Delay", *IEEE MWCL*, Vol. 17, No. 12, Dec. 2007, pp. 861-863.
- [61] B. Ravelo, A. Perennec and M. Le Roy, "Negative Group Delay Active Topologies Respectively Dedicated to Microwave Frequencies and Baseband Signals", *Journal of the EuMA*, Vol. 4, June 2008, pp. 124-130.
- [62] B. Ravelo, "Synthesis of RF Circuits with Negative Time Delay by Using LNA", *Advanced Electromagnetics (AEM)*, Vol. 2, No. 1, Feb. 2013, pp. 44-54.
- [63] F. Wan, N. Li, B. Ravelo, Q. Ji, B. Li and J. Ge, "The Design Method of the Active Negative Group Delay Circuits Based on a Microwave Amplifier and an RL-series Network", *IEEE Access*, Vol. 6, No. 1, Dec. 2018, pp. 33849-33858.
- [64] B. Ravelo and S. De Blasi, "An FET-Based Microwave Active Circuit with Dual-Band Negative Group Delay", *JMOe*, Vol. 10, No. 2, Dec. 2011, pp. 355-366.
- [65] X. Zhou, B. Li, N. Li, B. Ravelo, X. Hu, Q. Ji, F. Wan and G. Fontgalland, "Analytical Design of Dual-Band Negative Group Delay Circuit with Multi-Coupled Lines," *IEEE Access*, Vol. 8, No. 1, Apr. 2020, pp. 72749-72756.
- [66] B. Ravelo, "Innovative Theory on Multiband Negative Group Delay Topology Based on Feedback Loop Power Combiner", *IEEE Tran. CAS II: Express Briefs*, Vol. 63, No. 8, Aug. 2016, pp. 738-742.
- [67] R. Vauché, R. A. Belhadj Mefteh, F. Haddad, W. Rahajandraibe, F. Wan, S. Lalléchère, G. Fontgalland, P. Thakur, A. Thakur and B. Ravelo, "Bandpass NGD Time-Domain Experimental Test of Double-li Microstrip Circuit," *IEEE Design & Test*, Vol. 39, No. 2, 2021, pp. 121-128.
- [68] X. Zhou, Z. Gu, Q. Ji, X. Hu, R. Vauché, F. Haddad, N. M. Murad, J. Frnda, W. Rahajandraibe, F. Wan and B. Ravelo, "Measurement characterization of bandpass NGD time-domain of 1010-topology passive circuit," *Radio Science*, pp. 1-17, 2022.
- [69] R. Vauché, R. Assila B. Mefteh, F. Haddad, J. Nebhen, W. Rahajandraibe, F. Wan, S. Lalléchère and B. Ravelo, "Experimental Time-Domain Study for Bandpass Negative Group Delay Analysis with lill-Shape Microstrip Circuit," *IEEE Access*, Vol. 9, No. 1, Feb. 2021, pp. 24155-24167.
- [70] L. Wu, F. Wan, R. A. Belhadj Mefteh, R. Vauché, G. Chan, X. Zhou, F. Haddad, W. Rahajandraibe and B. Ravelo, "Innovative Transient Study of Tri-Bandpass Negative Group Delay Applied to Microstrip Barcode-Circuit," *IEEE Access*, Vol. 9, No. 1, pp. 115030-115041, Aug. 2021.
- [71] J. Nebhen and B. Ravelo, "Bandpass NGD analysis of symmetric lumped Y-tree via tensorial analysis of networks formalism," *Journal of Electromagnetic Waves and Applications*, Vol. 35, No. 16, 2021, pp. 2125-2140.

- 
- [72] E. J. R. Sambatra, A. Jaomiary, S. Ngoho, S. S. Yazdani, N. M. Murad, G. Chan and B. Ravelo, "Low-pass negative group delay modelling and experimentation with tri-port resistorless passive cross-circuit," *PIER M*, Vol. 108, pp. 39-51, 2022.
- [73] H. Jia, F. Wan, J. Frnda, M. Guerin, W. Rahajandraibe, P. Thakur, A. Thakur, B. Agnus and B. Ravelo, "Novel Tee-Shaped Topology Theory of Low- and High-Pass NGD Double-Type Function," *IEEE Access*, Vol. 10, No. 1, 2022, pp. 28445 - 28460.
- [74] B. Ravelo, A. Douyère, Y. Liu, W. Rahajandraibe, F. Wan, G. Chan, and M. Guerin, "Fully Microstrip 3-Port Circuit Bandpass NGD Design and Test," *IEEE Design & Test*, Early Access, Mar. 2022, pp. 1-7.
- [75] F. Wan, Y. Liu, J. Nebhen, Z. Xu, G. Chan, S. Lalléchère, R. Vauche, W. Rahajandraibe and B. Ravelo, "Bandpass Negative Group Delay Theory of Fully Capacitive Δ -Network," *IEEE Access*, Vol. 9, No. 1, pp. 62430 - 62445, Apr. 2021.
- [76] B. Ravelo, J. Nebhen, M. Guerin, G. Chan and W. Rahajandraibe, "Tensorial-analysis-of-networks applied to bandpass negative-group-delay analysis of resistorless LC-coupler-network," *Radio Science*, pp. 1-18, 2022.
- [77] B. Ravelo, F. Wan, J. Nebhen, G. Chan, W. Rahajandraibe and S. Lalléchère, "Bandpass NGD TAN of Symmetric H-Tree with Resistorless Lumped-Network," *IEEE Access*, Vol. 9, pp. 41383-41396, Mar. 2021.
- [78] B. Ravelo, "Delay modelling of high-speed distributed interconnect for the signal integrity prediction", *Eur. Phys. J. Appl. Phys.*, Vol. 57 (31002), Feb. 2012, pp. 1-8.
- [79] B. Ravelo and O. Maurice, "Kron-Branin Modeling of Y-Y-Tree Interconnects for the PCB Signal Integrity Analysis", *IEEE Tran. EMC*, Vol. 59, No. 2, Apr. 2017, pp. 411-419.
- [80] B. Ravelo, S. Lalléchère, A. Thakur, A. Saini and P. Thakur, "Theory and circuit modelling of baseband and modulated signal delay compensations with low- and band-pass NGD effects", *Int. J. Electron. Commun.*, Vol. 70, No. 9, Sept. 2016, pp. 1122-1127.
- [81] T. Eudes and B. Ravelo, "Cancellation of Delays in the High-Rate Interconnects with UWB NGD Active Cells", *Applied Physics Research*, Vol. 3, No. 2, Nov. 2011, pp. 81-88.
- [82] F. Wan, X. Miao, B. Ravelo, Q. Yuan, J. Cheng, Q. Ji, and J. Ge, "Design of Multi-Scale Negative Group Delay Circuit for Sensors Signal Time-Delay Cancellation," *IEEE Sensors Journal*, Vol. 19, No. 19, Oct. 2019, pp. 8951-8962.
- [83] B. Ravelo and A. K. Jastrzebski, "UWB NGD Circuit for Time-Delay Reduction", *Proc. of 2012 Asia-Pacific Symposium on Electromagnetic Compatibility (APEMC 2012)*, Singapore, 21-24 May 2012, pp. 789-792.
- [84] B. Ravelo, A. Pérennec and M. Le Roy, « Equalization of Interconnect Propagation Delay with Negative Group Delay Active Circuits », *11th IEEE Workshop on Signal Propagation On Interconnects (SPI)*, Genova, Italy, 13-16 May 2007, pp. 15-18.
- [85] B. Ravelo, A. Pérennec and M. Le Roy, « Application of negative group delay active circuits to reduce the 50% propagation Delay of RC-line model », *12th IEEE Workshop on Signal Propagation on Interconnects (SPI)*, Avignon, France, 12-15 May 2008, pp. 1-4.
- [86] B. Ravelo, A. Pérennec and M. Le Roy, "Experimental Validation of the RC-Interconnect Effect Equalization with Negative Group Delay Active Circuit in

- Planar Hybrid Technology,” 13th IEEE Workshop on Signal Propagation on Interconnects (SPI), Strasbourg, France, 12-15 May 2009, pp. 1-4.
- [87] B. Ravelo, A. Perennec and M. Le Roy, “New Technique of Inter-Chip Interconnect Effects Equalization with Negative Group Delay Active Circuits”, VLSI, Chap. 20, Intech Book, Ed. by Prof. Z. Wang, ISBN: 978-953-307-049-0, Feb. 2010, pp. 409-434.
- [88] B. Ravelo, “Neutralization of LC- and RC-Effects with Left-Handed and NGD Circuits”, *Advanced Electromagnetics (AEM)*, Vol. 2, No. 1, Sept. 2013, pp. 73-84.
- [89] B. Ravelo and Y. Liu, “Microwave/Digital Signal Correction with Integrable NGD Circuits,” *Proc. of 2012 IEEE MTT-S International Microwave Symposium Digest (MTT)*, Montréal, QC, Canada, 17-22 June 2012, pp. 1-3.
- [90] B. Ravelo and J. Ben Hadj Slama, “Equalization of Digital/Mixed-Signal Disturbances with an Negative Group Delay Circuit,” *Proc. of 16th IEEE Mediterranean Electrotechnical Conference (MELECON 2012)*, Medine Yasmine Hammamet, Tunisia, 25-28 Mar. 2012, pp. 844-847.
- [91] B. Ravelo and A. K. Jastrzebski, “NGD circuit using a microwave amplifier for the signal integrity improvement”, *Proc. of 2012 Asia-Pacific Symposium on Electromagnetic Compatibility (APEMC 2012)*, Singapore, 21-24 May 2012, pp. 797-800.
- [92] B. Ravelo and F. Wan, “Low-Speed Signal Integrity Enhancement with Low-Pass NGD Function”, *Proc. of 13th International Workshop on Electromagnetic Compatibility of Integrated Circuits, EMC Compo 2019*, Hangzhou, China, 21-23 Oct. 2019, pp. 1-5.
- [93] B. Ravelo, “Recovery of Microwave-Digital Signal Integrity with NGD Circuits”, *Photonics and Optoelectronics (P&O)*, Vol. 2, No. 1, Jan. 2013, pp. 8-16.
- [94] B. Ravelo, A. Perennec and M. Le Roy, “Study and Application of Microwave Active Circuits with Negative Group Delay”, *Microwave and Millimeter Wave Technologies Modern UWB antennas and equipment*, Chap. 21, Intech Book, Ed. by Prof. I. Minin, ISBN: 978-953-7619-67-1, Mar. 2010, pp. 415- 439.
- [95] B. Ravelo, “Investigation on the microwave pulse signal compression with NGD circuit”, *PIER C*, Vol. 20, 2011, pp. 155-171.
- [96] B. Ravelo, F. Wan, J. Nebhen, W. Rahajandraibe, and S. Lalléchère, “Resonance Effect Reduction with Bandpass Negative Group Delay Fully Passive Function”, *IEEE Tran. CAS II: Express Briefs*, Vol. 68, No. 7, July 2021, pp. 2364-2368.
- [97] B. Ravelo, S. Lalléchère, W. Rahajandraibe, and F. Wan, “Electromagnetic Cavity Resonance Equalization with Bandpass Negative Group Delay,” *IEEE Tran. EMC*, Vol. 63, No. 4, Aug. 2021, pp. 1248-1257.
- [98] B. Ravelo, F. Wan, M. Guerin, W. Rahajandraibe, G. Fontagalland and G. Chan, “Resonance and Time-Delay Annihilation with Bandpass NGD Active Circuit (Invited)”, *Proc. of the 2022 3rd URSI AT-AP-RASC*, Gran Canaria, 29 May - 3 June 2022, pp. 1-4.
- [99] S. Lalléchère, L. Rajaoarisoa, L. Clavier, R. S. Galan and B. Ravelo, “Bandpass NGD function design for 5G microwave signal delay synchronization application (Conception de fonction NGD passe-bande pour la synchronisation des signaux 5G)”, *Comptes Rendus Physique (CRAS)*, Tome 22, no. S1, pp. 53-71, 2021.
- [100] F. Wan, N. Li, W. Rahajandraibe and B. Ravelo, “Reduction Technique of Differential Propagation Delay with Negative Group Delay Function,” *Proc. of IEEE EuCAP 2020*, Copenhagen, Denmark, 15-20 March 2020, pp. 1-5.

- 
- [101] B. Ravelo, A. Perennec and M. Le Roy, "Synthesis of frequency-independent phase shifters using negative group delay active circuit", *Int. J. RFMiCAE*, Vol. 21, No. 1, Jan. 2011, pp. 17-24.
- [102] B. Ravelo, M. Le Roy and A. Perennec, "Application of negative group delay active circuits to the design of broadband and constant phase shifters", *Microwave and Optical Technology Letters*, Vol. 50, No. 12, Dec. 2008, pp. 3077-3080.
- [103] B. Ravelo, M. Le Roy and A. Pérennec, "Frequency-Independent Active Phase Shifters for UWB applications," *Proc. of the 40th European Microwave Conference*, Paris, France, 28-30 Sept. 2010, pp. 1774-1777.
- [104] B. Ravelo, "Distributed NGD active circuit for RF-microwave communication", *Int. J. Electron. Commun.*, Vol. 68, No. 4, Apr. 2014, pp. 282-290.
- [105] J. Nebhen and B. Ravelo, "Innovative microwave design of frequency-independent passive phase shifter with LCL-network and bandpass NGD circuit," *PIER C*, Vol. 109, pp. 187-203, 2021.
- [106] B. Ravelo, G. Fontgalland, H. S. Silva, J. Nebhen, W. Rahajandraibe, M. Guerin, G. Chan, and F. Wan, "Original Application of Stop-Band Negative Group Delay Microwave Passive Circuit for Two-Step Stair Phase Shifter Designing," *IEEE Access*, Vol. 10, No. 1, 2022, pp. 1493-1508.
- [107] B. Ravelo, *Negative Group Delay Devices: From concept to applications*, IET Materials, Circuit and Devices Series 43, Publisher Michael Faraday House, Six Hills Way, Stevenage, Hertfordshire, UK, Ed. by Dr. B. Ravelo, 375 pages.
- [108] B. Ravelo, A. Perennec and M. Le Roy, "Broadband Balun Using Active Negative Group Delay Circuit," *Proc. of the 37th EuMC*, Munich, Germany, 8-12 Oct. 2007, pp. 466-469.
- [109] E. Zaraket, N. M. Murad, S. S. Yazdani, L. Rajaoarisoa and B. Ravelo, "An Overview on Low Energy Wake-up Radio Technology: Active and Passive Circuits Associated with MAC and Routing Protocols," *Journal of Network and Computer Applications*, Vol. 109, No. 103140, Sept. 2021, pp. 1-23.
- [110] N. M. Murad, L. Rajaoarisoa, S. Lalléchère, G. Fontgalland, and B. Ravelo, "Analysis of Microstrip Coupled Line Based Data-Signal and Energy Hybrid Receiver," *Journal of Electromagnetic Waves and Applications*, Vol. 34, No. 18, Sept. 2020, pp. 2433-2454.
- [111] B. Ravelo, W. Rahajandraibe, Y. Gan, F. Wan, N. M. Murad and A. Douyère, "Reconstruction Technique of Distorted Sensor Signals with Low-Pass NGD Function," *IEEE Access*, Vol. 8, No. 1, Dec. 2020, pp. 92182-92195.
- [112] B. Ravelo, F. Wan and J. Ge, "Anticipating Actuator Arbitrary Action with a Low-Pass Negative Group Delay Function," *IEEE Tran. IE*, Vol. 68, No. 1, Jan. 2021, pp. 694-702.
- [113] B. Ravelo, F. Wan, Z. Yuan and L. Rajaoarisoa, "Pre-Detection Sensing with Multi-Stage Low-Pass Type Negative Group Delay Circuit," *IEEE Sensors Journal*, Early Access, 2022, pp. 1-13.

OVERVIEW ON BANDPASS NGD BASED SIGNAL PROPAGATION DELAY SUPPRESSION FOR UAV BASE STATION CELLULAR NETWORK

DOI: 10.51859/amplla.sst631.1122-2

Valencia Lala¹
Wang Desheng²
Lala Rajaoarisoa³
Glauco Fontgalland Filho⁴
Glauco Fontgalland⁴
Preeti Thakur⁵
Atul Thakur⁵
Blaise Ravelo⁶

¹ Institut Supérieur de Technologie D'Antsiranana (IST-D), BP 509, Antsiranana 201, Madagascar

² Huazhong University of Science and Technology, Electronic Information and Communications, Wuhan, Hubei, China

³ IMT Nord Europe, University of Lille, Centre for Digital Systems, F-59000 Lille, France

⁴ Federal University of Campina Grande, Applied Electromagnetic and Microwave Lab., Campina Grande/PB, 58429, Brazil

⁵ Amity University Haryana, Gurgaon, 122413 India

⁶ Nanjing University of Information Science & Technology (NUIST), School of Electronic & Information Engineering Nanjing, China 210044.

ABSTRACT

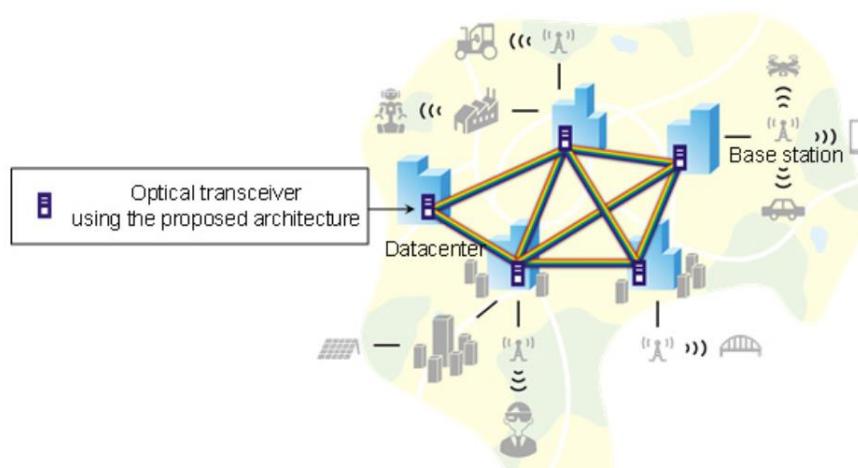
This paper presents a literature review on the propagation delay effect of microwave and millimeter wave (mmW) wireless network. The review study is focused on the cases of mobile wireless system based unmanned aerial vehicle (UAV) base station (BS) cellular network. The two last decades, the UAVs are exploited in 5G network and internet-of-things (IoT) to improve the performances of information communication technology (ICT). Different potential applications of UAV-BS in the modern urban cities are indicated. The main specifications of UAVs in wireless communication are presented. One of main parameters influencing the UAV-UAV and UAV-BS communication performance is the signal propagation delay issue. A potential future research on the improvement of mobile communication system using UAVs by using negative group delay (NGD) electronic function is reviewed. This unfamiliar NGD function enables to suppress the propagation signal delay.

Key words: Cellular network; Unmanned aerial vehicle (UAV) base station (BS); Mobile wireless system; Negative group delay (NGD); Delay suppression technique.

1. INTRODUCTION

Nowadays, the daily life dependence on the performances of microwave and millimeter wave (mmW) wireless system constituting the information communication technologies (ICTs) is incessantly increasing [1-13]. Behind this development, the microwave and mmW wireless engineering plays a key role for the development of ICT system [5-7]. We can understand from the illustrative scenario of Fig. 1 how the metropolitan area works with wireless network implemented in distributed computing platform [10].

Figure 1 – A metropolitan area datacenter network implementing a distributed computing platform.



Source: [10].

To meet the users' demand with respect to this urban city scenario, mobile communication network using internet of things (IoT) and smart things are expected as better solution [1-2,6-8]. The deployment of mobile network using different machines as unmanned aerial vehicle (UAV) as drone is expected as a solution to ensure the network reliability [14]. To satisfy the large number of users, a robust and reliable ICT network overcoming technological challenges and opportunities is required [14-17]. In addition, international telecommunication union (ITU) standards must also be complained [18]. As illustrated by Fig. 2, the IoT is identified as a key component of tomorrow's smart cities [8].

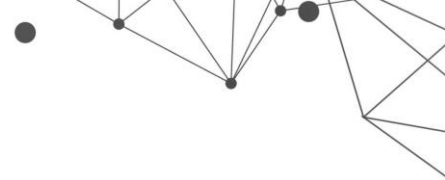
Figure 2 – Illustration of needs for IoTs in the scenario of smart city.



Source: [8].

Various studies have already invested in the wireless communication network based fifth generation (5G), technology to meet all the user's needs [3-11]. In addition, a review of different generations of emerging wireless ICTs has been made [10,19-26]. The growth of the number of mobile users and their demands involved the appearance of different generations of cellular network technology. From the first generation (1G) to the fourth generation (4G), there were differences in technology, functionality, services provided, and the device [27-30]. The 5G technology will be designed to meet all user needs with high quality and safety [27-30].

Different works introduced that using UAV as base stations (BSs) can bring a reliable and efficient alternative to coverage and capacity requirements for the 5G network [14,16,22]. A microwave and mmW wireless cellular network are the most widely used communication network in the world [1-10]. It allows different portable devices to communicate with each other via BSs. Before deploying BSs to serve the users, microwave and mmW wireless cellular network planning is necessary [31-32]. It allows finding the optimal locations for the BS that can serve the targeted area properly at a low cost [33-35]. For terrestrial and aerial BSs, the microwave and mmW wireless cellular network planning is different because of their difference in terms of characteristics and parameters. Planning UAV-base network communication is more complicated compared to ground cellular network planning. Drone-BSs can bring more benefits to the coverage and quality of service because of their high probability of the line-of-sight (LoS) link [33-35]. The use of



microwave and mmW wireless UAV-BS can bring advantages for certain situations in cellular network communications [15-17].

Despite the progress of UAV-BS cellular network ICT, technical challenges [14-17] are still to overcome to improve the performances and QoS. For example, the UAV-BS wireless system performance can be limited by the propagation signal delay signal from transmitter (Tx) to receiver (Rx). As solution on such delay issues, an unfamiliar delay suppression technique [36-37] and distorted signal reconstruction [38] based on negative group delay (NGD) electronic circuits was proposed. The innovative technique can be applied to improve UAV-BS wireless system communication via delay suppression. This UAV-UAV and UAV-BS system performance improvement principle can be integrated in Tx-Rx wireless communication of multi-point to single-point scenario. A modified aspect of delay suppression enables also to design frequency independent phase shifter operating with zero delay [39-42]. The basic principle of the NGD delay suppression techniques will be illustrated in the present paper.

2. CHALLENGING APPLICATIONS OF UAV WIRELESS SYSTEM

There are diverse applications of IoT and UAV devices. In the field of wireless networking, UAVs can serve as aerial BSs for different circumstances like public safety scenarios or hotspot coverage, caching apparatus or IoT enablers, and they also can be used as user equipment.

2.1. SMART CITIES WITH UAVS

Achieving a global vision of smart and connected cities is a major technological challenge [4-8]. Smart cities must effectively integrate several technologies and services such as the IoT environment, reliable wireless cellular network, resilience to disasters, and large amounts of data [43]. In smart cities, the 5G mmW frequency spectrum ICT has multiple use cases of applications [44]. As illustrated in Fig. 3, the 5G UAV wireless ICTs present significant complexity [44].

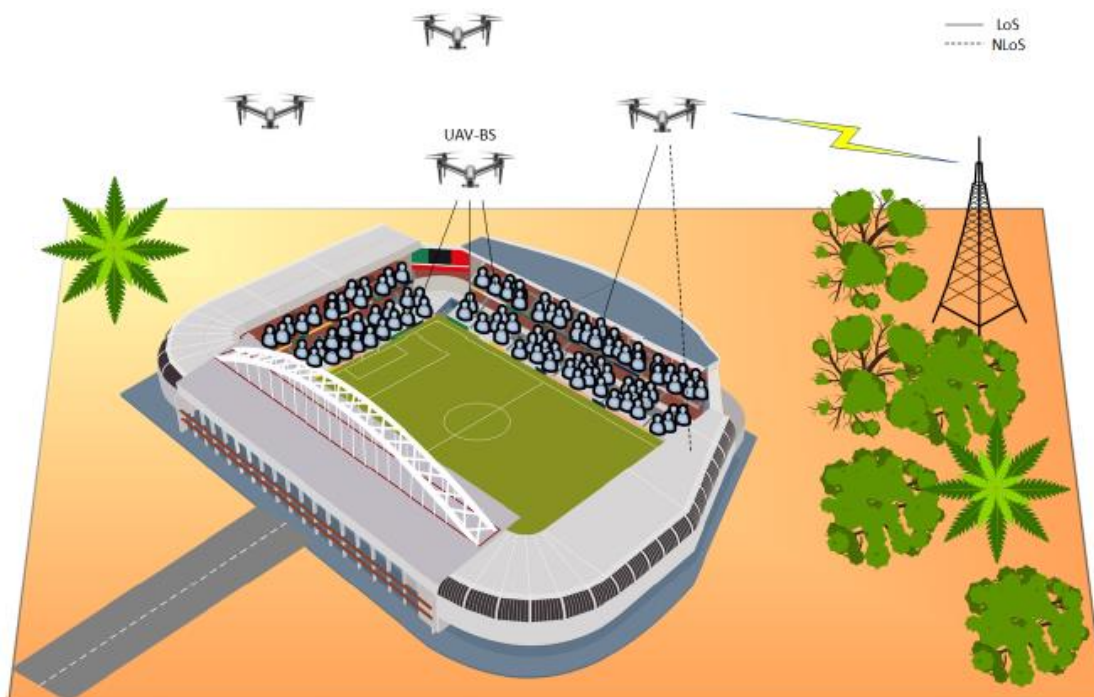
Figure 3 – Wireless communication city sketch of 5G mmW applications.



Source: [44].

For data collection, they can be used to collect large amounts of data from various geographic regions of a city and deliver it to cloud units for the big data analytics center. UAV-BSs can be deployed to improve cellular network coverage in cities or to meet emergency needs. Moreover, UAVs can serve as mobile cloud computing systems in smart cities [34]. Therefore, from wireless and operational prospects, UAVs will have an important part in smart cities. To ensure the wireless network performance, modelling and optimization techniques of UAV-BS cellular network system need to be developed. Fig. 4 shows the scenario of the sport event based on UAV-BS cellular network system with challenge on positioning.

Figure 4 – 3-D perspective view representing the UAV-BS system model of sport event scenario.

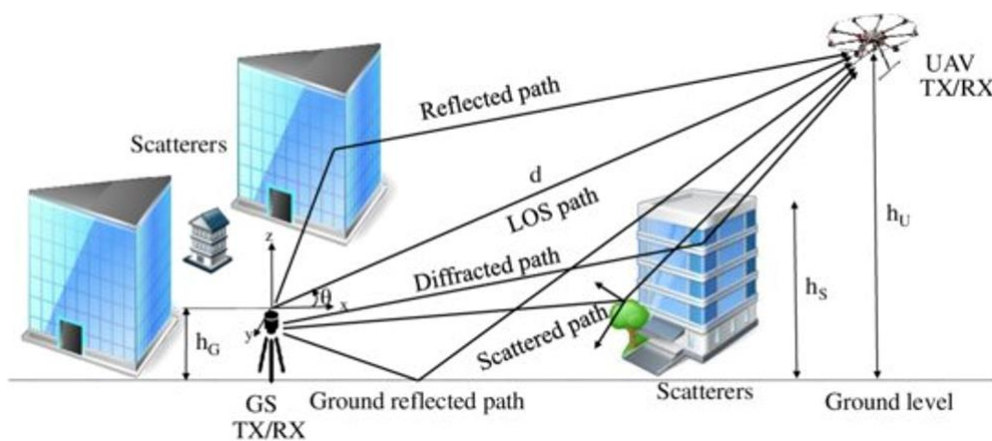


In this scenario, the main goal of optimization technique is to find the minimum number of UAV-BSs and their 3-D locations to serve users in the region. Mobility in one of the important features of the aerial BS, so it is helpful for the deployment based on the user's location. When the user moves, the drone-BS may take another position if needed. The number of users will refer to the seating capacity of the stadium.

2.2. UAVS TX/RX FOR IOT COMMUNICATIONS

The implication rapid of wireless network technologies into the IoT environment integrates a heterogeneous mix of devices such as smartphones, tablets, vehicles, sensors, wearables, and UAVs. The application of the IoT in smart cities, healthcare, transportation, and energy management requires efficient wireless connectivity between a large number of IoT devices [1-4,8]. In an IoT environment, reliability, ultra-low latency, and high-speed uplink communications are not typically the main challenges in cellular network use cases [31]. In particular, IoT devices have a battery limitation [2]. The mobile communicating devices are unable to transmit over a long distance due to their energy constraints. The use of mobile UAVs is an effective solution to solve the challenges of IoT networks. UAV-BSs can be deployed based on the locations of IoT devices, which enable those devices to connect to the network with a minimum transmit power. Moreover, they could be deployed in environments without ground wireless infrastructures like mountains and desert areas. A survey of Air-to-Ground (A2G) propagation channel modeling for UAVs as shown in Fig. 5 points out some problem signal interference and signal propagation delays [45].

Figure 5 – A typical A2G propagation scenario with a UAV.



Source: [45].

2.3. CACHE-ENABLED UAVS

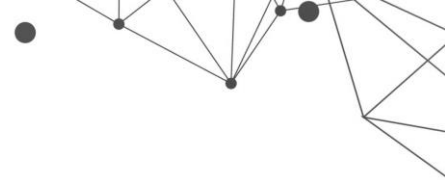
To enhance users' throughput and to reduce the transmission delay, one of the promising approaches is caching at small BSs (SBSs) [7]. In static terrestrial BSs, caching may not be effective in serving mobile users, especially in the case of frequent handovers like in ultra-dense networks with moving users. When users switch to a new cell, their request may not be available to the new BS, which involves that users' needs will not be met properly. To effectively serve those mobile users, each request content must be cached at multiple BSs, but it is not effective, due to signaling overheads and additional storage uses. Thus, deploying flexible BSs as UAVs is needed to improve caching efficiency because they can easily track the users' movement and deliver the required contents [35].

2.4. UAVS AS USER EQUIPMENT'S

As user equipment, UAVs can be used for surveillance, package delivery, and remote sensing. For instance, Amazon uses drones for delivery service and autonomous delivery for emergency drugs [46]. To enable IoT, the use of cellular-connected UAVs will be one of the important keys. Their mobility and their ability to optimize their path rapidly to complete their missions are the advantages of UAV-users. To properly deploy UAVs as user devices, reliable and low-latency communications are needed between UAVs and the ground BSs. Beyond those requirements, the use of UAV-users in surveillance purposes demand high-speed uplink communication from the ground network and other UAV-BSs. The current deployment for cellular networks may not be able to properly support UAVs as user devices. Because they were designed for ground users with operations, mobility, and traffic characteristics different from the UAV-users.

2.5. UAVS IN FLYING AD-HOC NETWORK

Flying ad-hoc networks (FANETs) is one of the use cases of UAVs which contain several UAVs communicate in an ad-hoc manner. Due to their mobility, FANETs can reinforce the connectivity and communication range in geographical regions with limited cellular infrastructure [47]. FANET plays a major role in several applications such as traffic monitoring, border surveillance, remote sensing, agricultural management, disaster management, forest fire management, and relay networks. Specifically, the use of UAVs to relay networks maintains reliable



communication between remote transmitters and receivers that cannot communicate directly due to obstacles or distances.

2.6. UAVS AS AERIAL BACKHAUL FOR TERRESTRIAL NETWORKS

For ground networks, the common approach to connect BSs to the core network is the wired backhauling. However, in ultra-dense cellular networks, this approach is not feasible, wired connections are expensive, and it also has geographical constraints [48]. Although wireless backhauling is a cost-effective and viable solution, it is limited due to blocking and interference that decreases the performance of the radio access network [49]. To overcome these limitations, UAVs can enable reliable, cost-effective, and high-speed wireless backhaul connectivity for terrestrial networks. To avoid obstacles and establish reliable communication links, UAVs can be deployed according to the users' locations. Furthermore, for high traffic demands in congested areas, high data rate wireless backhauling can be established by using UAVs with mmW capabilities. The flexibility of UAV-based backhaul networks can significantly enhance the capacity, reliability, and operation cost of backhauling for ground networks.

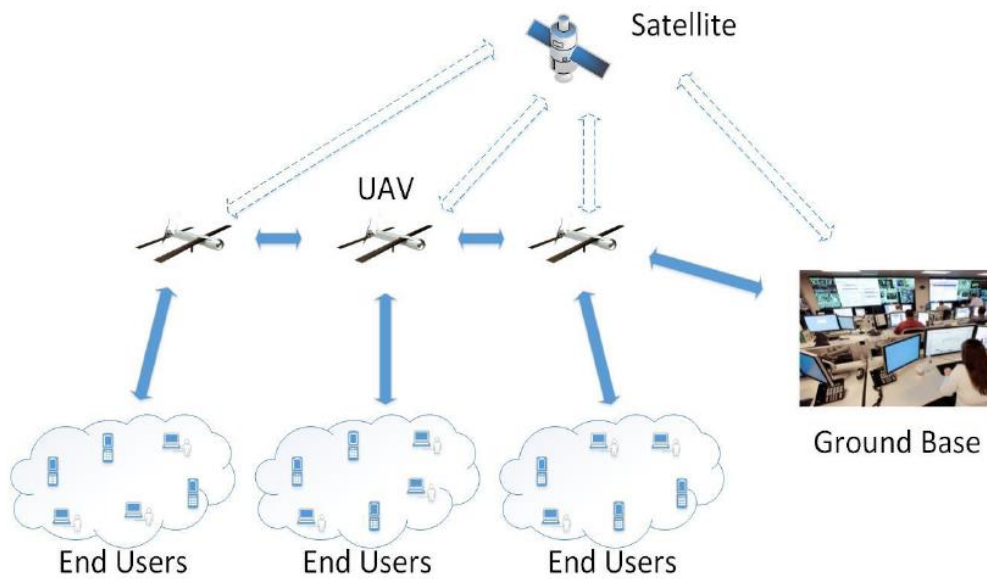
3. WIRELESS NETWORKING WITH UAV

In the field of wireless networking, UAVs can serve as aerial BSs for different circumstances like public safety scenarios or hotspot coverage, caching apparatus or IoT enablers, and they also can be used as user equipment.

3.1. UAVS AS AERIAL BSS FOR PUBLIC SAFETY

In different countries, natural disasters such as floods, tornadoes, hurricanes, and severe snowstorms can have devastating effects. The multi-UAV network as shown in Fig. 6 can be a better solution for such applications [50]. During or after natural disasters, terrestrial communication networks can be damaged or even destroyed, which will involve overloading to the other BSs as experienced after Hurricanes Sandy and Irma [32].

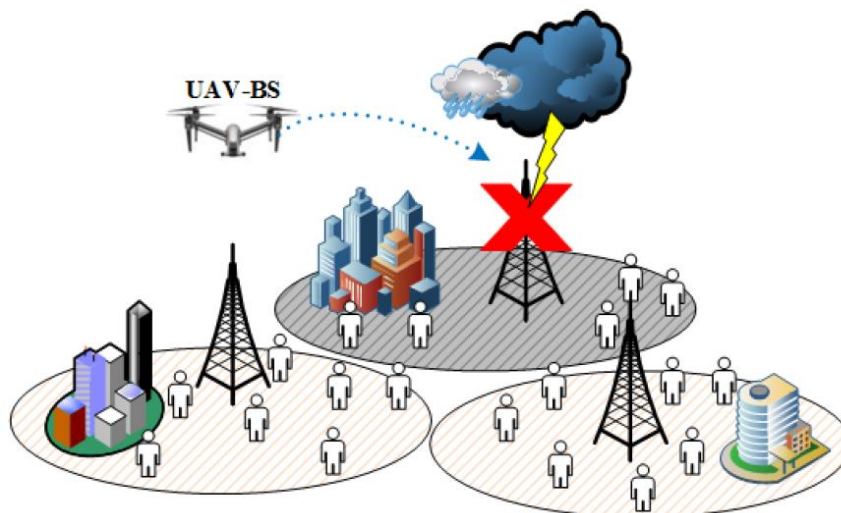
Figure 6 – Network model with multi-UAVs.



Source: [50].

In particular, during natural disasters, there is a vital need for a communications network for public safety because first responders must contact victims for search and rescue operations. In such situations, to enable a fast, flexible, and reliable wireless network, the use of UAV-based aerial networks is a promising solution [51], as shown in Fig. 7.

Figure 7 – UAV in public safety scenario.



Source: [51].

Since UAVs deployment does not need a highly expensive and constrained infrastructure, they can easily fly and change their positions dynamically to provide the required communications to ground users in an emergency. Thus, UAVs can be

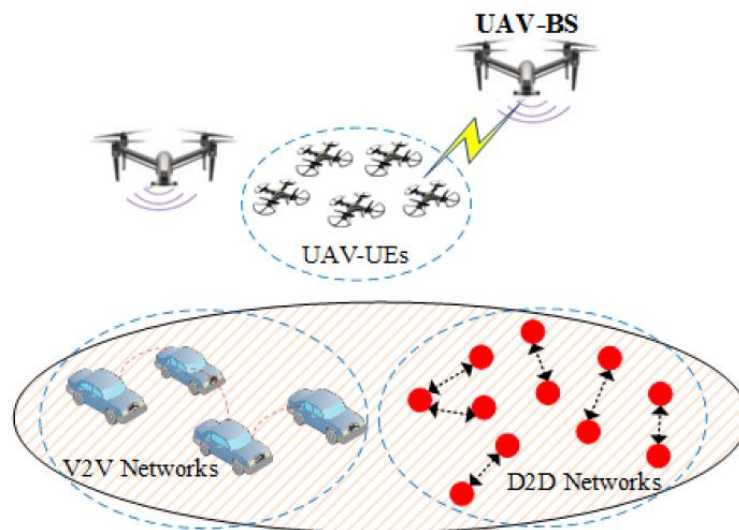
deployed as aerial BSs to provide broadband connectivity to the zones with damaged terrestrial wireless infrastructure. Moreover, it can be an appropriate solution to deliver a robust communication system in public safety scenarios.

3.2. UAV-ASSISTED GROUND NETWORKS FOR INFORMATION DISSEMINATION

UAVs can help terrestrial networks disseminate information and improve their connectivity because of their mobility and their high probability of having LoS connection [17]. Fig. 8 shows that drones can be deployed as aerial BSs to support a D2D network or an ad hoc mobile network in the dissemination of information.

In terms of offloading cellular data traffic and improving capacity and network coverage, D2D networks can offer an effective solution, but their performance is limited due to the devices' short range of communication, which could increase interference. In this case, UAVs can intelligently disseminate information by broadcasting common files between ground devices. Furthermore, by disseminating vehicle safety information, UAVs can play an important role in V2V communication networks. They can also enhance the reliability and connectivity of D2D and V2V communication channels.

Figure 8 – UAV-assisted terrestrial networks.



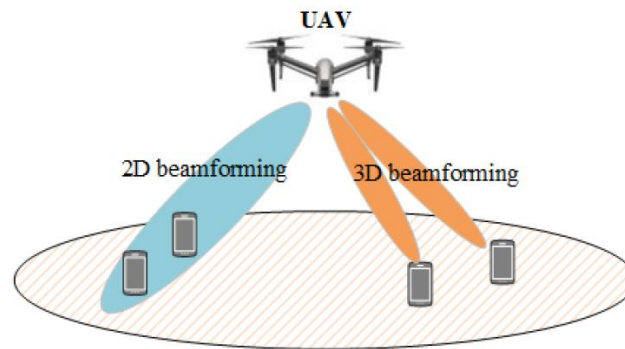
Source: [17].

3.3. 3-D MIMO AND MMW COMMUNICATIONS WITH UAVS

UAVs are considered flying antenna systems that can be used to perform massive MIMO, 3-D network and mmW communications because of their mobility and aerial positions. Recently, there is considerable interest in the use of 3-D MIMO

or full-dimension MIMO, by the exploitation of the horizontal and vertical dimensions in terrestrial cellular networks [52]. 3-D beamforming permits the establishment of separate beams in 3-D space at the same time, as shown in Fig. 9.

Figure 9 – 3-D beamforming using a UAV.



The 3-D MIMO solutions can provide higher system throughput and can support a larger number of users compared to the conventional 2-D MIMO. Generally, to serve a large number of users distributed in three dimensions with different elevation angles, 3-D MIMO is the more suitable solution. Therefore, UAV-BSs are the appropriate contestants for employing 3-D MIMO.

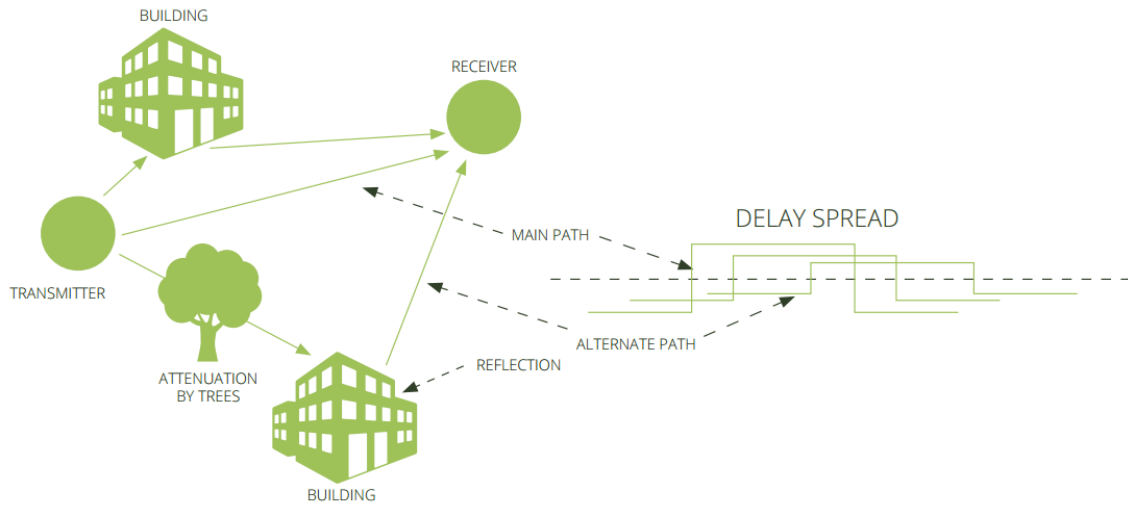
4. DELAY SUPPRESSION TX-RX WIRELESS SYSTEM WITH NGD FUNCTION

The present section introduces a future potential candidate [36-38] for suppressing the issue related to the signal propagation delay in the microwave and mmW wireless communication system. The technique can be applied to UAV-BS cellular network system. The following subsections explain the basic principle of the NGD microwave and mmW wireless propagation delay suppression technique.

4.1. PROPAGATION DELAY ISSUE IN MULTI-PATH TX-RX WIRELESS COMMUNICATION

As introduced earlier, the UAVs are present in different possibilities of TX-RX wireless communication applications. However, the 5G wireless communication scenarios of [44-45,49-50] are susceptible to present propagation delay issues during the multi-channel operating. An illustration of delay spread due to multipath propagation is illustrated by the scenario displayed in Fig. 10 [52].

Figure 10 – Illustration of multipath propagation and delay spread effect.



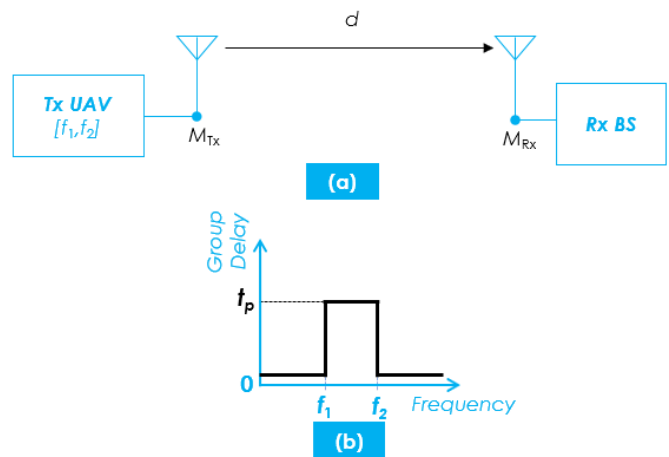
Source: [52].

Based on this scenario, we can imagine that multiple data can be transmitted from Tx-Rx wireless communication standards as WiFi, GSM, LTE or 5G [53-54].

4.2. DIAGRAM OF PROPAGATION DELAY SPECTRUM

The wireless communication system can be explained with the Tx and Rx equivalent diagram of Fig. 11(a). The propagation channel transmission system is supposed operating in the frequency band.

Figure 11 – (a) Synoptic and (b) group delay (GD) diagram of Tx-Rx system.



Source: [36].

Because of the signal travelling through distance $d=M_{Tx}M_{Rx}$, the communication is penalized by the propagation or also group delay (GD) supposed independent to f depicted by the delay diagram of Fig. 11(b):

$$t_{Tx \rightarrow Rx}(\omega) = \frac{d}{c} = t_p \quad (1)$$

with $c=300000$ km/s the speed of light and the angular frequency:

$$\omega = 2\pi f \quad (2)$$

4.3. BP-NGD FUNCTION PRINCIPLE

The bandpass (BP) NGD circuit classes [55] behave as an intriguing function recently attracting the attention of microwave and mmW engineers. Different investigations enable to emphasize that the BP-NGD aspect can be generated with various topologies of microstrip passive circuits [56-60]. By denoting the transmission phase $\varphi(\omega)$ of the BP-NGD microwave and mmW circuit black box shown in Fig. 12(a), the GD is mathematically defined by:

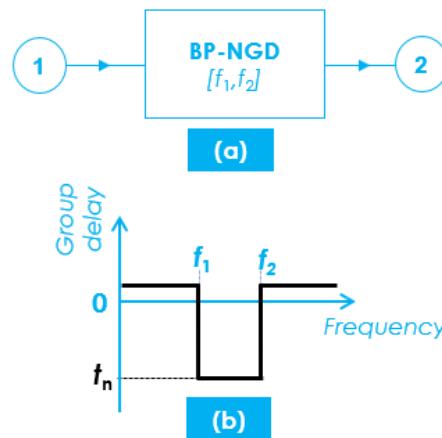
$$GD(\omega) = \frac{-\partial\varphi(\omega)}{\partial\omega} \quad (3)$$

Therefore, in the frequency domain, the BP-NGD identification can be performed with spectral analysis where the GD is becoming negative:

$$\tau(\omega) = t_n < 0 \quad (4)$$

in the frequency band $[f_1, f_2]$ can be represented in Fig. 12(b).

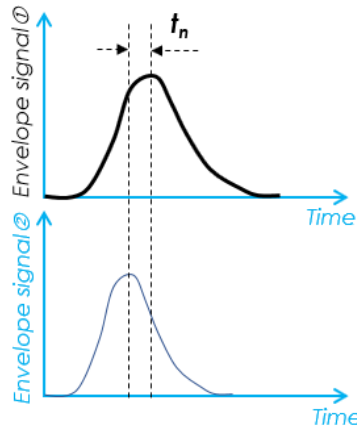
Figure 12 – (a) BP-NGD circuit black box with input ① and output ② and (b) the NGD delay spectrum diagram.



Source: [56-58].

In the time-domain, the spectrum of Fig. 13 is traduced by the properties to make output signal envelope leading and trailing edges travelling literally in advance compared to its own input envelope as experimented in [55]. This operation signal property was investigated with different microwave and mmW passive circuits [56-60].

Figure 13 – Illustration of NGD circuit input ① and output ② envelope chronograms.



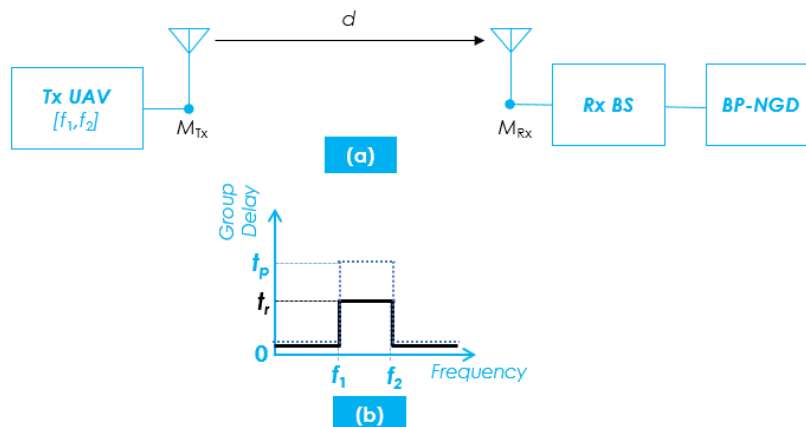
Source: [61-63].

4.4. BP-NGD BASED SIGNAL PROPAGATION DELAY SUPPRESSION PRINCIPLE

In the more current cases of multi-UAVs, information can be transmitted from UAV-UAV or UAV-BS included in a Tx-Rx system. The illustration of BP-NGD based delay suppression technique [36-38] between different UAV-UAV or UAV-BS is illustrated in Fig. 14(a). In this case, we assume that there is an ideal matching between the BP-NGD circuit and the output of Rx system. The impact of the UAV-BS delay suppression technique is highlighted by the time spectral budget shown in Fig. 14(b). In this spectrum, when the system operates in ideal condition, the corrected propagation delay is represented by:

$$t_r = t_p + t_n. \quad (5)$$

Figure 14 – (a) Tx-Rx system with BP-NGD circuit suppressor, and (b) delay spectrum diagram without and with NGD circuit.



Source: [36-37].

In other words, the total delay for each channel can be expected as:


$$delay_{total} = t_n + \frac{d}{c} . \quad (6)$$

5. CONCLUSIONS

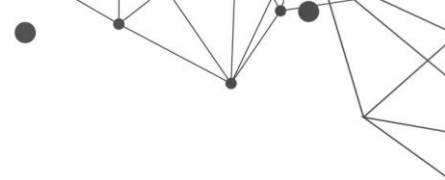
The mobile ICT using UAV or drone becomes ubiquitous in the today way of life. The different needs of 5G UAV-BS based microwave and mmW wireless ICTs are described. The state-of-the-art on wireless networking with UAVs including the classification and specifications added by technology regulation is synthesized. The principal social objectives of 5G technology and the challenges on UAV-BS design are indicated. The microwave and mmW propagation delay issues of wireless networking scenario using UAVs are also discussed. It is introduced how such delay issue can be suppressed with NGD delay suppression technique introduced in [36-38]. The operation principle of the propagation delay suppression the issue of signal propagation delay in the microwave and mmW wireless communication system is illustrated with spectral analysis.

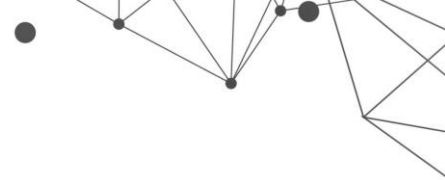
ACKNOWLEDGEMENTS

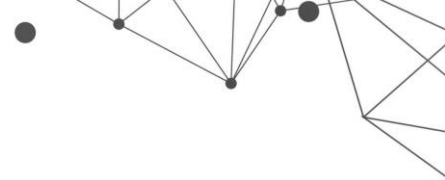
This research work was supported the Chinese government by Chinese Scholarship Council (CSC). This research work was also supported in part by NSFC under Grant 61971230, and in part by the Jiangsu Specially Appointed Professor program and Six Major Talents Summit of Jiangsu Province (2019-DZXX-022) and in part by the Startup Foundation for Introducing Talent of NUIST.

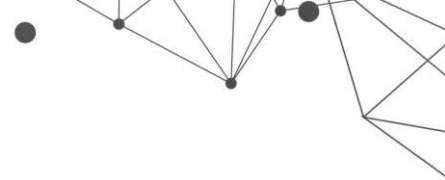
REFERENCES

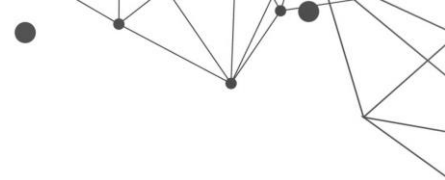
- [1] A. Zanella, N. Bui, A. Castellani, L. Vangelista and M. Zorzi, "Internet of things for smart cities," IEEE Internet of Things Journal, vol. 1, pp. 22–32, 02 2014.
- [2] M. Mozaffari, W. Saad, M. Bennis, and M. Debbah, "Mobile unmanned aerial vehicles (UAVs) for energy efficient internet of things communications," IEEE Transactions on Wireless Communications, vol. 16, no. 11, pp. 7574–7589, 2017.
- [3] Available online, accessed 28 March 2022, <https://5g-ppp.eu/>
- [4] Available online, accessed 28 March 2022, <https://www.urbanairmobilitynews.com/research/read-free-report-using-uam-to-advance-smart-cities/>

- 
- [5] Available online, accessed 28 March 2022, <https://www.techplayon.com/drone-wireless-video-transmission-technologies-challenges-probable-solutions/>
- [6] Siddique, Uzma and Tabassum, Hina and Hossain, Ekram and Kim, Dong In, “Wireless backhauling of 5G small cells: Challenges and solution approaches,” *IEEE Wireless Communications*, vol. 22, no. 5, pp. 22–31, 2015.
- [7] J. Qiao, Y. He and X. S. Shen, “Proactive caching for mobile video streaming in millimeter wave 5G networks,” *IEEE Transactions on Wireless Communications*, vol. 15, pp. 7187–7198, 10 2016.
- [8] Karl Torvmark, “Why Wi-Fi 6 Will Be a Key Component of Tomorrow’s IoT,” Nov. 2021, Accessed Mar. 28 2022, <https://www.mwrf.com/technologies/systems/article/21182182/nordic-semiconductor-why-wifi-6-will-be-a-key-component-of-tomorrows-iot>
- [9] Available online, accessed 25 March 2022, www.informationQ.com
- [10] Accessed Mar. 28 2022, <https://www.fujitsu.com/global/about/resources/news/press-releases/2016/0322-01.html>
- [11] J. Miranda, J. Cabral, S. Wagner, C. F. Pedersen, B. Ravelo, M. Memon and M. Mathiesen, “Open Platform for Seamless Sensor Support in Healthcare for the Internet of Things,” *Sensors*, Vol. 16, No. 2 (2089), 2016, pp. 1-22.
- [12] J. Miranda, M. Memon, J. Cabral, B. Ravelo, S. Wagner, C. F. Pedersen, M. Mathiesen and C. Nielsen, “Eye on Patient Care: Continuous Health Monitoring: Design and Implementation of a Wireless Platform for Healthcare Applications”, *IEEE Microwave Magazine*, Vol. 18, No. 12, Mar.-Apr. 2017, pp. 83-94.
- [13] J. Miranda, J. Cabral, B. Ravelo, S. Wagner, C. F. Pedersen, M. Memon and M. Mathiesen, “Radiated EMC immunity investigation of Common Recognition Identification Platform for medical applications”, *Eur. Phys. J. Appl. Phys. (EPJAP)*, Vol. 69, No. 1 (11002), Jan. 2015, pp. 1-8.
- [14] H. C. Nguyen, R. Amorim, J. Wigard, I. Z. Kovács, T. B. Sørensen, and P. E. Mogensen, “How to ensure reliable connectivity for aerial vehicles over cellular networks,” *IEEE Access*, vol. 6, pp. 12304–12317, 2018.
- [15] M. Mozaffari, W. Saad, M. Bennis, Y.-H. Nam, and M. Debbah, “A tutorial on UAVs for wireless networks: Applications, challenges, and open problems,” *IEEE Communications Surveys & Tutorials*, 2019.
- [16] A. Fotouhi, H. Qiang, M. Ding, M. Hassan, L. G. Giordano, A. Garcia-Rodriguez, and J. Yuan, “Survey on UAV cellular communications: Practical aspects, standardization advancements, regulation, and security challenges,” *IEEE Communications Surveys & Tutorials*, 2019.

- 
- [17] Y. Zeng, R. Zhang, and T. J. Lim, "Wireless communications with unmanned aerial vehicles: Opportunities and challenges," *IEEE Communications Magazine*, vol. 54, no. 5, pp. 36–42, 2016.
- [18] ETRI graphic, from ITU-R IMT 2020 requirements, Available online, accessed 25 March 2022, https://www.itu.int/itu-t/workprog/wp_item.aspx?isn=14091
- [19] A. Singh, "A review of different generations of mobile technology," *International Journal of Advanced Research in Computer Engineering & Technology*, vol. 4, 08 2015.
- [20] C.-X. Wang et al., "Cellular architecture and key technologies for 5G wireless communication networks," *IEEE Communications Magazine*, vol. 52, pp. 122–130, 02 2014.
- [21] P. K. Agyapong, M. Iwamura, D. Staehle, W. Kiess and A. Benjebbour, "Design considerations for a 5G network architecture," *IEEE Communications Magazine*, vol. 52, pp. 65–72, 11 2014.
- [22] R. Shahzadi, M. Ali, H. Z. Khan, and M. Naeem, "UAV assisted 5G and beyond wireless networks: A survey," *Journal of Network and Computer Applications*, Vol. 189, No. 103114, Sept.2021, pp. 1-20.
- [23] N. Bhushan, J. Li, D. Malladi, R. Gilmore, D. Brenner, A. Damnjanovic, R. T. Sukhavasi, C. Patel, and S. Geirhofer, "Network densification: the dominant theme for wireless evolution into 5G," *IEEE Communications Magazine*, vol. 52, no. 2, pp. 82–89, 2014.
- [24] M. Agiwal, A. Roy, and N. Saxena, "Next generation 5G wireless networks: A comprehensive survey," *IEEE Communications Surveys and Tutorials*, vol. 18, no. 3, pp. 1617–1655, 2016.
- [25] A. Gupta and R. K. Jha, "A survey of 5G network: Architecture and emerging technologies," *IEEE access*, vol. 3, pp. 1206–1232, 2015.
- [26] D. Liu, L. Wang, Y. Chen, M. ElKashlan, K. Wong, R. Schober, and L. Hanzo, "User association in 5G networks: A survey and an outlook," *IEEE Communications Surveys Tutorials*, vol. 18, no. 2, pp. 1018–1044, 2016.
- [27] P. Sharma, "Evolution of mobile wireless communication networks-1G to 5G as well as future prospective of next generation communication network," *IJCSMC*, vol. 2, pp. 47–53, 08 2013.
- [28] Kalra, Bharti and Chauhan, D, "A comparative study of mobile wireless communication network: 1G to 5G," *International Journal of Computer Science and Information Technology Research*, vol. 2, pp. 430–433, 09 2014.
- [29] Vivek Sanghvi Jain, Sanchit Jain, Lakshmi Kurup, Aruna Gawade, "Overview of generations of network: 1G, 2G, 3G, 4G, 5G," *IJCTA*, vol. 5, pp. 1789–1794, 10 2014.

- 
- [30] Mohammad Meraj ud in Mir, Dr. Sumit Kumar, “Evolution of mobile wireless technology from 0G to 5G,” *IJCSIT*, vol. 6, no. 3, pp. 2545–12551, 2015.
- [31] Z. Dawy, W. Saad, A. Ghosh, J. G. Andrews and E. Yaacoub, “Toward massive machine type cellular communications,” *IEEE Wireless Communications*, vol. 24, pp. 120–128, 02 2017.
- [32] K. Gomez, A. Hourani, L. Goratti, R. Riggio, S. Kandeepan and I. Bucaille, “Capacity evaluation of aerial LTE base-stations for public safety communications,” *European Conference on Networks and Communications (EuCNC)*, pp. 133–138, 2015.
- [33] A. Orsino, A. Ometov, G. Fodor, D. Moltchanov, L. Militano, S. Andreev, O. N. Yilmaz, T. Tirronen, J. Torsner, G. Araniti, et al., “Effects of heterogeneous mobility on D2-D and drone-assisted mission-critical MTC in 5G,” *IEEE Communications Magazine*, vol. 55, no. 2, pp. 79–87, 2017.
- [34] Jeong, Seongah and Simeone, Osvaldo and Kang, Joonhyuk, “Mobile edge computing via a UAV-mounted cloudlet: Optimal bit allocation and path planning,” *IEEE Transactions on Vehicular Technology*, Early access, 2017.
- [35] M. Chen, M. Mozaffari, W. Saad, C. Yin, M. Debbah and C. S. Hong, “Caching in the sky: Proactive deployment of Cache-Enabled unmanned aerial vehicles for optimized quality-of-experience,” *IEEE Journal on Selected Areas in Communications*, vol. 35, pp. 1046–1061, 05 2017.
- [36] S. Lalléchère, L. Rajaoarisoa, L. Clavier, R. Sanchez Galan, and B. Ravelo, “Bandpass NGD function design for 5G microwave signal delay synchronization application (Conception de fonction NGD passe-bande pour la synchronisation des signaux 5G)”, *Comptes Rendus Physique (CRAS)*, Tome 22, no. S1, pp. 53-71, 2021.
- [37] B. Ravelo, S. Lalléchère, A. Thakur, A. Saini and P. Thakur, “Theory and circuit modelling of baseband and modulated signal delay compensations with low-and band-pass NGD effects”, *Int. J. Electron. Commun.*, Vol. 70, No. 9, Sept. 2016, pp. 1122–1127.
- [38] B. Ravelo, W. Rahajandraibe, Y. Gan, F. Wan, N. M. Murad and A. Douyère, “Reconstruction Technique of Distorted Sensor Signals with Low-Pass NGD Function,” *IEEE Access*, Vol. 8, No. 1, Dec. 2020, pp. 92182-92195.
- [39] B. Ravelo, M. Le Roy and A. Perennec, “Application of negative group delay active circuits to the design of broadband and constant phase shifters”, *Microwave and Optical Technology Letters*, Vol. 50, No. 12, Dec. 2008, pp. 3077-3080.
- [40] B. Ravelo, A. Perennec and M. Le Roy, “Synthesis of frequency-independent phase shifters using negative group delay active circuit”, *Int. J. RF and Microwave Computer-Aided Engineering (RFMiCAE)*, Vol. 21, No. 1, Jan. 2011, pp. 17-24.

- 
- [41] B. Ravelo, "Distributed NGD active circuit for RF-microwave communication", *Int. J. Electron. Commun.*, Vol. 68, No. 4, Apr. 2014, pp. 282-290.
- [42] B. Ravelo, G. Fontgalland, H. S. Silva, J. Nebhen, W. Rahajandraibe, M. Guerin, G. Chan, and F. Wan, "Original Application of Stop-Band Negative Group Delay Microwave Passive Circuit for Two-Step Stair Phase Shifter Designing," *IEEE Access*, Vol. 10, No. 1, 2022, pp. 1493-1508.
- [43] Ferdowsi, Aidin and Saad, Walid and Mandayam, Narayan B, "Colonel blotto game for secure state estimation in interdependent critical infrastructure," *arXiv preprint arXiv:1709.09768*, 2017.
- [44] Available online, accessed 29 March 2022, https://resources.system-analysis.cadence.com/blog/msa2022-the-5g-millimeter-wave-frequency-spectrum-and-its-applications?utm_source=social&utm_medium=blog&utm_campaign=RF
- [45] W. Khawaja, I. Guvenc, D. W. Matolak, U. -C. Fiebig and N. Schneckenburger, "A Survey of Air-to-Ground Propagation Channel Modeling for Unmanned Aerial Vehicles," in *IEEE Communications Surveys & Tutorials*, vol. 21, no. 3, pp. 2361-2391, thirdquarter 2019, doi: 10.1109/COMST.2019.2915069.
- [46] D. Bamburly, "Drones: Designed for product delivery," *Design Management Review*, vol. 26, no. 1, pp. 40-48, 2015.
- [47] I. Bekmezci, O. K. Sahingoz, and S. Temel, "Flying ad-hoc networks (FANETs): A survey," *Ad Hoc Networks*, vol. 11, no. 3, pp. 1254-1270, 2013.
- [48] N. Bhushan, J. Li, D. Malladi, R. Gilmore, D. Brenner, A. Damnjanovic, R. T. Sukhavasi, C. Patel, and S. Geirhofer, "Network densification: the dominant theme for wireless evolution into 5G," *IEEE Communications Magazine*, vol. 52, no. 2, pp. 82-89, 2014.
- [49] Sixiao Wei, Linqiang Ge, Wei Yu, Genshe Chen, Khanh Pham, Erik Blasch, Dan Shen, and Chao Lu "Simulation study of unmanned aerial vehicle communication networks addressing bandwidth disruptions", *Proc. SPIE 9085, Sensors and Systems for Space Applications VII*, 908500 (3 June 2014).
- [50] A. Merwaday and I. Guvenc, "UAV assisted heterogeneous networks for public safety communications," *IEEE Wireless Communications and Networking Conference Workshops (WCNCW)*, pp. 329-334, 2015.
- [51] Y.-H. Nam et al., "Full-dimension MIMO (FD-MIMO) for next generation cellular technology," *IEEE Communications Magazine*, vol. 51, pp. 172-179, 06 2013.
- [52] Accessed Mar. 28 2022, <https://datarespons.com/drones-wireless-video/>
- [53] National Instruments, "The Race to 5G: The Latest 5G News and Analysis," Accessed Mar. 28 2022, <https://spectrum.ieee.org/static/the-race-to-5g>

- 
- [54] S. Arunachalam, S. Kumar, H. Kshatriya and M. Patil, “Analyzing 5G: Prospects of Future Technological Advancements in Mobile, International Conference on Innovative and Advanced Technologies in Engineering”, IOSR Journal of Engineering, pp. 6-11.
- [55] B. Ravelo, “Similitude between the NGD function and filter gain behaviours”, *Int. J. Circ. Theor. Appl.*, Vol. 42, No. 10, Oct. 2014, pp. 1016–1032.
- [56] B. Ravelo, “Negative Group-Delay Phenomenon Analysis with Distributed Parallel Interconnect Line”, *IEEE Transactions on Electromagnetic Compatibility*, Vol. 58, No. 2, Apr. 2016, pp. 573-580.
- [57] B. Ravelo, “Theory on Coupled Line Coupler-Based Negative Group Delay Microwave Circuit,” *IEEE Transactions on Microwave Theory and Techniques*, Vol. 64, No. 11, Nov. 2016, pp. 3604-3611.
- [58] B. Ravelo, “Innovative Theory on Multiband Negative Group Delay Topology Based on Feedback Loop Power Combiner”, *IEEE Transactions on Circuits and Systems II: Express Briefs*, Vol. 63, No. 8, Aug. 2016, pp. 738-742.
- [59] B. Ravelo, F. Wan and J. Feng, “Design, Modelling and Synthesis of Negative Group Delay IL-Shape Topology,” *IEEE Access*, Vol. 7, No. 1, Dec. 2019, pp. 153900-153909.
- [60] B. Ravelo, L. Wu, F. Wan, W. Rahajandraibe and N. M. Murad, “Negative Group Delay Theory on li Topology,” *IEEE Access*, Vol. 8, No. 1, Mar. 2020, pp. 47596-47606.
- [61] Rémy Vauché, Rym Assila Belhadj Mefteh, Fayrouz Haddad, Wenceslas Rahajandraibe, Fayu Wan, Sébastien Lalléchère, Glauco Fontgalland, Preeti Thakur, Atul Thakur and Blaise Ravelo, “Bandpass NGD Time-Domain Experimental Test of Double-li Microstrip Circuit,” *IEEE Design & Test*, Vol. 39, No. 2, 2021, pp. 121-128.
- [62] Rémy Vauché, Rym Assila Belhadj Mefteh, Fayrouz Haddad, Jamel Nebhen, Wenceslas Rahajandraibe, Fayu Wan, Sébastien Lalléchère and Blaise Ravelo, “Experimental Time-Domain Study for Bandpass Negative Group Delay Analysis with lill-Shape Microstrip Circuit,” *IEEE Access*, Vol. 9, No. 1, Feb. 2021, pp. 24155-24167.
- [63] Xiang Zhou, Zhaoyuan Gu, Qizheng Ji, Xiaofeng Hu, Rémy Vauché, Fayrouz Haddad, Nour Mohammad Murad, Jaroslav Frnda, Wenceslas Rahajandraibe, Fayu Wan and Blaise Ravelo, “Measurement characterization of bandpass NGD time-domain of 1010-topology passive circuit,” *Radio Science*, accepted, pp. 1-17, 2022.

A REVIEW OF RECENT RESULTS OF WHITE LIGHT GENERATION AND TUNABLE VISIBLE LIGHT EMISSION BY AG NANOCCLUSERS: UNDOPED AND DOPED Tm^{3+} / Yb^{3+} DOPED GeO_2 -PBO GLASSES

DOI: 10.51859/amplla.sst631.1122-3

Marcos Vinicius de Morais Nishimura¹
Camila Dias da Silva Bordon²
Lucas Magalhães Miretzcky³
Luciana Reyes Pires Kassab⁴

¹ Technologist in Materials, methods and electronic components from Faculdade de Tecnologia de São Paulo – FATEC-SP.

² MSc in Microelectronics from Escola Politécnica da Universidade de São Paulo – Poli-USP.

³ Technologist in Microelectronics from Faculdade de Tecnologia de São Paulo – FATEC-SP.

⁴ PhD in Nuclear Physics from Instituto de Física da USP – IFUSP.

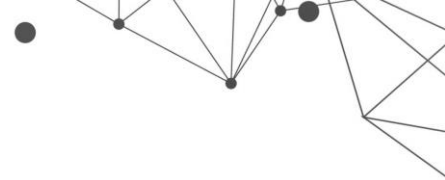
ABSTRACT

The incorporation of rare-earth ions and nucleation of metallic nanoparticles was largely explored in GeO_2 -PbO glasses. However silver nanoclusters were not investigated in the literature in this host. This fact motivated us to develop a methodology to produce these nanoclusters in GeO_2 -PbO glasses. The present work shows a review and also some new results regarding Ag nanoclusters in GeO_2 -PbO glasses undoped and doped with Yb^{3+} and Tm^{3+} ions. The melt-quenching technique was used to produce GeO_2 -PbO glasses prepared with $AgNO_3$, without and with Tm_2O_3 and Yb_2O_3 , followed by adequate annealing to reduce internal stress and using different temperatures (400 and 470 °C) to see the influence on Ag nanoclusters formation. So, annealing below and above the glass transition temperature was used to evaluate the best condition to produce Ag nanoclusters. Annealing below the glass transition temperature favors Ag nanoclusters production whereas above this temperature, Ag nanoparticles are easily obtained. Ag nanoclusters are amorphous and emit light, unlike Ag nanoparticles that are crystalline and do not exhibit luminescence. It is the clustering of Ag atoms and Ag^+ free ions that form Ag nanoclusters. Undoped samples with Ag nanoclusters showed tunable light emission from blue to orange, depending on the concentration of $AgNO_3$ used. Samples doped with Tm^{3+} and Yb^{3+} with Ag nanoclusters emitted white light for specific concentration of $AgNO_3$. This review demonstrates the potential of GeO_2 -PbO glasses with Ag nanoclusters for tunable visible light emission and for white light emitting devices applications.

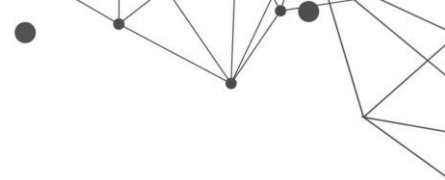
Key words: Glasses. Silver nanoclusters. Rare-earth ions.

1. INTRODUCTION

It is important to investigate and identify alternative low-cost materials for applications concerning photoluminescence emission in the visible and near infrared regions. The discovery of new glasses with luminescent Ag nanoclusters plays an important role as they represent a way to find alternative materials with low-cost for photonic and optoelectronic applications. The present study is motivated by the lack of reports of Ag nanoclusters in lead-germanium oxide glasses ($\text{GeO}_2\text{-PbO}$). They demonstrated to be suitable hosts for incorporation of rare earth ions. They exhibit large transmission window (400-5000 nm), stability against devitrification and a high refractive index (~ 2.0). Besides their low cut-off phonon energy ($\sim 800 \text{ cm}^{-1}$), in contrast to silicate and phosphate glasses, reduces the nonradiative losses, and allows high photoluminescence quantum efficiency and consequently radiative transitions that do not take place in materials with higher phonon energy. The optical response improvement of rare-earth ions doped $\text{GeO}_2\text{-PbO}$ glasses due to the nucleation of metallic (Ag/Au) nanoparticles was largely investigated (Karmakar, Rademann, & Stepanov, 2016; Rivera & Manzani, 2017; Raouf, 2018; Amjad, et al., 2014). In almost all the cases it was shown photoluminescence increase due to the plasmonic effects associated to the metallic nanoparticles. Then the enhanced linear and nonlinear optical properties showed several applications for photonics as cover to enhance Si solar cell performance, waveguides for operation at the infrared region (Carvalho, Kassab, Del Cacho, & Alayo, 2018), among others. All these facts combined with the absence of studies of Ag nanoclusters in $\text{GeO}_2\text{-PbO}$ glasses, motivated us to develop a methodology to form the aforementioned nanoclusters and investigate their influence on the optical properties of $\text{GeO}_2\text{-PbO}$ glasses undoped and doped with rare-earth ions. Ag nanoclusters are amorphous and emit light, unlike Ag nanoparticles that are crystalline, exhibit the localized surface plasmon resonance and are not luminescent (Fares, et al., 2017; Fares, Castro, Orives, Franco, & Nalin, 2017). It is the clustering of Ag atoms and Ag^+ free ions that form molecule like silver nanoclusters (also expressed as Ag_m^{X+} where m is the number of atoms and X is the charge) (Fares, Castro, Orives, Franco, & Nalin, 2017). Different colors can be generated by the nanoclusters, depending on their size and excitation wavelength, and different



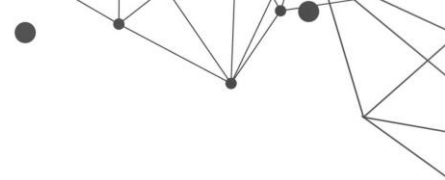
photonic applications can be found. UV driven flexible color monitors, mercury-free white light generation under UV pumping, tunable light sources/lasers, and solar cells (Lim, et al., 2004; Fares, et al., 2020), among others are some applications that have to be highlighted. Excitation in the 325-430 nm range demonstrated to be more efficient (Tikhomirov, et al., 2010) and typically Ag nanoclusters emission bands cover the visible and near-infrared region (350-750 nm). We cannot forget to mention the role of the host as the viscosity of the medium influences the diffusion of Ag atoms (Fares, Castro, Orives, Franco, & Nalin, 2017). Then the present work reviews recent results of white light generation and tunable visible light emission by Ag nanoclusters in undoped and Tm^{3+}/Yb^{3+} doped GeO_2 -PbO glasses; the production of silver (Ag) nanoclusters in GeO_2 -PbO glasses is performed by the melt-quenching technique followed by adequate annealing. The annealing was performed with different temperatures, below and above the glass transition temperature, to evaluate the best condition to produce Ag nanoclusters. The viscosity of the materials is managed by the annealing. Annealing below the glass transition temperature favors the growth of Ag nanoclusters as the diffusion of Ag ions is slower in the medium with high viscosity (Fares, et al., 2017). On the other hand, annealing above the glass transition temperature promotes a medium with lower viscosity and Ag nanoparticles are obtained easily. A detailed previous investigation (Nishimura, Bordon, Miretzcky, & Kassab, 2021) showed us that annealing above the glass transition temperature (470 °C) is more adequate to form Ag nanocrystalline nanoparticles, whereas above the glass transition temperature (420 °C), Ag nanoclusters are formed. This is explained by the viscosity of the material that is lower above glass transition temperature and consequently influences Ag^+ ions mobility making it more difficult to form Ag nanoparticles; on the other hand, as the viscosity of the material is higher, below glass transition temperature, it is easier to grow Ag nanoclusters. Based on these results we decided to investigate the influence of an even smaller annealing temperature (400 °C) and prepared GeO_2 -PbO samples with Ag nanoclusters, with and without Tm^{3+} and Yb^{3+} ions (Nishimura, Bordon, da Silva, & Kassab, 2021). The present review will show these results that demonstrated the potential for tunable visible light emission and also for white light emitting devices applications in different conditions: GeO_2 -PbO undoped samples with Ag nanoclusters showed tunable light emission from blue to orange, depending



on the concentration of AgNO₃ used whereas GeO₂-PbO samples doped with Tm³⁺ and Yb³⁺ with Ag nanoclusters emitted white light for specific concentration of AgNO₃. This work includes new results regarding the size of the Ag nanoclusters for samples prepared with different concentration of Ag nanoclusters and annealed 400 °C. The present work also reviews the influence of annealing temperature above glass transition temperature (470 °C) (Nishimura, Bordon, Miretzcky, & Kassab, 2021) in order to show the crystalline nanoparticles formed and also the plasmonic effects observed by absorption measurements. The intention is to highlight the importance of the annealing temperature used with respect to Ag nanoclusters growth in GeO₂-PbO glasses.

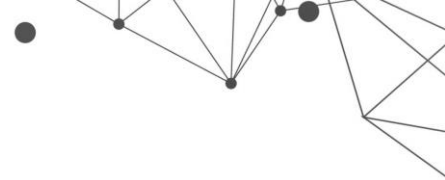
2. LITERATURE REVIEW

The energy levels of Ag nanoclusters presented are based on Velazquez model (Velázquez, et al., 2012). The electronic transitions occur either around the blue (S₁→S₀), the green-yellow (T₂→S₀) and the yellow-red range (T₁→S₀) of the spectrum. Although it is possible to obtain several applications with glasses with Ag nanocluster, the addition of rare-earth ions also represents an interesting alternative for several technological applications. At high concentration Ag nanoclusters tend to easily agglomerate into metallic Ag nanoparticles and lose their broad emission in the visible range. Besides many factors influence the size distribution of the nanoclusters as the annealing, Ag concentration, glass network changes and rare-earth doping. It has also been reported that the photoluminescence of rare-earth dopants may be enhanced in glasses embedded with larger Ag nanoclusters with sizes ranging from 5 to 10 nm. In these cases, the Ag nanoclusters emit themselves visible light and transfer part of the excitation energy to the rare-earth ions (Tikhomirov, et al., 2012). Moreover, the efficient energy transfer from Ag nanoclusters to the rare-earth ions results in the emission of both, nanoclusters and rare-earth ions, whose photoluminescence bands can be mixed to produce tunable visible emission and white light (Tikhomirov, et al., 2012). The control of these emissions can be achieved by changing the doping levels, chemical composition of the host glass or excitation wavelength. In this section we review recent results of undoped and rare-earth ions doped glasses with Ag nanoclusters in different hosts as in oxyfluorides (Tikhomirov, et al., 2012),



fluorophosphates (Fares, et al., 2017; Fares, Castro, Orives, Franco, & Nalin, 2017; Fares, et al., 2020; Castro, et al., 2019), zinc borate (Liu, Guo, Ye, Peng, & Zhang, 2015) and CaBAI (Sandrini, et al., 2018).

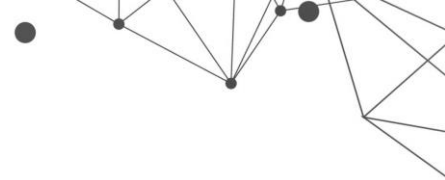
Inorganic glasses, such as oxyfluoride, have been proven to be suitable hosts providing stability and homogeneous dispersion for Ag nanoclusters. Oxyfluoride glasses with Ag nanoclusters and Yb³⁺ ions also presented the role of the energy transfer mechanism to promote enhanced luminescence of the rare-earth ions in the infrared region (Tikhomirov, et al., 2012). In this case Yb³⁺ emission at 1000 nm was reached by resonant and non-resonant excitation of Ag nanoclusters. We highlight that this was one of the first report regarding the interaction between rare-earth ions and nanoclusters. It was demonstrated for the first time the feasibility of producing luminescence 3D waveguides by fluorophosphate glasses with Ag nanoclusters; the influence of the particle size on the emission properties of Ag nanoclusters was also presented as well as the use of the melt-quenching technique to produce the glasses (Fares, et al., 2017). Besides, in this report a detailed study showed the importance of the material viscosity and of the adequate temperature for the annealing, with respect to the glass transition temperature, to obtain Ag nanoclusters. It was shown that the silver concentration has to be carefully adjusted and that adequate annealing (temperature and time) led to glasses with interesting properties for several photonic applications. Moreover, using the same host, the authors showed white light and tunable visible light emission by Ag nanoclusters (Fares, et al., 2017; Fares, Castro, Orives, Franco, & Nalin, 2017). Fluorophosphate glasses codoped with Tm³⁺ and Mn²⁺ ions also reported tunable multicolor emission attributed to the presence of Ag nanocluster and the energy transfer process between them and the rare-earth ions (Fares, et al., 2020). Taking the advantage of the above-mentioned sensitizer behavior of Ag nanoclusters, the visible Tm³⁺ and Mn²⁺ emission could be obtained via Ag nanoclusters excitation at 270, 290 and 310 nm where Tm³⁺ and Mn²⁺ do not have absorption. The typical blue emission of Tm³⁺ ions at 450 and 480 nm, and the red emission of the Mn²⁺ ranging from 560 to 760 nm were observed and tunable light emission from blue to white was obtained. Such results proved the energy transfer process from Ag nanoclusters to Tm³⁺ and Mn²⁺ ions and revealed that blue, green and red nanoclusters could sensitize the Tm³⁺ and Mn²⁺ ions. In fact, the samples without rare-earth ions showed a broad band



emission covering the whole visible spectrum, from 400 to 700 nm, and a redshift with increasing excitation wavelength, attributed to the emission of nanoclusters with different sizes. Another example of the use of fluorophosphates glasses with Ag nanoclusters and codoped with $\text{Pr}^{3+}/\text{Yb}^{3+}$ was reported and demonstrated tunable visible emission and energy transfer from Ag nanoclusters to $\text{Pr}^{3+}/\text{Yb}^{3+}$ ions for different Ag concentration (Castro, et al., 2019). It was noticed that for excitation at 240 nm the Ag nanocluster response predominates covering the visible to the near infrared region, and the increase of the Ag concentration promotes a quenching of the rare- earth ions luminescence. However, for longer wavelength (>370 nm), the rare- earth ions emission predominates and even increases with the Ag concentration growth. Transparent Ag/Mn^{2+} codoped zinc borate glasses demonstrated enhanced tunable color emission for broad band light source applications (Liu, Guo, Ye, Peng, & Zhang, 2015). The tunable broadband emission is achieved by the selection of either proper Mn^{2+} content or excitation wavelength. It was demonstrated that efficient energy transfer takes place not only from isolated Ag^+ to Mn^{2+} ions, but from Ag nanoclusters to Mn^{2+} , as well. It was also reported that increase of Mn^{2+} contributed to the generation of more Ag nanoclusters, that led to the enhancement of emission intensity by 13 times, which was not expected. An important contribution of this study that has to be point out is the investigation of the interaction mechanism between noble metal nanoclusters and transition metal. Eu^{3+} doped CABAl glasses (Sandrini, et al., 2018) with Ag nanoclusters showed to be adequate materials for tunable white light emission too. A significant intensity increases in Eu^{3+} emission and a lifetime decrease for Ag nanocluster emission were observed under 335 nm excitation, reinforcing the assumption of an energy transfer process. In this investigation glasses exhibited an intense wide emission band centered at about 500 nm, due to Ag nanoclusters, which combined with the Eu^{3+} ions characteristic emission produces white light. All these examples motivated the use of GeO_2 - PbO glasses to host Ag nanoclusters undoped and doped with rare-earth ions in order to cover the lack in the literature regarding this host.

3. MATERIALS AND METHODS

Glasses with composition 40 GeO_2 -60 PbO (GP) (in wt%) were prepared adding Tm_2O_3 (1.5 wt%), Yb_2O_3 (2.0 wt%) and AgNO_3 (2.25/4.5 wt%) to the original

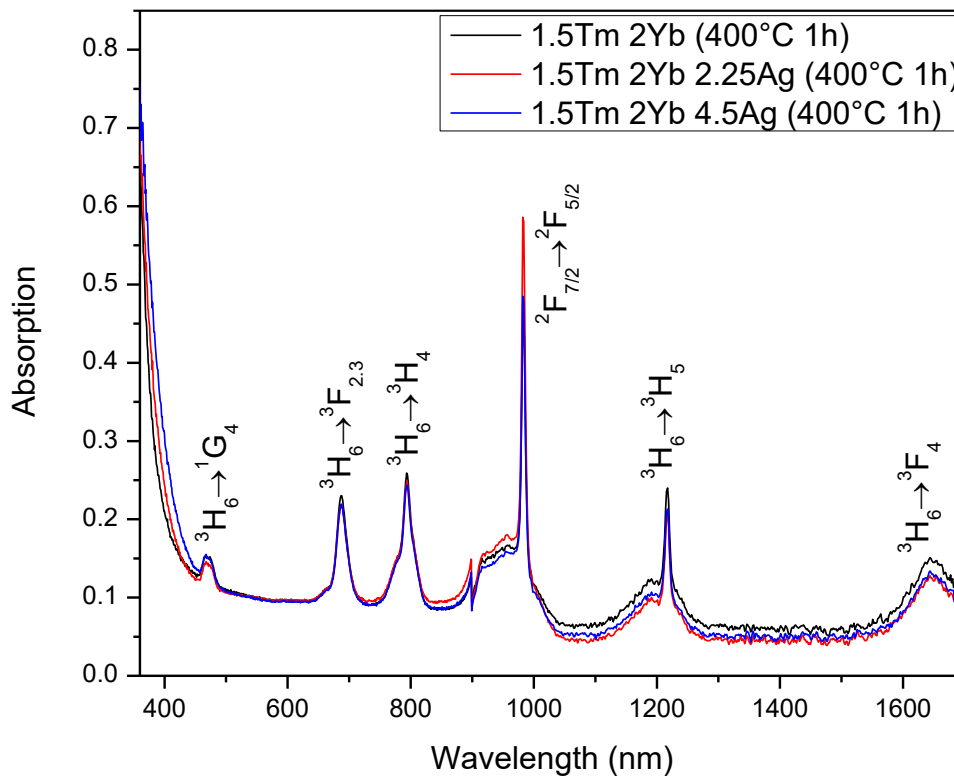


composition. Samples with only AgNO_3 (2.25/4.5 wt%) were prepared with only Tm_2O_3 and Yb_2O_3 . The reagents were melted in an alumina crucible for 1 h at 1200 °C, quenched in air in a preheated brass mold, and annealed at 400 °C, below the glass transition temperature for 1 h in order to reduce internal stress. Samples prepared with only 4.5 wt% of AgNO_3 were annealed at 470 °C, above the glass transition temperature. Bases on previous experiments (Nishimura, Bordon, Miretzcky, & Kassab, 2021) we noticed that this procedure made it easier the formation of Ag crystalline nanoparticles, and that is why we included in the present review. Then, after the annealing the samples were then polished and cut to be characterized. The linear optical absorption spectra were measured with a OceanOptics QE65 PRO spectrophotometer operating from 400 to 800 nm. Photoluminescent experiments were performed by different ways, as follows. Samples were excited by an Optical Parametric Oscillator (OPO), OPOTEK INC., Opollete™ HE 355 LD model pumped by the third harmonic of a Q-switched Nd: YAG laser (5 ns, 20 Hz). In this case the excitation wavelength was tuned to at 355 nm. The light beam from the OPO was focused on the sample and then collected in a direction perpendicular to the incident beam by an optical fiber connected to the mentioned OceanOptics spectrophotometer. A filter was positioned at the entrance of the spectrophotometer fiber to remove the laser harmonic signal at 710 nm. Photoluminescent measurements were also performed with a commercial broadband ultraviolet lamp with a peak emission at 365 nm. Then a multimode optical fiber connected to the OceanOptics spectrophotometer was used to collect the output signal. Photoluminescence measurements under 340, 360 380 and 400 nm were also conducted with a Varian Cary Eclipse Fluorescence Spectrophotometer. All the measurements were performed at room temperature. A Transmission Electron Microscopy (HR-TEM), at 200 kV, was used to analyze the images of size and shape of Ag nanoclusters and Ag nanoparticles. To determine the crystalline structure, it was used the electron diffraction measurements of Ag nanoparticles and the amorphous nature of Ag nanoclusters; then it was possible to correlate the results obtained regarding the amorphous and crystalline structures with respect to the temperatures used for their annealing. This correlation is important as it helps to determine the best methodology (annealing temperature) to obtain Ag nanocluster and Ag nanoparticles.

4. RESULTS AND DISCUSSION

The absorption spectra of $\text{Tm}^{3+}/\text{Yb}^{3+}$ doped $\text{GeO}_2\text{-PO}$ glasses with/without Ag nanoclusters are presented in figure 1. The absorption bands presented in this figure are associated with Tm^{3+} and Yb^{3+} . The electronic transitions from the ground state; then these bands corroborate the incorporation of the rare-earth ions in trivalent form that are responsible for the photoluminescence emissions.

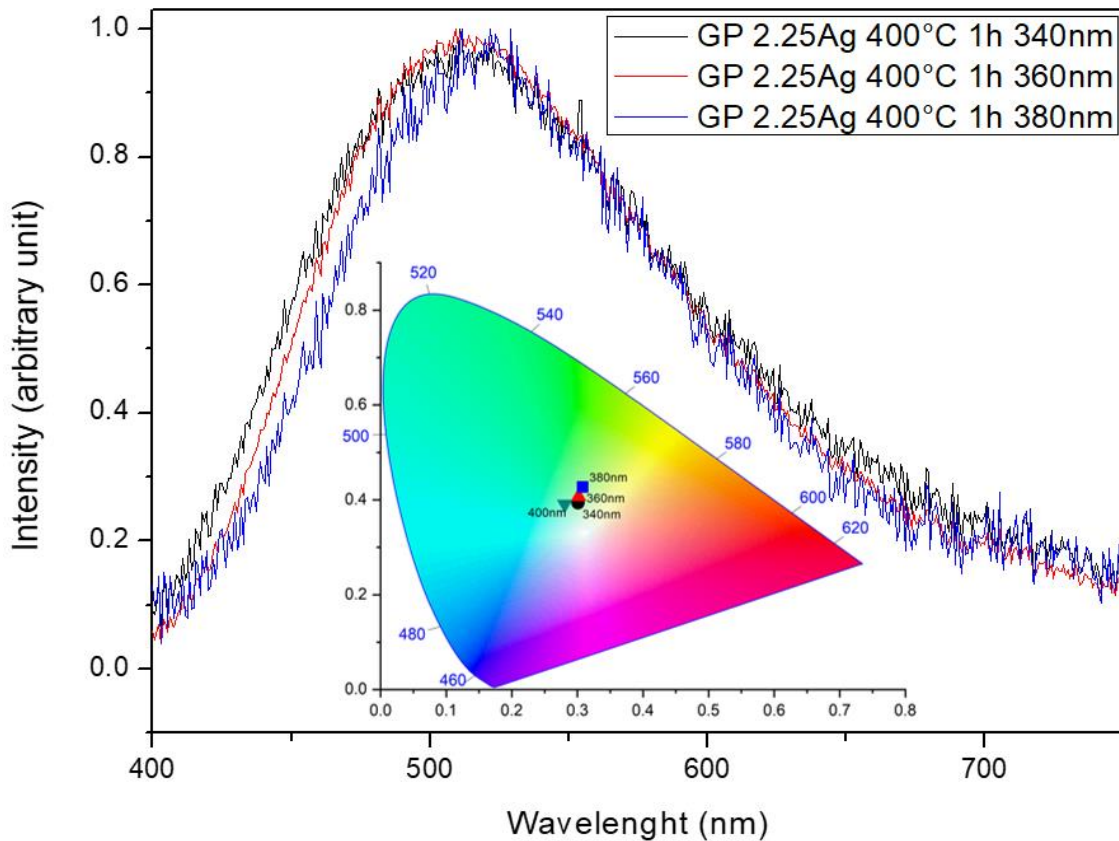
Figure 1 – Absorption spectra for $\text{GeO}_2\text{-PbO}$ glass with doped with Tm_2O_3 and Yb_2O_3 without and with different concentrations of AgNO_3



Source: The authors

Results of photoluminescence under excitation at 340, 360, 380 and 400 nm are presented in Figures 2 and 3 for $\text{GeO}_2\text{-PbO}$ glasses prepared with different concentrations of AgNO_3 , 2.25 and 4.5 wt%, respectively. Different colors are emitted from Ag nanoclusters by varying the excitation wavelength as can be noticed in the CIE Chromaticity diagram presented in the inset of figures 2 and 3.

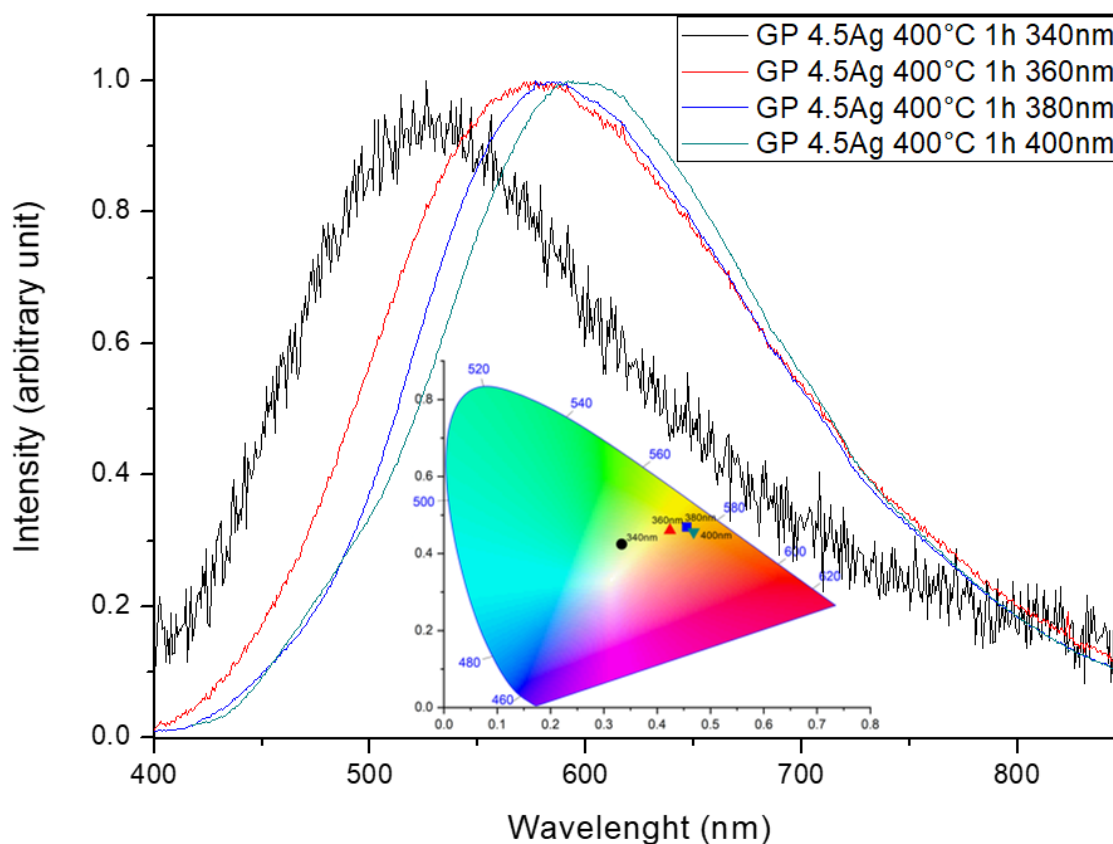
Figure 2 – Normalized photoluminescence emission for GeO₂-PbO glass prepared with 2.25 wt% of AgNO₃, annealed at 400 °C, under different excitations; the inset presents the Chromaticity diagram (CIE-1931) of the sample.



Source: The authors

In both cases we observe that the increase of the excitation wavelength promotes a redshift in the photoluminescence. For the sample with 2.25 wt% of AgNO₃ we observe photoluminescence for different shades of green (emission at 410 nm is extremely low and was not included) whereas for 4.5 wt% of AgNO₃ light is tuned from greenish yellow to orange. These different colors indicate Ag nanoclusters with different sizes as already reported (Fares, et al., 2017; Fares, Castro, Orives, Franco, & Nalin, 2017). In other words, the blue photoluminescence corresponds to the emission of smaller Ag nanoclusters, whereas the green, orange and red ones are associated to the emission of larger ones.

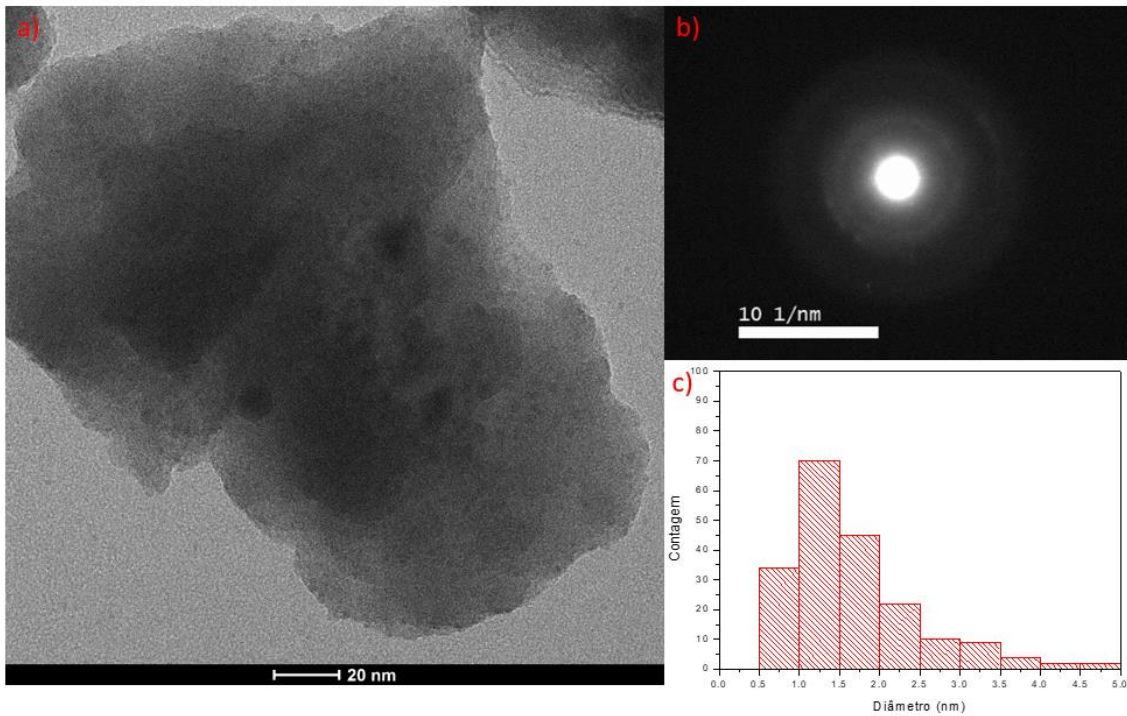
Figure 3 – Normalized photoluminescence emission for GeO₂-PbO glass prepared with 4.5 wt% of AgNO₃, annealed at 400 °C, under different excitations; inset presents the Chromaticity diagram (CIE-1931) of the sample.



Source: The authors

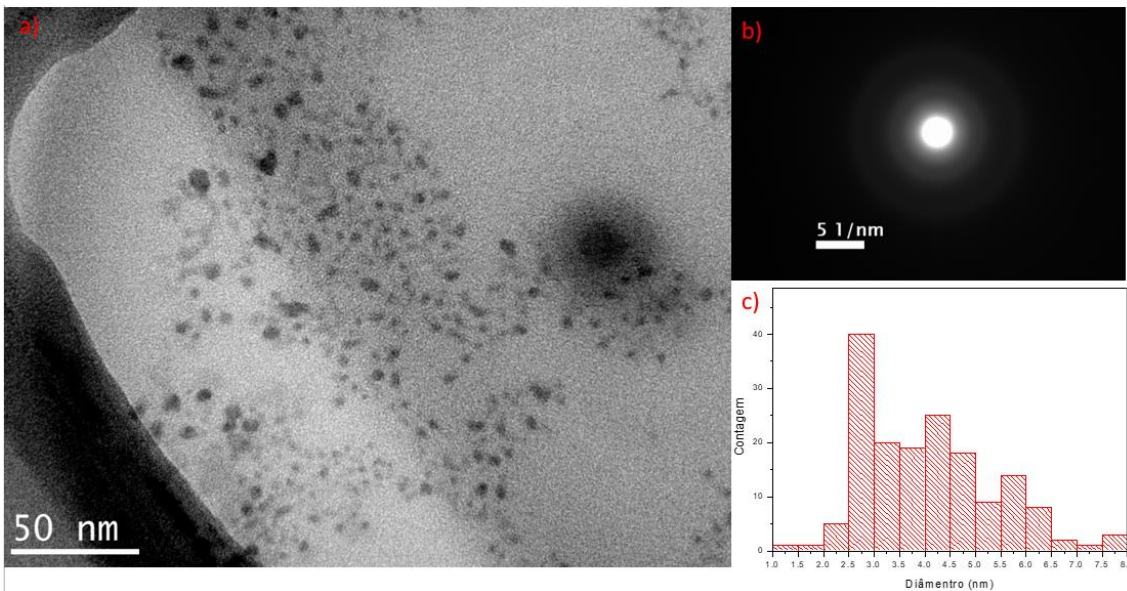
These facts can be corroborated by the results of TEM shown in figures 4 and 5, for samples prepared with 2.25 and 4.5 wt%, respectively. These figures also present, for each case, the results of electron diffraction measurements and size distribution of Ag nanoclusters. The electron diffraction results (figures 4b and 5b) demonstrate the amorphous character of Ag nanocluster due to the diffuse diffraction rings that are typical for an amorphous phase. Regarding the size of Ag nanoclusters (figures 4c and 5c) we observe smaller sizes for the sample with 2.5 wt% of AgNO₃ (large concentration of Ag nanoclusters in the range of 1.0 to 2.0 nm), with respect to the one with 4.5 wt% of AgNO₃ (large concentration of Ag nanoclusters in the range of 2.5 to 4.5 nm), as demonstrated by the Chromaticity diagram (inset of figures 2 and 3).

Figure 4 – GeO₂-PbO glass prepared with 2.25 wt% of AgNO₃ annealed at 400 °C a) TEM image b) electron diffraction results c) size distribution.



Source: The authors

Figure 5 – GeO₂-PbO glass prepared with 4.5 wt% of AgNO₃ annealed at 400 °C a) TEM image b) electron diffraction results c) size distribution.

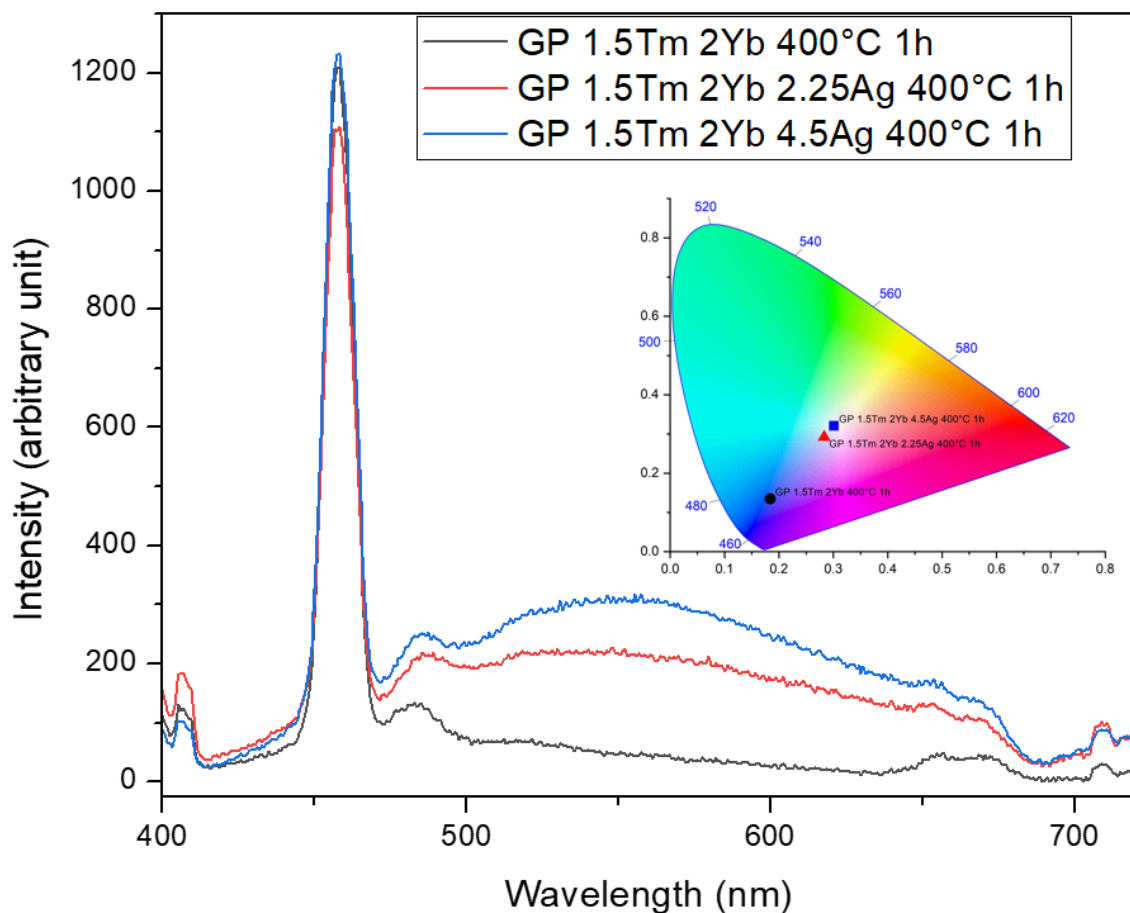


Source: The authors

Photoluminescence results under excitation by a 365 nm broadband UV lamp are shown in figure 6 for Tm³⁺/Yb³⁺ codoped GeO₂-PbO glasses with and without Ag nanoclusters. Bands centered at ~460, 480 and 660 nm are related to the following Tm³⁺ transitions, respectively: ¹D₂ → ³F₄, ¹G₄ → ³H₆ and ¹G₄ → ³F₄ (Lim, et al., 2004;

Shestakov, et al., 2014). The photoluminescence bands form ~500 to 700 nm is ascribed to the Ag nanoclusters whose intensities increase with AgNO₃ concentration growth. The CIE Chromaticity diagram (inset of figure 6) shows the contribution from both Tm³⁺ and Ag nanoclusters that gives rise to white color emission of different tint, for the samples prepared with 2.5 and 4.5 wt% of AgNO₃, as already reported to oxyfluoride glasses (Lim, et al., 2004). For the Tm³⁺/Yb³⁺ codoped GeO₂-PbO sample prepared without AgNO₃ only a strong blue emission is observed, related to ¹D₂→³F₄ and ¹G₄→³H₆ transitions of Tm³⁺. These phenomena show light control by Ag nanoclusters.

Figure 6 – Photoluminescence spectra of GeO₂-PbO glass doped with Tm₂O₃ and Yb₂O₃ prepared without and with 2.25 and 4.5 wt% of AgNO₃, annealed at 400 °C (excitation with a commercial 365nm broadband UV lamp); the inset shows the Chromaticity diagram of all the samples.

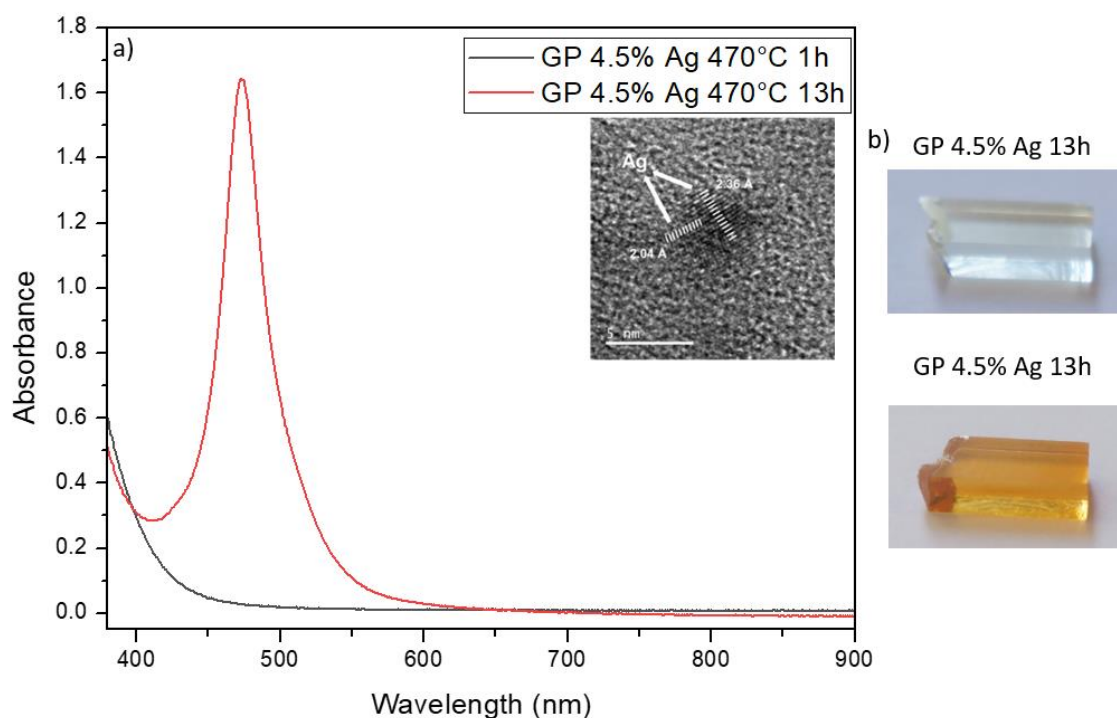


Source: The authors

Now we will focus on the results regarding the sample prepared at 470 °C with 4.5 wt% of AgNO₃ to review results that showed that annealing above the glass transition temperature promotes a medium with lower viscosity, easing Ag nanoparticles growth (Nishimura, Bordon, Miretzcky, & Kassab, 2021). Figure 7a

presents the absorption spectra and the presence of the plasmon absorption band related to Ag nanoparticles, centered at 470 nm (Nishimura, Bordon, Miretzcky, & Kassab, 2021), for annealing during 13h. The inset of Figure 7a shows the interplanar distances ($d = 2.36 \text{ \AA}$ and $d = 2.04 \text{ \AA}$) and the corresponding crystal planes of Ag ($hkl=111$ and $hkl=200$) and corroborates the presence of Ag crystalline nanoparticles. In order to highlight the color change due to the nucleation of Ag nanoparticles, Figure 7b shows daylight pictures of both samples.

Figure 7 - GeO₂-PbO glass prepared with 4.5 wt% of AgNO₃ and annealed at 470 °C, for 1 and 13 h, a) absorption spectra and inset with the interplanar distances ($d = 2.36 \text{ \AA}$ and $d = 2.04 \text{ \AA}$) and the corresponding crystal planes of Ag ($hkl=111$ and $hkl=200$) of the annealing for 13h b) daylight pictures of both samples.

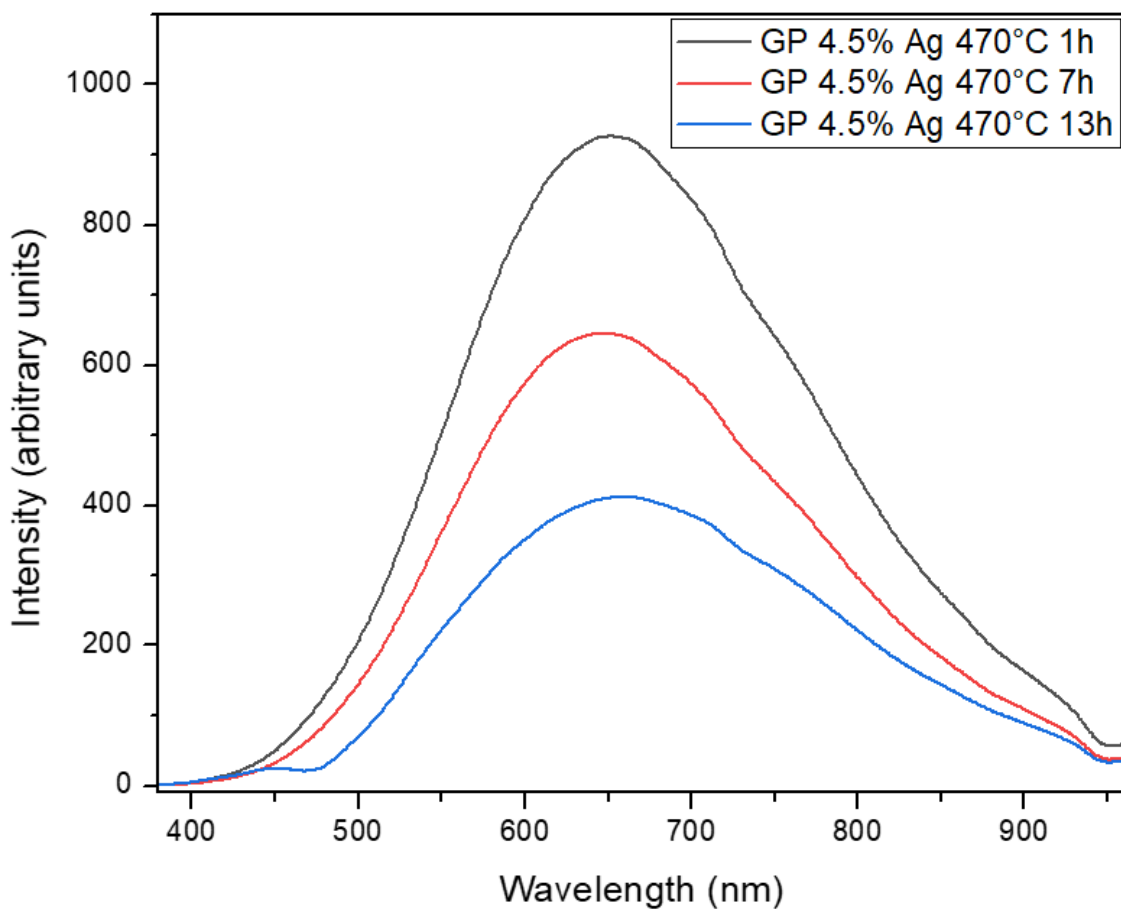


Source: The authors

Photoluminescence results are shown in Figure 8 for different annealing times: 1, 7 and 13 h. A broadband in the visible region extending to the near-infrared one can be noticed with applications for broadband visible light sources, CW lasers tunable across the whole visible range and panel displays based on the selection of red, green and blue parts of the Ag nanoclusters emission band. Although Ag nanoparticles are produced for annealing of 13 h, there is still the presence of Ag nanoclusters, that emit at 650 nm, as can be seen in figure 8. However, unlike the results of our previous studies using 420 °C (Nishimura, Bordon, Miretzcky, & Kassab, 2021), a great photoluminescence decrease is observed for a shorter

annealing of 7 h whereas for samples annealed at 420 °C, similar decrease was observed for longer annealing of about 37 h. The emission quenching is due to the evolution of Ag nanoclusters, as it is during the annealing the Ag nanocluster aggregates in Ag nanoparticles that cease to emit light; similar behavior was observed for fluorophosphates glasses_(Fares, et al., 2017). So, these results indicate that samples annealed at 420 °C tends to form Ag nanoclusters more easily because annealing below the glass transition temperature promotes a medium with higher viscosity, as already explained.

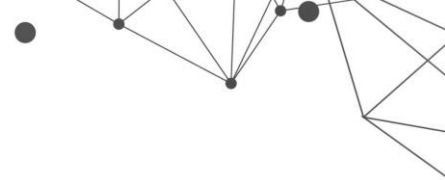
Figure 8 - Photoluminescence of GeO₂-PbO glass prepared with 4.5 wt% of AgNO₃, annealing at 470 °C for 1, 7 and 13 h (excitation at 355 nm)



Source: The authors

5. CONCLUSIONS

Luminescent Ag nanoclusters, consisting of a few Ag atoms, have been attracting major interest because of a variety of applications such as white light generation, flexible monitors, solar cells, among others. Ag nanoclusters are amorphous and emit light. Different colors can be generated depending on their size



and excitation wavelength. The host plays an important role as the viscosity of the medium influences the diffusion of Ag atoms. We discussed the factors that influence the size distribution of the nanoclusters (annealing, Ag concentration, glass network changes and rare-earth doping) and showed that smaller Ag nanoclusters are formed for samples prepared with smaller AgNO₃ concentration. The efficient energy transfer from Ag nanoclusters to the rare-earth ions results in the emission of both, nanoclusters and rare-earth ions, and consequently promote tunable visible emission and white light generation. Then the present work reviewed recent results of Ag nanoclusters in undoped and Tm³⁺/Yb³⁺ doped GeO₂-PbO glasses; the melt-quenching technique was used to produce the samples followed by adequate annealing. The annealing was performed with different temperatures, below and above the glass transition temperature, to evaluate the best condition to produce Ag nanoclusters. Annealing performed below glass transition temperature (400 °C) favored the formation of Ag nanoclusters, corroborated by TEM measurements. Then, GeO₂-PbO undoped samples with Ag nanoclusters showed tunable light emission from blue to orange, depending on the concentration of AgNO₃ used, whereas samples doped with Tm³⁺ and Yb³⁺ and Ag nanoclusters emitted white light for specific concentration of AgNO₃.

The present review showed the potential of GeO₂-PbO glasses with Ag nanoclusters for white light emitting devices, broadband visible light sources, panel displays based on the selection of red, green and blue light of the Ag nanoclusters emission bands, and tunable visible light emission applications as CW lasers tunable across the visible range.

ACKNOWLEDGMENTS

We acknowledge financial support from Conselho Nacional de Desenvolvimento Científico e Tecnológico - Grant: INCT/CNPq 465.763/2014 (Instituto Nacional de Ciência e Tecnologia de Fotônica) and Grant: 302532/2019-6. The Nanotechnology National Laboratory (LNNano) of the CNPEM-Campinas/Brazil, is also acknowledged for the TEM measurements.

REFERENCES

- Amjad, R. J., Dousti, M., Sahar, M., Shaukat, S., Ghoshal, S., Sazali, E., & Nawaz, F. (2014). Silver nanoparticles enhanced luminescence of Eu³⁺-doped tellurite glass. *Journal of Luminescence*, *154*, 316-321.
- Carvalho, D. O., Kassab, L. R., Del Cacho, V. D., & Alayo, M. I. (2018). A review on pedestal waveguides for low loss optical guiding, optical amplifiers and nonlinear optics applications. *Journal of Luminescence*, *203*, 135-144.
- Castro, T., Jubera, V., Fares, H., Petit, Y., Fargues, A., Carndinal, T., . . . Ribeiro, S. (2019). Photoluminescence of Ag⁺ and Ag^{m+} doped. *Journal of Materials Science: Materials in Electronics*, *30*, 16878-16885.
- Fares, H., Castro, T., Franco, D. F., Fucikova, A., da Silva, R. R., Valenta, J., . . . Nalin, M. (2020). Tuning multicolor emission in AgNCs/Tm³⁺/Mn²⁺-doped fluorophosphate. *Journal of Non-Crystalline Solids*, *535*, 119968.
- Fares, H., Castro, T., Orives, J. R., Franco, D. F., & Nalin, M. (2017). White light and multicolor emission tuning in Ag. *Royal Society of Chemistry Advances*, *7*, 44356-44365.
- Fares, H., Santos, S. N., Santos, M. V., Franco, D. F., Souza, A. E., Manzani, D., . . . Nalin, M. (2017). Highly luminescent silver nanocluster-doped. *Royal Society of Chemistry Advances*, *7*, 55935-55944.
- Karmakar, B., Rademann, K., & Stepanov, A. (2016). *Glass Nanocomposites*. William Andrew.
- Lim, K.-S., Babu, P., Jayasankar, C. K., Lee, S.-K., Pham, V.-T., & Seo, H.-J. (2004). Optical spectroscopy of thulium-doped oxyfluoroborate glass. *Journal of Alloys and Compounds*, *385*, 12-18.
- Liu, X. Y., Guo, H., Ye, S., Peng, M. Y., & Zhang, Q. Y. (2015). Enhanced tunable color emission in transparent Ag/Mn²⁺ codoped zinc borate glasses for broad band light source. *Journal of Materials Chemistry C*, *3*, 5183-5191.
- Nishimura, M. M., Bordon, C. D., da Silva, D. M., & Kassab, L. R. (2021). Tunable visible emission and white light generation by Ag nanoclusters in Tm³⁺/Yb³⁺ doped GeO₂-PbO glasses. *2021 35th Symposium on Microelectronics Technology and Devices (SBMicro)* (pp. 1-4). Campinas, Brazil: IEEE.
- Nishimura, M. M., Bordon, C. D., Miretzcky, L. M., & Kassab, L. R. (2021). Broadband visible light emission by GeO₂-PbO glasses doped with Ag nanoclusters. *2021 SBMO/IEEE MTT-S International Conference on Microwave and Optoelectronics (IMOC)* (pp. 1-3). Fortaleza, Brazil: IEEE. doi:10.1109/IMOC53012.2021.9624793.
- Raouf, E.-M. (2018). *Tellurite Glass Smart Materials Applications in Optics and Beyond*. Springer.



Rivera, V. A., & Manzani, D. (2017). *Technological Advances in Tellurite Glasses: Properties, Processing, and Applications*. Springer.

Sandrini, M., Muniz, R. F., Zanuto, V. S., Pedrochi, F., Guyot, Y., Bento, A. C., . . . Neto, A. M. (2018). Enhanced and tunable white light emission from Ag nanoclusters and Eu³⁺-co-doped CaBaI glasses. *The Royal Society of Chemistry Advances*, 8, 35263-35270.

Shestakov, M. V., Chen, X. M., Kaydashev, V., Baeckelant, W., Tikhomirov, V. K., Vanacken, J., . . . Moshchalkov, V. V. (2014). Oxyfluoride glass(SiO₂-PbF₂) co-doped with Ag nanoclusters and Tm³⁺ ions for UV-driven, Hg-free, white light generation with a tuneable tint. *Optical Materials Express*, 4(6), 1227-1235.

Tikhomirov, V. K., Rodríguez, V. D., Kuznetsov, A., Kirilenko, D., Van Tendeloo, G., & Moshchalkov, V. V. (2010). Preparation and luminescence of bulk. *Optics Express*, 18(21), 22032-22040.

Tikhomirov, V. K., Vosch, T., Fron, E., Rodríguez, V. D., Velázquez, J. J., Kirilenko, D., . . . Moshchalkov, V. V. (2012). Luminescence of oxyfluoride glasses co-doped with Ag nanoclusters and Yb³⁺ ions. *The Royal Society of Chemistry Advances*, 2, 1496-1501.

Velázquez, J. J., Tikhomirov, V. K., Chibotaru, L. F., Cuong, N. T., Kuznetsov, A. S., Rodríguez, V. D., . . . Moshchalkov, V. V. (2012). Energy level diagram and kinetics of. *Optics Express*, 20(12), 13582-13591.

SMART MONITORING SYSTEM BY OPTICAL DEVICE FOR VEHICLE TRAJECTORY PREDICTION

DOI: [10.51859/ampla.sst631.1122-4](https://doi.org/10.51859/ampla.sst631.1122-4)

Lucilene Ferreira Mouzinho¹
Ronaldo da Silva Ferreira²
Lucius Vinicius R. Machado Filho²
Tagleorge Marques Silveira²

¹ Professor at the Federal Institute of Maranhão-IFMA, Departamento de Eletro-eletronica-DEE, PhD, Postdoc UA, Portugal.

² Universidade de Aveiro – UA, Departamento de Eletrónica, Telecomunicações e Informática – DETI.

ABSTRACT

The diversity of research on vehicle tracking still presents some challenges, which is why it is important to study methods that present better performances. In this work, the extended Kalman filter is used to track and estimate the vehicle's trajectory using two types of inputs. From a scenario, images from a fixed optical device installed on the highway and data provided by radar were used. Two algorithms were developed and compared. To compare the two algorithms, the simulation was carried out in this scenario, considering, initially, the optical device images. At another time, a simulation was performed, considering the data provided by the radar. The results indicate that the method tracks and estimates the vehicle's trajectory, and that the computational complexity is greatly influenced by the type of input to be used, that is, for inputs via optical device images, the impact of extracting information from the images is significantly high, with an execution time about one hundred times longer than that of the radar, as shown by the results.

Key words: Extended Kalman Filter. State estimation. Trajectory prediction. Vehicle tracking.

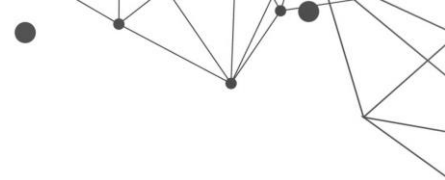
1. INTRODUCTION

Although automotive radar systems are the most widely used, there is a growing trend in the use of roadside optical devices as a complementary feature to vehicle monitoring. In this work, the proposed system will use as input variables both data supplied by a radar and the monitoring optical device installed on the highway, aiming to estimate the coordinates (x, y) and the speed with the smallest possible error/deviation. The initial studies considered the optical device's input information without occlusion. Initially, after acquiring the information provided by radar and optical device images, as the initial treatment of image acquisition is different from the treatment of radar information. Since both radar and optical device information is associated with unavoidable noise, the control system was based on filtering this information.

In this case, considering that the state of vehicle movement is nonlinear, and the system runs in real-time, the best performance for Kalman Filter (*KF*) is the use of Extended (*EKF*). Thus, for both the output attributes of the processed images and the initial radar data, filtering was applied to the information by to reduce/correct system errors and provide the estimated trajectory.

2. LITERATURE REVIEW

Wu and Meng Hong-Son proposed a tracking method based on linked list of associated vehicles (Wu and Meng, 2019). They used a method that uses the Bhattacharyya distance to occlusion identification and Kalman filter to predict the location of vehicles, accurate vehicle tracking can be realized under occlusion. Experimental results showed that the algorithm could achieve a robust and accurate vehicle tracking under different traffic. In (Tian et al., 2018), a vehicle tracking system was proposed that fused the radar and vehicle-to-vehicle (V2V) information to improve the target tracking accuracy. A Kalman filter was also used to improve the accuracy of target tracking. In the authors' analysis, the tracking system in real road environment showed that the proposed fusion approach for target tracking could reduce the data association error and improve the accuracy of vehicle target tracking. Kim and Lim also used fusion sensors to track vehicles (Kim et al., 2017). Heuristic fusion with adaptive gating and track to track fusion were applied to track



fusion of optical device and radar sensor for forward vehicle tracking system and the two algorithms were compared. In (Fang et al., 2019), they proposed a part-based particle filter for on-road vehicle tracking. The method used was based on part-based modelling in a particle filter framework. Liu and Deng proposed a novel deep learning-based network named Vehicle Tracking Context (VTC) to extract features from the real-time and active vehicle tracking context (Liu et al., 2020). The tracking system has been integrated, including vehicle detection, vehicle Re-ID and vehicle search. In (Yu et al., 2019) the intelligent vehicle trajectory tracking algorithm based on Model Predictive Controller (MPC) using Laguerre functions was designed. The algorithm used a group of orthonormal Laguerre functions to design discrete time MPC. Jeon and Rajamani developed and used of a nonlinear observer for tracking of vehicle motion trajectories while using a radar sensor (Jeon et al., 2019). The exponential stability of the observer was established using Lyapunov techniques. The observer design with the developed technique was then implemented in both simulations and experiments.

In this work we focus on vehicle tracking using information from the radar and optical device image installed at a point on the highway. The method consists of using the *EKF* to track, estimate and predict the vehicle's trajectory from the input information. Some advantages of the method proposed in this work in relation to the methods shown in this Section involve the low computational effort required by the *EKF* and the ability to estimate states of a system distorted by white Gaussian noise. The Kalman filter smooths the noise present in the data and reduces the prediction error.

3. BACKGROUND

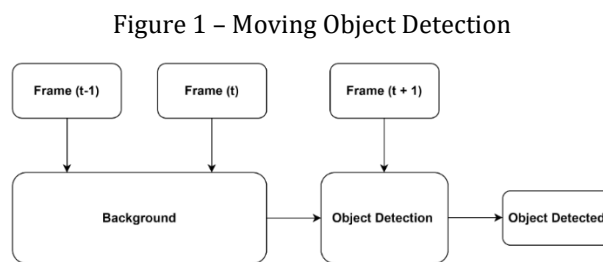
With the continuing increase in traffic volume and the limited construction of new road installations in urban, long-distance, and rural areas, traffic monitoring, as well as an ability to collect information either through radar data or optical devices, is a vital component for keeping roads running smoothly. This information helps you understand the volume of road traffic, contributing to maintenance requirements and predicting growth needs in specific areas.

As inputs for system analysis in this work, the information provided by the radar and the monitoring optical device on the highway was used. The installed

radar information consists of: Object ID, Object length, X-position, Y-position, X-speed, Y-speed, Date and Time. And the second input source for the system is video.

3.1. MOVING OBJECT DETECTION (MOD)

Moving Object Detecting (MOD) in a video is an essential step for complex applications such as object tracking and video retrieval. The purpose of moving object detection is to locate foreground objects to extract useful information from the system such as trajectory, orientation, and velocity (Ferreira et al., 2022). The Figure 1 shows the block diagram of a MOD.



Source: (Cho et al., 2019) adapted.

In this stage, information loss can be caused by complex or dynamic backgrounds, lighting changes, shadows, occlusion, etc. Thus, video object tracking can be defined as the process of segmenting objects of interest from video scenes.

3.2. GAUSSIAN MIXTURE MODELS (GMM)

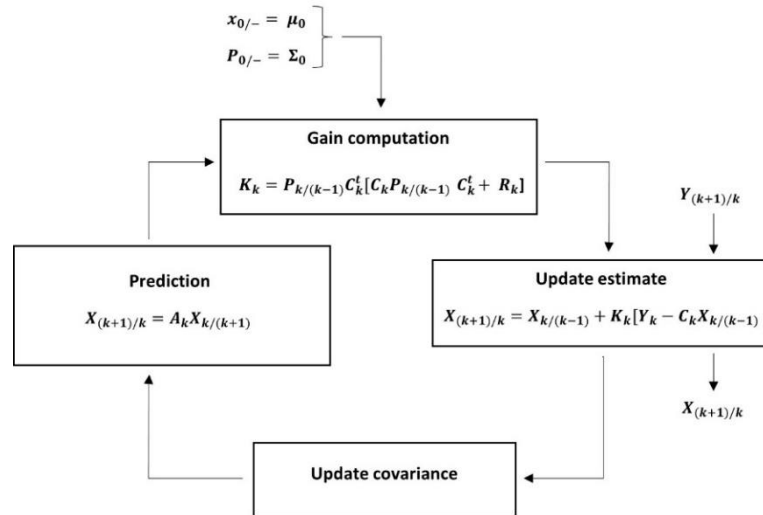
The generalized use Gaussian Mixture Model (GMM) is because a Gaussian distribution has a simple and concise representation that requires only two parameters, the average μ and variance σ^2 (Zhuang et al., 1996). GMM is a form of time series modelling consisting of the grouping of probability densities Gaussian with individual characteristics. It has as desirable characteristics for a model, need little stored information and little computational load to perform probability density estimates, especially when using data set n dimensions. In signal processing and data analysis, GMM are widely studied and applied (Bishop and Nasrabadi, 2006).

3.3. EXTENDED KALMAN FILTER (EKF)

Extended Kalman Filter, Figure 2, is a variant of Kalman Filter in its linear version, applied to nonlinear dynamic systems. The equations for the *KF* fall into two groups: the *prediction step* and the *correction step*. The prediction step equations are responsible for projecting forward (in time) the current state and

error-covariance estimates to obtain the *a priori* estimates for the next time step. The correction step equations are responsible for the feedback, i.e., for incorporating a new measurement into the *a priori* estimate to obtain an improved *a posteriori* estimate.

Figure 2 – Extended Kalman Filter Algorithm.



Source: (Meghana et al., 2019).

1. *Tracking of Moving Vehicle with Kalman Filtering:* to better frame the theme of *KF*, is shown in (Meghana et al., 2019; Mouzinho et al., 2005; Mouzinho, 2007; Mouzinho et al., 2005) the use of these filters in tracking moving vehicle in real systems.
2. *Description use the EKF:* the *KF* offers an efficient and iterative method to collect sensor information to estimate the state of a vehicle. Compared to standard *KF*, the *EKF* is widely used in nonlinear systems such as vehicle movement.

Considering that the motion state of a vehicle is a nonlinear model, in this case, *EKF* is used to estimate the trajectory of vehicles.

The filter model used is showed in equation (1):

$$\begin{cases} X_{(t)} = a(X_{(t-1)}, (t-1)) + w_{Q(t-1)} \\ Y_{(t)} = c(X_{(t)}, (t)) + w_{R(t)}. \end{cases} \quad (1)$$

Where $X_{(t)}$ is the state; $Y_{(t)}$, the measurement; a , dynamic model function; c , measurement model function; $w_{R(t)}$, measurement noise in system with known covariance; $w_{Q(t-1)}$ the process noise in system with known covariance.

4. MATHEMATICAL MODEL OF VEHICLE TRACKING VIA EKF

Similarly, to the mathematical model of the system dynamics developed in (Mouzinho et al., 2005) and (Mouzinho, 2007), we have:

$$x = x_0 + v_x \Delta t + \frac{1}{2} a_x \Delta t^2 \quad (2)$$

$$y = y_0 + v_y \Delta t + \frac{1}{2} a_y \Delta t^2 \quad (3)$$

$$v_x = v_{x0} + a_x \Delta t \quad (4)$$

$$v_y = v_{y0} + a_y \Delta t \quad (5)$$

The system model is described by four equations in the state space for the x and y coordinates and the v_x and v_y speeds. If $x(t), 0 \leq t < \infty$ specifies of the vehicle trajectory, with t being the time variable and $t > 0$ the sampling period. The x_k vector in the state space contains position and velocity coordinates on the x and y axis:

$$x_k = [x_k, y_k, v_{xk}, v_{yk}]^T \quad (6)$$

Where T corresponds to the transposed matrix, x_k and y_k are the Cartesian coordinates in time k and v_{xk} and v_{yk} are the respective derivatives, that is, the coordinates of the speeds. The equations (2), (3), (4) and (5) can be written, in matrix form, as:

$$\begin{bmatrix} x \\ y \\ v_x \\ v_y \end{bmatrix} = \begin{bmatrix} 1 & 0 & \Delta t & 0 \\ 0 & 1 & 0 & \Delta t \\ 0 & 0 & 1 & 0 \\ 0 & 0 & 0 & 1 \end{bmatrix} \begin{bmatrix} x_0 \\ y_0 \\ v_{x0} \\ v_{y0} \end{bmatrix} + \begin{bmatrix} \frac{\Delta t^2}{2} & 0 \\ \frac{1\Delta t^2}{2} & \frac{1\Delta t^2}{2} \\ \Delta t & 0 \\ 0 & \Delta t \end{bmatrix} \begin{bmatrix} a_x \\ a_y \end{bmatrix} \quad (7)$$

and the system measurement is given by the vector y_{xk} :

$$y_k = [x_k, y_k, v_{xk}, v_{yk}]^T. \quad (8)$$

$$\begin{bmatrix} x \\ y \\ v_x \\ v_y \end{bmatrix} = \begin{bmatrix} 1 & 0 & 0 & 0 \\ 0 & 1 & 0 & 0 \\ 0 & 0 & 1 & 0 \\ 0 & 0 & 0 & 1 \end{bmatrix} \begin{bmatrix} x_0 \\ y_0 \\ v_{x0} \\ v_{y0} \end{bmatrix}. \quad (9)$$

From the control system theory, the state space model is represented as,

$$x(k) = Ax_{k-1} + Bu(k-1) + w_Q \quad (10)$$

and

$$(11)$$

$$y(k) = Cx_k + w_R \quad (11)$$

where (10) is the state equation and (11) is the system output equation; w_Q and w_R are the control process noise and measurement noise, respectively. The w_Q and w_R are considered zero mean white noise sequences *Gaussian* with Q_k defined non-negative symmetric matrix, $Q_k > 0$ for all k and R_k the covariance of the measurement noise. From the equations (7) and (9), the matrices A , B and C are given as:

$$A = \begin{bmatrix} 1 & 0 & \Delta t & 0 \\ 0 & 1 & 0 & \Delta t \\ 0 & 0 & 1 & 0 \\ 0 & 0 & 0 & 1 \end{bmatrix}, B = \begin{bmatrix} \frac{\Delta t^2}{2} & 0 \\ 0 & \frac{\Delta t^2}{2} \\ \Delta t & 0 \\ 0 & \Delta t \end{bmatrix} \text{ and } C = \begin{bmatrix} 1 & 0 & 0 & 0 \\ 0 & 1 & 0 & 0 \\ 0 & 0 & 1 & 0 \\ 0 & 0 & 0 & 1 \end{bmatrix}.$$

Where:

x_k - state vector

y_k - measurement vector

u - system input control

A - states matrix

B - input matrix

C - output matrix

k - time/state previous

$k + 1$ - time/state actual

4.1. VEHICLE TRACKING VIA EKF

As mentioned, *KF* is used for different types of moving object tracking. This type of filter combines noise, measurements, and state of a vehicle to obtain an estimate of the physical quantity to be known.

For this case, the matrices used were the following:

$$A = \begin{bmatrix} 1 & 0 & \Delta T & 0 \\ 0 & 1 & 0 & \Delta T \\ 0 & 0 & 1 & 0 \\ 0 & 0 & 0 & 1 \end{bmatrix}, B = \begin{bmatrix} \frac{\Delta T^2}{2} & 0 \\ 0 & \frac{\Delta T^2}{2} \\ \Delta T & 0 \\ 0 & \Delta T \end{bmatrix}, C = \begin{bmatrix} 1 & 0 & 0 & 0 \\ 0 & 1 & 0 & 0 \\ 0 & 0 & 1 & 0 \\ 0 & 0 & 0 & 1 \end{bmatrix},$$

$$K_0 = \begin{bmatrix} 1 & 0 & 0 & 0 \\ 0 & 1 & 0 & 0 \\ 0 & 0 & 1 & 0 \\ 0 & 0 & 0 & 1 \end{bmatrix}, Q = \begin{bmatrix} \frac{\Delta T^4}{4} & 0 & \frac{\Delta T^3}{2} & 0 \\ 0 & \frac{\Delta T^4}{4} & 0 & \frac{\Delta T^3}{2} \\ \frac{\Delta T^3}{2} & 0 & \Delta T^2 & 0 \\ 0 & \frac{\Delta T^3}{2} & 0 & \Delta T^2 \end{bmatrix}, R = \begin{bmatrix} \frac{\Delta T^4}{4} & 0 & 0 & 0 \\ 0 & \frac{\Delta T^4}{4} & 0 & 0 \\ 0 & 0 & \Delta T^2 & 0 \\ 0 & 0 & 0 & \Delta T^2 \end{bmatrix}$$

and

$$P_0 = \begin{bmatrix} \frac{\Delta T^4}{4} & \frac{\Delta T^4}{4} & \frac{\Delta T^3}{2} & \frac{\Delta T^3}{2} \\ \frac{\Delta T^4}{4} & \frac{\Delta T^4}{4} & \frac{\Delta T^3}{2} & \frac{\Delta T^3}{2} \\ \frac{\Delta T^3}{2} & \frac{\Delta T^3}{2} & \Delta T^2 & \Delta T^2 \\ \frac{\Delta T^3}{2} & \frac{\Delta T^3}{2} & \Delta T^2 & \Delta T^2 \end{bmatrix}.$$

Where ΔT - sampling period; A - state array; B - input matrix; C - output matrix; Q - process-noise covariance matrix; R - measurement-noise covariance matrix; K - Kalman gain matrix and P - estimated error covariance matrix. The order of the arrays is: A , Q , R , and P are arrays 4×4 ; B is an array 4×2 ; C and K_0 are 4×4 identity arrays; Q is symmetric matrix, positive semi definite and R is symmetric matrix positive definite.

5. INPUT DATA

In the context of tracking, segmentation is the process of separating foreground objects from the background of the video sequence. Detection is the process of identifying which segmented foreground objects are of interest for tracking. This step is facilitated by pre-treatment of the image through the segmentation process, to significantly eliminate the existing noise, leaving only to analyse the regions of interest. Once an object has been segmented and detected, it and its kinetic properties must be represented in some way.

In this case, moving vehicles, have different dimensions, however, it is possible to perform the detection of vehicle types from pre-established references, such as, for example, use of the area of the identified object. For the information provided by the radar, the processing is simpler, because the radar already provides directly necessary the input data the system, i.e., the coordinates of the position and speeds of the vehicle. Vehicle detection elements assume that vehicles have an identity (ID) that differentiates them from each other and characterizes them as unique.

Vehicle images are captured by means of a monitoring optical device installed high, fixed, and independent of the road being monitored, with panoramic view and contemplating the view of the traffic lanes at angled angles to the traffic flow. The optical device is installed at a strategic point to monitor real-time traffic

flow conditions. Figure (3) shown the optical device's panoramic view, as well as the angle of view it covers. The video is about *22 seconds* long, (Vecteezy, 2022). The video was fragmented and a new video with a time of *5 seconds* of traffic data was used for analysis. In Figures (4), (5) and (6) the figures obtained in the pre and post-processing stages of the video are shown.

Figure 3 – Viewing angle of installed video optical device.



Source: frame extracted by authors.

Figure 4 – Foreground.



Source: The authors.

5.1. CONSIDERATIONS ABOUT THE EKF

For a good performance of the *KF's* it is necessary to adjust and tune three parameters, the matrices Q and R , which represent the covariance of the process noise and the measurement noise, respectively, and the matrix P_0 , which represents the covariance of the initial estimation errors. The matrix Q is square, with dimension equal to the number of states, and is associated with the process model reliability used in the Kalman Filter, that is, the higher the model reliability, the lower the values of the matrix components. For this case, the matrix Q has dimension 4×4 . The R matrix is square, with a dimension corresponding to the number of model outputs, and is associated with the reliability of the measured process variables. Then, the higher the reliability of the measured variables, the lower the values of the matrix elements. For this case, the matrix R has dimension 4×4 . The Q and R arrays you choose are described in the *Section 4*. The initial covariance matrix, P_0 , is square and has a dimension corresponding to the number of process model states used in the filter and is required to initialize the covariance

matrix, which is updated at each instant of time. Here, the dimension of P_0 is 4×4 . The pseudo code of *EKF* is given in Algorithm (1).

Figure 5 – Vehicles detected 1.



Source: The authors.

Figure 6 – Vehicles detected 2.



Source: The authors.

Algorithm 1: Extended Kalman Filter for tracking and estimation of a vehicle

```

1  INPUT: video monitoring or data radar,  $y_k$ 
2  OUTPUT: vehicle tracking,  $\hat{x}_k^-$ , and vehicle trajectory estimation,  $\hat{x}_k$ .
3  Initialization
4       $x_{0,0} = x_0$ 
5       $P_{0,0} = P_0$ 
6      for  $k = 1$  to  $N$  do
7          Time update
8               $\hat{x}_k^- = x_{k-1} = A_{k-1}x_{k-1,k-1}$ 
9               $P_{x,k}^- = P_{x,k-1} + Q_k = A_{k-1}P_{k-1,k-1}A_{k-1}^T + Q_k$ 
10              $r_k = y_k - C(u_k, \hat{x}_k^-)$ 
11              $P_{y,k} = (C_k P_{x,k}^- C_k^T + R_k)$ 
12         End for
13         Measurement update
14              $K_k = P_{x,k}^- C_k^T P_{y,k}^{-1}$ 
15              $\hat{x}_k = \hat{x}_k^- + K_k r_k$ 
16              $P_{x,k} = (I - K_k C_k) P_{x,k}^-$ 
17         End
End Algorithm

```

6. SIMULATIONS AND RESULTS

The *Matlab*[®] 2020a tool was used for algorithm development. For the case where the system input refers to the monitoring optical device images, there were initial steps of approaches for the detection and segmentation of moving video objects. *Matlab*[®] has some initial specific linear filtering commands for images using *image processing functions*. Subsequently, after the preprocessing and segmentation steps of these images, the attributes of interest were extracted in the sequence of each frame. In subsection 4.1, the ΔT , sampling period, for images, is the period it takes *Matlab*[®] to process each frame. The detection of the moving object is evaluated by parameterization pre-existing solutions, namely in the class called *Object Detectors*, part of *Computer Vision System*.

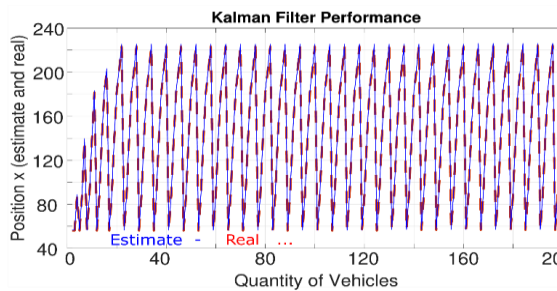
In estimation of trajectory via *EKF*, in the tests with greater confidence in the model ($Q < R$), the process noise covariance matrix (Q) is a parameter that requires attention as it is related to the uncertainties of the process model. Normally, the matrix Q is considered constant since the variability is not always uniform. The initial covariance P_0 was considered as mentioned in the subsection 4.1 as well as the matrices Q and R . However, the values of the Q and R arrays were changed and tested to analyse the behaviour of the filter.

From these results, the greater the confidence in the process model, the worse is the estimation of the vehicle trajectory. This error increase can be justified using a model that has not negligible modelling errors. Tests with heather measurement confidence, ($R < Q$), can also be referred to as filtering tests, as one of the characteristics of *KF*'s is the filtering of measurement noise over process output variables. This requires a good quality model, as well as the knowledge of the variability of the measured variables. Measured variables can be used, for example, in control systems, and for this purpose, the measured values must be as accurate as possible to provide adequate control actions. Hence the need for filtering steps of the measured variables.

Several tests were performed varying the value of R as a function of Q . The results of the best performance indices are shown in Figures (8) and (10), considering the radar data. Filter sampling time is a very important tuning parameter, especially when using discrete version estimators. For models with large

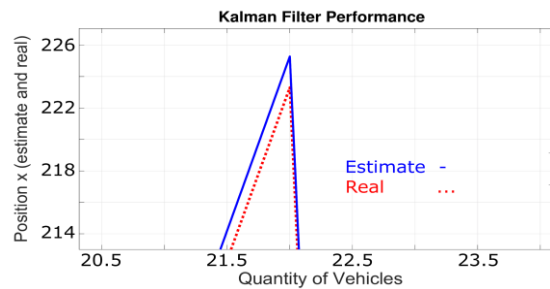
errors or when a better estimation quality is obtained for the condition of greater confidence in the measured value than in the model ($R \ll Q$), a lower value for Sampling will result in better state estimation quality. In this case, as expected, the greater computational effort is required. In all graphs, the values in red color correspond the real value, i.e., the measured value, and blue color are the estimated values. In Figures (8) and (9), have the results obtained in a better performance index of the Q and R matrices for 200 consecutive radar data samples. The tracking and estimation of vehicle movement were satisfactory, as can be seen in the analysis of displacement of the horizontal component (x axis) in the movement of the vehicle, Figures (9) and (11). In Figure (12) shown the vehicle detected and have better *EKF* performance indexes for input data extracted from the video. The sampling time, ΔT , for the video input information is the amount of time it takes *Matlab*[®] to process each frame.

Figure 8 – Vehicle trajectory estimation considering radar data with 200 samples.



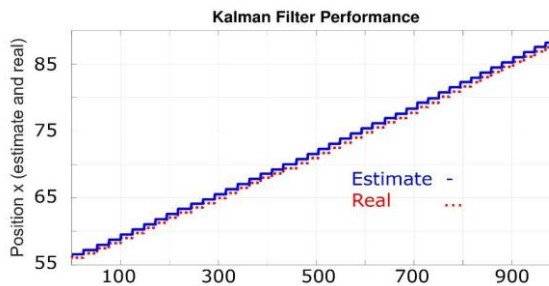
Source: The authors.

Figure 9 – Zoom of the difference between the estimated value and the measured value for 200 samples.



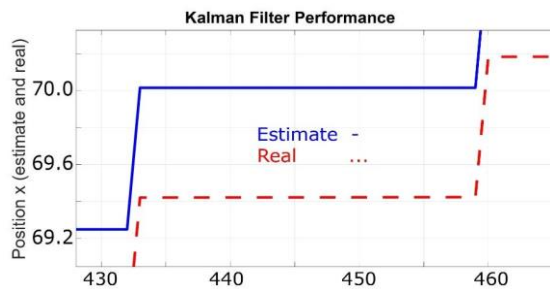
Source: The authors.

Figure 10 – Vehicle trajectory estimation considering radar data for 1000 samples.



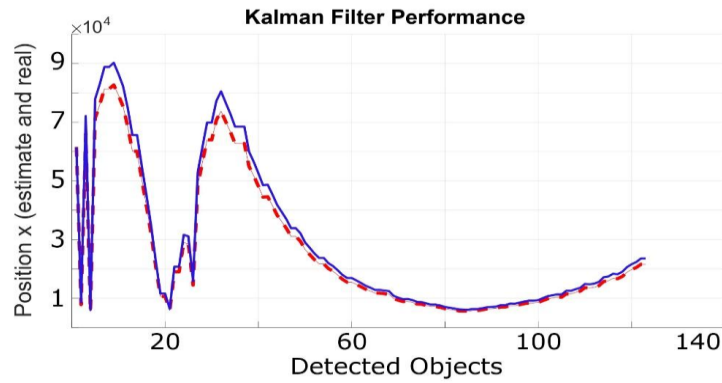
Source: The authors.

Figure 11 – Zoom of the difference between the estimated value and the measured value for 1000 samples.



Source: The authors.

Figure 12 – Detected vehicle by frames.



Source: The authors.

7. COMPUTATIONAL COMPLEXITY ANALYSIS

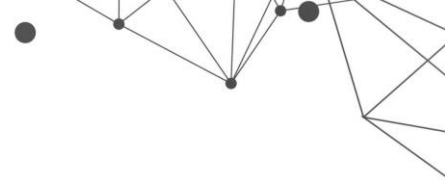
The complexity estimation analysis for the main loop in Algorithm 1, illustrated in subsection 5.1, was based in *big (O) notation*. Different input data has different costs. In this case, the use of data from an optical device has a much longer processing time, since the video must be processed to extract the information that will be used in the algorithm. In the case of radar data, there is no such step, the data is already ready for use in the algorithm. Extracting video image attributes and estimator development/execution via *EKF* were performed on the Intel(R) Core(TM) i7-4600U CPU @ 2.10 GHz processor, 64-bit, OS Windows, 8 GB RAM. The processing speed was around 25 frame per second (*fps*) and a total of 307 frames were tested. In Table 1 were shown the execution time for video processing where the information for the *EKF* algorithm is extracted; the *EKF* algorithm for the inputs video; and the execution time for processing *EKF* with radar data for 200 and 1000 samples. In this table it is observed that the time to extract the information from the video is quite high about the execution time of the *EKF*.

Table 1 – Complexity Algorithms.

Data base	Execution Time (s)	Space Memory (KB)
Processing video	141.546	7
EKF video	0.392	3
EKF Radar 200	1.087	5
EKF Radar 1000	1.317	5

Source: The authors.

For the radar data inputs, the operations in lines dominant were be executed n times, where n is the quantity of the data samples of the radar. The complexity for

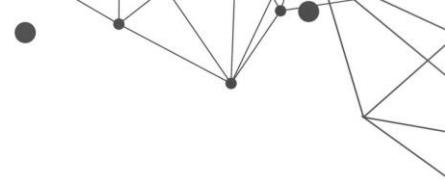


this case $O(n^2)$ have quadratic complexity. For the values of the variables used extracted from the radar used in input, two matrices were declared: one with 200 elements and the other containing 1000 elements. When calculating the complexity considering the video data input, we got quadratic time complexity, but in this case, the complexity depended on more variables (number of frames, height, and width of each frame), the result of the function was $O(n^2 \cdot N)$, where N is the image size and n the quantity of the frames. From the analysis of the processing of the developed algorithms, the worst-case time complexity occurs when the input data are images for the *EKF* estimator. It turns out that the number of steps that the algorithm takes for this input is much more unfavourable compared to the data obtained directly from the radar.

8. INTERPRETATION OF THE RESULTS

For the use of *EKF* in the radar data, tests with the estimator adjustment matrices (P_0 , Q and R) showed that changes in these parameters not only change the quality of the estimated states but also modify the quality of the filtered output signal. From the changes of these matrices, it is possible to evaluate the estimation and filtering capacity by *EKF*. There was no variation of the initial covariance matrix (P_0). On the other hand, higher confidence in the filter model resulted in lower filter performance, probably due to modelling errors. Higher confidence in measurement resulted in better performance for the estimated trajectory. Sampling time proved to be a parameter of greater impact on filter performance, and for smaller values, the filter was more effective.

From the results obtained in the processing of the algorithms, considering the two inputs, i.e., radar data and video data, the initial image processing requires not only an optimal estimator for the process but also software and hardware with adequate conditions for the analysis of this type of data. This is because the impact of extracting information from video images is significantly high and has a considerable influence on the estimator's processing time, as shown in Table 1. The estimated trajectory via *EKF* using 200 consecutive samples of the signal approximates the real trajectory as shown in Figure (9) with an error of approximately 2.0 m. For a single vehicle with 1000 signal samples, the error was 0.6 m between the real and estimated value, Figure (11). The estimated trajectory of the



area of vehicle detected from optical device images presented an error of 0.02 to 0.7 $pixel/m$, according to Figure (12). This analysis will future serve to identify the type of vehicle.

9. CONCLUSION

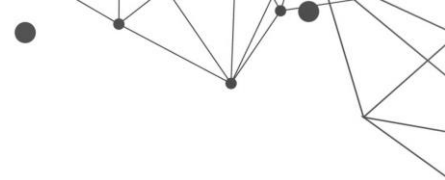
In this paper we have proposed a method to track and estimate a vehicle in movement on the highway. To do so, we used a *EKF* which can predict and estimate the tracked vehicle position. The input data considered were obtained by radar and by video from an optical device installed on the highway. For the optical device, the incorporation of the data captured by optical device for each image frame was done via *Matlab*[®]. The results obtained for the data extracted from the radar were analysed for a set of 200 samples and then the set was increased to 1000 samples of the position and speed values on x and y axes. The results extracted from the video, considered video images in a time interval of 5 s of traffic data. From this time, the frames used by *EKF* were extracted. The proposed function for tracking vehicle is based on the results obtained from our tracking approach in the covariance matrices P_0 , Q and R from the *EKF*, and one vehicle being tracked. As processing the algorithm, it was found that, although the computational complexity was quadratic for both inputs, the impact on the processing of extraction in image processing information is significantly high compared to processing the information provided by the radar: an execution time about one hundred times higher than that of the radar. The system is controllable and observable. We showed that with the proposed approach, the vehicle can have your trajectory tracked and estimated correctly.

ACKNOWLEDGEMENTS

The authors of this paper thanks the Departamento de Eletrônica, Telecomunicações e Informática (DETI) by Universidade de Aveiro - Portugal, Instituto Federal do Maranhão (IFMA) - Brazil and the Fundação de Amparo à Pesquisa e Desenvolvimento Científico e Tecnológico do Maranhão (FAPEMA) – Brazil, for funding this study.

REFERENCES

- Wu, H., & Meng, Y. (2019, July). A novel multi-vehicle tracking method based on linked list of associated vehicles. In 2019 IEEE 4th international conference on image, vision and computing (ICIVC) (pp. 376-381). IEEE.
- Tian, Z., Cai, Y., Huang, S., Hu, F., Li, Y., & Cen, M. (2018, June). Vehicle tracking system for intelligent and connected vehicle based on radar and V2V fusion. In 2018 Chinese Control And Decision Conference (CCDC) (pp. 6598-6603). IEEE.
- Kim, K. E., Lee, C. J., Pae, D. S., & Lim, M. T. (2017, October). Sensor fusion for vehicle tracking with camera and radar sensor. In 2017 17th International Conference on Control, Automation and Systems (ICCAS) (pp. 1075-1077). IEEE.
- Fang, Y., Wang, C., Yao, W., Zhao, X., Zhao, H., & Zha, H. (2019). On-road vehicle tracking using part-based particle filter. *IEEE transactions on intelligent transportation systems*, 20(12), 4538-4552.
- Liu, X., Dong, Y., & Deng, Z. (2020, June). Deep Highway Multi-Camera Vehicle Re-ID with Tracking Context. In 2020 IEEE 4th Information Technology, Networking, Electronic and Automation Control Conference (ITNEC) (Vol. 1, pp. 2090-2093). IEEE.
- Yu, J., Ji, Y., & Nie, C. (2019, November). Intelligent Vehicle Trajectory Tracking Algorithm Based on MPC Using Laguerre Functions. In 2019 Chinese Automation Congress (CAC) (pp. 1939-1943). IEEE.
- Ferreira, R., de Castro Ferreira, J. J., & Neves, A. J. R. (2022). Object Tracking Using Adapted Optical Flow. In A. J. R. J. R. Neves, & F. J. Gallegos-Funes (Eds.), *Information Extraction and Object Tracking in Digital Video* [Working Title]. IntechOpen. <https://doi.org/10.5772/intechopen.102863>
- Jeon, W., Zemouche, A., & Rajamani, R. (2019). Tracking of vehicle motion on highways and urban roads using a nonlinear observer. *IEEE/ASME transactions on mechatronics*, 24(2), 644-655.
- Cho, J., Jung, Y., Kim, D. S., Lee, S., & Jung, Y. (2019). Moving object detection based on optical flow estimation and a Gaussian mixture model for advanced driver assistance systems. *Sensors*, 19(14), 3217.
- Zhuang, X., Huang, Y., Palaniappan, K., & Zhao, Y. (1996). Gaussian mixture density modelling, decomposition, and applications. *IEEE Transactions on Image Processing*, 5(9), 1293-1302.
- Bishop, C. M., & Nasrabadi, N. M. (2006). *Pattern recognition and machine learning* (Vol. 4, No. 4, p. 738). New York: springer.
- Meghana, R. K., Chitkara, Y., & Apoorva, S. (2019, March). Background-modelling techniques for foreground detection and Tracking using Gaussian Mixture Model. In 2019 3rd International Conference on Computing Methodologies and Communication (ICCMC) (pp. 1129-1134). IEEE.



Mouzinho, L. F., Fonsecaneto, J. V., Luciano, B. A., Freire, R. C. S., de Barros, J., & Fontgalland, G. (2005, May). Kalman filter in real time for indirect measurement of space vehicle position using a reconfigurable architecture. In 2005 IEEE Instrumentation and Measurement Technology Conference Proceedings (Vol. 2, pp. 853-858). IEEE.

Mouzinho, L. F. (2007). Medição indireta ótima estocástica e neuronal em sistemas dinâmicos. PhD thesis, Federal University of Campina Grande.

Mouzinho, L. F., Fonsecaneto, J. V., Luciano, B. A., Freire, R. C. S., de Barros, J., & Fontgalland, G. (2005, May). Kalman filter in real time for indirect measurement of space vehicle position using a reconfigurable architecture. In 2005 IEEE Instrumentation and Measurement Technology Conference Proceedings (Vol. 2, pp. 853-858). IEEE.

Vecteezy, (2022). "Light road traffic." Retrieved from <https://www.videezy.com/transportation/45771-light-road-traffic>.

HIGH SENSITIVITY ENVELOPE DETECTOR ASSISTED BY MICROWAVE PHOTONICS

DOI: 10.51859/ampla.sst631.1122-5

André Paim Gonçalves¹
Felipe Streitenberger Ivo²
Olympio Lucchini Coutinho³

¹ Doctoral student in the Space Technology Sciences program. Instituto Tecnológico de Aeronáutica. ITA

² Doctoral student in the Space Technology Sciences program. Instituto Tecnológico de Aeronáutica. ITA

³ Photonics professor at Space Technology Sciences program. Instituto Tecnológico de Aeronáutica. ITA

ABSTRACT

This article presents a concept of an envelope detector with a high sensitivity value based on Microwave Photonics (MWP). The process of envelope detecting RF signals is achieved by the translation of the RF spectrum to the optical spectrum range. It is followed by optical filtering to cut the lower sideband and the carrier and finally beating the optical components of the remaining upper sideband into a low-speed photodetector, as a self-homodyne process. This approach depends only on the RF passing band of the phase modulator and the optical filter transfer function. This concept is experimentally demonstrated by reaching envelope detector sensitivity values around 53,000 V/W for the RF input frequency range of 10 GHz to 20 GHz. The proposed architecture does not use any optical or video signal amplifier. The implementation of this approach is simple, employs few components, and Commercial off-the-Shelf (COTS).

Key words: Envelope detection. High sensitivity. Microwave photonics.

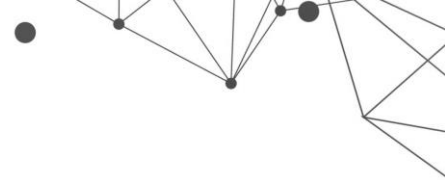


1. INTRODUCTION

The MWP is an area of human knowledge that since the 1970s has been consolidated as the study of photonic devices operating in microwave frequencies and their application in microwave systems. The initial idea was to use the advantages of photonic technologies to provide functions in very complex or even impossible microwave systems directly in the Knowledge of radio frequency (RF). These advantages are low weight, volume, and power consumption, as well as their band (Capmany & Novak, 2007). Using the knowledge developed by MWP, it was sought the development of an envelope detector (ED) that presented a better performance than those implemented by electronics. EDs are devices present in several telecommunication applications, such as wireless communications, electronic warfare, and radar processing (Adamy, 2006; Granja et al., 2017). There are processes aimed at reducing energy consumption, low volume, weight, and increasing radio frequency bandwidth (Viswanathan et al., 2018). Microwave photonics emerged to overcome the electronics in the fulfillment of such a difficult requirement (Ghelfi et al., 2019).

2. LITERATURE REVIEW

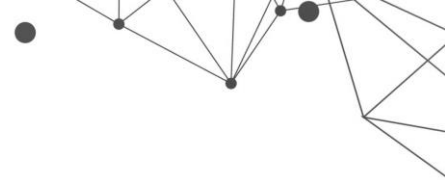
EDs are components that demodulate amplitude modulated signals. They take advantage of the same process performed by heterodyne mixers. EDs do not depend on local oscillators (LO) to make the beats of RF signals to the frequency baseband, they are simpler devices, but there is the inconvenience of having low sensitivity and reduction of the basic schemes of demodulation (Granja et al., 2017). An ED uses one or more non-linear components, such as diodes or transistors, to convert the microwave amplitude modulated signal to a baseband signal (Cimoli et al., 2018). The input signal can be processed by a structure composed of one diode or a set of diodes arranged in a balanced way, in other words, it employs quantities of diodes multiple of two. EDs with one diode present a spurious production of harmonic frequencies of the fundamental. Balanced EDs overcome this limitation using destructive interference for harmonic frequencies (Pozar, 2012). Balanced structures, however, have a cost in terms of complexity, low impedance matching for the operating frequency range, and low sensitivity. This is because they require



at least two non-linear parallel and differential devices that normally employ a 180° coupler with input loss (Pozar, 2012). For HEMT-based (High Electron Mobility Transistor) structures, they have an advantage over diode-based EDs in sensitivity and conversion gain that can be positive. It must be remembered that except for the ZBD, the other electronic EDs depend on biases and their control. This fact can make the circuit more complex and more energy-consuming.

The sensitivity metric can be used to compare ED performance. A High-performance HEMT-based ED can achieve a sensitivity of around 12,000 V/W for the microwave W band (Changfei et al., 2015). Low barrier Schottky diode can be found at 3,000 V/W for few tens of GHz (Santoruvo et al., 2020).

Some photonic EDs have been proposed to try to solve the problem of bandwidth, circuit simplicity, avoidance of LO, and power consumption, such as (Monroy et al., 2007; Prince et al., 2008; Sambaraju et al., 2008). The work presented by Prince et al employed an Electron Absorption Modulator (EAM) operating at the 20 GHz RF carrier (Prince et al., 2008). The gain suppression effect of a DFB laser is used to detect the envelope of the optical signal modulated by an EAM. The work presented by Monroy et al employed an EAM with the same concept for the 38 GHz RF carrier (Monroy et al., 2007), but a low-frequency response photodetector is used as an envelope detector. At both works, an RF signal is properly biased and amplified to operate at the inflection point of the absorption curve of an EAM. The choosing to operate at this point, instead of the conventional linear region of the power transfer function of EAM, a parcel of the radio frequency signal exceeding the inflection point experiences a large absorption and, in this way, half-wave rectification is achieved. The work presented by Sambaraju et al employed an MZM and an optical fiber Bragg grating to generate single-sideband modulated optical signal carriers to undergo direct photodetection (Sambaraju et al., 2008). A similar architecture was implemented by Zadeh and Levi. The authors considered it a frequency downconverter. It was implemented using an MZM and a Bragg grating (Hosseini-Zadeh & Levi, 2008). In the same paper, the authors compare the performance of this architecture by employing an optical microdisk modulator in place of the MZM. The system using a microdisk modulator performed better because the half-maximum modulation voltage (HMMV) was about 0.6 V, but its bandwidth is limited due to the quality factor of the modulator. Zadeh and Levi



employ the concept of receiving signals in a narrower band aiming at a target RF carrier. This system used an optical disk modulator aiming to reduce the input bandwidth of the receiver to improve its signal-to-noise ratio. These three proposed architectures rely on modulators that need bias points to operate in their linear regimes. Compared to intensity modulators, phase modulators offer lower insertion loss and do not need sophisticated bias control circuitry. Such control mechanisms can complicate their implementation and their subsequent integration, as well as increase power consumption (Lv et al., 2011).

This work presents a new concept that explores a little more the concept of envelope detection with the use of MWP. It points out a function for this system, that is, to employ it as an ED-based on a few low-cost photonic devices found on the shelf. We demonstrate the system sensitivity of around 53,000 V/W from the 10 GHz to 20 GHz frequency range. It can introduce input RF photonic gain as well as output transimpedance video gain on the system. This structure makes use of a broadband phase modulator, where there is the advantage of not needing the use of bias voltage control. A relevant benefit of using MWP in this work is the fact the RF signal exists only at the optical phase modulator (PM) input stage, which generally presents good flatness and high operation frequency bandwidth (Ren et al., 2019). The processing is implemented in optical frequency by optical devices. After the photodetector (PD) stage, all the signal processed is low frequency. This frequency range signal permits an electric low-frequency and transimpedance gain circuitry.

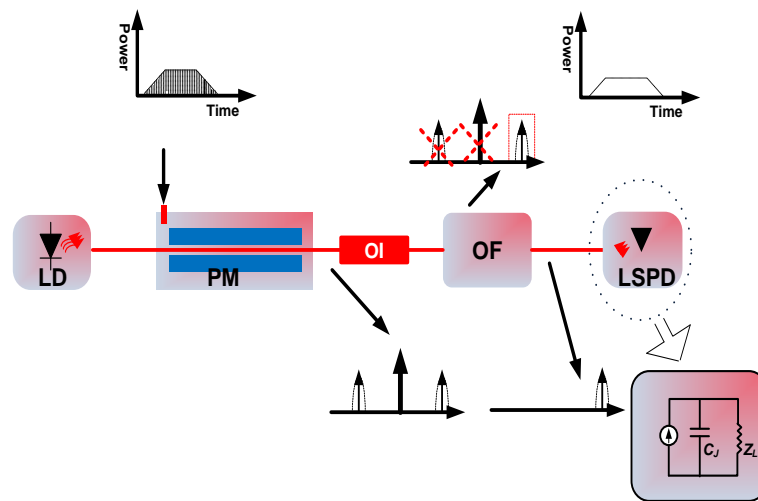
The sensitivity flatness at the frequency range depends only on the roll-off optical filter. The performance of the receiver can be improved by reducing the signal band at the output of the device as necessary, reducing the value of V_{π} , and increasing the load impedance. Where V_{π} is the half-wave voltage of the phase modulator that will be explained in the next section. The values obtained for such merit figures observed for electronic devices demonstrate that MWP-assisted envelope detection may present a better performance for these electronic types.

3. SYSTEM CONFIGURATION

The principle of operating the fully photonic envelope detector is shown in Figure 1. The laser light wave is coupled to the phase modulator and undergoes optical phase modulation by the RF signal. The modulated optical signal passes

through an optical filter. The optical carrier and the lower sideband of the modulated signal are rejected. The upper sideband portion of the modulated optical signal is transmitted through the filter to the photodetector, to be converted into a baseband electrical signal by direct detection. This process is similar to the one used by Zadeh and Levi (Hossein-Zadeh & Levi, 2008), where the authors presented this structure as a down converter for an RF receiver.

Figure 1 - Schematic diagram of the photonic ED. LD – Laser Diode, PM – Phase Modulator, OI – Optical Isolator, OF – Optical Filter, LSPD – Low-Speed Photodetector, C_j – Junction Capacitance, and Z_L - Output Load.

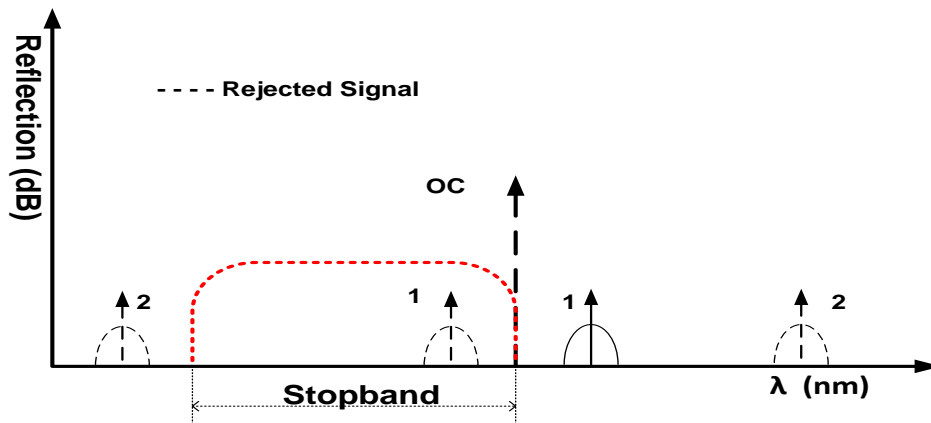


Source: The authors.

There are two important processes to consider in the proper operation of this system. The first is the conversion of the phase to intensity optic modulation. The optical phase-modulated has an optical carrier and lower sideband filtered, only the upper sideband coupled to the photodetector. Figure 2 illustrates how this filtering is done. The most common process is the use of an optical filter to eliminate one of the lateral sidebands of the modulated signal and inject the optical carrier and the remaining sideband into the photodetector (Urlick et al., 2015). The second process is self-homodyne detection. The upper sideband frequency components are beating themselves. If a low-speed photodetector (LSPD) is chosen, it works as a low pass filter, because the RF output response is low frequency and its equivalent circuit is a current source with load in parallel junction capacitance, as the Figure 1. The result of this process is the detection of the RF pulse envelope. The LSPD equivalent circuit behavior allows transimpedance gain in the output signal.

A common technique is using the optic spectrum beating of the carrier and sideband to recover the RF components in the photodetector (Urick et al., 2015). However, our approach is quite different, letting the optical filter transmit only one of the sidebands of the modulated optical signal to reach the photodetector, avoiding from other sidebands and optical carrier to beat on the photodetector. The result of this process is the detection of the RF pulse envelope which is called self-homodyne detection.

Figure 2 - Schematic diagram of the behavior of the optical filter and the optical carrier tuning. OC – Optical Carrier; 1 and 2 mean the sidebands of the optical signal modulated in the optical filter.



Source: The authors.

3.1. MATHEMATICAL MODELING OF THE ENVELOPE DETECTOR ASSISTED BY MWP

An optical signal generated by a laser diode with an electric field phasor equal to

$$E(t)_o = E_o \exp[j(\omega_o t + \varphi_i)], \quad (1)$$

where E_o is the electric field amplitude of the signal coming from the laser diode, ω_o is angular frequency of electric field phasor, and φ_i is the phase, focuses on a phase modulator. To facilitate the analysis of the electric field, the phase is considered $\varphi_i = 0$.

Considering an electrical RF signal acting on the RF input of a phase modulator, its voltage is defined as:

$$V(t)_{RF} = V \cos(\omega_{RF} t + \varphi_{RF}), \quad (2)$$

where V is the amplitude of the incident RF voltage, ω_{RF} is the angular frequency, and φ_{RF} is the phase of RF voltage. In the phase modulator, the optical signal undergoes a phase change as:

$$E(t)_O = \{E_O \exp[j\omega_o t] \times \exp[jm \cos([\omega_{RF} + \Delta\omega_{RF}]t + \varphi_{RF})] \times \exp[jm \cos([\omega_{RF} - \Delta\omega_{RF}]t + \varphi_{RF})]\}, \quad (3)$$

where $\Delta\omega_{RF}$ is half of instantaneous bandwidth RF pulse. The modulation index m is defined as:

$$m = \frac{V}{V_\pi} \pi, \quad (4)$$

where V_π is phase modulator half-wave voltage. The V_π is a voltage value corresponds to the π phase optical signal changing.

Considering a special operating condition of the modulator, which is called a small signal operating regime, where $m \ll 1$, the (3) can be mathematically rewritten in a simplified way according to the Bessel series. In this way, the output signal of the modulator in the small-signal operation mode can be expressed, in modulus value, by:

$$E(t)_M = E_O J_0(m) \exp[j(\omega_o t)] + E_O J_1(m) \exp[j(A t + \varphi_{RF} + \pi/2)] + E_O J_1(m) \exp[j(B t + \varphi_{RF} + \pi/2)] - E_O J_1(m) \exp[j(C t - \varphi_{RF} - \pi/2)] - E_O J_1(m) \exp[j(D t + \varphi_{RF} + \pi/2)] \quad (5)$$

where $J_0(m)$ and $J_1(m)$ are Bessel functions of first species and order 0 and 1, respectively. $A = [\omega_o + \omega_{RF} + \Delta\omega_{RF}]$, $B = [\omega_o + \omega_{RF} - \Delta\omega_{RF}]$, $C = [\omega_o - \omega_{RF} - \Delta\omega_{RF}]$ and $D = [\omega_o - \omega_{RF} + \Delta\omega_{RF}]$ are variable substitution.

In expression (5), the optical signal at the output of the phase modulator has the same amplitude and symmetrical phase sidebands, which gives a DC signal at the output of the photodetector if the spectral components do not change in phase or amplitude. This output signal of the phase modulator is then coupled to a fiber

optic filter as shown in Figure 1 and tuned to the stopband operation point shown in Figure 2.

The optical filter, employed at the operating point of Figure 2, is considered an ideal optical filter with a spectral behavior like a step function. The lower region of the step function would be the signal transmission and the maximum reflection region of the optical signal would be the top of the step function. Placing the tuned optical carrier close to one of the step function's corners allows correct laser tuning and maximum extinction of the optical carrier and one of the sidebands. In Figure 2, signal number 2 is operating in the transmission region. This fact doesn't eliminate one of the lateral bands of the optically modulated signal and doesn't allow the phase conversion to intensity modulation. It is important to note that the optical filter is designed to have a high coefficient of optical reflectivity, being practically constant for the stopband region.

In the tuning of the optical filter as in Figure 2, only the lower sideband of the signal impacts the photodetector. The signal is expressed by:

$$E(t)_T \cong \sqrt{T(\omega)} E_0 J_1(m) \times \left\{ \exp \left[j \left(At + \varphi_{RF} + \pi/2 + \varphi(\omega) \right) \right] + \exp \left[j \left(Bt + \varphi_{RF} + \pi/2 + \varphi(\omega) \right) \right] \right\} \quad (6)$$

In expression (6) depends directly on the frequency response of the filter transmissivity parameters $T(\omega)$ and phase $\varphi(\omega)$.

As the photodetector is sensitive to the intensity of the incident optical signal, it will be necessary to calculate the value of the Poynting vector, knowing that the magnetic field is:

$$H(t)_T \cong \frac{1}{\eta} \left[\sqrt{T(\omega)} E_0 J_1(m) \right] \times \left\{ \exp \left[j \left(At + \varphi_{RF} + \pi/2 + \varphi(\omega) \right) \right] + \exp \left[j \left(Bt + \varphi_{RF} + \pi/2 + \varphi(\omega) \right) \right] \right\}, \quad (7)$$

where η is the intrinsic impedance of the material. The Poynting vector modulus is given by:

$$S(t) = E(t)_T \times H(t)_T^*. \quad (8)$$

Employing (6) and (7) in (8) one has:

$$\begin{aligned} S(t) = & \frac{1}{\eta} \left(\sqrt{T(\omega)} E_0 J_1(m) \right)^2 \\ & \times \left\{ \exp \left[j \left(At + \varphi_{RF} + \frac{\pi}{2} + \varphi(\omega) \right) \right] \right. \\ & \left. + \exp \left[j \left(Bt + \varphi_{RF} + \frac{\pi}{2} + \varphi(\omega) \right) \right] \right\} \\ & \times \left\{ \exp \left[-j \left(At + \varphi_{RF} + \frac{\pi}{2} + \varphi(\omega) \right) \right] \right. \\ & \left. + \exp \left[-j \left(Bt + \varphi_{RF} + \frac{\pi}{2} + \varphi(\omega) \right) \right] \right\}. \end{aligned} \quad (9)$$

Results in:

$$S(t) = \frac{1}{\eta} \left(\sqrt{T(\omega)} E_0 J_1(m) \right)^2 \exp[-2j(\Delta\omega_{RF}t)] + \exp[+2j(\Delta\omega_{RF}t)]. \quad (10)$$

Knowing that (10) corresponds to the trigonometric relationship:

$$2\cos(F) = \exp[-j(F)] + \exp[+j(F)], \quad (11)$$

the modulus of the Poynting vector is expressed by:

$$S(t) = \frac{[2T(\omega)(E_0 J_1(m))^2 \cos(2\Delta\omega_{RF}t)]}{\eta}. \quad (12)$$

It should be noted that $\Delta\omega_{RF}$ corresponds to the half of baseband bandwidth of RF signal. The result (12) is obtained by replacing (10) with (11) in the form. The electrical current, $i(t)$, at the photodetector output at the baseband frequency is calculated by multiplying (12) by the photodetector area, A , and by the photodetector responsiveness, \mathfrak{R} , conform:

$$i(t) = \frac{2A\mathfrak{R}T(\omega)(E_0 J_1(m))^2 \cos(2\Delta\omega_{RF}t)}{\eta}. \quad (13)$$

Knowing that optical power in input system is:

$$P_o = \frac{A(E_o)^2}{\eta} \quad (14)$$

and knowing that $J_1(m) = \pi V / 2V_\pi$ for $m \ll 1$, substituting in (13), the current is:

$$i(t) = \frac{P_o \Re T(\omega) \pi^2 V^2}{2V_\pi^2} \cos(2\Delta\omega_{RF}t), \quad (15)$$

where $V = \sqrt{2P_{RF}Z}$, P_{RF} is RF input power, and Z is input impedance. The baseband voltage at output ED is:

$$V_{OUT} = \frac{P_o \Re T(\omega) \pi^2 P_{RF} Z Z_L}{V_\pi^2}, \quad (16)$$

where Z_L is an ED output impedance load.

Observing (16) is possible to notice that the electric signal at the photodetector output is the baseband signal of the RF phase modulator input. The result is the envelope of the input signal converted to current at the photodetector output. Faced with this fact, this architecture can explore a slow-speed photodetector, that is, a photodetector with an output band in the baseband, a few kHz. With the signal band in the order of kHz, it becomes possible to implement transimpedance gain with the increase of the load on the device output. The PD output voltage value (V_{out}) was estimated according to (16) and Table 1. The carrier frequency considered was 17 GHz and the losses values were 8 dB.

Table 1 - Theoretical forecasted P_{RF} values.

P_{RF} (dBm)	P_{RF} (mW)	P_o (mW)	\Re (W/A)	V_π (V)	Z (M Ω)	i (μ A)	V_{out} (V)	Sensitivity (mV/mW)
10.41	11	50	1	10.5	0.027	630	17	1,545.45
0.79	1.2	50	1	10.5	0.5	60	30	25,000
-3.3	0.467	100	1	10.5	0.5	44.93	23.46	50.24 10^3
-50	10^{-5}	100	1	3.5	1	$9.03 \cdot 10^{-3}$	$9.03 \cdot 10^{-3}$	$903 \cdot 10^3$
-70	10^{-7}	100	1	0.35	1	$9.03 \cdot 10^{-3}$	$9.03 \cdot 10^{-3}$	$90.3 \cdot 10^6$

Source: The authors.

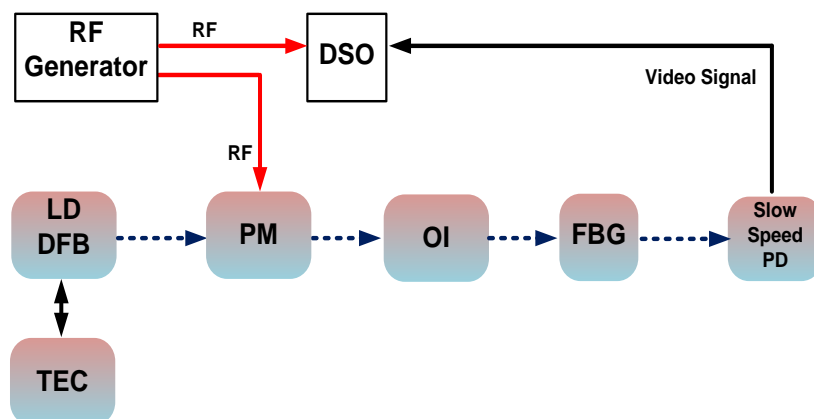
The performance of the ED can be improved by reducing the value of V_π , according to (16), and increasing the load impedance (Hosseini-Zadeh & Levi, 2008;

Lipsky, 2004; Ziemer & William H. TRANTER, 2015). The value of V_{π} can reach up to 0.3 V when an electro-optical polymer modulator was used (Liu et al., 2015).

4. EXPERIMENTAL DEMONSTRATION OF THE PHOTONIC ENVELOPE DETECTOR

To demonstrate and measure the sensitivity of the photonic envelope detector, an experiment was carried out. Sensitivity was calculated by taking the ratio between the output photodetector load voltage and the RF power at PM. The schematic diagram is shown in Figure 3. A DFB laser is used as an optical source. The phase modulator operates at frequencies up to 20 GHz. A uniform FBG was used as an optical filter followed by a 1.5 GHz low-speed photodetector. The RF signal generator is used to perform the pulse radar signal and a high-speed digital sampling oscilloscope (DSO) is used to measure the input RF modulated signal and the output video signal, in other words, the envelope of the input signal.

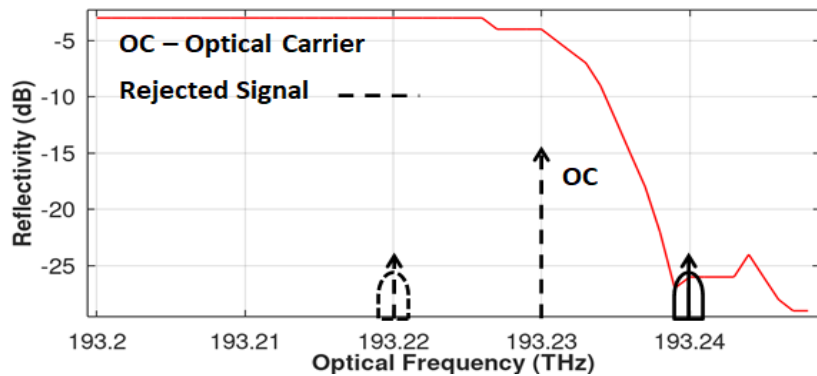
Figure 3 - Schematic diagram setup of the receiver. DFB - Distributed Feedback Laser, TEC - Thermal Electronic Cooler, PM - Phase Modulator; OI - Optical Isolator, RF - Radio Frequency, PD - Photodetector, and FBG - Fiber Bragg Grating.



Source: The authors.

For the sake of simplicity, Figure 4 shows only the right side of the rejection passband optical filter, cut right on the center frequency. The right edge has a roll-off starting from the total transmission and ending at the beginning of the region's maximum optical signal reflection.

Figure 4 - Right side of rejection passband optical filter, cut right on the center frequency. This center is around 193.200 THz.

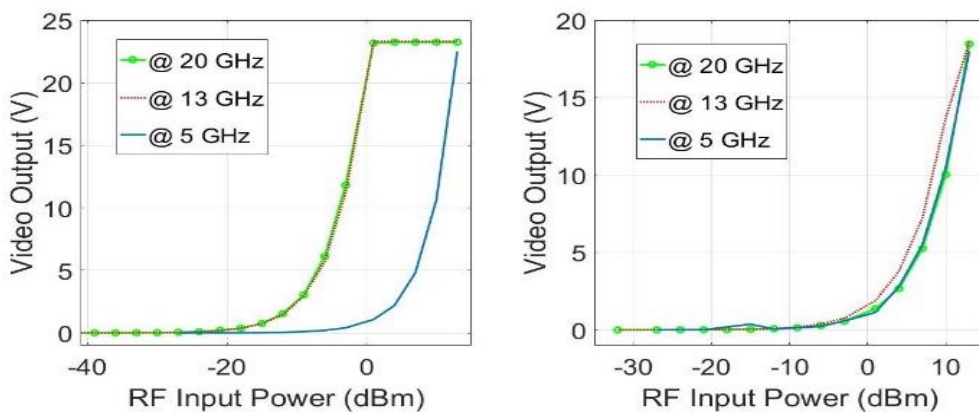


Source: The authors.

The transition region between stopband and transmission band has a roll-off around 2.86 dB/GHz. This imposes a limitation on the flatness RF response operation band, starting at 10 GHz, considering the laser carrier tuned at a frequency right on the edge of the optic stopband.

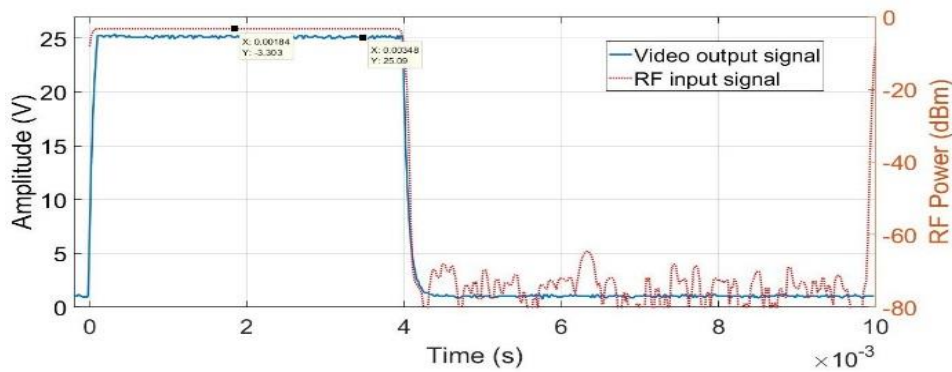
The ED tuning occurs as explained previously. To measure ED sensitivity, a test was performed with laser tuning as explained in Figure 4, and then applying a continuous wave RF signal at the phase modulator input and varying its frequency from 0 to 20 GHz. Laser power was set on 50 mW. The photodetector load impedance was 27 kΩ. The process was repeated with another load equal to 500 kΩ. Another test was performed with RF pulsed signal. The pulse width was 4 ms and Pulse Repetition Interval was equal to 10 ms. The sensitivity curve is shown in Figure 5. The RF pulses and the baseband pulses are observed in Figure 6.

Figure 5 - Sensitivity curve for the RF frequencies of 20, 13, and 5 GHz with the various RF powers at the input compared to the voltage at the output (video signal). The load is 500 kΩ and the voltage ranges from 1.52 mV to 23.63 V on the right side. The load is 27 kΩ and the voltage ranges from 1.5 mV to 18.63 V on the left side.



Source: The authors.

Figure 6 - The RF input power at 17 GHz is shown in the red line and it has an RF power value equal to -3.3 dBm. The load is 500 k Ω .



Source: The authors.

The sensitivity curve is shown in Figure 5 right and the left side was measured using laser power equal to 50 mW and the environment temperature around 25 °C. On the left side of Figure 5, one can notice that the signal presents saturation for the frequencies 20 GHz and 13 GHz, and the curve for 5 GHz detaches from the previous two because of the roll-off of the Bragg grating response. The measured values of sensitivity obtained are 28,818.27 mV/mW for 20 GHz and 29,787.31 mV/mW for 13 GHz that can be considered very high values according to what is observed in conventional devices that perform the same function of both low barrier Schottky diode-based envelope detectors without bias and HEMT based envelope detectors. The photodetector saturates on an input of RF power from 0 dBm to 16 dBm at the range frequency from 10 GHz to 20 GHz. However, the baseband signal at PD output is linear even with the PD is saturated. On the left side of Figure 5, one can note an unsaturated result for the three frequencies. Note that there is a small detachment of the curves. The highest voltage value observed was 18.63 V, lower than the voltage measured with the 500 k Ω load of 23.63 V. The power and temperature were the same for the measure with both tests. The maximum sensitivity results for the 27 k Ω load for 20 GHz were 2,244.99 mV/mW and 4,358.46 mV/mW for 13 GHz. These values are better than those observed for Schottky diode-based envelope detectors.

The RF input power was -3.3 dBm and the video output voltage was around 25 V in Figure 6. The laser was operated at 100 mW and the environment temperature was around 25 °C. The sensitivity of the system was 53,000 mV/mW. This value is better than the 22,700 mV/mW presented by Hou et al (Hou et al.,

2017). The value achieved in the experiment was near values achieved in Table 1 for the same conditions.

5. CONCLUSIONS

This article presented a microwave photonic approach to RF envelope detection. As this system uses an optic phase modulator it brings the advantage of needing the employment of bias voltage control circuit compared with the ones that use intensity modulators. The photonic envelope detector sensitivity reaches 53,000 mV/mW with the available devices. However, if the V_{π} value of the phase modulator decreases, these values could get even higher. The result obtained is already much higher than what is available in the literature presented in previous sections.

REFERENCES

- Adamy, D. L. (2006). Introduction to electronic warfare modeling and simulation. In *Introduction to Electronic Warfare Modeling and Simulation*. Institution of Engineering and Technology. <https://doi.org/10.1049/SBRA011E>
- Capmany, J., & Novak, D. (2007). Microwave photonics combines two worlds. In *Nature Photonics*. <https://doi.org/10.1038/nphoton.2007.89>
- Changfei, Y., Ming, Z., Yunsheng, L., & Conghai, X. (2015). Millimeter wave broadband high sensitivity detectors with zero-bias Schottky diodes. *Journal of Semiconductors*, 36. <https://doi.org/10.1088/1674-4926/36/6/065002>
- Cimoli, B., Paez, J. S. R., Turhaner, A., Johansen, T. K., & Olmos, J. J. V. (2018). Active HEMT based envelope detector for ultra-wideband wireless communication systems. In: *IEEE/MTT-S INTERNATIONAL MICROWAVE SYMPOSIUM - IMS, 2018-June*, 923–926. <https://doi.org/10.1109/MWSYM.2018.8439661>
- Ghelfi, P., Scotti, F., Onori, D., & Bogoni, A. (2019). Photonics for ultrawideband RF spectral analysis in electronic warfare applications. *IEEE Journal of Selected Topics in Quantum Electronics*. <https://doi.org/10.1109/JSTQE.2019.2902917>
- Granja, A. B., Cimoli, B., Rodriguez, S., Jakoby, R., Bevensen Jensen, J., Penirschke, A., Monroy, I. T., & Johansen, T. K. (2017). Ultra-wideband balanced schottky envelope detector for data communication with high bitrate to carrier frequency ratio. In: *IEEE MTT-S INTERNATIONAL MICROWAVE SYMPOSIUM (IMS), October, 2052–2055*. <https://doi.org/10.1109/MWSYM.2017.8059074>
- Hosseini-Zadeh, M., & Levi, A. F. J. (2008). Selfhomodyne photonic microwave receiver architecture based on linear optical modulation and filtering. *Microwave*



and *Optical Technology Letters*, 50(2), 345–350.
<https://doi.org/10.1002/mop.23065>

Hosseini-Zadeh, M., & Levi, A. F. J. (2008). Self-homodyne photonic microwave receiver architecture based on linear optical modulation and filtering. *Microwave and Optical Technology Letters*, 50(2), 345–350.

Hou, H. W., Liu, Z., Teng, J. H., Palacios, T., & Chua, S. J. (2017). High temperature terahertz detectors realized by a GaN high electron mobility transistor. *Scientific Reports*, 7(1), 46664. <https://doi.org/10.1038/srep46664>

Lipsky, S. E. (2004). *Microwave passive direction finding*. SciTech Publishing.

Liu, J., Xu, G., Liu, F., Kityk, I., Liu, X., & Zhen, Z. (2015). Recent advances in polymer electro-optic modulators. *RSC Advances*. <https://doi.org/10.1039/c4ra13250e>

Lv, Q., Xu, K., Dai, Y., Li, Y., Wu, J., & Lin, J. (2011). A novel simple RF-to-digital photonic link based on a single phase modulator. In: *INTERNATIONAL CONFERENCE ON INFORMATION PHOTONICS AND OPTICAL COMMUNICATIONS*, 1–3. <https://doi.org/10.1109/IPOC.2011.6122862>

Monroy, I. T., Seoane, J., & Jeppesen, P. (2007). All-optical envelope detection for wireless photonic communication. In: *33RD EUROPEAN CONFERENCE AND EXHIBITION ON OPTICAL COMMUNICATION - ECOC 2007*, 2007(1), 744–744. <https://doi.org/10.1049/ic:20070270>

Pozar, D. M. (2012). Microwave engineering. In *John Wiley & Sons, Inc* (4th ed.).

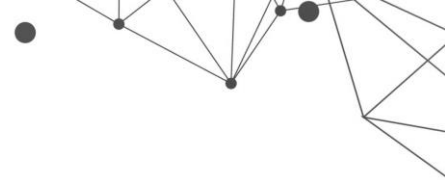
Prince, K., Tafur Monroy, I., Seoane, J., & Jeppesen, P. (2008). All-optical envelope detection for radio-over-fiber links using external optical injection of a DFB laser. *Optics Express*, 16(3), 2005. <https://doi.org/10.1364/OE.16.002005>

Ren, T., Zhang, M., Wang, C., Shao, L., Reimer, C., Zhang, Y., King, O., Esman, R., Cullen, T., & Lončar, M. (2019). An Integrated Low-Voltage Broadband Lithium Niobate Phase Modulator. *IEEE Photonics Technology Letters*, 31(11), 889–892. <https://doi.org/10.1109/LPT.2019.2911876>

Sambaraju, R., Palaci, J., Polo, V., & Corral, J. L. (2008). Photonic envelope detector for broadband wireless signals using a single Mach-Zehnder modulator and a fibre Bragg grating. In: *34TH EUROPEAN CONFERENCE ON OPTICAL COMMUNICATION, October*, 1–2. <https://doi.org/10.1109/ECOC.2008.4729527>

Santoruvo, G., Nikoo, M. S., & Matioli, E. (2020). Broadband zero-bias RF field-effect rectifiers based on AlGaIn/GaN nanowires. *IEEE Microwave and Wireless Components Letters*, 30(1), 66–69. <https://doi.org/10.1109/LMWC.2019.2953632>

Urlick, V. J., McKinney, J. D., & Williams, K. J. (2015). Fundamentals of microwave photonics. In *Fundamentals of Microwave Photonics*. John Wiley & Sons, Inc. <https://doi.org/10.1002/9781119029816>



Viswanathan, B., Rissons, A., Destic, F., Destrez, S. L., Escudier, B., & Compin, M. (2018). Radiation analysis of CubeSat Nimph. *Proceedings of the International Astronautical Congress, IAC*.

Ziemer, R. E. and, & William H. TRANTER. (2015). *PRINCIPLES OF COMMUNICATIONS: Systems, Modulation, and Noise*.

INVESTIGATION OF ELECTROMAGNETIC AND ABSORBER PROPERTIES OF DOUBLE-LAYER SYSTEM USING IRON CARBONYL AND FERRITE COMPOSITES

DOI: 10.51859/ampla.sst631.1122-6

Plínio Ivo Gama Tenório¹
Ana Paula Silva de Oliveira²
Rafael Cardoso Toledo³
Mauricio Ribeiro Baldan⁴
Sérgio Luiz Mineiro⁵

¹ PhD candidate in Space Engineering and Technology from Instituto Nacional de Pesquisas Espaciais - INPE

² MSc in Space Engineering and Technology from Instituto Nacional de Pesquisas Espaciais - INPE

³ PhD in Space Engineering and Technology from Instituto Nacional de Pesquisas Espaciais - INPE

^{4,5} Researcher at Instituto Nacional de Pesquisas Espaciais - INPE

ABSTRACT

The double-layer structure has more requirements to create a good electromagnetic wave absorber material due to the combination of different layers properties. Therefore, this work aims to develop a double-layer absorber material using polymer matrix composites with iron carbonyl and manganese and zinc ferrite. Among the different combinations studied, the best result was observed for combinations with CI composite as layer 2. The combination with the best bandwidth was obtained with the combination 2 mm CI + 3 mm Ferrite. This configuration absorbed more than 90% of the EM wave in at least 70% of the frequency range, 3.9 GHz (12.4 to 16.06 GHz). In addition, the 3 mm CI + 3 mm Ferrite combination had the best attenuation, -23.64 dB at 12.4 GHz.

Key words: Electromagnetic properties. microwave absorption. double-layer absorber. Multilayer absorber

1. INTRODUCTION

Radar absorber materials (RAM) have been widely researched due to their importance in many fields, e.g., stealth aircraft, radar detection, medical devices, electromagnetic device housing and other applications. The challenge in developing RAM development is to select of magnetic and dielectric materials with maximum wave absorption properties (Das et al., 2015; Ding et al., 2020). For this, two important conditions must be satisfied: first, the impedance of the properties must be matched, and second, the incident electromagnetic wave must penetrate through the material layer and be quickly attenuated (Meng et al., 2009).

The Ku band has become the most widely used communications technology for satellite communications because of its advantages over bands below the Ku band (12.4-18 GHz), such as higher throughput, smaller size, wider spectrum bandwidth and reduced susceptibility to rain attenuation. Other applications for this band include very small aperture terminal antenna systems, security applications, mobile communications, remote sensing technologies, satellite and terrestrial data mapping, weather forecasting, radio communications, ISI communications, communications services with vehicles sent to other planets, satellites and space exploration services (Ansal et al., 2021).

The objective of this work is to develop an absorber material for Ku-band. Single-layer materials can hardly meet most of the requirements for EM absorption due to a limited number of parameters. On the other hand, multilayer absorbers can easily achieve these conditions by combining the properties of different material layers by adding an absorption layer or creating impedance-matched layers (Liu et al., 2014; Meng et al., 2009). For the development of multilayer broadband absorbers, iron carbonyl (CI) and manganese and zinc ferrite ($\text{Mn}_{0.6}\text{Zn}_{0.4}\text{Fe}_2\text{O}_4$) were used as additives. Both of them are widely used in absorber materials due to some advantages, such as simple fabrication process, low cost, large magnetic loss angle and strong absorption capability (Liu et al., 2014).

2. MATERIALS AND METHODS

2.1. SAMPLE PREPARATION

The composites were prepared by hand mixing the silicone rubber matrix, catalyst and fillers. The composition used was 60 wt% (Table 1). The layers have a rectangular geometry corresponding to the Ku-band waveguide (15.7 mm x 7.9 mm) and a thickness of 1, 2 or 3 mm. A commercial carbonyl iron (CI) powder from BASF and $Mn_{0,6}Zn_{0,4}Fe_2O_4$ (ferrite) from Sontag S.A. were used as fillers.

Table 1 – Composites composition and thickness.

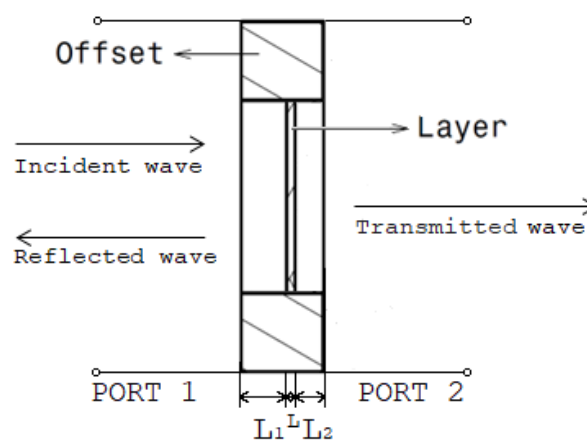
wt% filler	Filler type	Thickness (mm)
60	Ferrite	1, 2 and 3
60	CI	1, 2 and 3

Source: The authors.

2.2. ELECTROMAGNETIC CHARACTERIZATIONS

The electromagnetic properties of each layer (complex ϵ_r and μ_r) were determined from the scattering parameters (S_{11} , S_{12} , S_{21} , and S_{22}) using a Keysight 50-GHz vector network analyzer (VNA), model N5232A. The waveguide used for the Ku-band region was WR -62 (P11644A/Agilent). According to the Nicolson-Ross-Weir (NRW) method for two-port devices, also known as the transmission and reflection method (TR) (Figure 2), the transmitted (S_{21} and S_{12}) and reflected (S_{11} and S_{22}) parameters can be expressed as follows (Nicolson & Ross, 1970):

Figure 1 – Electromagnetic properties measurement.



Source: The authors.

$$S_{21} = R_1^2 \frac{\Gamma(1 - T^2)}{1 - \Gamma^2 T^2} \quad (1)$$

$$S_{21} = R_1 R_2 \frac{T(1 - \Gamma^2)}{1 - \Gamma^2 T^2} \quad (2)$$

where, Γ and T are the reflection and transmission coefficient, respectively; $R_1 = e^{-\gamma_0 L_1}$ and $R_2 = e^{-\gamma_0 L_2}$ are the expression used for adjusting the reference plane of S_{11} and S_{21} ; and L_1 and L_2 the distance of calibration plans in reference to sample (Baker-Jarvis, 1990).

Thus, through these parameters is possible to determine reflection and transmission coefficient:

$$\Gamma = K \pm \sqrt{K^2 - 1} \quad (3)$$

K is given by:

$$K = \frac{S_{11}^2 + S_{21}^2 + 1}{2S_{11}} \quad (4)$$

$$T = \frac{S_{11} + S_{21} - \Gamma}{1 - (S_{11} + S_{12})\Gamma} \quad (5)$$

Wherefore, permittivity (ϵ_r) and permeability (μ_r) are given by:

$$\mu_r = \frac{1 + \Gamma}{(1 - \Gamma)\Lambda \sqrt{\frac{1}{\lambda_0^2} - \frac{1}{\lambda_c^2}}} \quad (6)$$

$$\epsilon_r = \frac{\lambda_0}{\mu_r} \left[\frac{1}{\lambda_c^2} \left[\frac{1}{2\pi L} \ln(T^{-1}) \right]^2 \right] \quad (7)$$

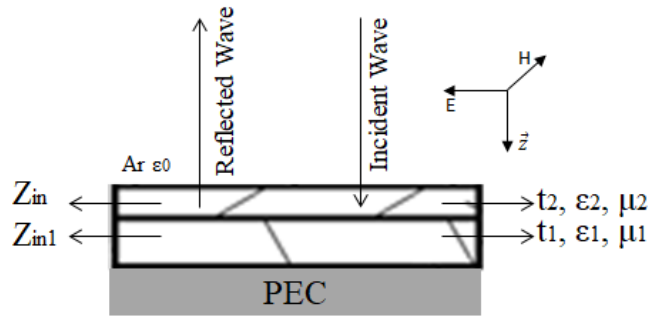
The term Λ is given by:

$$\Lambda = j \frac{L}{2\pi \ln(T^{-1})} \quad (8)$$

2.3. DOUBLE-LAYER REFLECTION LOSS

The measurement of double-layers reflection loss consists of adjusting the configuration with each layer in its position within the offset; the structure is shown in Figure 1, where layer 2 is closest to the air and layer 1 is closest to the perfect electrical conductor (PEC). When an electromagnetic wave propagating in the positive z -direction strikes the absorber normally, a series of waves begin to propagate within the layers, both in the positive and negative z -directions (Meshram et al., 2004).

Figure 2 – Double-layer system.



Source: The authors.

The entrance impedance (Z_{ini}) of layer i ($i = 1, 2, 3, \dots, n$) in systems with a PEC at the end is describe by equation 1 (Liu et al., 2014; Naito & Suetake, 1971):

$$Z_{ini} = \eta_i \left[\frac{Z_{i+1} + \eta_i \tanh(\gamma_i t_i)}{\eta_i + Z_{i+1} \tanh(\gamma_i t_i)} \right] \quad (9)$$

However, the impedance of last layer (n -layer) before the PEC describes as equation 2:

$$Z_{inn} = \eta_n \tanh(\gamma_n t_n) \quad (10)$$

The characteristics impedance (equation 3) and complex propagation constant (equation 4) are expressed in terms of complex permittivity (ϵ_r) and permeability (μ_r) of layer (Meng et al., 2009):

$$\eta = \sqrt{\frac{\mu_0}{\epsilon_0}} \sqrt{\frac{\mu_r}{\epsilon_r}} = \sqrt{\frac{\mu_0}{\epsilon_0}} \sqrt{\frac{\mu_r' - j\mu_r''}{\epsilon_r' - j\epsilon_r''}} \quad (11)$$

$$\gamma = \frac{j\omega\sqrt{\mu_0\epsilon_0}\sqrt{\mu_r\epsilon_r}}{c} = \frac{j2\pi f}{c} \sqrt{\mu_0\epsilon_0} \sqrt{(\mu_r' + j\mu_r'')(\epsilon_r' + j\epsilon_r'')} \quad (12)$$

Where, t , η and γ are thickness, characteristics impedance and complex propagation constant, respectively; ϵ_0 is the permittivity and μ_0 the permeability of air; f is the frequency of the electromagnetic (EM) wave in free space and c is the velocity of light. According to the theory of the transmission line, the reflection coefficient (Γ) is a relation between the impedances of the layers and the characteristic impedance of the material (η_0), where η_0 is 50Ω due to the configuration of the vector network analyzer.

$$\Gamma = \left| \frac{Z_{in} - \eta_0}{Z_{in} + \eta_0} \right| \quad (13)$$

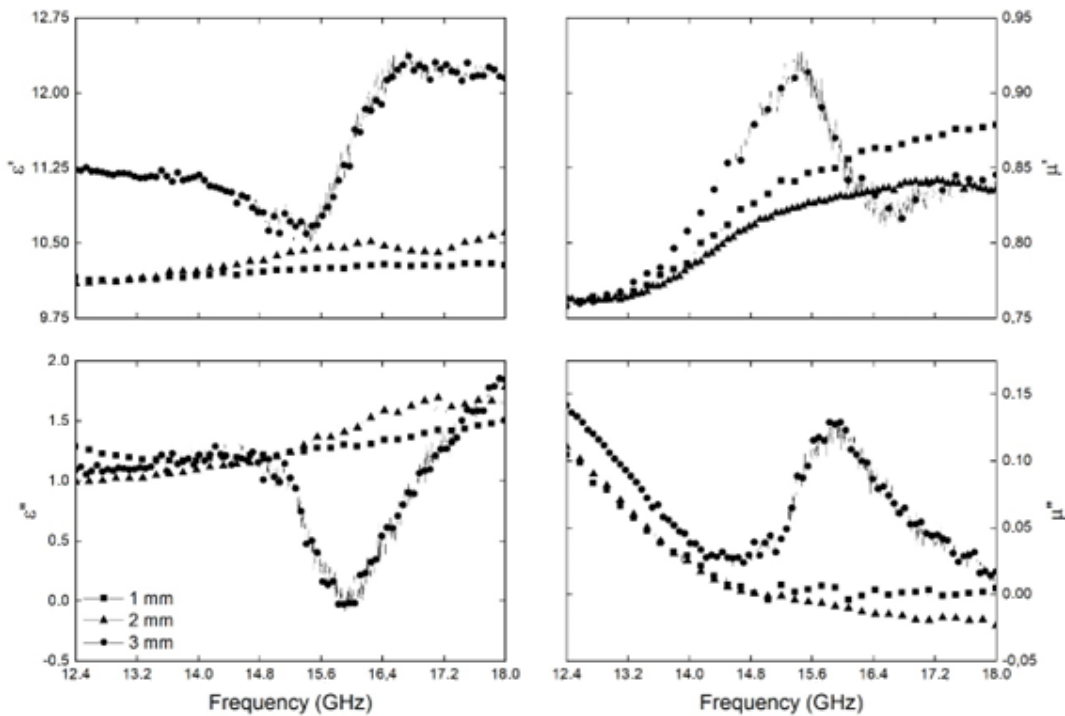
So, the reflection loss (RL) is given by equation 6:

$$RL (dB) = 20 \log_{10} \Gamma \quad (14)$$

3. RESULTS AND DISCUSSION

The complex permittivity ($\epsilon_r = \epsilon' + j\epsilon''$) and permeability ($\mu_r = \mu' + j\mu''$) of single-layer manganese and zinc ferrites are shown in Figure 3. For the composites with thicknesses of 1 and 2 mm, the real permittivity (ϵ') is constant over the entire frequency range. The imaginary permittivity (ϵ'') increases with the increase of the frequency from 1 to 1.5.

Figure 3 – Real and complex permittivity and permeability of manganese and zinc ferrite samples with 1, 2 and 3 mm of thickness.



Source: The authors.

In the ferrite sample with 3 mm was found the material resonant frequency (ω_0) at 15,97 GHz with an inversion of population, according to Lorentz dielectric model (S. J. Orfanidis, 2016):

$$\epsilon(\omega) = \epsilon_0 + \frac{\epsilon_0 \omega_p^2}{\omega_0^2 - \omega^2 + j\omega\gamma} \quad (15)$$

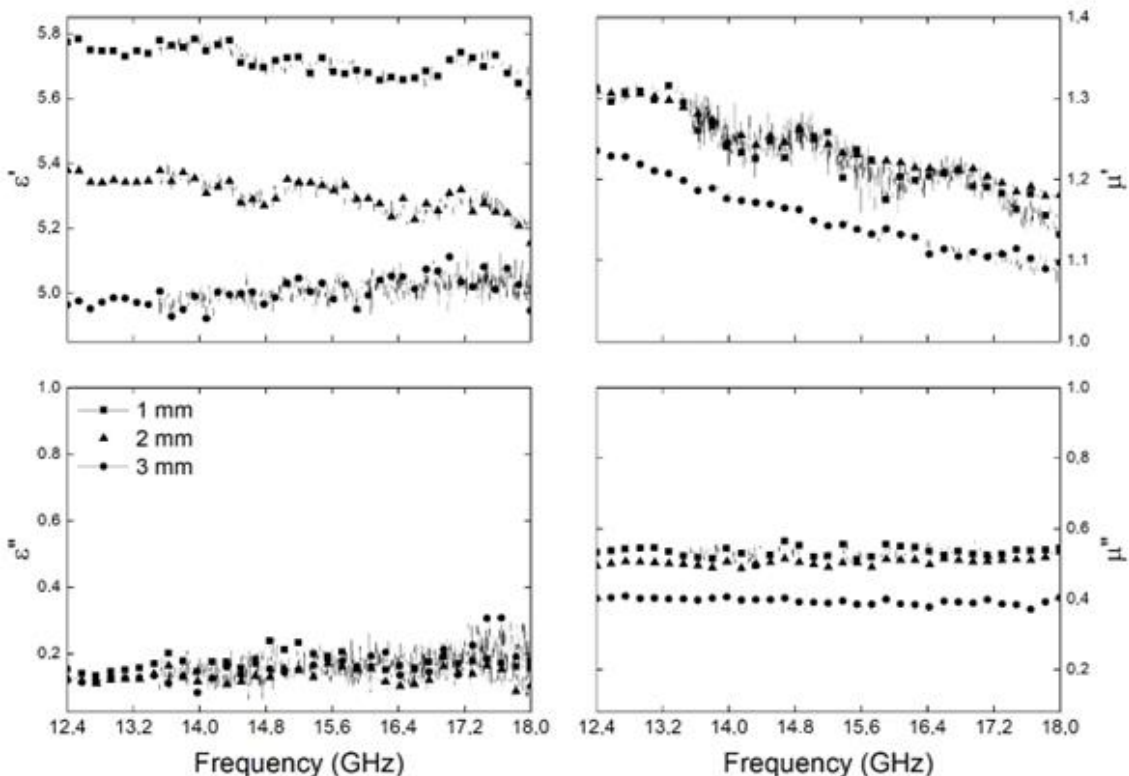
Where, ω_p is the plasma frequency, γ is a measure of the rate of electrons collisions per unit time and ω the frequency. The inversion of the population is related to the fact that the number of populations at the upper energy levels is larger than at the lower ones. When this is the case, the ϵ' behaves anomalously and grows

rapidly with abundance, in the ferrite composite from 11.02 to 11.92. At ω_0 the ϵ'' drops to 0.24, which represents a gain (S. J. Orfanidis, 2016).

The real permeability (μ') of ferrite samples increases with frequency, implying an increase in the energy storage property. On the other hand, the imaginary permeability of the sample (μ'') decreases with frequency. Samples with a thickness of 3 mm have an increase in μ'' values at 15.19 GHz, with a maximum value at 15.91 GHz. It is possible that there is an increase in energy loss due to dissipative mechanisms in this frequency range (15.19 to 15.91 GHz). (de Souza Pinto et al., 2019).

The ϵ' , ϵ'' , μ' and μ'' of carbonyl iron single-layer are show in Figure 4. In general, the composites permittivity and permeability properties were constant all over the frequency range.

Figure 4 - Real and complex permittivity and permeability of carbonyl iron samples with 1, 2 and 3 mm of thickness.



Source: The authors.

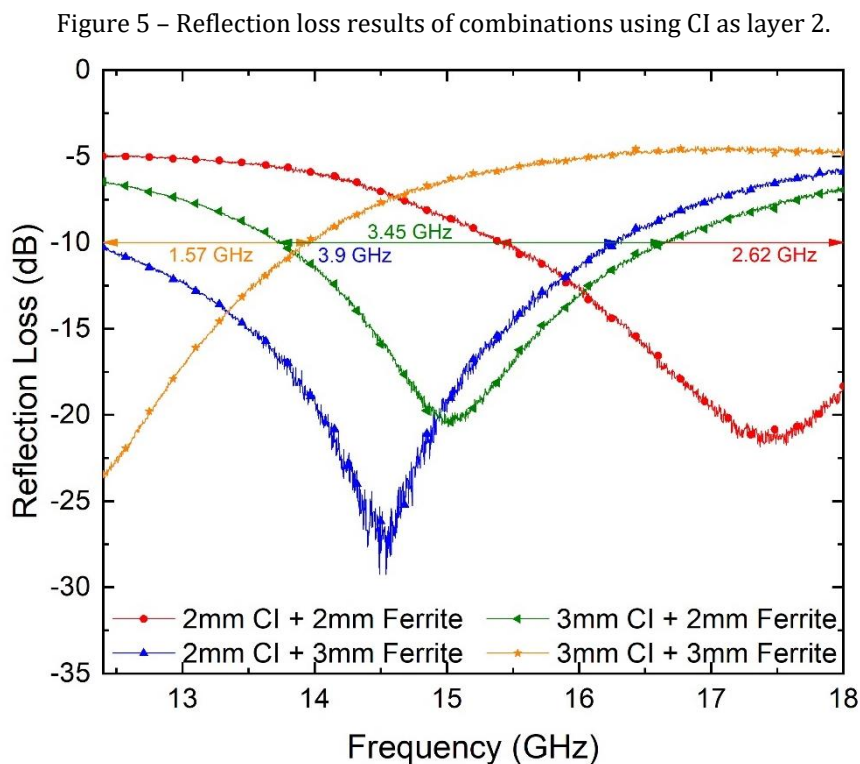
The double-layer combinations were named based on the thickening and filler type in the form Layer 2 + Layer 1. Six of 18 layer combinations have characteristics that absorb 90% (-10 dB) or more of the EM wave in the frequency range of the Ku band. The reflection loss (RL) value, which represents this

percentage of EM wave absorption, is -10 dB or more according to the following relationship (Mohammed et al., 2019):

$$Absorption (\%) = 100 - \left(10^{\frac{RL}{10}}\right) \times 100 \quad (16)$$

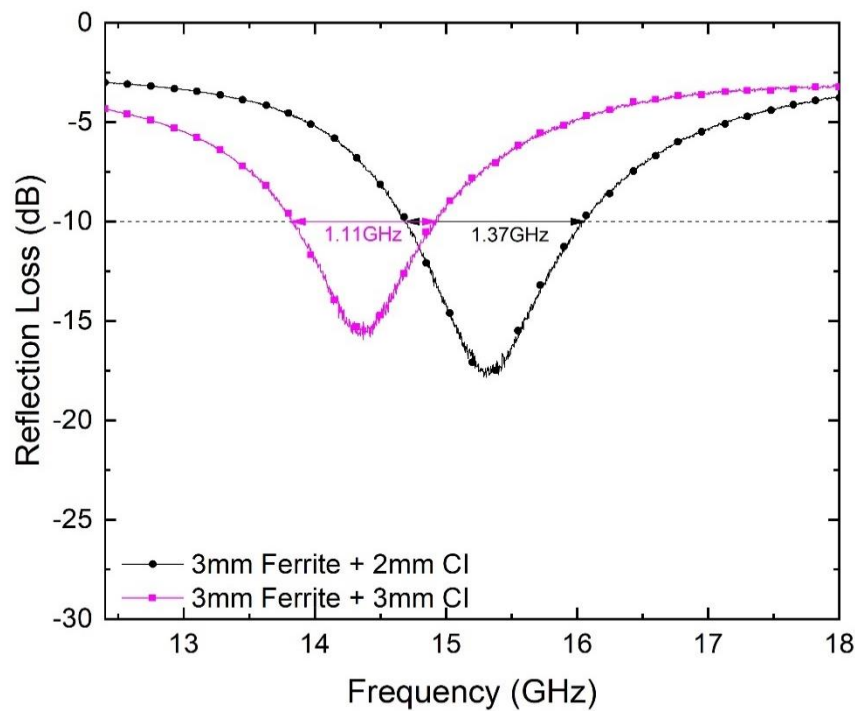
The combination with CI composite as the second layer shows the best results for the application of double-layer absorbers in Ku-band (Figure 5). Two combinations absorb more than 90% of the wave EM for at least half of the frequency range from 12.4 to 18 GHz, namely, 2 mm CI + 3 mm Ferrite and 3 mm CI + 2 mm Ferrite, the latter having the largest bandwidth value of 3.9 GHz (12.4 to 16.06 GHz). The other combination, 2 mm CI + 2 mm Ferrite, absorbed 46% of the Ku band, 2.62 GHz (15.38 to 18 GHz), and its bandwidth could be larger, including the K band. Moreover, these double layer combinations with CI composite as layer 2 show the best results in RL. The 2 mm CI + 3 mm Ferrite and 3 mm CI + 3 mm Ferrite combinations have -21.86 dB at 17.37 GHz and -23.64 dB at 12.4 GHz, respectively. This means an absorption of more than 99% of the wave energy EM.

When combined with manganese and zinc ferrite composites as layer 2 (Figure 6), only the combination with a thickness of 3 mm achieved RL values of more than -10 dB in the Ku band. The 3 mm Ferrite + 2 mm CI combination has the best bandwidth and RL values, 1.37 GHz and -17.85 at 15.31 GHz, respectively.



Source: The authors.

Figure 6 – Reflection loss results of combinations using Ferrite as layer 2.



Source: The authors.

4. CONCLUSIONS

In this work, composites with carbonyl iron and manganese and zinc ferrite as fillers were prepared, with a composition of 60 wt% filler and 40 wt% silicone rubber (matrix) and thicknesses of 1, 2 and 3 mm. The EM properties of the composites were measured in Ku-band and the RL values were determined using the double layer configuration.

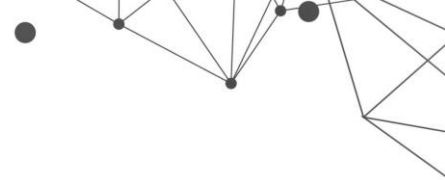
The best bandwidth result was obtained with the 2 mm CI + 3 mm Ferrite combination, which absorbed more than 90% of the EM wave in at least 70% of the frequency range, 3.9 GHz (12.4 to 16.06 GHz). Moreover, the combination 3 mm CI + 3 mm Ferrite has the best attenuation, -23.64 dB at 12.4 GHz. Combinations with ferrite as layer 2 show two combinations with RL results below -10 dB.

ACKNOWLEDGEMENTS

This study was financed in part by the Coordenação de Aperfeiçoamento de Pessoal de Nível Superior - Brasil (CAPES) - Finance Code 001, and by Financiadora de Estudos e Projetos – Brasil (FINEP).

REFERENCES

- Ansal, K. A., Susan Rajan, C., Ragamalika, C. S., & Baby, S. M. (2021). A CPW fed monopole antenna for UWB/KU band applications. *Materials Today: Proceedings*, *xxxx*, 2–7. <https://doi.org/10.1016/j.matpr.2021.06.002>
- Baker-Jarvis, J. (1990). *Transmission/reflection and short-circuit line permittivity measurements*. <https://doi.org/10.6028/NIST.TN.1341>
- Das, S., Nayak, G. C., Sahu, S. K., Routray, P. C., Roy, A. K., & Baskey, H. (2015). Microwave absorption properties of double-layer composites using CoZn/NiZn/MnZn-ferrite and titanium dioxide. *Journal of Magnetism and Magnetic Materials*, *377*, 111–116. <https://doi.org/10.1016/j.jmmm.2014.10.059>
- de Souza Pinto, S., Machado, J. P. B., Gomes, N. A. S., & Rezende, M. C. (2019). The influence of morphology, structure, and weight fraction of magnetic additives on the electromagnetic characteristics of composites. *Journal of Magnetism and Magnetic Materials*, *484*(March), 126–138. <https://doi.org/10.1016/j.jmmm.2019.03.085>
- Ding, L., Huang, Y., Liu, X., Xu, Z., Li, S., Yan, J., & Liu, P. (2020). Broadband and multilayer core-shell FeCo@C@mSiO₂ nanoparticles for microwave absorption. *Journal of Alloys and Compounds*, *812*, 152168. <https://doi.org/10.1016/j.jallcom.2019.152168>
- Liu, Y., Liu, X., & Wang, X. (2014). Double-layer microwave absorber based on CoFe₂O₄ ferrite and carbonyl iron composites. *Journal of Alloys and Compounds*, *584*, 249–253. <https://doi.org/10.1016/j.jallcom.2013.09.049>
- Meng, W., Yuping, D., Shunhua, L., Xiaogang, L., & Zhijiang, J. (2009). Absorption properties of carbonyl-iron/carbon black double-layer microwave absorbers. *Journal of Magnetism and Magnetic Materials*, *321*(20), 3442–3446. <https://doi.org/10.1016/j.jmmm.2009.06.040>
- Meshram, M. R., Agrawal, N. K., Sinha, B., & Misra, P. S. (2004). Characterization of M-type barium hexagonal ferrite-based wide band microwave absorber. *Journal of Magnetism and Magnetic Materials*, *271*(2–3), 207–214. <https://doi.org/10.1016/j.jmmm.2003.09.045>
- Mohammed, J., Tchouank Tekou Carol, T., Hafeez, H. Y., Basandrai, D., Bhadu, G. R., Godara, S. K., Narang, S. B., & Srivastava, A. K. (2019). Electromagnetic interference (EMI) shielding, microwave absorption, and optical sensing properties of BaM/CCTO composites in K u -band. *Results in Physics*, *13*(June). <https://doi.org/10.1016/j.rinp.2019.102307>
- Naito, Y., & Suetake, K. (1971). Application of ferrite to electromagnetic wave absorber and its characteristics. In *IEEE Transactions on Microwave Theory and Techniques* (Vol. 19, Issue 1, pp. 65–72). <https://doi.org/10.1109/TMTT.1971.1127446>



Nicolson, A. M., & Ross, G. F. (1970). Measurement of the Intrinsic Properties Of Materials by Time-Domain Techniques. *IEEE Transactions on Instrumentation and Measurement*, 19(4), 377–382. <https://doi.org/10.1109/TIM.1970.4313932>

S. J. Orfanidis. (2016). *Electromagnetic Waves and Antennas*. <https://www.ece.rutgers.edu/~orfanidi/ewa/>

OPTICAL MULTIMODE INTERFERENCE WAVEGUIDES AS SENSING DEVICES

DOI: [10.51859/ampla.sst631.1122-7](https://doi.org/10.51859/ampla.sst631.1122-7)

Yuri Hayashi Isayama¹
Jhonattan Cordoba Ramirez²
Lucas Heitzmann Gabrielli³
Hugo Enrique Hernández-Figueroa⁴

¹ PhD in Electrical Engineering from University of Campinas - UNICAMP

² Assistant Professor at the School of Engineering, Federal University of Minas Gerais - UFMG

³ Associate Professor at the School of Electric and Computer Engineering, University of Campinas - UNICAMP

⁴ Full Professor at the School of Electric and Computer Engineering, University of Campinas - UNICAMP

ABSTRACT

Optical interferometers are important and versatile building blocks in integrated optics. They can present a wide variety of operating mechanisms and have several distinct applications, where one of them is optical sensing. The multimode interferometer (MMI) is an established structure but has only recently received attention as a sensing device. These devices can be designed to be compact, highly sensitive and present fast response times, which led them to be explored as refractive index sensors. Most recently, due to this high sensitivity and real-time monitoring capabilities, in addition to the possibility for dense integration, MMI sensors were intensively investigated for biosensing applications. The first MMI sensors were simple in construction, as they operated only with the first two propagating modes of a multimode waveguide. As higher order modes were employed, significant gains in sensor performance were achieved, but the device also grew in complexity. This chapter aims to provide a short history of MMI sensors, present the theory behind its operation (multimode waveguide design, device excitation and detection methods) and recent advances both in theoretical modeling and experimental demonstrations.

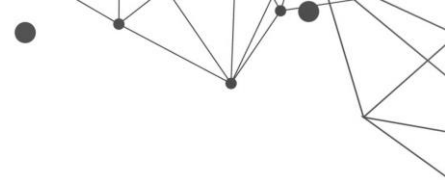
Key words: Integrated optics. Multimode interference. Modal interferometer. Sensor. Optical waveguide devices.

1. INTRODUCTION

Interferometers belong to one of the most important class of devices for many areas such as telecommunications (WILKES *et al.*, 2016; CHILES; FATHPOUR, 2014; YURTSEVER *et al.*, 2014; FANDIÑO; MUÑOZ, 2013), sensing (ZINOVIEV *et al.*, 2011; GONZÁLEZ-GUERRERO *et al.*, 2017; ESTEVEZ; ALVAREZ; LECHUGA, 2012; KOZMA *et al.*, 2014) and other applications in fundamental physics (CRESPI *et al.*, 2013; BERRADA *et al.*, 2013). Progress and developments in the field of photonic sensors, with the implementation of a variety of devices, such as ring resonators and interferometers, have allowed the production of sensing devices characterized by compactness, high sensitivity (with limit of detection between 10^{-6} and 10^{-8} refractive index units – RIU), very fast response times, label-free and real-time monitoring capabilities (GAVELA *et al.*, 2016) in applications related to sensing and biosensing. In this context, Multimode Interference (MMI) sensors have received plenty of attention over the last decades.

The first suggestions of the use of planar multimode waveguides as multimode interferometers arose during the 1970s (ULRICH, 1975). Throughout the 1990s, several possible applications for this type of structure were idealized, such as couplers (SOLDANO; PENNINGS, 1995; SOLDANO *et al.*, 1992), filters (LEUTHOLD *et al.*, 1996), modal converters (LEUTHOLD *et al.*, 1998), and power splitters (RASMUSSEN; RASMUSSEN; POVLSEN, 1995; LEUTHOLD; JOYNER, 2001; SOLDANO; PENNINGS, 1995). In the 2000s, works regarding MMI were no longer limited to planar waveguides, also including proposals and demonstrations of the same applications utilizing optical fibers (MOHAMMED; MEHTA; JOHNSON, 2004; MOHAMMED; SMITH; GU, 2006; ANTONIO-LOPEZ *et al.*, 2010).

The first use of a MMI with a sensing function was proposed by Gut *et al.* in 1999 (GUT *et al.*, 1999). This work demonstrated both theoretically and experimentally how the interaction between fundamental and first order Transverse Electric (TE) modes could be utilized for gas detection. In addition, it also suggested the possibility of using fundamental TE and Transverse Magnetic (TM) modes with the same purpose, without, however, the experimental demonstration. From this point, many other attempts to expand this initial proposition arose, both as planar MMI waveguides (SOLER *et al.*, 2020; ELSAYED *et*



al., 2017), as well as fiber optics MMI (MEHTA; MOHAMMED; JOHNSON, 2003; MOHAMMED; SMITH; GU, 2006; WANG; FARRELL, 2006; ANTONIO-LOPEZ *et al.*, 2010).

Regarding planar MMI waveguide sensors, the main contributions are basically divided in sensors called bimodal (Bimodal Waveguide - BiMW) and trimodal (Trimodal Waveguide - TriMW), which have both theoretical and experimental demonstrations. Recently, there were also theoretical proposals of MMI sensors that operated with high order modes. The main difference between these types of sensors are the interfering modes excited within the multimode waveguide: bimodal sensors operate with fundamental and first order modes, trimodal sensors operate with fundamental and second order modes, and high order sensors use the fundamental and a higher order (third and above) mode.

In 2005, Kribich *et al.* demonstrated the use of a MMI as a humidity sensor and suggested, for the first time, that this device could be used in the future as a biosensing device (KRIBICH *et al.*, 2005). From this point on, most advancements in MMI sensing technology were directed towards biosensing applications, exemplified by Zinoviev *et al.* in 2011, where an experimental demonstration of a MMI biosensor was developed, detecting BSA (Bovine Serum Albumin) protein (ZINOVIEV *et al.*, 2011). The limit of detection (LOD) for this device was estimated as $LOD = 2.5 \times 10^{-7}$ Refractive Index Unit (RIU). The sensing device consisted of a MMI that supported the first two TE propagating modes and it was denominated Bimodal Waveguide (BiMW) biosensor.

Attempting to improve device sensitivity, different proposals were developed altering MMI geometry (EBIHARA; ASAKAWA; SUZUKI, 2021, TORRIJOS-MORÁN *et al.*, 2021, TSAREV, 2021), mode excitation (HOPPE *et al.*, 2017, LIANG *et al.*, 2018, EBIHARA *et al.*, 2019), in-chip light coupling (GRAJALES *et al.*, 2019), MMI materials (DWIVEDI; KUMAR, 2017), sensor detection methods (DWIVEDI; KUMAR, 2018), and mode order within the MMI (RAMIREZ *et al.*, 2015, GAVELA *et al.*, 2016, RAMIREZ *et al.*, 2019, ISAYAMA; HERNÁNDEZ-FIGUEROA, 2021). In the context of biosensing applications, several advancements were made, such as Lab-on-a-chip demonstrations (DUVAL *et al.*, 2012, MALDONADO *et al.*, 2020) and detection of biomolecules in solutions as blood (KIM *et al.*, 2017) and urine (GONZÁLEZ-GUERRERO *et al.*, 2017).

2. MULTIMODE WAVEGUIDE INTERFERENCE (MMI) SENSOR

The basic operating principle of MMI sensors consists of comparing how the fundamental mode and a higher order mode respond to variations in the cladding layer of the sensing waveguide. If the higher order mode of the MMI sensor is the first order mode, it is denominated bimodal waveguide (BiMW) sensor and if the higher order mode is the second order, than it is called trimodal waveguide (TriMW) sensor. Initially, since the fundamental mode and the higher order mode have different propagation constants (β), a phase shift will be observed between them at the end of the multimode waveguide (MMW). Then, because the Electromagnetic (EM) field distribution of each mode is different, altering the constitution (i.e., the refractive index) of the cladding will result in different variations in each mode's β . By knowing how the two propagating modes will behave with this change in the cladding and measuring how much the phase difference between the two modes has been altered, it is, therefore, possible to evaluate the variation in the refractive index of the cladding with high precision. If the sensing waveguide is subject to biofunctionalization, this interferometer may be employed as a biosensing device.

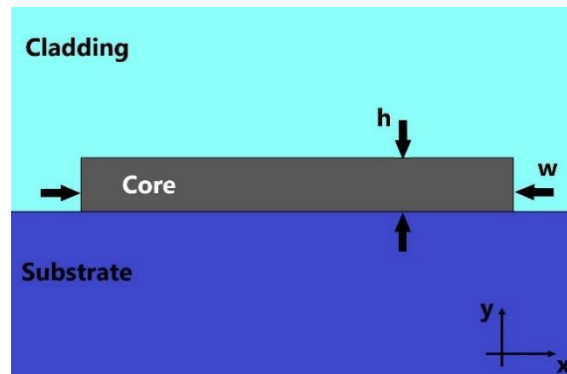
2.1. DESIGN PROCEDURE AND IMPORTANT PARAMETERS

When designing a MMI sensor and trying to optimize its sensitivity, one fundamental factor should be considered: the device operates fundamentally by comparing the propagation constants of two given modes and, hence, it is reasonable to assume that the bigger the $\Delta\beta = \beta_{00} - \beta_{0n}$ (where β_{00} and β_{0n} are the propagation constants of the fundamental and the high-order mode, respectively) the more sensitive the device should be. If $\Delta\beta$ is naturally large, it means both propagating modes present very different guiding regimes, that is, one mode interacts more with variations in the cladding than the other (ISAYAMA; HERNÁNDEZ-FIGUEROA, 2021).

To properly design a MMI sensor, one must choose the geometry of the MMW and the operating modes in a way that maximizes the amount of the EM fields of the higher order mode in the cladding region. Figure 1 shows the MMW cross-section, where the waveguide's core height and width are denoted by h and w , respectively. For each combination of h and w chosen, the propagation constants of the modes are calculated, as exemplified in Figure 2 (assuming a Si₃N₄ ($n_{\text{Si}_3\text{N}_4} = 2.0394$))

channel waveguide, for operation in 633 nm wavelength, with core height (h) of 150 nm, SiO₂ substrate ($n_{\text{SiO}_2} = 1.4570$) and a cladding with refractive index $n_{\text{clad}} = 1.32$).

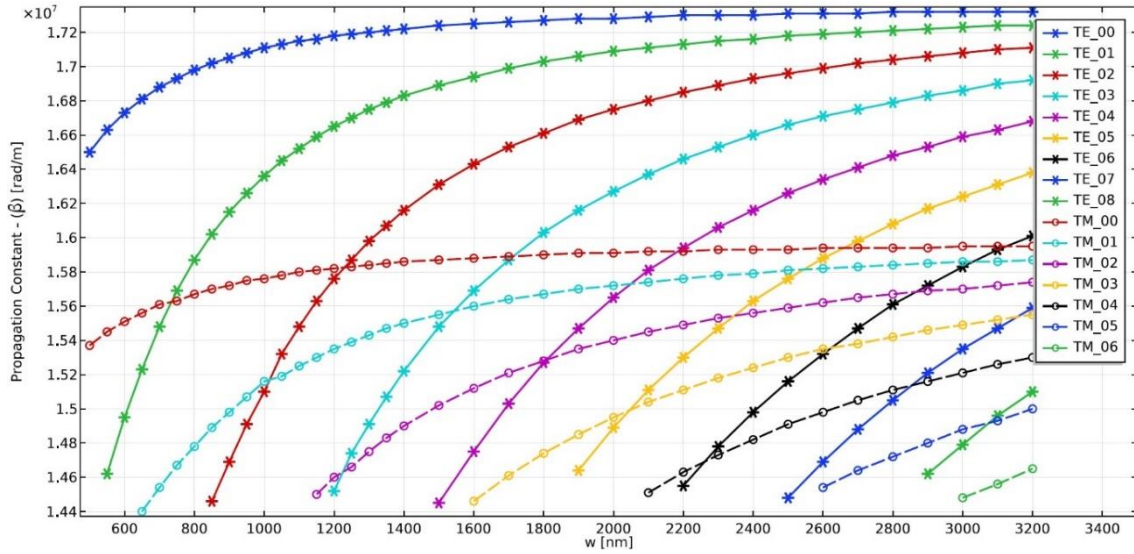
Figure 1 – Cross-section view of the multimode waveguide. The waveguide's core height and width are denoted by h and w , respectively. The propagation is assumed to be in the z -direction. Reproduced with permission from Isayama, Y.H. and Hernández-Figueroa, H.E., published by Sensors, 2021.



Source: ISAYAMA, Y. H.; HERNÁNDEZ-FIGUEROA, H.E. High-order multimode waveguide interferometer for optical biosensing applications. *Sensors*, v. 21(9), 2021.

The waveguide's core height (h) is fixed, the width (w) is varied, and the propagation constants of the modes are calculated. The solid lines are the curves for TE modes and the dashed lines are for TM modes. Due to the aspect ratio of the waveguide (width of the core much larger than its height), TM modes present much smaller propagation constants, as the modes are not well-confined in the core and much of their power propagates through both the cladding and the substrate. For TE modes, however, it is interesting to note that, if we compare the fundamental TE mode (TE₀₀ in Figure 2) with other higher-order TE_{0n} modes when they are close to cutoff condition, as we increase the order of the mode, or the value of n , larger values for $\Delta\beta(w = w_{\text{cutoff}})$ are obtained. There is, naturally, a limit to this increase, since the value of β_{00} cannot grow indefinitely, which suggests there is an optimal mode order for each waveguide height design. Employing further higher-order modes will not bring any improvements in terms of device sensitivity (ISAYAMA; HERNÁNDEZ-FIGUEROA, 2021).

Figure 2 – Propagation constants for TE and TM modes of a Si3N4 channel waveguide with $h = 150$ nm, SiO2 substrate and $n_{\text{clad}} = 1.32$. Reproduced with permission from Isayama, Y.H. and Hernández-Figueroa, H.E., published by Sensors, 2021.



Source: ISAYAMA, Y. H.; HERNÁNDEZ-FIGUEROA, H.E. High-order multimode waveguide interferometer for optical biosensing applications. *Sensors*, v. 21(9), 2021.

Another important aspect to be considered is the distribution of power in the core, cladding, and substrate (P_{core} , P_{clad} and P_{subs} , respectively). The time average of the power flow through a surface S is given by

$$P_S = \iint_S \frac{1}{2} \text{Re}\{(\mathbf{E} \times \mathbf{H}^*) \cdot \mathbf{u}_z\} dS, \quad (1)$$

where \mathbf{E} is the electric field, \mathbf{H}^* is the complex conjugate of the magnetic field, and \mathbf{u}_z denotes a unit vector in the z -direction (which is assumed to be the direction of propagation, perpendicular to the surface S). The surface S can be any of the regions: core, cladding, or substrate. Calculating the power flow in each region, one can obtain the power distribution by evaluating

$$P_{\text{Region}}[\%] = \frac{P_A}{P_{\text{total}}} \times 100\%, \quad (2)$$

where P_A denotes the power calculated by Equation (1) in the core, cladding, or substrate and P_{total} denotes the total power. Results for the example of Figure 2 are shown in Table 1.

Table 1 – Power distribution for TE_{0n} modes, for Si₃N₄ channel waveguide with h = 150 nm. Reproduced with permission from Isayama, Y.H. and Hernández-Figueroa, H.E., published by Sensors, 2021.

Mode Number (n)	w [nm]	P _{core} TE ₀₀ [%]	P _{core} TE ₀₀ [%]	P _{core} TE ₀₀ [%]
0	600	69.4	13.1	17.5
0	900	70.9	12.2	16.9
0	1300	71.4	11.9	16.7
0	1600	71.5	11.9	16.7
0	1900	71.5	11.8	16.6
0	2200	71.6	11.8	16.6
0	2500	71.6	11.8	16.6
0	2900	71.6	11.8	16.6

Mode Number (n)	w [nm]	P _{core} TE ₀₀ [%]	P _{core} TE ₀₀ [%]	P _{core} TE ₀₀ [%]
1	600	56.1	20.7	23.2
2	900	56.0	20.0	24.0
3	1300	61.7	15.6	22.7
4	1600	62.1	15.8	22.0
5	1900	62.1	15.8	22.1
6	2200	61.6	15.6	22.8
7	2500	60.5	15.2	24.4
8	2900	64.8	15.0	20.2

Source: ISAYAMA, Y. H.; HERNÁNDEZ-FIGUEROA, H.E. High-order multimode waveguide interferometer for optical biosensing applications. *Sensors*, v. 21(9), 2021.

Even though we observe from Figure 2 that $\Delta\beta$ increases until mode TE₀₇ and, thus, an increase in sensitivity is expected, from Table 1, we draw different conclusions. Most of the power of the fundamental TE mode is concentrated in the core of the waveguide, and for higher-order TE modes, less of the power is inside the core. The issue is that a large part of the outside power is concentrated in the substrate, with no use for the sensing device. In fact, the amount of power in the substrate is actually larger than the portion in the cladding. One must optimize the combination of dimensions h and w and find the high order mode that produces large $\Delta\beta$ (which can be achieved by delocalizing the higher order modes from the core or increasing confinement of the fundamental mode) while also having power majorly concentrated in the cladding region.

2.2. BULK SENSITIVITY CALCULATIONS

Once the more fundamental aspects of the MMI sensor were addressed, the next step is to calculate the device's sensitivity. The bulk sensitivity is related to the

effective index variation of the interfering modes when subject to a bulk change in the refractive index of the sensing region of the interferometer. In other words, variations in the sensing region's refractive index cause the effective indexes of the interfering modes to change, which, in turn, cause a phase difference between the two of them to arise at the end of the interferometric region. This phase difference ($\Delta\phi$) may be calculated by

$$\Delta\phi = \frac{2\pi\Delta n_{\text{eff}}L}{\lambda} \quad (3)$$

$$\Delta n_{\text{eff}} = n_{\text{eff},n} - n_{\text{eff},0} \quad (4)$$

where $n_{\text{eff},n}$ is the effective index of the n^{th} order mode ($n = 1$ for the BiMW and $n = 2$ for the TriMW), $n_{\text{eff},0}$ is the effective index of the fundamental mode, L is the length of the interferometer sensing area, and λ is the vacuum wavelength at the operating frequency. Then, the bulk sensitivity can be calculated by

$$S_{\text{bulk}} = \frac{\partial(\Delta\phi)}{\partial n_{\text{clad}}} = \frac{2\pi L}{\lambda} \eta_{\text{bulk}} \quad (5)$$

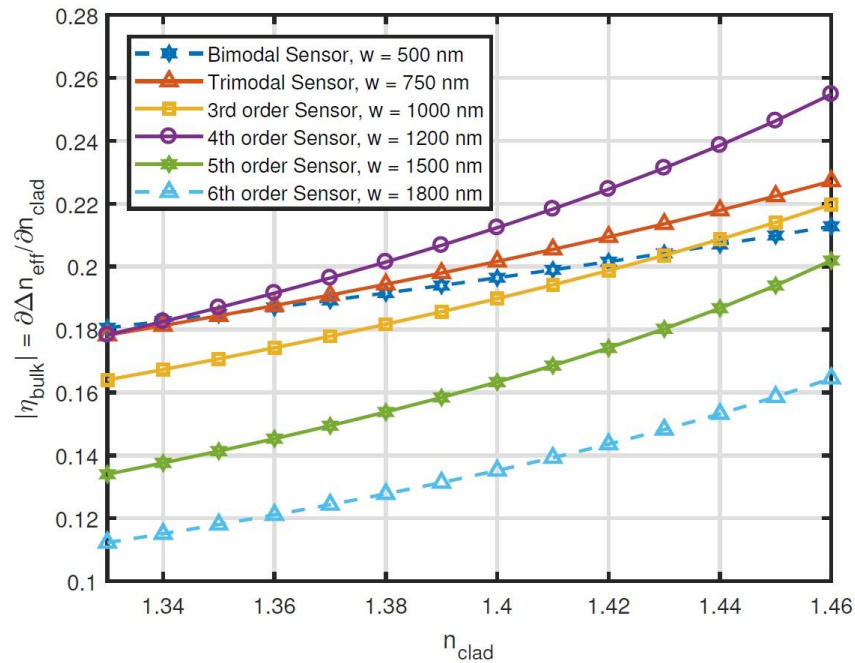
$$\eta_{\text{bulk}} = \frac{\partial(\Delta n_{\text{eff}})}{\partial n_{\text{clad}}}, \quad (6)$$

where n_{clad} is the refractive index of the cladding. The parameter η_{bulk} is called intrinsic bulk sensitivity. Since the MMI interference sensor's sensitivity is dependent on the device's length (L), η_{bulk} is a good comparative parameter for different sensors within this technology.

Using Equations (3)-(6), one may calculate the intrinsic bulk sensitivity for an MMI sensor. Figure 3 shows the obtained values of η_{bulk} as a function of n_{clad} for a Si_3N_4 channel waveguide with $h = 300$ nm.

It is observed that the 4th order MMI sensor presented the highest intrinsic bulk sensitivity of all designs for practically all values of n_{clad} . In addition, it can be pointed out how η_{bulk} decreased for mode orders superior to 4, which tells us that simply increasing mode order does not necessarily result in a performance improvement for this type of sensor.

Figure 3 – Intrinsic bulk sensitivity as a function of n_{clad} for Si3N4 channel waveguides with $h = 300$ nm. Reproduced with permission from Isayama, Y.H. and Hernández-Figueroa, H.E., published by Sensors, 2021.



Source: ISAYAMA, Y. H.; HERNÁNDEZ-FIGUEROA, H.E. High-order multimode waveguide interferometer for optical biosensing applications. *Sensors*, v. 21(9), 2021.

Finally, a good metric to compare the presented sensor with other devices from other technologies is the limit of detection (LOD), which represents the smallest variation in the refractive index of the cladding that could be measured, and can be calculated by

$$\text{LOD} = \frac{3 \cdot N/S}{S_{\text{bulk}}}, \quad (7)$$

where N/S is the noise-to-signal ratio. In practical terms, a good MMI sensor requires not only high S_{bulk} , but it also depends on the experimental setup, which affects the value of N/S .

3. MULTIMODE WAVEGUIDE INTERFERENCE EXCITATION SCHEMES

After establishing how the design of the multimode waveguide is to be developed, the next step is to determine how the desired modes are to be excited within the MMI. There are two requirements for this matter: exciting the fundamental and high order modes, while guaranteeing that these are the sole propagating modes within the multimode waveguide (sensing region) of the sensor

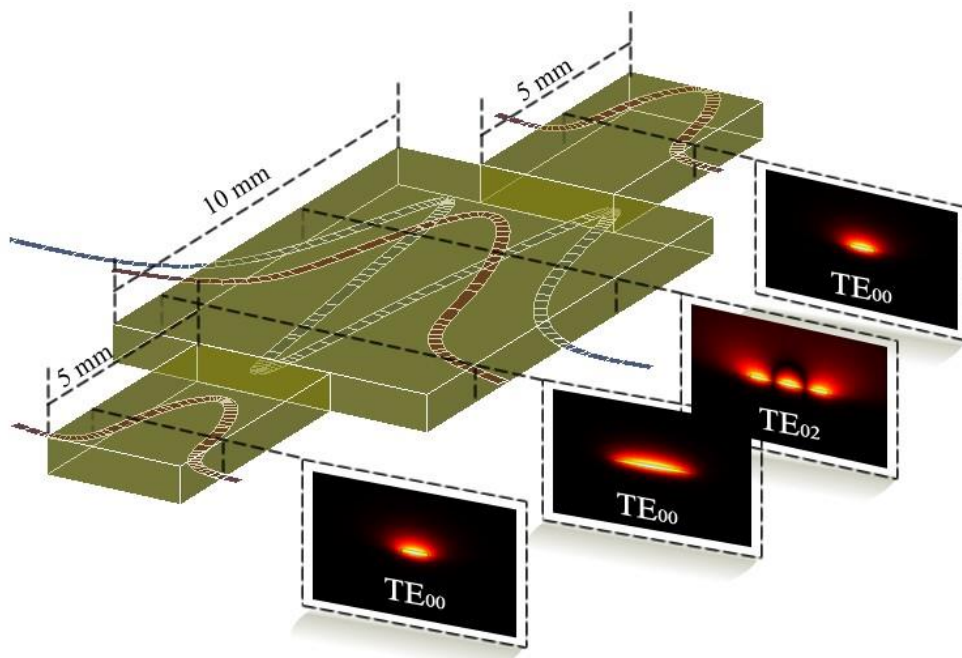
and obtaining an equal input power distribution between the modes (ISAYAMA; HERNÁNDEZ-FIGUEROA, 2021).

3.1. SINGLE-MODE WAVEGUIDE WITH ABRUPT TRANSITION (STEP JUNCTION)

For the BiMW and TriMW, both fundamental and high order modes can be excited through an abrupt transition (step junction) from a single-mode waveguide to the multimode waveguide, as illustrated in Figure 4. The butt-coupling coefficients (c_n) determine how the mode from the input single-mode waveguide (E, H) will couple to each propagating mode of the MMI (e_n, h_n):

$$c_n = \frac{\iint_S \mathbf{E} \times \mathbf{h}_n \cdot d\mathbf{S}}{\iint_S \mathbf{e}_n \times \mathbf{h}_n \cdot d\mathbf{S}} \quad (8)$$

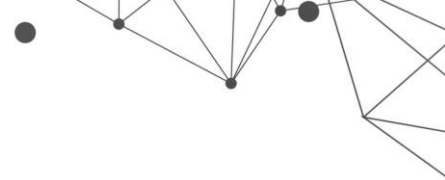
Figure 4 – Scheme of the Trimodal waveguide sensor showing the expected light modes in each section. Reproduced with permission from Ramirez, J. C., published by Sensors, 2019.



Source: RAMIREZ, J. C. et al. Trimodal waveguide demonstration and its implementation as a high order mode interferometer for sensing application. *Sensors (Basel)*, v. 19, n. 12, p. 2821, 6 2019.

For the BiMW, because the MMI only supports two propagating modes, if there is an offset between the input single-mode waveguide and the MMI, both the fundamental and the first order modes will be excited. The optimization of the excitation structure will determine the width of the input waveguide and the offset that produces the desired excitation.

In the case of the TriMW, to ensure the sole propagation of the fundamental and second order mode, the input single-mode waveguide must be positioned at the



center of the MMI. From Equation 8, because the first order mode in the MMI presents odd symmetry, if the input waveguide is connected to the center of the multimode waveguide, the coupling coefficient (c_1) goes to zero. Then, the parameters to be optimized is only the input single-mode waveguide width.

For higher order MMI sensors, the abrupt transition will not guarantee that only the two desired modes propagate and, therefore, a different excitation scheme is necessary.

3.2. BUTT-COUPLING AND DIRECTIONAL COUPLING

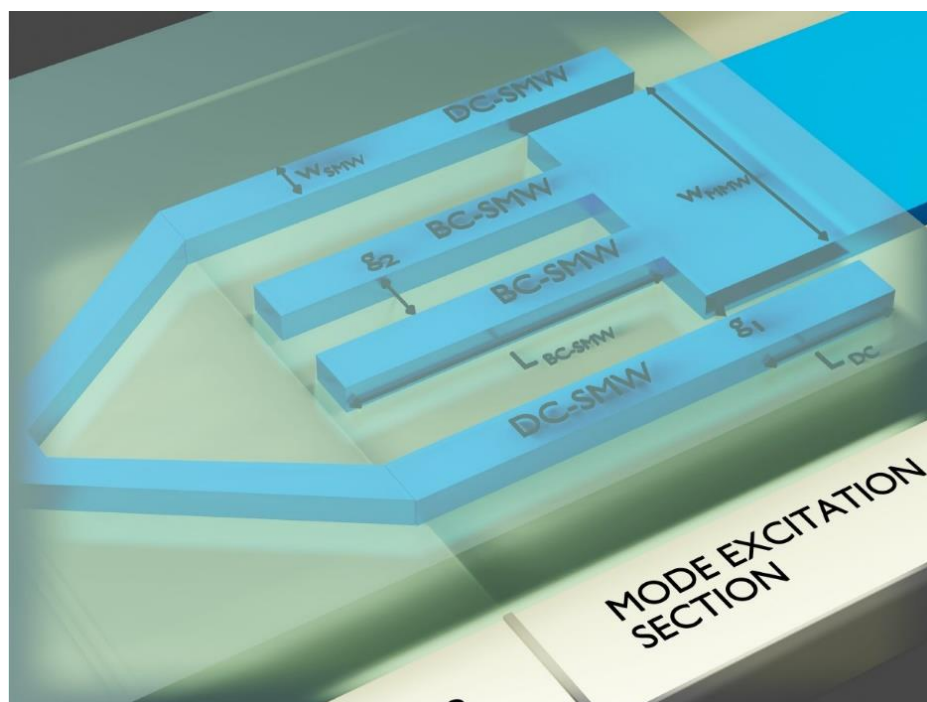
The step junction from single-mode to multimode waveguide depicted in Figure 4 is simple to implement but has two major drawbacks: it is not adequate for exciting MMI sensors of order higher than the second and it does not provide fine control over power distribution between excited modes. To solve these issues, a mixed approach can be employed, by exciting the fundamental mode through butt-coupling effect and the higher order mode through directional coupling mechanism (ISAYAMA; HERNÁNDEZ-FIGUEROA, 2021).

Using Equation 8, one or more input waveguides may be designed to excite the fundamental mode in the MMI through butt-coupling (BC-SMW – Butt-coupling single-mode waveguide). The idea is to produce an EM field distribution that is very similar to the EM field distribution of the fundamental mode of the multimode waveguide so the value of c_0 (fundamental mode coupling coefficient) is maximized, while minimizing the values of c_1 , c_2 , c_3 , etc.

The excitation of the high order mode is realized through directional coupling: if the desired mode has even symmetry, then a couple of additional waveguides is needed; if the desired mode has odd symmetry, only one additional waveguide is necessary. The new single-mode waveguides (DC-SMW – Directional coupling single-mode waveguide) are designed to satisfy the phase matching condition, meaning the propagation constant of the fundamental mode of the DC-SMW should be the same as the propagation constant of the high order mode within the MMI. This will result in the sole excitation of the desired mode, without the presence of other undesired modes. An example of such structure is shown in Figure 5, where w_{SMW} is the width of both BC-SMWs and DCSMWs, w_{MMW} is the width of the MMW sensor, g_1 is the gap between the DC-SMW and the MMW, g_2 is the separation between the BC-SMWs, L_{BC-SMW} is the length of the BC-SMWs, and L_{DC} is the length

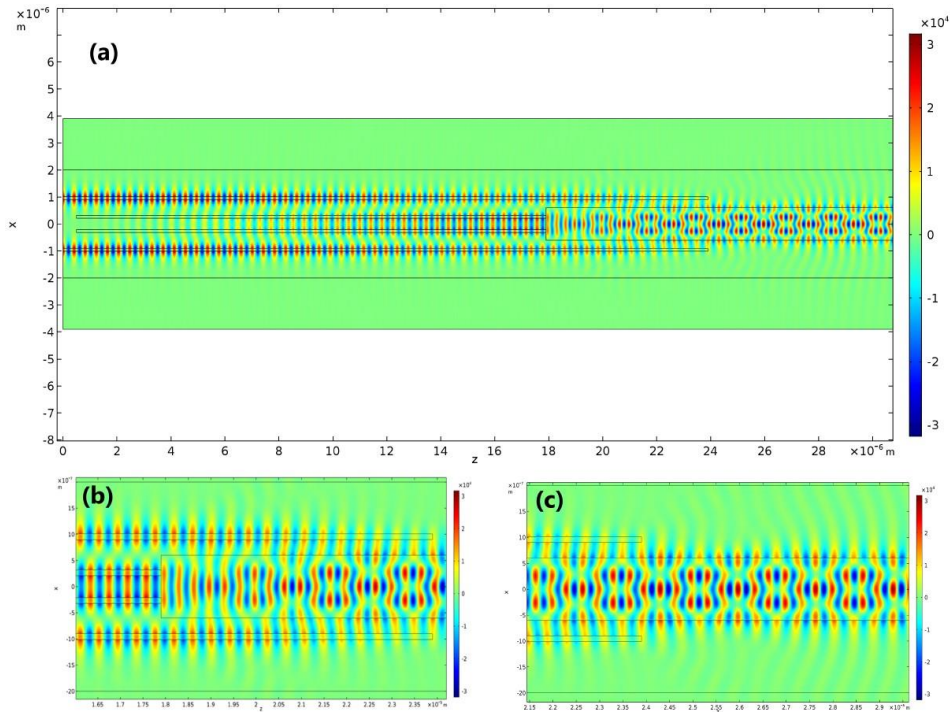
where the DC-SMWs couple to the MMW (the total length of the DC-SMW is $L_{BC-SMW} + L_{DC}$). The values of w_{MMW} , g_1 , g_2 , L_{BC-SMW} , and L_{DC} should be optimized to produce the sole excitation of fundamental and higher order modes in the MMI, while also providing the same power distribution in both. Figure 6 shows simulation results for the excitation of a 4th order MMI sensor (ISAYAMA; HERNÁNDEZ-FIGUEROA, 2021).

Figure 5 – BC-SMW/DC-SMW excitation scheme. w_{SMW} is the width of both BC-SMWs and DC-SMWs, w_{MMW} is the width of the MMW sensor, g_1 is the gap between the DC-SMW and the MMW, g_2 is the separation between the BC-SMWs, L_{BC-SMW} is the length of the BC-SMWs, and L_{DC} is the length where the DC-SMWs couple to the MMW (the total length of the DC-SMW is $L_{BC-SMW} + L_{DC}$). Reproduced with permission from Isayama, Y.H. and Hernández-Figueroa, H.E., published by Sensors, 2021.



Source: ISAYAMA, Y. H.; HERNÁNDEZ-FIGUEROA, H.E. High-order multimode waveguide interferometer for optical biosensing applications. Sensors, v. 21(9), 2021.

Figure 6 – Electric field distribution (E_x component) for the simulated 4th order Si_3N_4 MMW. (a) Simulation starting from the two single-mode waveguides originated from the two input single-mode waveguides. (b) Detail of the excitation section, where the BC-SMWs and DC-SMWs transfer power to the TE_{00} and TE_{04} modes. (c) Detail of the propagating field in the sensing area of the device. Reproduced with permission from Isayama, Y.H. and Hernández-Figueroa, H.E., published by Sensors, 2021.



Source: ISAYAMA, Y. H.; HERNÁNDEZ-FIGUEROA, H.E. High-order multimode waveguide interferometer for optical biosensing applications. *Sensors*, v. 21(9), 2021.

4. DETECTION METHODS

Signal detection and interpretation for MMI sensors have some different possibilities: measuring the output signal directly from the MMW or connecting an output single-mode waveguide after the MMW section and measuring the power coupled to this waveguide. The signal obtained directly from the MMW output will require some postprocessing whereas the output signal from a single-mode waveguide can be interpreted directly.

4.1. SINGLE-MODE WAVEGUIDE OUTPUT

If the chosen detection method is the single-mode waveguide output, as depicted in Figure 4, we have the following relation:

$$d = \sum_{n=0}^N c_n e^{-j\beta_n L} \frac{\iint_S \mathbf{e}_n \times \mathbf{H}_n \cdot d\mathbf{S}}{\iint_S \mathbf{E} \times \mathbf{H} \cdot d\mathbf{S}}, \quad (9)$$

where $|d|^2$ is the power fraction at the output of the interferometric device. It represents an interferometric signal that can be directly related to changes in the sensing area, since perturbations on the cladding region will produce variations in β_n . The total phase ($\beta_n L$) accumulated by each propagating mode inside the MMI will vary and, thus, the amount of optical power coupled to the output waveguide will also be different. Therefore, the measured output power is a function of the material in the sensing area.

4.2. MULTIMODE WAVEGUIDE OUTPUT

If we choose to measure the optical power exiting the multimode section directly, the information must be postprocessed. The information about the accumulated phase for each mode will be present in the EM field distribution obtained. For instance, if we consider a BiMW, which operates with the first order mode, it is known that this mode presents two power peaks. By measuring the output power with two photodiodes, one for each half of the multimode waveguide cross section, the phase difference, $\Delta\phi = \Delta\beta L$, between the modes can be determined by (DUVAL, D. *et al.*, 2012)

$$S [\%] = \frac{I_{\text{up}} - I_{\text{down}}}{I_{\text{up}} + I_{\text{down}}} \times 100\% \quad (10)$$

$$S(t) \propto \cos(\Delta\phi(t)) \quad (11)$$

Where I_{up} and I_{down} are the currents generated in each photodiode and the sensor signal S is proportional to the phase difference $\Delta\phi$ (which, in turn, is related to the refractive index of the sensing area).

As the MMI sensor order gets higher than two, the EM field distribution at the output of the MMI becomes more and more complex. For example, a 4th order MMI sensor requires five photodiodes to measure the output signal, which must be positioned where the five peaks of the 4th order mode are located (ISAYAMA, Y. H.; HERNÁNDEZ-FIGUEROA, 2021)

$$S = \frac{4}{11} \left[\left(\cos^2 \frac{\pi}{5} - \cos^2 \frac{2\pi}{5} \right) + 2 \left(\cos \frac{\pi}{5} - \cos \frac{2\pi}{5} \right) \cos \Delta\phi \right]. \quad (12)$$

The sensor signal S is proportional to $\cos \Delta\phi$ and can still be used to establish the relationship with refractive index changes in the cladding in the same way as before.

5. EXPERIMENTAL DEMONSTRATION OF A TRIMODAL SENSOR

Over the last years, MMI sensors were mostly investigated and employed as biosensors or refractive index sensors for fluids. However, there has been an interesting demonstration of its application as a temperature sensor as well, using polymeric waveguides, as shown in Figure 6 (RAMIREZ *et al.*, 2019). The device utilizes step junctions at the input and output of the MMI and excites the second order TE mode, which makes this a TriMW sensor. The input power is inserted in the chip through a lensed fiber and the output power is measured at the end of a single-mode waveguide.

A sample interferometric signal obtained from the device with single-mode section width of $3.5\mu\text{m}$ and trimodal section width of $10.5\mu\text{m}$ is shown in Figure 7a. In this configuration the coupling efficiency to the fundamental and second-order modes are 77% and 13%, respectively, which results in a signal visibility of about 5.8 dB and a free spectral range (FSR) of 20.3 nm.

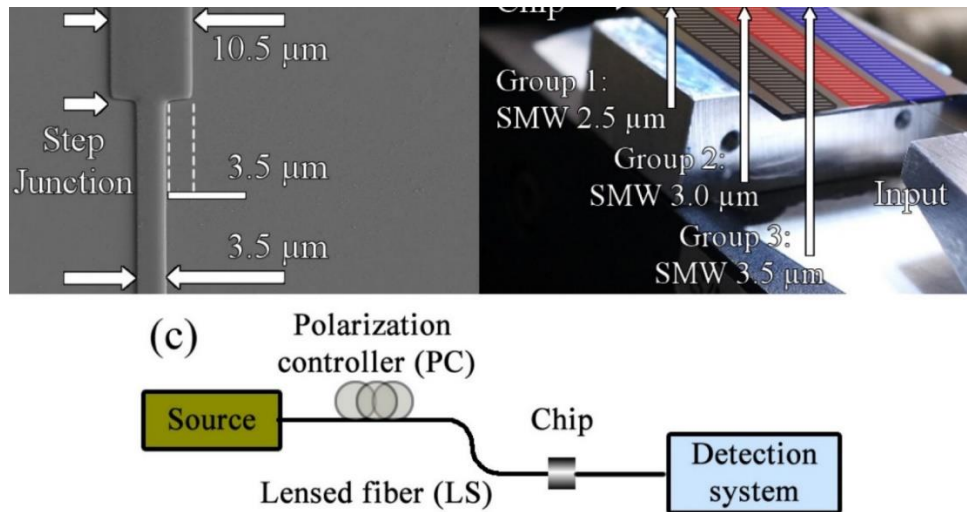
The sensitivity of an interferometric sensor will depend strongly on the visibility of the signal and the FSR reached by the photonic component, by guaranteeing a small FSR and high visibility, a highly sensitive device will be obtained. Variations in the width of the trimodal section can be controlled to improve visibility or free spectral range depending on whether the detection method is based on power measurement, wavelength tuning, or a combination of both, as shown in Figure 7b.

A sample interferometric signal obtained from the device with single-mode section width of $3.5\mu\text{m}$ and trimodal section width of $10.5\mu\text{m}$ is shown in Figure 7a. In this configuration the coupling efficiency to the fundamental and second-order modes are 77% and 13%, respectively, which results in a signal visibility of about 5.8 dB and a free spectral range (FSR) of 20.3 nm.

The high order mode interferometer was tested as a temperature sensing device to probe its sensitivity. By varying the temperature from 22°C up to 27°C , it was possible to observe changes in the resulting interferometric signal as shown in Figure 8. By adjusting a line to the measured transmission data at 1486 nm the obtained temperature sensitivity was $0.059\text{ dB}/^\circ\text{C}$. This value is twice as high as

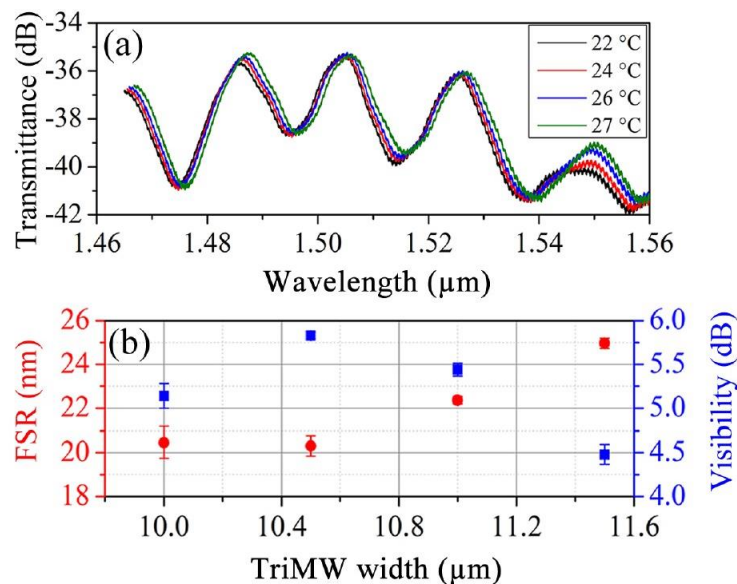
those found in the state-of-the-art for compact and low-loss fiber optical sensors (SUN, Q. *et al.*, 2015).

Figure 7 – Fabrication and characterization system of the trimodal interferometer device. (a) The SEM image of a trimodal device, highlighting the single- and multimode area and the step junction section, respectively. (b) The experimental setup for the trimodal interferometers. (c) Design of the experimental setup to characterize the manufactured interferometric devices.



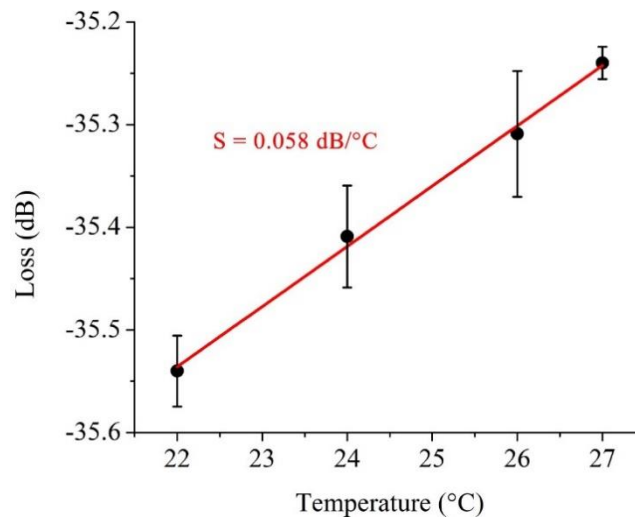
Source: RAMIREZ, J. C. et al. Trimodal waveguide demonstration and its implementation as a high order mode interferometer for sensing application. *Sensors (Basel)*, v. 19, n. 12, p. 2821, 6 2019. Reproduced with permission from Ramirez, J. C., published by Sensors, 2019.

Figure 8 – Sensitivity measurement in trimodal devices. (a) Measured interferometric signal resulting from the modal interaction within a trimodal interferometer with 3.5μm width in the single-mode section and 10.5μm width in the multimodal region. (b) FSR and visibility analysis for a trimodal interferometric device with 600nm height and cross-section with single-mode section width of 3.5μm and variable multimode section width between 10μm and 12μm, with a 0.5μm pitch.



Source: RAMIREZ, J. C. et al. Trimodal waveguide demonstration and its implementation as a high order mode interferometer for sensing application. *Sensors (Basel)*, v. 19, n. 12, p. 2821, 6 2019. Reproduced with permission from Ramirez, J. C., published by Sensors, 2019.

Figure 9 – Fringe power measured as function of temperature variation at 1485nm wavelength peak. Reproduced with permission from Ramirez, J. C., published by Sensors, 2019.

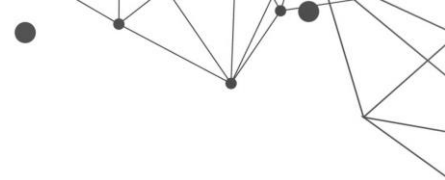


Source: RAMIREZ, J. C. et al. Trimodal waveguide demonstration and its implementation as a high order mode interferometer for sensing application. *Sensors (Basel)*, v. 19, n. 12, p. 2821, 6 2019.

6. CONCLUSIONS AND FINAL REMARKS

In this chapter, the theory about the operation of MMI sensors was presented. There are three structures to be designed or determined: multimode section, excitation structures and detection method. The design of the multimode section consists of choosing a MMI sensor order (i.e. determining what will be the highest order mode supported by the multimode waveguide) and then optimizing the multimode waveguide core geometry (width and height) to maximize device sensitivity. This can be achieved by balancing two aspects of the MMI: increasing the fundamental mode confinement while keeping the high order mode EM field distribution concentrated on the sensing area. The excitation scheme can be chosen to be simpler in terms of construction (step transition) or to be more efficient but complex (BC-SMW and DC-SMW). There are two basic options for the detection method: single-mode output, with simpler detection equipment and interpretation, or multimode output, with more sophisticated measuring schemes and postprocessing.

An experimental demonstration of a TriMW operating as a temperature sensor was also presented. MMI sensors can be built with low-cost materials, such as polymers, and still present good sensitivity characteristics, 0.058 dB/°C at room temperature. Furthermore, the sensitivity obtained is even higher than state-of-the-



art compact low-loss fiber optic sensors, suggesting that MMI sensors could potentially be a viable candidate for other applications as well, such as biosensing.

Even though a large amount of research has been performed regarding MMI sensing and biosensing, there are still many future works and possibilities for the area. With advances in fabrication technologies, new materials or a different composition of materials still need further investigation, as well as different waveguide types and geometries (slot, subwavelength grating, plasmonic, among others). The recent focus was mostly in biosensing applications, but the MMI sensor has shown its merits in terms of sensitivity and capacity for integration, rendering it an interesting option in the most varied types of sensing applications.

ACKNOWLEDGEMENTS

This work was supported by the Brazilian Agencies CAPES and CNPq. The latter under Projects N° 465757/2014-6 (INCT FOTONICOM) and N° 312714/2019-2 (HEHF's Research Productivity Grant); and by the São Paulo Research Foundation (FAPESP) under Project "Photonics for Next Generation Internet".

REFERENCES

ANTONIO-LOPEZ, J. E. *et al.* Tunable multimode-interference bandpass fiber filter. *Opt. Lett.*, v. 35, p. 324–326, 2010.

BERRADA, T. *et al.* Integrated Mach–Zehnder interferometer for Bose–Einstein condensates. *Nat. Commun.* 2013, 4, 2077.

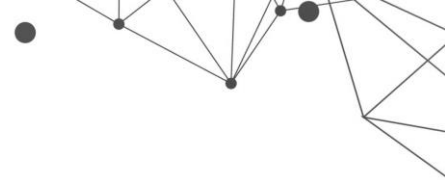
CHILES, J.; FATHPOUR, S. Mid-infrared integrated waveguide modulators based on silicon-on-lithium-niobate photonics. *Optica* 2014, 1, 350–355. doi:10.1364/OPTICA.1.000350.

CRESPI, A. *et al.* Integrated multimode interferometers with arbitrary designs for photonic boson sampling. *Nat. Photonics* 2013, 7, 545–549.

DUVAL, D. *et al.* Nanophotonic lab-on-a-chip platforms including novel bimodal interferometers, microfluidics and grating couplers. *Lab Chip*, The Royal Society of Chemistry, v. 12, p. 1987–1994, 2012.

DWIVEDI, R.; KUMAR, A. A compact and ultra high sensitive RI sensor using modal interference in an integrated optic waveguide with metal under-cladding. *Sensors and Actuators B: Chemical*, v. 240, p. 1302–1307, 2017.

DWIVEDI, R.; KUMAR, A. Refractive index sensing using silicon-on-insulator waveguide based modal interferometer. *Optik*, v. 156, p. 961–967, 2018.



EBIHARA, K.; ASAKAWA, K.; SUZUKI, H. Selectively excited bimodal interferometer for highly sensitive refractive index sensing. *Optical Engineering*, v. 60, n. 2, p. 027103, 2021.

EBIHARA, K. *et al.* Trimodal polymer waveguide interferometer for chemical sensing. *Japanese Journal of Applied Physics*, IOP Publishing, v. 58, n. 6, p. 062005, Jun. 2019.

ELSAYED, M. Y. *et al.* Integrated lab-on-a-chip sensor using shallow silicon waveguide multimode interference (mmi) device. *Proceedings Volume 10106, Integrated Optics: Devices, Materials, and Technologies XXI*, v. 101060X, 2017.

ESTEVEZ, M.; ALVAREZ, M.; LECHUGA, L. Integrated optical devices for lab-on-a-chip biosensing applications. *Laser Photonics Rev.* 2012, 6, 463–487. doi:10.1002/lpor.201100025.

FANDIÑO, J.S.; MUÑOZ, P. Photonics-based microwave frequency measurement using a double-sideband suppressed-carrier modulation and an InP integrated ring-assisted Mach–Zehnder interferometer filter. *Opt. Lett.* 2013, 38, 4316–4319. doi:10.1364/OL.38.004316.

GAVELA, A. F. *et al.* Last advances in silicon-based optical biosensors. *Sensors*, v. 16, n. 3, 2016.

GONZÁLEZ-GUERRERO, A. B. *et al.* Direct and label-free detection of the human growth hormone in urine by an ultrasensitive bimodal waveguide biosensor. *J. Biophotonics*, v. 1, p. 61–67, 2017.

GRAJALES, D. *et al.* Low-cost vertical taper for highly efficient light in-coupling in bimodal nanointerferometric waveguide biosensors. *J. Phys. Photonics*, v. 1, p. 025002, 2019.

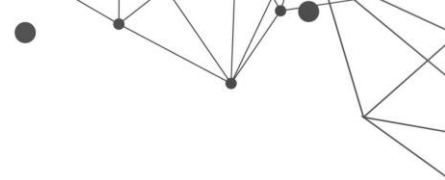
GUT, K. *et al.* Applicability of interference te_0 - tm_0 modes and te_0 - te_1 modes to the construction of waveguide sensors. *Optica Applicata*, v. 29, p. 101–110, 1999.

HOPPE, N. *et al.* Design of an integrated dual-mode interferometer on 250 nm silicon-on-insulator. *IEEE Journal of Selected Topics in Quantum Electronics*, v. 23, n. 2, p. 444–451, 2017.

ISAYAMA, Y. H.; HERNÁNDEZ-FIGUEROA, H.E. High-order multimode waveguide interferometer for optical biosensing applications. *Sensors*, v. 21(9), 2021.

KOZMA, P. *et al.* Integrated planar optical waveguide interferometer biosensors: A comparative review. *Biosens. Bioelectron.* 2014, 58, 287–307. doi:10.1016/j.bios.2014.02.049.

KRIBICH, K. R. *et al.* Novel chemical sensor/biosensor platform based on optical multimode interference (mmi) couplers. *Sensors and Actuators B: Chemical*, v. 107, p. 188–192, 2005.



LEUTHOLD, J.; JOYNER, C. W. Multimode interference couplers with tunable power splitting ratios. *Journal of Lightwave Technology*, v. 19, n. 5, p. 700–707, 2001.

LEUTHOLD, J. *et al.* Spatial mode filters realized with multimode interference couplers. *Opt. Lett.*, v. 21, p. 836–838, 1996.

LEUTHOLD, J. *et al.* Multimode interference couplers for the conversion and combining of zero- and first-order modes. *Journal of Lightwave Technology*, v. 16, n. 7, p. 1228–1239, 1998.

LIANG, Y. *et al.* Investigation of grating-assisted trimodal interferometer biosensors based on a polymer platform. *Sensors*, v. 18, n. 5, 2018. ISSN 1424-8220.

MALDONADO, J. *et al.* Ultrasensitive label-free detection of unamplified multidrugresistance bacteria genes with a bimodal waveguide interferometric biosensor. *Diagnostics*, v. 10, 2020.

MEHTA, A.; MOHAMMED, W.; JOHNSON, E. G. Multimode interference-based fiber-optic displacement sensor. *IEEE Photonics Technology Letters*, v. 15, n. 8, p. 1129–1131, 2003.

MOHAMMED, W. S.; MEHTA, A.; JOHNSON, E. G. Wavelength tunable fiber lens based on multimode interference. *Journal of Lightwave Technology*, v. 22, n. 2, p. 469–477, 2004.

MOHAMMED, W. S.; SMITH, P. W. E.; GU, X. All-fiber multimode interference bandpass filter. *Opt. Lett.*, v. 31, p. 2547–2549, 2006.

RAMIREZ, J. C. *et al.* Trimodal waveguide demonstration and its implementation as a high order mode interferometer for sensing application. *Sensors (Basel)*, v. 19, n. 12, p. 2821, 6 2019.

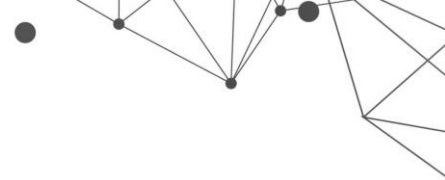
RAMIREZ, J. C. *et al.* Study of a low-cost trimodal polymer waveguide for interferometric optical biosensors. *Opt. Express, OSA*, v. 23, n. 9, p. 11985–11994, May 2015.

RASMUSSEN, T.; RASMUSSEN, J. K.; POVLSEN, J. H. Design and performance evaluation of 1-by-64 multimode interference power splitter for optical communications. *Journal of Lightwave Technology*, v. 13, n. 10, p. 2069–2074, 1995.

SOLDANO, L. B. *et al.* Planar monomode optical couplers based on multimode interference effects. *Journal of Lightwave Technology*, v. 10, n. 12, p. 1843–1850, 1992.

SOLDANO, L. B.; PENNING, E. C. M. Optical multi-mode interference devices based on self-imaging: principles and applications. *Journal of Lightwave Technology*, v. 13, n. 4, p. 615–627, 1995.

Sun, Q. *et al.* Multimode microfiber interferometer for dual-parameters sensing assisted by Fresnel reflection. *Opt. Express* 2015, 23, 12777–12783. doi:10.1364/OE.23.012777.



TORRIJOS-MORÁN, L. *et al.* Slow light bimodal interferometry in one-dimensional photonic crystal waveguides. *Light: Science & Applications*, v. 10, 2021.

TSAREV, A. Effect of dispersion-enhanced sensitivity in a two-mode optical waveguide with an asymmetric diffraction grating. *Sensors*, v. 21, p. 5492, 2021.

ULRICH, R. Image formation by phase coincidences in optical waveguides. *Optics Communications*, v. 13, n. 3, 1975.

SOLER, M. *et al.* How nanophotonic label-free biosensors can contribute to rapid and massive diagnostics of respiratory virus infections: Covid-19 case. *ACS sensors*, v. 5, n. 9, p. 0c01180, 7 2020.

WANG, Q.; FARRELL, G. All-fiber multimode-interference-based refractometer sensor: proposal and design. *Opt. Lett.*, v. 31, p. 317–319, 2006.

WILKES, C.M. *et al.* 60 dB high-extinction auto-configured Mach–Zehnder interferometer. *Opt. Lett.* 2016, 41, 5318–5321. doi:10.1364/OL.41.005318.

YURTSEVER, G. *et al.* Ultra-compact silicon photonic integrated interferometer for swept-source optical coherence tomography. *Opt. Lett.* 2014, 39, 5228–5231. doi:10.1364/OL.39.005228.

ZINOVIEV, K. E. *et al.* Integrated bimodal waveguide interferometric biosensor for label-free analysis. *J. Lightwave Technol., OSA*, v. 29, n. 13, p. 1926–1930, Jul 2011.

DEVELOPMENT OF METAMATERIAL-BASED MICROWAVE DIELECTRIC SENSORS

DOI: [10.51859/amplla.sst631.1122-8](https://doi.org/10.51859/amplla.sst631.1122-8)

Euclides Lourenço Chuma¹
Yuzo Iano²
Glauco Fontgalland³

¹ Researcher at School of Electrical and Computer Engineering, University of Campinas - UNICAMP, Campinas-SP, Brazil.

² Professor at School of Electrical and Computer Engineering, University of Campinas - UNICAMP, Campinas-SP, Brazil.

³ Professor at Applied Electromagnetics and Microwave Lab, Federal University of Campina Grande, Campina Grande-PB, Brazil.

ABSTRACT

Metamaterials, which have properties different from those found in nature, have introduced a new platform for the development of microwave frequency sensors that are gaining importance in many research areas, mainly because of their high sensitivity, robustness, and low cost. In this study, a sensor suitable for liquid dielectric spectroscopy based on a metamaterial complementary split-ring resonator (CSRR) structure is developed and tested. Liquid samples placed in glass capillary tubes normal to the surface of the sensor modified the resonant frequency and Q factor of the CSRR sensor, enabling the relationship among the sensor resonant frequency, Q factor, and complex permittivity of the liquid samples to be estimated. The proposed sensor was evaluated to identify binary mixtures of ethanol and water and successfully exhibited detection in steps of 10%. The proposed sensor was compact, inexpensive, contactless with the sample, reusable, easy to manufacture, and easy to use.

Key words: sensor, dielectric, liquid, microwave, metamaterial.

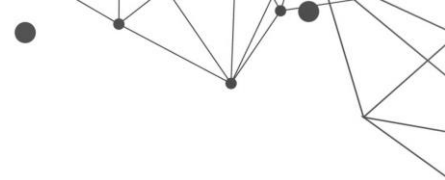
1. INTRODUCTION

Dielectric microwave spectroscopy is an analytical methodology used to study the molecular structure of materials in the presence of electromagnetic fields in the frequency range of 0.3–300 GHz. As electromagnetic waves can penetrate through the layers of dielectric materials, dielectric spectroscopy can be applied in a nondestructive manner without any contact with the material under analysis.

Therefore, microwave dielectric spectroscopy has great potential for applications such as the identification of cancer cells (Martellosio et al., 2017; Ahmad et al., 2018; Bourqui et al., 2016; Mirza et al., 2017), measurement of concentrations of chemical substances (Chen et al., 2018; Saghat et al., 2017), measurement of moisture in materials (Trabelsi et al., 2016; Wang et al., 2018; Nelson et al., 2016), identification of contaminants in food (Yadav et al., 2016), imaging of biological tissues (Chandra et al., 2015; Colgan et al., 2015; Ambrosanio et al., 2018), and even identification of whether fruits are suitable for consumption (Nelson, 2006; Tantisopharak et al., 2016).

In recent years, there have been significant improvements in the development of devices for the generation and detection of microwave signals motivated by the telecommunications sector (Shafi et al., 2017; Neil et al., 2017; Remley et al., 2017), which has allowed the development of equipment with precision, accuracy, and miniaturization superior to previous generations of equipment. Consequently, microwave dielectric spectroscopy has also benefited from this evolution, employing these new devices (Nehring et al., 2016; Nasr et al., 2014) together with new methods and techniques (Zhao et al., 2010; Stumper et al., 2014) for new applications previously limited by the barriers of the technologies used (Li et al., 2013; Hörberg et al., 2017; Azizi et al., 2013).

Recently, a new and alternative sensing platform using metamaterials has been introduced (Chen et al., 2012; Huang et al., 2011). Electromagnetic metamaterials are artificially engineered materials made of subwavelength resonators that can manipulate electromagnetic waves, causing changes in electromagnetic properties that do not occur or may not be readily available in nature (Ziolkowski et al., 2006).



Metamaterials are being investigated for use in material sensing over a very broad spectral range, through microwave (Holloway et al., 2018; Salim et al., 2018), terahertz (Chowdhury et al., 2013; Al-Naib et al., 2017), and optical (Luk'yanchuk et al., 2010) wavelengths. The kind of substances under test can be solid dielectrics (Li, 2017), liquids (Su et al., 2018), and biomolecules (Leea et al., 2008). Metamaterial studies have been performed to characterize the complex dielectric permittivity, which contains complete information on the dielectric constant and loss tangent of samples (Ebrahimi et al., 2014; Withayachumnankula et al., 2013).

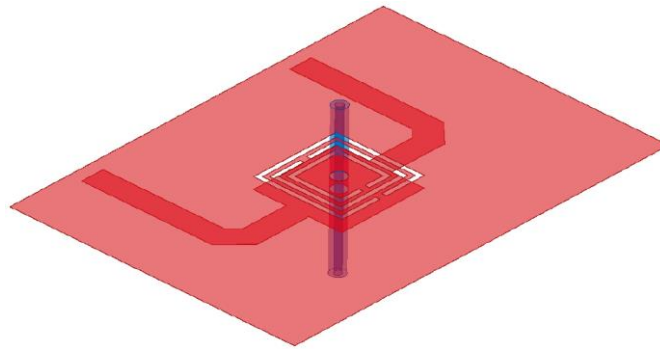
The main components of metamaterial-based microwave sensors are split-ring resonators (SRRs) or complementary split-ring resonators (CSRRs). These are fabricated using various techniques such as microstrips (Dong et al., 2012; Alibakhshi-Kenari et al., 2015; Alibakhshikenari et al., 2017) and thin films (Rani et al., 2014). CSRRs and SRRs can exhibit a well-established electric field along the metamaterial structure; this field is sensitive to dielectric materials placed close to it, producing changes in the resonant frequency and Q factor of the electric field.

This study presents the development and fabrication of a CSRR sensor operating at 2.4 GHz for the identification of liquid substances. The developed sensor was tested in a binary mixture of ethanol and water. The motivation to test ethanol comes from its high concentration and use in vehicle fuel, industrial processes, pharmaceuticals, and medical compositions. In such environments, the sensors must be safe and highly sensitive to accurately monitor ethanol concentration.

2. SENSOR DESIGN AND THEORETICAL STUDY

The main parts of the developed sensor are the CSRR on the ground plane side and the transmission line on the other face. The structure of the CSRR and the transmission line must be aligned such that there is a hole in the center of the CSRR and the transmission line to place the liquid samples under testing. Figure 1 shows a three-dimensional view of the developed sensor structure.

Figure 1 – Three-dimensional view of the proposed sensor.

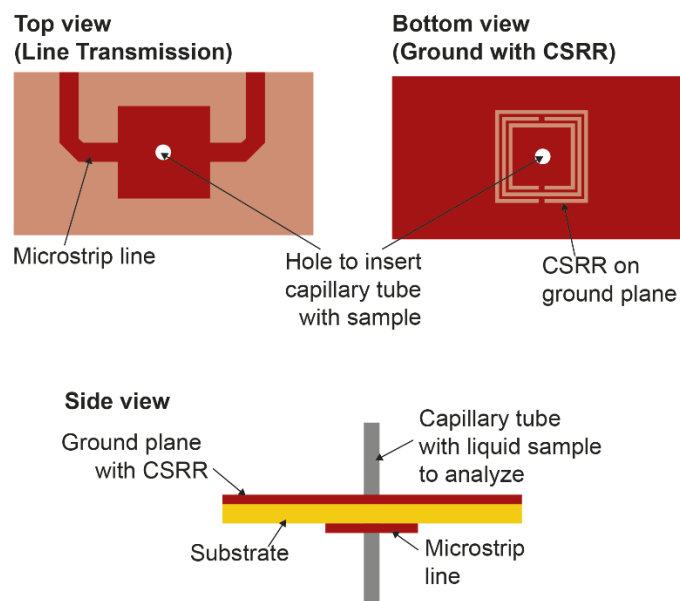


Source: The authors.

In the developed sensor, a CSSR was adopted instead of an SRR because the CSRR can be applied on the ground plane and on the transmission line positioned on the other side. A sample of the liquid material can be placed at the center of the resonator and transmission line. Furthermore, the use of a CSSR does not require an extra circuit area, making the sensor with a CSRR more compact than that with an SRR.

A rectangular geometry was adopted to allow greater miniaturization of the sensor (Chen et al., 2012). CSRRs have advantages over other types of microwave resonators, as they can resonate at a much smaller size, have low radiation losses, and have large Q factors. Several split-ring resonators were used to improve the Q factor of the developed sensor (Bilotti et al., 2007). Figure 2 shows the details of the developed CSRR sensor structure.

Figure 2 – CSRR sensor proposed to measure complex permittivity of liquid samples.

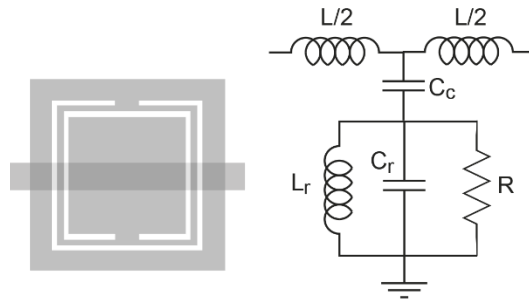


Source: The authors.

During resonance, an electric field is established across the gap between the capacitive plate and square resonator slits, making the region near and within the CSRR sensitive to dielectric changes. Therefore, it is possible to use the central region of the CSRR to measure the dielectric properties of materials.

A CSRR coupled to a transmission line with an equivalent circuit model is shown in Figure 3.

Figure 3 – Example of a CSRR and its equivalent circuit model.



Source: The authors.

Therefore, by placing a material near the center of the CSRR, the value of capacitor C will change, so that

$$C = C_0 + \epsilon_{sample} C_e \quad (1)$$

where C_0 represents the capacitive effects of the dielectric used to manufacture the sensor with the CSRR, the empty glass capillary tube, and the space nearby, and the term $\epsilon_{sample} C_e$ is the capacitive effect of the liquid sample placed inside the glass capillary tube given by the complex permittivity ϵ_{sample} and its capacitance C_e . The complex permittivity of the sample, ϵ_{sample} , is given by

$$\epsilon_{sample} = \epsilon'_{sample} + j\epsilon''_{sample} \quad (2)$$

For a transmission line coupled to the C_s resonator, two frequencies can be identified: the frequency that cancels out the shunt impedance (f_z) and the frequency that cancels out the shunt admittance (f_0) (Bonache et al., 2006). These frequencies are given by the following expressions:

$$f_z = \frac{1}{2\pi\sqrt{L_c(C + C_c)}} \quad (3)$$

$$f_0 = \frac{1}{2\pi\sqrt{L_c C_c}} \quad (4)$$

and the resonance factor Q is given by

$$Q = R\sqrt{\frac{C + C_c}{L_c}} \quad (5)$$

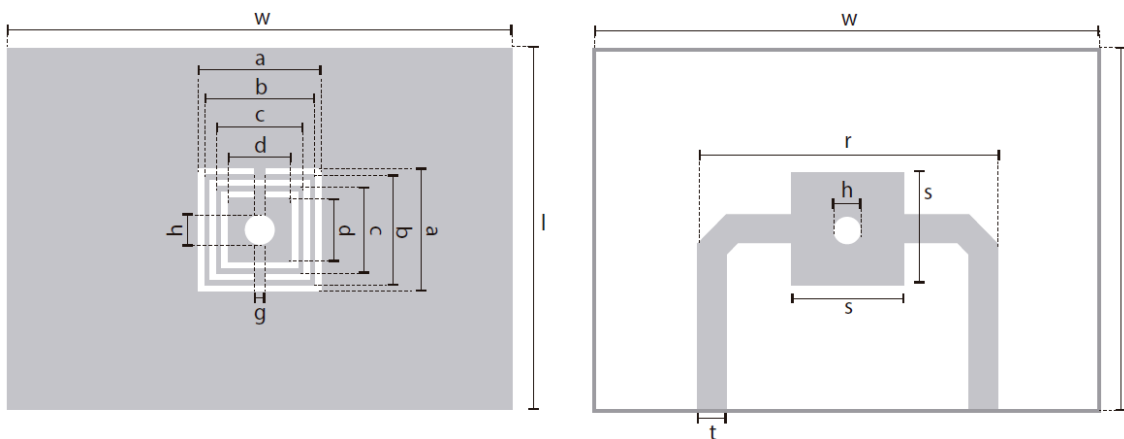
Therefore, from equations (1)–(5), it is possible to find expressions to define the resonant frequency and the Q factor of the sensor with a CSRR as a function of the complex permittivity of the liquid sample inside the glass capillary tube.

The dimensions of the CSRR were initially calculated to resonate at 2.4 GHz without considering coupling with the transmission line and the hole through which the capillary tube passes. To calculate the initial dimensions, it was necessary to calculate the inductance and total effective capacitance to obtain the resonant frequency. The work of Bilotti *et al.* (Bilotti et al., 2007) was the starting point for calculating the inductance and total effective capacitance.

The sensor was designed and built with the Rogers® RO3035 substrate used in the development of microwave circuits and components because it has good parameter stability operating at microwave frequencies. The Rogers® RO3035 has a dielectric constant of $\epsilon = 3.5$ and $\tan\delta = 0.0015$. The thickness of the substrate used was 0.75 mm.

After calculating the initial dimensions, a model was developed in the ANSYS HFSS full-wave simulator by considering the glass capillary tube and transmission line. Figure 4 shows the final dimensions of the sensor.

Figure 4 - Dimensions of the CSRR and the transmission line: $a = 6,20$ mm; $b = 5,55$ mm; $c = 4,37$ mm; $d = 3,19$ mm; $g = 0,50$ mm; $h = 1,50$ mm; $l = 20,00$ mm; $r = 16,60$ mm; $s = 6,20$ mm; $t = 1,60$ mm; $w = 28,00$ mm'



Source: The authors.

3. FABRICATION AND MEASUREMENT

The prototype of the sensor with the CSRR built with SubMiniature version A connectors to be connected to a vector network analyzer (VNA) is shown in Figure 5.

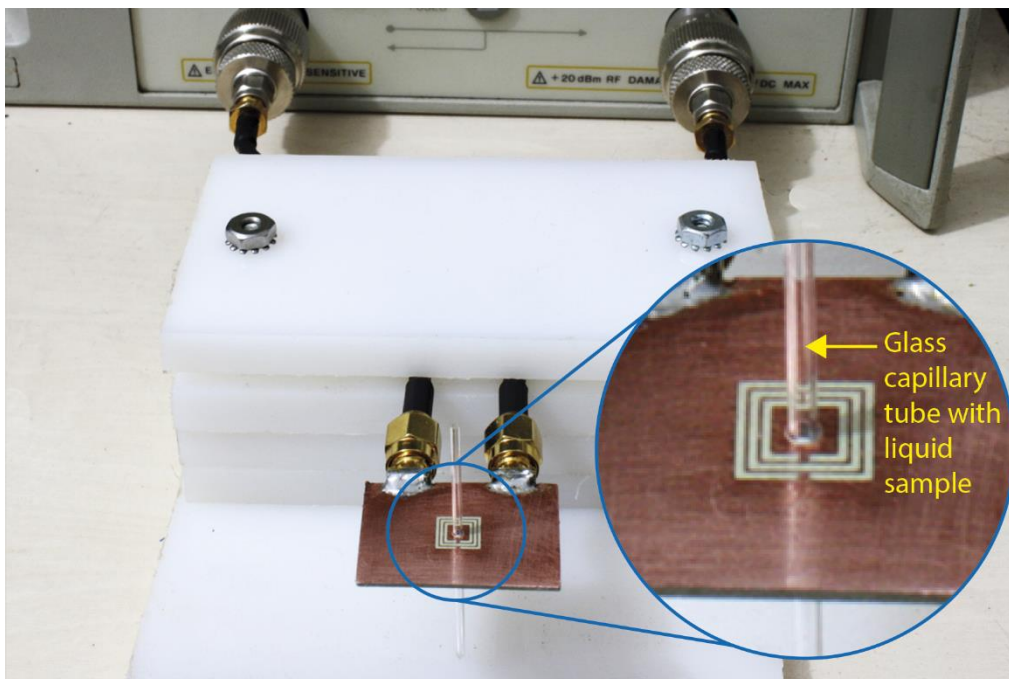
Figure 5 – Sensor prototype.



Source: The authors.

The test setup used to perform the measurements and obtain the S parameters was mounted using a VNA connected to the sensor prototype. A nylon support was used to hold the CSRR sensor and keep the glass capillary tubes in the correct position during the measurements. The test setup is illustrated in Figure 6.

Figure 6 – Support with a CSRR sensor connected to a VNA, and capillary tube with a liquid sample.



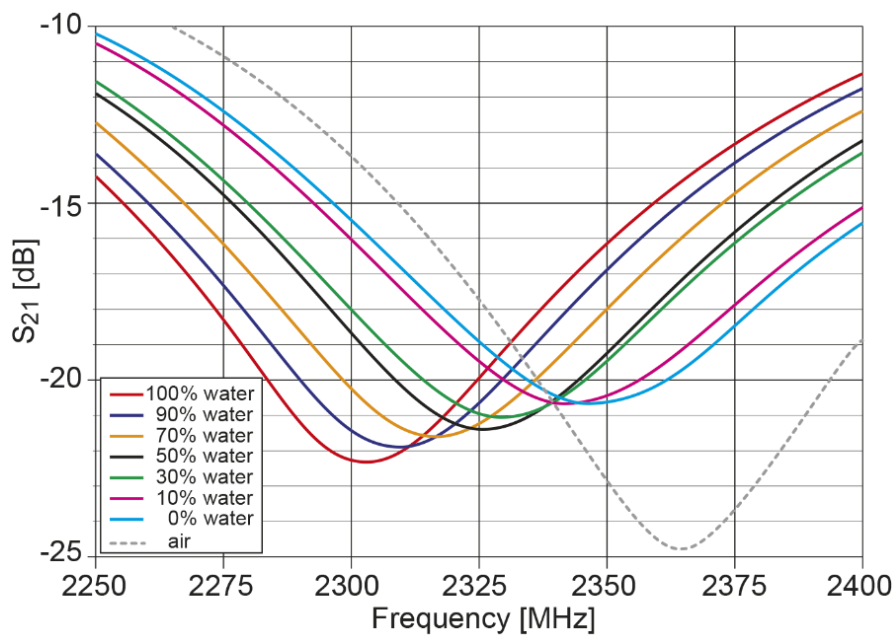
Source: The authors.

Binary mixtures of water and ethanol used in the measurements were prepared using ethanol and distilled water. Glass capillary tubes are used in clinical laboratories with an outer diameter of 1.5 mm, an inner diameter of 1 mm, and a length of 75 mm. Each prepared mixture was filled with a different capillary tube to prevent contamination.

4. RESULTS

The curves of parameter S_{21} measured with a VNA of the water–ethanol mixtures in different fractions are shown in Figure 7. It can be observed that the resonance frequencies were shifted to lower frequencies for different ratios of water–ethanol binary mixtures. This displacement agrees with the results predicted by the numerical and simulation methods reported in other studies (Ebrahimi et al., 2014; Salim et al., 2016; Chakyar et al., 2017).

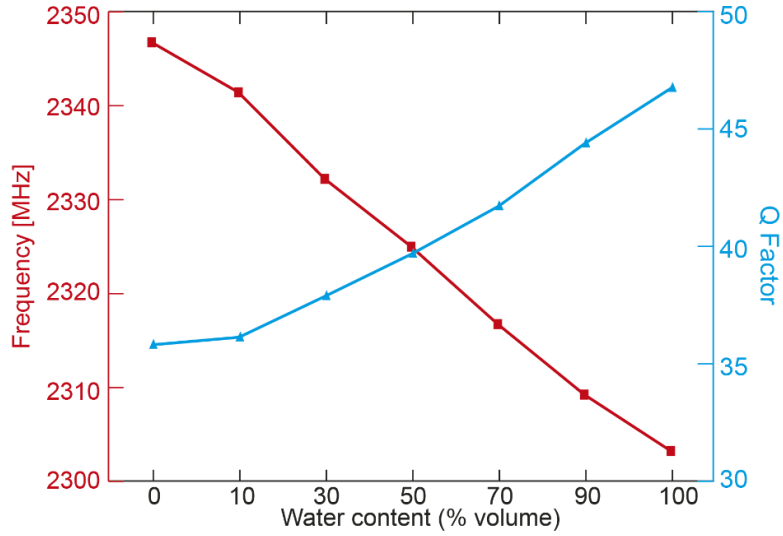
Figure 7 – S_{21} curves measured with a VNA of water–ethanol mixtures with different fractions.



Source: The authors.

Figure 8 shows the resonance frequencies and measured Q factors of the binary water–ethanol mixtures for different volume fractions. This behavior entails a decrease in the resonant frequency and an increase in the Q factor when there is an increase in the proportion of water in the mixture.

Figure 8 – Resonant frequency and Q factor measured for different water–ethanol volume fractions.



Source: The authors.

To find approximations of the interdependence among the resonance frequency deviation, variations in the Q factor, and complex permittivity of the samples, the following set of linear functions was used:

$$\begin{bmatrix} \Delta f_r \\ \Delta Q \end{bmatrix} = \begin{bmatrix} m_{11} & m_{12} \\ m_{21} & m_{22} \end{bmatrix} \cdot \begin{bmatrix} \Delta \epsilon' \\ \Delta \epsilon'' \end{bmatrix} \quad (6)$$

where

$$\Delta \epsilon' = \epsilon'_{\text{sample}} - \epsilon'_{\text{reference}} \quad (7)$$

$$\Delta \epsilon'' = \epsilon''_{\text{sample}} - \epsilon''_{\text{reference}} \quad (8)$$

$$\Delta f_r = f_{\text{sample}} - f_{\text{reference}} \quad (9)$$

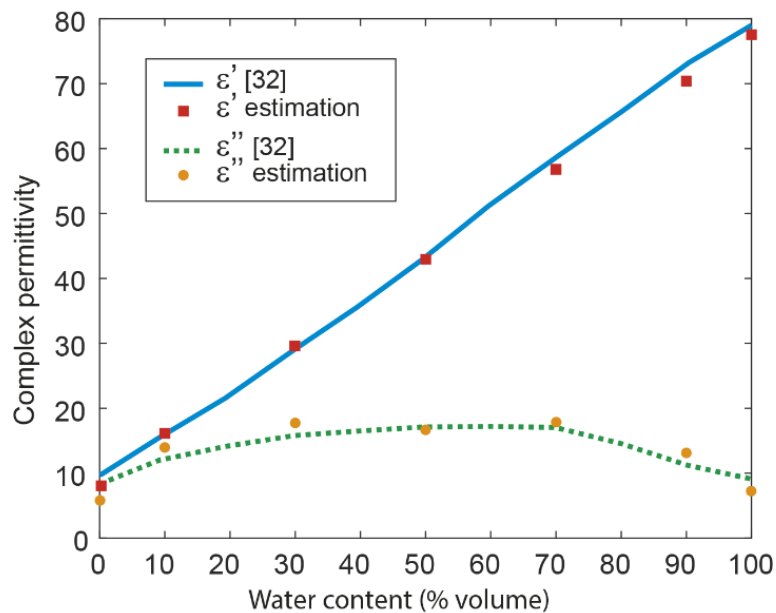
$$\Delta Q = Q_{\text{sample}} - Q_{\text{reference}} \quad (10)$$

The coefficients m_{11} , m_{12} , m_{21} , and m_{22} of the characteristic matrix can be obtained using the least squares method with a set of measurements with controlled samples.

For reference purposes, a mixture of 50% volumetric fractions (50% water and 50% ethanol) was used. The complex permittivity of unknown water–ethanol mixtures was determined by measuring the resonance characteristics and applying matrix inversion.

For comparison, the complex permittivity values measured by Bao *et al.* (Bao *et al.*, 1996) for water–ethanol binary mixtures using the coaxial probe technique at microwave frequencies were used. Figure 9 presents a comparison between the estimates obtained from the measurement results of the developed CSRR sensor and the values found in (Bao *et al.*, 1996). The estimated complex permittivity values were in agreement with that from the literature. The small differences between the values estimated through the measurements and the values in the literature are due to the uncertainties of the measurements and first-order approximation (linear interdependence relationships).

Figure 9 – Comparison between estimated values and values presented in [55].



Source: The authors.

5. CONCLUSIONS AND FINAL CONSIDERATIONS

The proposed CSRR sensor operated at a frequency of ~2.4 GHz and the liquid samples were placed inside common glass capillary tubes. As the capillary tubes with liquid samples pass through inside of the CSRR structure and transmission line (normal direction), it is possible to swap the capillary tubes quickly and simply. Therefore, this is a good choice for field measurements.

In terms of concept validation, an empirical model was successfully used to determine the complex dielectric properties of liquid samples of water–ethanol

mixtures from the measured resonant frequency and Q factor. Consequently, it was possible to determine the volume fraction of water in the water–ethanol mixtures.

REFERENCES

Martellosio, A., et al., (2017), Dielectric properties characterization from 0.5 to 50 ghz of breast cancer tissues, *IEEE Transactions on Microwave Theory and Techniques*, 65, 3, 998–1011.

Ahmad, M. A., Ain, A., Natour, Z. A., Mustafa, F., & Rizvi, T. A., (2018), Electrical characterization of normal and cancer cells, *IEEE Access*, 6, 25 979–25 986.

Bourqui, J., & Fear, E. C., (2016), System for bulk dielectric permittivity estimation of breast tissues at microwave frequencies, *IEEE Transactions on Microwave Theory and Techniques*, 64, 3001–3009.

Mirza, A. F., et al., (2017), An active microwave sensor for near field imaging,” *IEEE Sensors Journal*, 17, 2749–2757.

Chen, W. T. S., & Mansour, R. R., 2018, Miniature gas sensor and sensor array with single and dual-mode rf dielectric resonators, *IEEE Transactions on Microwave Theory and Techniques*, 66, 3697–3704.

Saghati, A. P., Batra, J. S., Kameoka, J., & Entesari, K., 2017, “A metamaterial-inspired wideband microwave interferometry sensor for dielectric spectroscopy of liquid chemicals,” *IEEE Transactions on Microwave Theory and Techniques*, 65, 2558–2571.

Trabelsi, S., & Nelson, S. O., (2016), Microwave sensing of quality attributes of agricultural and food products, *IEEE Instrumentation & Measurement Magazine*, 1, 36–41.

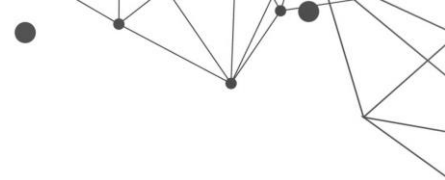
Wang, J., et al., 2018, Rapid determination of meat moisture content using radiofrequency dielectric measurement, *IEEE Access*, 6, 51 384–51 391.

Nelson, S. O., & Trabelsi, S., 2016, Historical development of grain moisture measurement and other food quality sensing through electrical properties, *IEEE Instrumentation & Measurement Magazine*, 19, 16–23.

Yadav, R., Patel, P. N., 2016, Experimental study of adulteration detection in fish oil using novel pdms cavity bonded ebg inspired patch sensor, *IEEE Sensors Journal*, v16, 4354–4361.

Chandra, R., Zhou, H., Balasingham, I., & Narayanan, R. M., 2015, On the opportunities and challenges in microwave medical sensing and imaging, *IEEE Transactions on Biomedical Engineering*, 62, 1667–1682.

Colgan, T. J., Hagness, S. C., & Veen, B. D. V., 2015, A 3-d level set method for microwave breast imaging, *IEEE Transactions on Biomedical Engineering*, 62, 2526–2534.



Ambrosanio, M., Kosmas, P., & Pascazio, V., 2018, A multithreshold iterative dbim-based algorithm for the imaging of heterogeneous breast tissues," *IEEE Transactions on Biomedical Engineering*, 66, 98–104.

Nelson, S. O., 2006, Agricultural applications of dielectric measurements, *IEEE Transactions on Dielectrics and Electrical Insulation*, 13, 688–702.

Tantisopharak, T., & et al., 2016, Nondestructive determination of the maturity of the durian fruit in the frequency domain using the change in the natural frequency, *IEEE Transactions on Antennas and Propagation*, 64, 1779–1787.

Shafi, M., et al., 2017, 5G: A tutorial overview of standards, trials, challenges, deployment, and practice, *IEEE Journal on Selected Areas in Communications*, 35, 1201–1221.

Neil, C. T., et al., 2017, Impact of microwave and mmwave channel models on 5g systems performance, *IEEE Transactions on Antennas and Propagation*, 65, 6505–6520.

Remley, K. A., et al., 2017, "Measurement challenges for 5g and beyond: An update from the national institute of standards and technology," *IEEE Microwave Magazine*, 18, 41–56.

Nehring, J. Nehring, et al., 2016, A 4–32-GHz chipset for a highly integrated heterodyne two-port vector network analyzer, *IEEE Transactions on Microwave Theory and Techniques*, 64, 892–905.

Nasr, I., et al., 2014, Single- and dual-port 50-100-ghz integrated vector network analyzers with on-chip dielectric sensors, *IEEE Transactions on Microwave Theory and Techniques*, 62, 2168–2179.

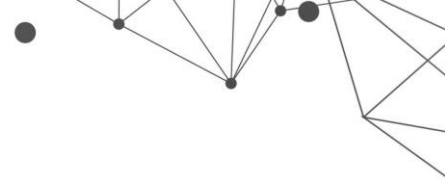
Zhao, W. Zhao, et al., 2010, Calibration algorithm of the n-port vector network analyser using the general node equation, *IET Science, Measurement and Technology*, 4, 298–302.

Stumper, U., & Schraderv, T., 2014, Calibration method for vector network analyzers using one or two known reflection standards, *IEEE Transactions on Instrumentation and Measurement*, 63, 1648–1655.

Li, W., Kong, F., & Yao, J., 2013, Arbitrary microwave waveform generation based on a tunable optoelectronic oscillator, *Journal of Lightwave Technology*, 31, 3780–3786.

Hörberg, M., et al., 2017, RF-MEMS tuned gan hemt based cavity oscillator for X-band, *IEEE Microwave and Wireless Components Letters*, 27, 3780–3786.

Azizi, M., Sarkar, N., & Mansour, R. R., 2013, Single-chip cmos-mems dual mode scanning microwave microscope, *IEEE Transactions on Microwave Theory and Techniques*, 61, 4621–4629.



Chen, T., Li, S., Sun, H., 2012, Metamaterials Application in Sensing, *Sensors*, 2012, 12, 3.

Huang, M., Yang, J., 2011, Microwave Sensor Using Metamaterials, *Wave Propagation, In Tech*, 2011, 13-36.

Ziolkowski, R. W., Engheta, N., 2006, Introduction, History, and Selected Topics in Fundamental Theories of Metamaterials, *Metamaterials Physics and Engineering Explorations*, IEEE Press, John Wiley & Sons.

Holloway, C. L., Kuester, E. F., Gordon, J. A., et al, 2012, An Overview of the Theory and Applications of Metasurfaces: The Two-Dimensional Equivalents of Metamaterials, *IEEE Antennas and Propagation Magazine*, 54, 2.

Salim, A., Lim, S., 2018, Review of Recent Metamaterial Microfluidic Sensors, *Sensors*, 18, 1.

Chowdhury, D. R., Azad, A. K., Zhang, W., Singh, R., 2013, Near Field Coupling in Passive and Active Terahertz Metamaterial Devices, *IEEE Transactions on Terahertz Science and Technology*, 3, 6, 783-790.

Al-Naib, I., 2017, Biomedical Sensing with Conductively Coupled Terahertz Metamaterial Resonators, *IEEE Journal of Selected Topics in Quantum Electronics*, 23, 4.

Luk'yanchuk, B., Zheludev, N. I., Maier, S. A., et. al, 2010, The Fano resonance in plasmonic nanostructures and metamaterials, *Nature Materials*, 9, 707-715.

Li, J., 2017, Permittivity Measurement of Low-Loss Substrates Based on Split Ring Resonators, *World Journal of Engineering and Technology*, 5, 4, 62-68.

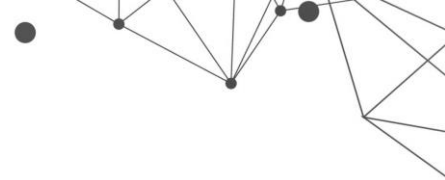
Su, L., Mata-Contreras, J., Vélez, P., et. al., 2018, Analytical Method to Estimate the Complex Permittivity of Oil Samples, *Sensors*, 18, 4

Leea, H-J., Yook, J-G., 2008, Biosensing using split-ring resonators at microwave regime, *Applied Physics Letters*, 92.

Ebrahimi, A., Withayachumnankul, W., Al-Sarawi, S., Abbott, D., 2014, High-Sensitivity Metamaterial-Inspired Sensor for Microfluidic Dielectric Characterization, *IEEE Sensors Journal*, 14, 5, 1345-1351.

Withayachumnankula, W., Jaruwongrungrongseeb, K., Tuantranontc, A., Fumeauxa, C., Abbott, D., 2013, Metamaterial-based microfluidic sensor for dielectric characterization, *Sensors and Actuators*, 189, 233-237

Dong, Y., Toyao, H., Itoh, T., 2012, Design and Characterization of Miniaturized Patch Antennas Loaded with Complementary Split-Ring Resonators, *IEEE Transactions on Antennas and Propagation*, 60, 2, 772-785.



Alibakhshi-Kenari, M., Naser-Moghadasi, M., Sadeghzadeh, R.A., 2015, Bandwidth and radiation specifications enhancement of monopole antennas loaded with split ring resonators, *IET Microwaves, Antennas & Propagation*, 9, 14, 1487-1496.

Alibakhshikenari, M., Virdee, B. S., Limiti, E., 2017, Compact Single Layer Travelling-Wave Antenna Design Using Metamaterial Transmission-Lines, *Radio Science*, 52, 12, 1510–1521.

Rani, M. S. A., Rahim, S. K. A., Kamarudin, M. R., et al, 2014, Electromagnetic Behaviors of Thin Film CPW-Fed CSRR Loaded on UWB Transparent Antenna, *IEEE Antennas and Wireless Propagation Letters*, 13, 1239-1242.

Chen, T., Li, S., Sun, H., 2012, Metamaterials application in sensing, *Sensors*, 2742–2765.

Bilotti, F., Toscano, A., Vegni, L., 2007, Design of spiral and multiple split-ring resonators for the realization of miniaturized metamaterial samples, *IEEE Transactions on Antennas and Propagation*, 55, 2258–2267.

Bonache, J. E. A., 2006, On the electrical characteristics of complementary metamaterial resonators, *IEEE Microwaves and Wireless Components Letters*, 16, 543–545.

Bilotti, F., et. al., 2007, Equivalent-circuit models for the design of metamaterials based on artificial magnetic inclusions, *IEEE Transactions on Microwave Theory and Techniques*, 55, 2865–2873.

Ebrahimi, A., Withayachumnankul, W., Al-Sarawi, S., & Abbott, D., 2014, High-sensitivity metamaterial-inspired sensor for microfluidic dielectric characterization, *IEEE Sensors Journal*, 14, 1345–1351.

Salim, A., Lim, S., 2016, Complementary split-ring resonator-loaded microfluidic ethanol chemical sensor, *Sensors*, 16.

Chakyar, S. P., Simon, S. K., Bindu, C., Andrews, J., & Joseph, V. P., 2017, Complex permittivity measurement using metamaterial split ring resonators, *Journal of Applied Physics*, 121.

Bao, J.-Z., Swicord, M. L., & Davis, C. C., 1996, Microwave dielectric characterization of binary mixtures of water, methanol, and ethanol, *The Journal of Chemical Physics*, 104, 4441–4450.

MONITORING BIOMETRIC PARAMETERS AND PREDICTION PRODUCTIVITY IN SUGARCANE CROPS USING DRONE-BORNE SYNTHETIC APERTURE RADAR

DOI: 10.51859/ampla.sst631.1122-9

Gian Oré¹
Luciano P. Oliveira²
Laila F. Moreira³
Hugo E. Hernandez-Figueroa⁴

¹ PhD student from University of Campinas, Brazil.

² PhD from University of Campinas, Brazil, Senior Researcher at the Technology Innovation Institute (TII), UEA.

³ PhD from University of Campinas, Brazil, Co-Founder of RADAZ S/A.

⁴ PhD in Physics from Imperial College London, Full Professor at University of Campinas, Brazil.

ABSTRACT

Tools for monitoring sugarcane crops based on remote sensing, such as synthetic aperture radar (SAR) and optical systems, have been proposed in recent years. In this work, different methodologies for monitoring sugarcane crops based on SAR systems are developed. For this, a drone-borne SAR system operating in L, P and C bands was used to monitor a sugarcane crop located at FEAGRI - UNICAMP. Data obtained by the SAR system together with biometric measurements are used to develop methodologies for the estimation of biometric parameters such as biomass and growth in a sugarcane crop. In addition, a methodology for the prediction of harvesting date and productivity of sugarcane is proposed. In the case of estimating the sugarcane biomass, a root-mean-square error (RMSE) of 2.05 kg m⁻² is obtained. Additionally, the history of biomass was used for the development of prediction methodologies, which were tested in different sugarcane crops in a test site, resulting in an average error of 8 days and 10.73 % for the prediction of harvesting date and productivity, respectively.

Key words: Biomass. Interferometry. Sugarcane. Synthetic aperture radar.

1. INTRODUCTION

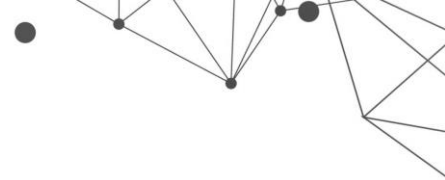
Different methodologies and techniques have been developed for monitoring the sugarcane crop based on biometric measurements and remote sensing. In the case of biometric measurements, in order to obtain an adequate representation of an area, a sampling with many measurements is necessary, therefore, this methodology has become saturated due to the extensive crops aimed at modern agricultural applications (Engelbrecht et al., 2018). Sugarcane monitoring techniques based on biometric measurements are very expensive and time consuming for large crops. This makes crop management and decision-making difficult, as information is not provided in a timely manner or is not sufficient. Methodologies based on remote sensing manage to overcome these disadvantages, so it is currently a research area of interest.

In this project, different methodologies are proposed for the estimation of biometric parameters in sugarcane based on SAR systems. For this, a sugarcane crop was monitored throughout its phenological stage by a drone-borne SAR system which works in the L, P and C bands. The above ground biomass (AGB) estimation is based on the method of curve fitting and backscattering values weighting, obtained with the L, P and C bands of the SAR system. Growth estimation is developed using DInSAR techniques. In the case of the growth estimation, a correction factor is proposed, obtained from the backscattering information, which varies over time. In addition, a methodology is developed for harvesting date and productivity prediction. This methodology is based on the historical data of AGB estimated in the sugarcane crop with the drone-borne SAR system.

The use of a 3-band drone-borne SAR system allows the area of interest to be revisited with the necessary frequency, performing different flight geometries, which is difficult to obtain in SAR systems embedded in satellites that fly over a different area each specified time with a fixed flight geometry. Also, this drone-based solution is more cost-effective compared to an airplane-based solution.

2. LITERATURE REVIEW

Initially, radars were for military use only, but over time they became available for civilian applications. The application of SAR images for monitoring in

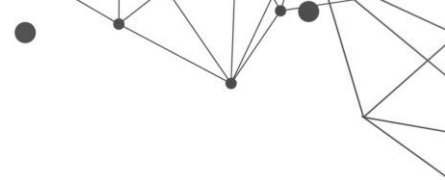


agriculture has become popular in recent years. Some attempts to estimate AGB have focused on different crops such as canola, soybean (Hosseini et al., 2018) and wheat (Wiseman et al., 2014). Forests are also monitored using SAR images (Gama et al., 2010). In addition, different techniques such as interferometry SAR (InSAR) (Rossi & Erten, 2015), polarimetric decomposition (Wang et al., 2016), polarimetric interferometry SAR (Pol-InSAR) (Erten et al., 2016) and differential interferometry SAR S (DInSAR) (Frey et al., 2019) have been applied to estimate different parameters of vegetation.

In the case of sugarcane, the monitoring of different characteristics of this crop based on SAR systems and optical systems was previously researched. With respect to SAR systems, some studies conclude that the L band performs better than the C and X bands to monitor sugarcane growth over time (Molijn et al., 2019), while the C band can be useful in small time windows. In other works, the height of sugarcane was estimated using C-band backscattering information at different polarizations and angles of incidence (Baghdadi et al., 2011), obtaining good results up to 150 cm of height. Other phenomena, such as sugarcane lodging problem, are monitored with a polarimetric C-band using time series data and the Wishart classifier (Chen et al., 2016). On the other hand, different methods of classifying the sugarcane crop in relation to other crops and objects were studied using the C band (Li et al., 2019), concluding that the HV polarization presents the best results. Furthermore, the first attempts at productivity prediction were presented with promising results (Stasolla & Neyt, 2019). In the case of optical systems, techniques were developed for the mapping and identification of sugarcane crops (Oliveira, 2015). Also, attempts were made to estimate sugarcane productivity based on empirical relationships and the Monteith model (Wang et al., 2020).

3. DRONE-BORNE SAR SYSTEM

Satellite-borne SAR systems supply the civil remote sensing market of large areas, starting with 10.000 km², and low map scales between 1:50.000 and 1:500.000. Airborne SAR systems supply the demand of areas larger than 500 km² with map scales between 1:5.000 and 1:50.000. Drone-borne SAR systems with a flight altitude higher than 400 feet above ground level and total take-off weight



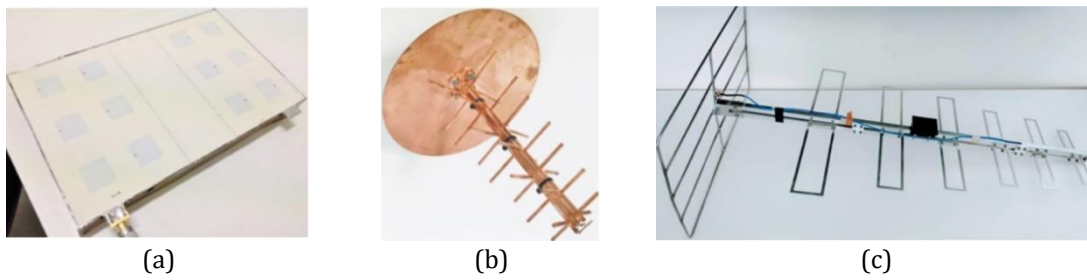
heavier than 25 kg supply the military market with map scales between 1:500 and 1:50.000 (Sambatti & Luebeck, 2015).

A low cost and high performance airborne and drone- borne SAR solution, adequate for the market of small areas, was designed starting with the requirements of the applications and a low-cost drone. The applications selected are precision agriculture, subsurface tomography, subsidence, and cartography. The selected drone has a maximum payload of 5 kg, a forward velocity of 15 m/s and a flight endurance of 25 minutes. Starting from those characteristics, the radar illumination geometry, antennas and radio frequency subsystems, analog-to-digital conversion, motion compensation, real-time and off-line processing, data acquisition, Global Navigation Satellite System (GNSS) and Inertial Measurement Unit (IMU) subsystems, and position and orientation processing were designed.

Three antennas were developed for the drone-borne SAR system, one for each operating band. Since the radar also operates at lower frequency bands (L and P), if compared to similar systems (Ludeno et al., 2018), the antennas can become quite large, heavy and with increased aerodynamic drag. Therefore, special care was taken to develop antennas that could be carried along with the radar by the drone without compromising its flight dynamics and hovering time.

For the C-band, a square microstrip patch antenna was chosen due to its linear polarization, lightness, low profile and simple construction. A microstrip array was designed in a 2×3 configuration, whose prototype is shown in Figure 1a. The manufactured microstrip antenna board has two identical antenna arrays for providing a cross-track interferometric baseline (Woodhouse, 2017). The L-band antenna comprises two log-periodic dipole arrays in quadrature and a parabolic reflector, as shown in Figure 1b. This design was chosen due to its high directivity, wide bandwidth, and ease of construction. The radar transmits and receives with both vertical and horizontal polarizations to collect full polarimetric data (Papathanassiou et al., 1998). The parabolic reflector is placed behind the array to increase directivity and sidelobe suppression. A single polarization log-periodic dipole antenna array was chosen for P-band. It contains a reflecting grid to increase directivity and side lobe suppression. The antenna prototype can be seen in Figure 1c.

Figure 1 – Antennas prototypes. (a) C band. (b) L band. (c) P band



Source: The authors.

Table 1 presents a summary of the characteristics of the antennas. It also shows that their combined weight adds up to 1.302 kg, well below the drone maximum payload capacity.

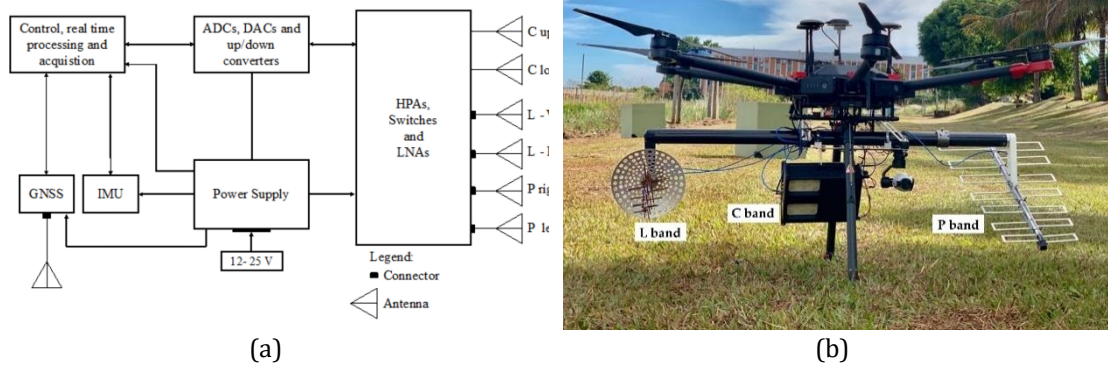
Table 1 – Main characteristics of the antennas.

Main Characteristics					
Antenna	Polarization	Bandwidth [MHz]	Max Gain [dB]	Azimuth Aperture [degrees]	Weight [grams]
C band	Vertical	400	12.1	32.5	105
L band	Vert./Horiz.	200	9.4	58.5 (horiz.) 77.2 (vert.)	463
P band	Horizontal	100	8.2	69.3	734

Source: The authors.

The C-band antennas are mounted together with the radar electronics, which were designed with state-of-the-art telecommunication and navigation components. The system can be supplied by 12 to 25 V, and its power consumption is less than 10 W. The radio frequency subsystem comprises a transceiver and a front-end with the P, L and C bands. The navigation subsystem is composed of a GNSS and an IMU which provide positioning data used to perform motion compensation. The control and processing board is responsible for the control, data acquisition and SD Card recording, and communications via serial, USB and Ethernet interfaces (Moreira et al., 2019). Figure 2 shows the block diagram of the radar and the drone equipped with the radar module and the 3 antennas.

Figure 2 – (a) Block diagram of the radar. (b) Drone and radar system



Source: The authors.

4. DATA COLLECTION CAMPAIGNS

The multiband drone-borne SAR system was employed for surveying an experimental area, in which the estimation methods were developed using the collected data, and a test site, in which the proposed methods were tested in a real scenario, carrying out several square survey flights along time.

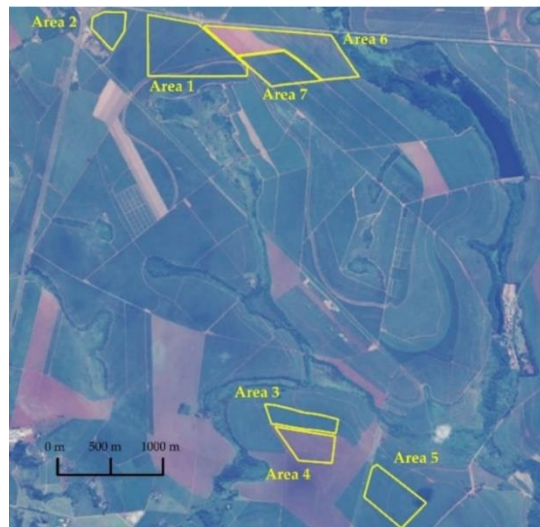
4.1. EXPERIMENTAL AREA

The experimental area of $10 \times 40 \text{ m}^2$ is located at the School of Agricultural Engineering at the University of Campinas (FEAGRI-UNICAMP), at $22^\circ 49' 12'' \text{ S}$, $47^\circ 03' 42'' \text{ W}$. The sugarcane type is IACSP97-4039, which has a nominal cycle of 12 months. Approximately 340 sugarcane plants were planted on 7 July 2019, distributed in seven lines separated by 1.5 m and 0.75 m between plants. The sugarcane crop was harvested on 1 July 2020, 360 days after planting.

4.2. TEST SITE

The test site, shown in Figure 3, is located on a sugarcane farm in Iracemápolis, São Paulo, Brazil. The monitored sugarcane crop is the RB975952 type, which has a nominal cycle of 18 months. The test site was divided into 7 areas with different harvest seasons. The survey flights and biometric measurements occurred on 9 April 2020 for areas 1 through 5 of the test site and 16 July 2020 for areas 1, 6, and 7. All SAR surveys were performed with linear flight paths. Moreover, areas 2 and 4 were harvested on 15 July 2020, and areas 6 and 7 were harvested on 7 October 2020.

Figure 3 – Test site, general view.

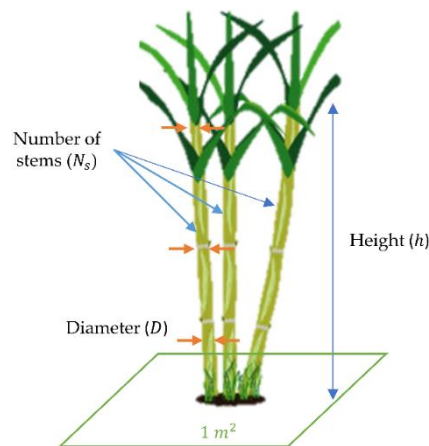


Source: Google Earth.

4.3. SUGARCANE AGB MEASUREMENTS

The methodology described in (Magro et al., 2011) was applied to calculate the measured AGB of sugarcane crops as reference data. Biometric parameters, illustrated in Figure 4, such as height, diameter, and the number of stems, were collected for each sugarcane plant in the experimental area. N_s is the total number of stems in an area of 1 m^2 .

Figure 4 – Representation of biometric parameters in a sugarcane plant.



Source: The authors.

A stem with medium height is selected in this 1 m^2 area as a representative from which the height h (m) and the diameters at the base, middle, and top of the stem can be measured. The final diameter D (m) is obtained by averaging those three measurements. A model with a Spearman's correlation of 0.95 (Molijn et al., 2018) is then employed to calculate the measured AGB by biometric parameters AGB_m ,

$$AGB_m = \pi \frac{D^2}{4} h \times N_s \times \rho \times \frac{0.977}{d_x}, \quad (1)$$

where d_x (m) is the space between crop lines; destructive analysis was performed in a few stems to calculate the stem density ρ (kg m^{-3}). Measured AGB obtained from (1) was used as reference data to develop the proposed AGB estimation method.

4.4. SAR SURVEY

Table 2 shows the days when the data collection campaign for biometric measurements and SAR surveys were performed in the experimental area. The sugarcane crop was harvested on 1 July 2020, 360 days after planting.

Table 2 – Dates of surveys carried out in the experimental area.

Survey Dates	Days after Planting
12 December 2019	165
25 January 2020	202
4 March 2020	241
10 April 2020	278
12 May 2020	310
1 June 2020	330
17 June 2020	346

Source: The authors.

5. ESTIMATION OF SUGARCANE BIOMETRIC PARAMETERS

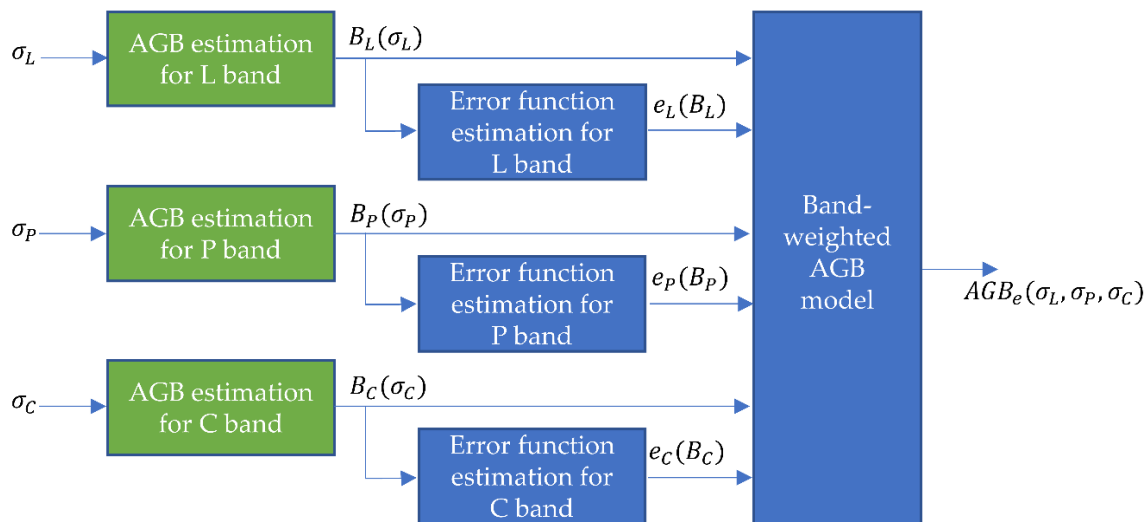
5.1. SAR IMAGING

Data collected during the survey flights were processed with a time-domain back-projection algorithm to construct complex-valued SAR images, which represent a measure of the scene backscattering (Moreira et al., 2013). The SAR images were radiometrically corrected considering the distance between the platform and the illuminated target, the bidirectional antenna pattern (Castro, 2018), and the number of pulses used to construct the synthetic aperture by the back-projection algorithm. For the SAR images' absolute calibration, corner reflectors with known theoretical radar cross-section (RCS) were used and located over the illuminated scene. The absolute calibration methodology used in this work is the integral method (Gray et al., 1990), which uses pixels from the radiometrically corrected SAR images corresponding to the corner reflector and the pixels from the areas adjacent to the reflector.

5.2. SUGARCANE AGB ESTIMATION

The methodology to estimate AGB from radar data can be represented as a block diagram, as shown in Figure 5 (Oré et al., 2022). This methodology is divided into two parts: first, the information obtained from each frequency band– σ_L , σ_P , and σ_C –is analyzed individually to create single-band AGB models (green blocks), and finally, these AGB models– $B_L(\sigma_L)$, $B_P(\sigma_P)$ and $B_C(\sigma_C)$ –are weighted according to their efficiency in different ranges of AGB values to generate a final model for the AGB estimation– $AGB_e(\sigma_L, \sigma_P, \sigma_C)$.

Figure 5 – Block diagram for the AGB estimation.



Source: The authors.

5.2.1. SINGLE-BAND AGB MODELS

Since the electromagnetic wave penetration in crops is different for each frequency band, each one presents different saturation points (Nizalapur et al., 2010). Based on that, the three frequency bands available on the drone-borne SAR system were independently analyzed to estimate single-band AGB models to evaluate each band's performance in different stages of crop growth and take advantage of the characteristics of each one of them.

Measured AGB and backscattering values for each frequency band – σ_L , σ_P , and σ_C – were calculated over the experimental area. The information was analyzed using a scatter plot of the backscattering for each band versus the measured AGB. Finally, using a curve-fitting procedure, the single-band AGB models – $B_L(\sigma_L)$, $B_P(\sigma_P)$ and $B_C(\sigma_C)$ – are estimated.

5.2.2. BAND-WEIGHTED AGB MODEL

The single-band AGB models are weighted to produce the final estimated AGB model, as described in Figure 5. The methodology adopted is the weighted-arithmetic average, where the weighting is based on the error functions for each band (Terr, 2020).

Table 3 shows three ranges of AGB values used to evaluate each single-band model, which is defined based on the saturation of each band according to the literature (Nizalapur et al., 2010). The root-mean-square error (RMSE) for each frequency band in the three ranges – $e_{L_{1,2,3}}$, $e_{P_{1,2,3}}$ and $e_{C_{1,2,3}}$ – are calculated by comparing the measured and estimated AGB.

Table 3 – Root-mean-square error (RMSE) evaluation of single-band AGB models in different ranges of AGB.

Band	Range 1: [0 to 4 kg m ⁻²]	Range 2: [4 to 11 kg m ⁻²]	Range 3: [11 to 21 kg m ⁻²]
L band: $B_L(\sigma_L)$	e_{L_1}	e_{L_2}	e_{L_3}
P band: $B_P(\sigma_P)$	e_{P_1}	e_{P_2}	e_{P_3}
C band: $B_C(\sigma_C)$	e_{C_1}	e_{C_2}	e_{C_3}

Source: The authors.

Then, a curve-fitting procedure using polynomial functions and the RMSE values from each single-band AGB model is used to estimate the error functions – $e_L(B_L)$, $e_P(B_P)$ and $e_C(B_C)$. Finally, the band-weighted AGB model, $AGB_e(\sigma_L, \sigma_P, \sigma_C)$, is obtained by weighting the AGB estimation of each band as shown in Figure 5:

$$AGB_e(\sigma_L, \sigma_P, \sigma_C) = \frac{B_L(\sigma_L)w_L(\sigma_L) + B_P(\sigma_P)w_P(\sigma_P) + B_C(\sigma_C)w_C(\sigma_C)}{w_L(\sigma_L) + w_P(\sigma_P) + w_C(\sigma_C)}, \quad (2)$$

$$w_L(\sigma_L) = \frac{1}{(e_L(\sigma_L))^2}, \quad (3)$$

$$w_P(\sigma_P) = \frac{1}{(e_P(\sigma_P))^2}, \quad (4)$$

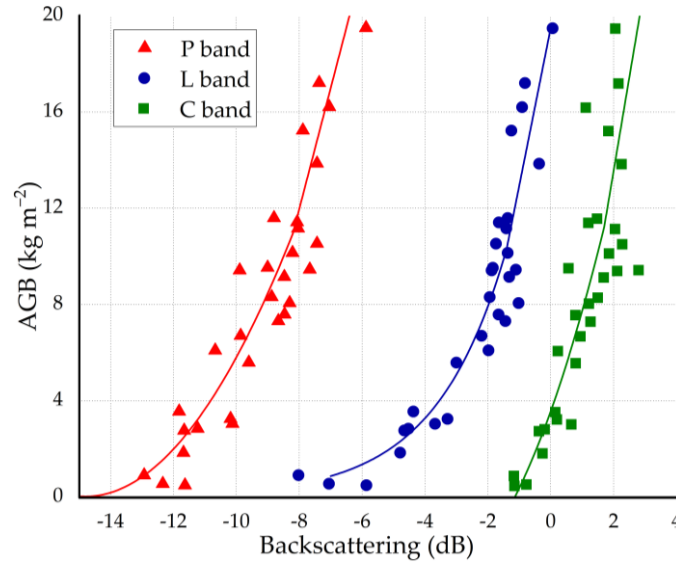
$$w_C(\sigma_C) = \frac{1}{(e_C(\sigma_C))^2}. \quad (5)$$

5.2.3. RESULTS IN THE EXPERIMENTAL AREA

The three-band backscattering values were calculated over the experimental area using the calibrated and radiometrically corrected SAR. The acquired dataset was divided into 75% for training and 25% for validation. Figure 6 presents the

backscattering results versus measured AGB using the training dataset from 19 December 2019 to 12 May 2020.

Figure 6 – Backscattering of the P, L, and C bands versus measured AGB.



Source: The authors.

To calculate the single-band models, piecewise-defined equations based on exponential functions and second-degree polynomials were used due to the saturation and changes in trend between the measured AGB and backscattering values. Applying a curve-fitting method, the measured AGB for each frequency can be expressed as:

$$B_L(\sigma_L) = \begin{cases} 19.15e^{0.4413\sigma_L}, & \sigma_L < -1.4dB \\ 6.55\sigma_L + 19.50, & \sigma_L \geq -1.4dB \end{cases} \quad (6)$$

$$B_P(\sigma_P) = \begin{cases} 0.25(\sigma_P)^2 + 7.43\sigma_P + 55.01, & \sigma_P < -8.2dB \\ 5.02\sigma_P + 52.15, & \sigma_P \geq -8.2dB \end{cases} \quad (7)$$

$$B_C(\sigma_C) = \begin{cases} 0.49(\sigma_C)^2 + 3.678\sigma_C + 3.57, & \sigma_C < 1.7dB \\ 7.77\sigma_C - 1.98, & \sigma_C \geq 1.7dB \end{cases} \quad (8)$$

An RMSE of 1.94 kg m⁻² was achieved for the L band model, 2.11 kg m⁻² for the P band model, and 3.46 kg m⁻² for the C band model. Furthermore, the R² for each model was 0.89, 0.84, and 0.55 for $B_L(\sigma_L)$, $B_P(\sigma_P)$ and $B_C(\sigma_C)$, respectively.

The RMSE criteria and the measured AGB were used to evaluate each single-band AGB model, as described in Section 5.2.2. These results were obtained considering the training dataset. The RMSE values for $B_L(\sigma_L)$, $B_P(\sigma_P)$, and $B_C(\sigma_C)$ were calculated over different ranges of AGB and are displayed in Table 4.

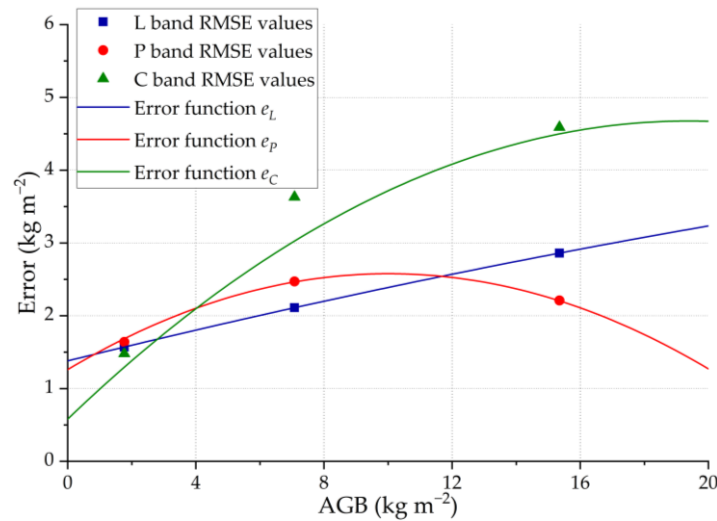
Table 4 – RMSE results when evaluating each single-band model in different ranges of AGB.

Band	Range 1:	Range 2:	Range 3:	Overall:
L band: $B_L(\sigma_L)$	1.57 kg m ⁻²	2.11 kg m ⁻²	2.86 kg m ⁻²	1.94 kg m ⁻²
P band: $B_P(\sigma_P)$	1.64 kg m ⁻²	2.47 kg m ⁻²	2.21 kg m ⁻²	2.11 kg m ⁻²
C band: $B_C(\sigma_C)$	1.48 kg m ⁻²	3.63 kg m ⁻²	4.59 kg m ⁻²	3.46 kg m ⁻²

Source: The authors.

Such results show that each single-band model presents better performance in different AGB ranges, which will be exploited in the weighted multi-band model. Figure 7 shows the RMSE values presented in Table 4.

Figure 7 – Error functions and RMSE values for the L, P, and C bands as a function of the measured AGB.



Source: The authors.

Figure 7 also shows error functions that were estimated from each band RMSE results presented in Table 4. Second-order curve-fitting equations were chosen to model the error functions, and can be expressed as:

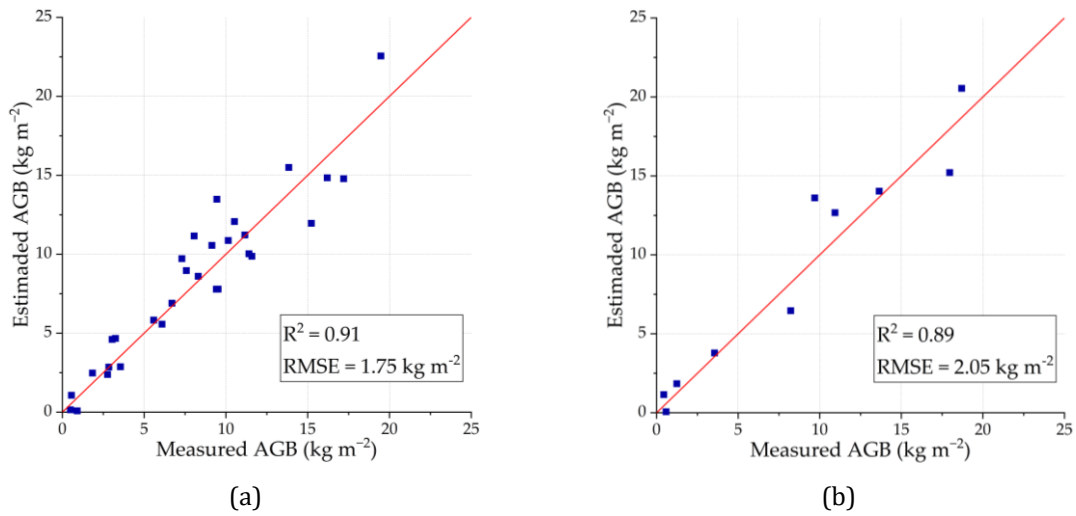
$$e_L(B_L) = -0.00081B_L^2 + 0.1089B_L + 1.38, \quad (9)$$

$$e_P(B_P) = -0.01313B_P^2 + 0.2631B_P + 1.26, \quad (10)$$

$$e_C(B_C) = -0.01090B_C^2 + 0.4226B_C + 0.5801. \quad (11)$$

These error functions are used to weight the single-band AGB models to finally obtain $AGB_e(\sigma_L, \sigma_P, \sigma_C)$, according to (2)–(5). The weighted-band AGB model achieved an RMSE of 1.75 kg m⁻² and an R² of 0.91 for the training dataset. For the validation dataset, an RMSE of 2.05 kg m⁻² and an R² of 0.89 were achieved. Figure 8 shows estimated AGB versus measured AGB for training and validation datasets.

Figure 8 – Estimated AGB vs. measured AGB. (a) Training dataset. (b) Validation dataset.



Source: The authors.

5.3. GROWTH SUGARCANE ESTIMATION

5.3.1. PROPOSED METHOD

Using the DInSAR technique described in Oré et al. (2020) to estimate the height difference ΔH from interferograms and considering the backscattering of the sugarcane crop and the soil with weed plants and others around it, a methodology for estimating the sugarcane growth between two different acquisition times is developed. In this case, the P band of the drone-borne SAR system is used. The backscattering data obtained from SAR images can be decomposed as (Lin et al., 2009):

$$\sigma_T = \sigma_{sc} + \sigma_{so} + \sigma_{db}, \quad (12)$$

where σ_T is the total backscattering measured by the radar in the sugarcane crop, σ_{sc} represents only the backscattering corresponding to sugarcane, σ_{so} is the backscattering of the soil with weed plants and others that can be measured in a region adjacent to the sugarcane crop, and σ_{db} is the double-bounce backscattering between the crop stalks and soil. At different stages of crop growth, the proportions of these backscattering vary.

It is considered that it is possible to estimate σ_{so} from the backscattering of regions close to the crop so that it can be subtracted from (12):

$$\sigma_R = \sigma_T - \sigma_{so} = \sigma_{sc} + \sigma_{db}, \quad (13)$$

assuming that σ_{sc} is proportional to σ_R by a contribution factor $K_R \in [0,1]$, then:

$$\sigma_{sc} = K_R \sigma_R, \quad (14)$$

also, from the variables K_R and σ_R , the double-bounce contribution can be expressed as:

$$\sigma_{db} = (1 - K_R) \sigma_R. \quad (15)$$

To calculate the height difference or growth between two different days, the two different stages of growth of a sugarcane crop visualized in Figure 9 are considered.

Figure 9 – Crop in two distinct stages. (a) Day 1. (b) Day 2.



Source: The authors.

According to Figure 9, on Day 1, the height of the crop is represented by $H_{sc(1)}$, the height of the weedy soil is $H_{so(1)}$ and the difference between them is calculated as $H_{T(1)} = H_{sc(1)} - H_{so(1)}$. Likewise, for Day 2, it is assumed that $H_{T(2)} = H_{sc(2)} - H_{so(2)}$. Then, the total height difference estimated by the radar $\Delta H_T = H_{T(2)} - H_{T(1)}$, can be expressed as:

$$\Delta H_T = \Delta H_{sc} - \Delta H_{so}, \quad (16)$$

where $\Delta H_{sc} = H_{sc(2)} - H_{sc(1)}$ is the height variation corresponding to the sugarcane crop and $\Delta H_{so} = H_{so(2)} - H_{so(1)}$ is the variation corresponding to weed plants and other objects.

The radar measures a sum of complex contributions. The amplitude of the return signal is proportional to $\sqrt{\sigma_T}$ and the interferometric phase is proportional to ΔH_T . As the ratio σ_{sc}/σ_T approaches unity, ΔH_{sc} becomes the main contribution in (16). The same reasoning can be done for σ_{so} and ΔH_{so} . Thus, a simple solution is to

correct (16) by weighting each contribution by its respective backscattering. First, (12) can be rewritten as:

$$1 = \frac{\sigma_{sc}}{\sigma_T} + \frac{\sigma_{db}}{\sigma_T} + \frac{\sigma_{so}}{\sigma_T} = K_{sc}^2 + K_{db}^2 + K_{so}^2, \quad (17)$$

where:

$$K_{sc} = \sqrt{\frac{\sigma_{sc}}{\sigma_T}} = \sqrt{K_R} \sqrt{\frac{\sigma_R}{\sigma_T}}, \quad (18)$$

$$K_{db} = \sqrt{\frac{\sigma_{db}}{\sigma_T}}, \quad (19)$$

$$K_{so} = \sqrt{\frac{\sigma_{so}}{\sigma_T}}, \quad (20)$$

are the contribution factors of sugarcane, soil with weed plants and double bounce. Assuming that each term presented in (16) can be weighted by its respective contribution factor, the difference in height estimated by the radar between two different days can be expressed by:

$$\Delta H_T = \Delta H_{sc} K_{sc} - \Delta H_{so} K_{so}. \quad (21)$$

Thus, from (18), (20) and (21), ΔH_{sc} is described as:

$$\Delta H_{sc} = \frac{1}{\sqrt{K_R}} \sqrt{\frac{\sigma_T}{\sigma_R}} (\Delta H_T + \Delta H_{so} K_{so}). \quad (22)$$

Then a new correction factor $K = 1/\sqrt{K_R}$ is defined. It can be estimated by using biometric measurements of height difference, as described in Oré et al. (2020). Finally, the estimated growth between two different acquisition times of a sugarcane crop ΔH_{sc-est} based on the estimated model for K and DInSAR data can be described as follows:

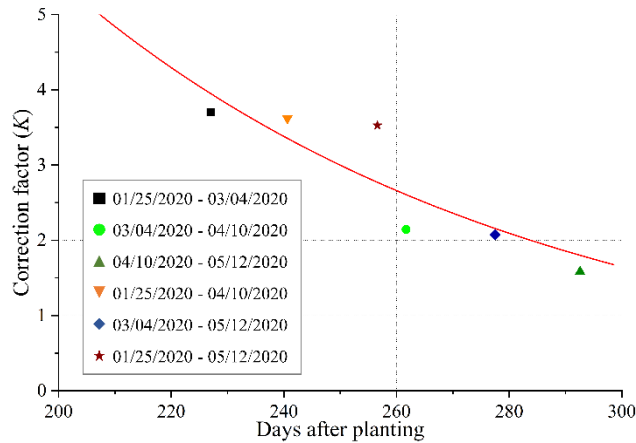
$$\Delta H_{sc-est} = K \sqrt{\frac{\sigma_T}{\sigma_R}} (\Delta H_T + H_{so} K_{so}). \quad (23)$$

5.3.2. RESULTS IN THE EXPERIMENTAL AREA

For the development of this methodology, SAR images based on the P band corresponding to the experimental area was used. The correction factor K was estimated to consider the contribution of soil with weed plants and others in the interferograms. The experimentally calculated correction factor values K_m and the

ranges of campaigns that were considered for these calculations are shown in Figure 10.

Figure 10 – Values calculated for estimating the correction factor K as a function of days after planting.



Source: The authors.

The points shown in Figure 10 belong to data from 4 campaigns between 25 January and 12 May 2020. The campaign on 19 December 2019 was not considered due to the unavailability of the P band for the circular flight. An estimated curve for K is also shown in Figure 10, which is a function of the phenological stage of sugarcane. The equation for the estimated correction factor K is represented as follows:

$$K(d) = 60.87e^{-0.01198d}, \quad (24)$$

where d represents the average number of days after planting, calculated over each data collection interval. An exponential function was chosen due to the smooth decrease that it presents within the range of worked values of d .

Table 5 presents the representative sugarcane growth values of the experimental area between two dates by biometric measurements and estimated by the proposed methodology based on DInSAR data, considering the estimated correction factor K . The RMSE obtained is 7.4 cm.

Table 5 – Comparison between sugarcane growth calculated by biometric measurements and estimated by the proposed methodology based on DInSAR data.

Data collection interval	d	Growth crop (biometric measurements)	Growth crop (SAR data)
25 January 2020 – 04 March 2020	227	53 cm	57 cm
04 March 2020 – 10 April 2020	263	39 cm	45 cm
10 April 2020 – 12 May 2020	294	05 cm	05 cm
25 January 2020 – 10 April 2020	242	92 cm	83 cm
04 March 2020 – 12 May 2020	279	44 cm	43 cm
25 January 2020 – 12 May 2020	258	97 cm	83 cm

Source: The authors.

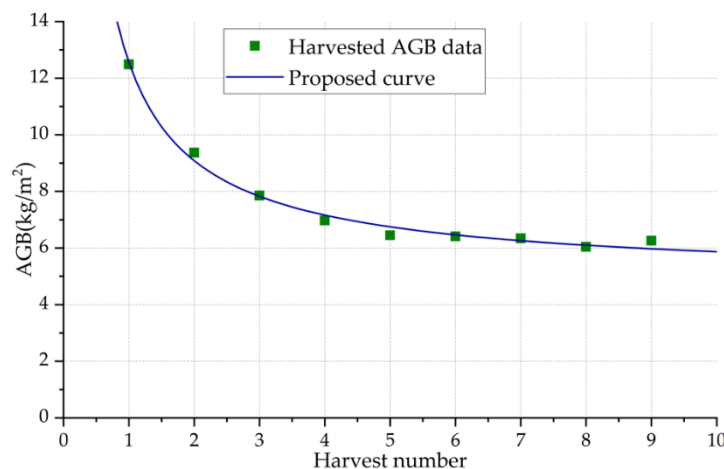
5.4. HARVESTING DATE AND PRODUCTIVITY ESTIMATION

5.4.1. AGB CURVE ADJUSTMENT

From the estimated AGB in the experimental area it is possible to obtain a proposed AGB curve. Because the sugarcane types planted in the experimental area and the test site are different, it is necessary to scale this AGB curve.

The sugarcane type planted in the test site has a life cycle of 18 months, while the life cycle in the experimental area is 12 months, so the AGB curve needs to be scaled in time. In addition, unlike the experimental area, the test site presents crops from different harvest seasons, which directly influences the final productivity. For this reason, historical data of the harvested AGB also need to be considered to scale the AGB curve in amplitude. Historical data about the sugarcane test site areas over the last 10 years provided by farm supervisors is plotted in Figure 11.

Figure 11 – Harvested AGB and a proposed fitting curve.



Source: The authors.

Since productivity decreased exponentially over the seasons, as can be seen in Figure 11, an exponential function can be used to model the productivity of the test site. The curve $c(s)$ is defined as:

$$c(s) = 7.776s^{-0.8545} + 4.784, \quad (25)$$

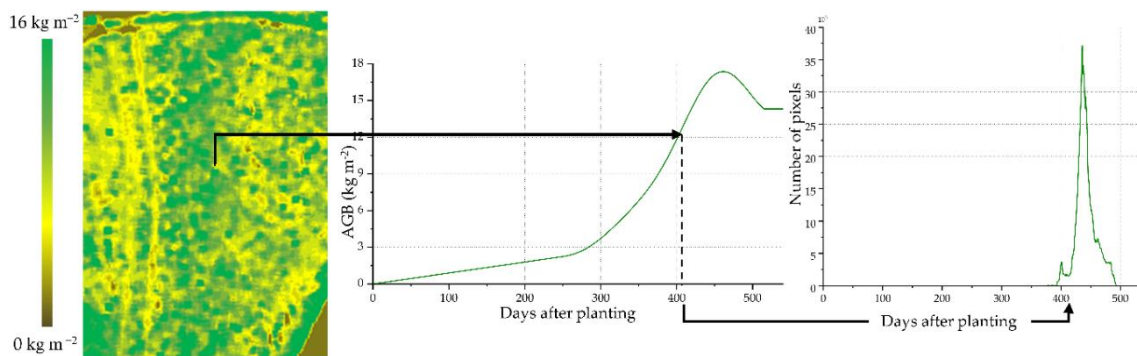
where s is the harvest season. This is used to scale the amplitude of the AGB curve from the experimental area and adapt it to the areas of the test site.

Next, an estimated AGB map of an area of the test site and the corresponding adjusted AGB curve, which varies according to the harvest season, are considered as examples to describe the prediction methods.

5.4.2. HARVESTING DATE PREDICTION

The estimated AGB map is analyzed to obtain a histogram of days according to the corresponding AGB curve. This procedure is carried out by taking the AGB value of each pixel, calculating the corresponding day after planting using the AGB curve, and storing the information in a histogram. This procedure, illustrated in Figure 12, is performed pixel-by-pixel until a final histogram is obtained. The day after planting of the analyzed area is calculated as the day corresponding to the maximum histogram value (Oré et al., 2022).

Figure 12 – Example of how a histogram is estimated. Left: AGB map. Center: AGB curve. Right: Histogram.



Source: The authors.

5.4.3. PRODUCTIVITY PREDICTION

From the estimated AGB map and the corresponding AGB curve, a predicted AGB map is obtained through a pixel-by-pixel procedure. In this procedure, the pixel AGB value of the estimated AGB map is associated with their corresponding day after planting according to the AGB curve. Then, a time interval is added to the obtained day after planting to calculate the predicted pixel AGB value. The time

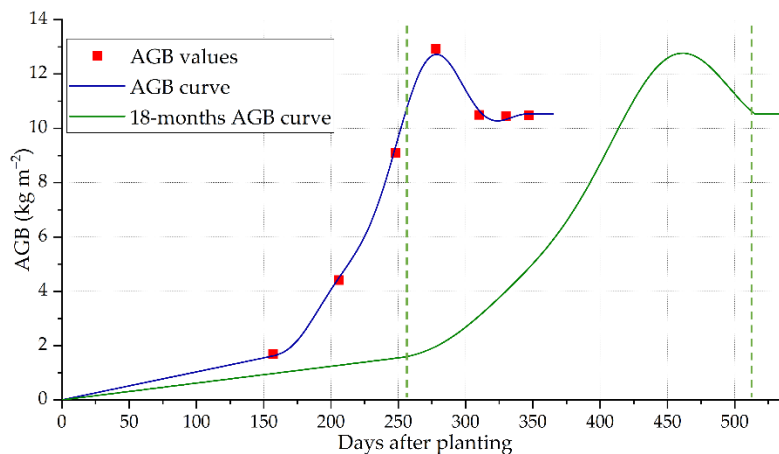
interval considered can be the days remaining for the predicted harvest or real harvesting date. The predicted productivity corresponding to the analyzed area is obtained as the average value of the predicted AGB map (Oré et al., 2022).

5.4.4. RESULTS IN THE TEST SITE

5.4.4.1. AGB CURVE ADJUSTMENT

Figure 13 shows the estimated AGB obtained in the experimental area (red) and the corresponding 12-month sugarcane AGB curve (blue). Due to the difference between the sugarcane type in the experimental area and test site, the red dots in Figure 13, corresponding to the experimental area, were scaled over time considering the change from 12 months to 18 months. Based on this scale, a proposed 18-month sugarcane AGB curve, $ac_g(d)$, for the test site (green) was obtained.

Figure 13 – AGB curve based on the AGB values of the experimental area and the 18-month sugarcane AGB curve. The dotted lines indicate the limit of the piecewise-defined function.



Source: The authors.

In this time scaling, the amplitude of the AGB curve remained constant. The 18-month sugarcane AGB curve $ac_g(d)$ could be described as follows:

$$ac_g(d) = \begin{cases} 0.00928d, & d < 255 \\ ac_f(d), & d \geq 255 \text{ \& } d < 515 \\ 10.53, & d \geq 515, \end{cases} \quad (26)$$

where $ac_f(d)$ is a Fourier series with eight elements expressed as:

$$ac_f(d) = 4.63 + 5.97 \cos(wd + 2.88) + 1.96 \cos(2wd - 0.51) + 0.06 \cos(3wd + 2.37) \\ + 0.74 \cos(4wd + 2.11) + 0.65 \cos(5wd - 1.28) + 0.49 \cos(6wd + 1.60) \\ + 0.32 \cos(7wd - 1.80) + 0.23 \cos(8wd + 1.08), \quad (27)$$

with $w = 0.0064$ constant and d the number of days after planting.

In order to obtain the final 18-month sugarcane model, an amplitude scaling procedure was performed using (25). Function $ac_g(d)$ is scaled to consider the harvest season of the analyzed sugarcane crop. The final 18-month sugarcane AGB curve $ac(d, s)$ depends on the days after planting and the harvest season:

$$ac(d, s) = \frac{1}{c_N} ac_g(d)c(s), \quad (28)$$

where $c_N = 10.53$ is the normalization factor and s is the harvest season.

5.4.4.2. HARVESTING DATE PREDICTION

To predict the harvesting date of each area, histograms were obtained using the $ac(d, 1)$, $ac(d, 3)$, $ac(d, 4)$, and $ac(d, 9)$ functions and the estimated AGB maps of areas 2, 4, 6, and 7 from 9 April and 16 July 2020, and applying the method described in Section 5.4.2.

The estimated days after planting for areas 2, 4, 6, and 7 are, respectively, 433, 455, 465, and 454. The predicted date for optimal harvesting is calculated by subtracting those values from 540 days. The results (107, 85, 75, and 86 days) correspond to the predicted harvesting dates of 25 July 2020, for area 2, 3 July 2020, for area 4, 30 September 2020, for area 6 and 11 October 2020, for area 7. According to their experience and monitoring of the areas, the managers of the test site chose the harvesting dates aiming at the highest productivity and sugarcane quality. The chosen dates, which are considered as reference, were 15 July 2020 for areas 2 and 4, and 7 October 2020 for areas 6 and 7. Finally, the average error between the predicted and the chosen dates is 8 days.

5.4.4.3. PRODUCTIVITY PREDICTION

The harvest season of each area, $ac(d, 1)$ and $ac(d, 4)$ and the estimated AGB maps, are used to generate the predicted AGB maps corresponding to the real harvesting date for areas 2 and 4, respectively. The time interval is 97 days (9 April to 15 July 2020). Similarly, $ac(d, 9)$ and $ac(d, 3)$ are used to generate the predicted AGB maps of areas 6 and 7, respectively, using the corresponding time interval of 82 days (16 July to 7 October 2020).

Table 6 shows the predicted AGB based on the predicted AGB maps for the test site areas 2, 4, 6, and 7, and the harvested AGB. The average error obtained with the methodology for productivity prediction is 10.7%.

Table 6 – Harvested and predicted AGB on test site areas 2, 4, 6, and 7.

Area	Harvested AGB (kg m ⁻²)	Predicted AGB (kg m ⁻²)	Harvest Season
Area 2	14.42	15.23	1st
Area 4	7.07	7.99	4th
Area 6	5.36	6.01	9th
Area 7	9.77	10.97	3rd

Source: The authors.

6. FUTURE WORKS

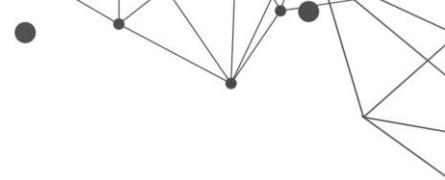
The drone-borne SAR system offers innumerable advantages due to its ability to work simultaneously in the 3 bands, offering high resolution SAR images and a great flexibility to carry out different flight paths.

A research project to be carried out shortly is the detection of leaf-cutting ant nests in industrial forests. Ant nests are underground structures made up of chambers and tunnels found in eucalyptus and pine forests. The presence of ant nests in industrial forests causes a significant drop in pulp productivity. It is possible to take advantage of the characteristics of the drone-borne SAR system to perform tomographic processing, which can be obtained from working with low frequency bands and more challenging flight paths, such as helical flight. Tomographic information, together with deep learning techniques, have great potential for ant nest detection.

7. CONCLUSIONS

In this work efficient methodologies to estimate biometric parameters in sugarcane crops such as AGB and growth have been presented. In addition, a methodology for prediction harvesting date and productivity has also been developed. For this, biometric data and radar data were obtained in a sugarcane crop for 6 months through a drone-borne SAR system.

In the case of AGB, an estimation model was developed for each band, obtaining an RMSE value of 1.94 kg m⁻², 2.11 kg m⁻² and 3.46 kg m⁻² for the L, P and C bands, respectively. It is concluded that the L band is the most adequate to estimate the AGB using only one frequency band, while the C band presents the worst results, mainly for high values of AGB. The advantage of the weighted band AGB model lies in the ability to take advantage of the optimal performance of each model of a band in different ranges of AGB values.



In the case of the growth estimation, the methodology used based on DInSAR data obtained an RMSE of 7.4 cm. In addition, it is possible to notice that as the interval between visits is longer, the error increases. The campaigns used to develop the methodology correspond to dates between 202 and 310 days after planting the monitored sugarcane. It is necessary to follow the phenological development of the culture as much as possible, making data collection campaigns with shorter visit intervals to obtain a more robust methodology.

Regarding harvesting date and productivity prediction, the methodology was based only on the results obtained in the experimental area, without considering meteorological conditions and other external factors. The methodology was tested only in four regions of the test site, obtaining an average error of 10.7% for the productivity prediction and an error of 8 days for the harvesting date prediction. Both the culture of the experimental area and the regions of the test site are contemporary, that is, they developed in almost the same space of time and under similar climatic conditions. In this case, although the results are promising, it is still necessary to develop a methodology that considers the external factors that can condition the prediction. In addition, it is necessary to test the methodology in more regions to obtain a better estimate of the error.

ACKNOWLEDGMENTS

This research was funded by government agencies CAPES, CNPq under Project No 312714/2019-2, and the São Paulo Research Foundation (FAPESP), under Projects PITE 2017/19416-3 and PIPE 2018/00601-8.

REFERENCES

Engelbrecht, J., Kemp, J., & Inggs, M. (2013, July 21–26). The phenology of an agricultural region as expressed by polarimetric decomposition and vegetation indices. IGARSS, Melbourne, VIC, Australia. <https://doi.org/10.1109/IGARSS.2013.6723543>.

Hosseini, M., McNairn, H., Mitchell, S., Davidson, A., & Robertson, L. D. (2018, July 22–27). Combination of optical and SAR sensors for monitoring biomass over corn fields. IGARSS, Valencia, Spain. <https://doi.org/10.1109/IGARSS.2018.8518998>.

Wiseman, G., McNairn, H., Homayouni, S., & Shang, J. (2014). RADARSAT-2 polarimetric SAR response to crop biomass for agricultural production monitoring. *IEEE Journal of Selected Topics in Applied Earth Observations and*

Remote Sensing, 7(11), 4461–4471. <https://doi.org/10.1109/JSTARS.2014.2322311>.

Gama, F., Santos, J., & Mura, J. (2010). Eucalyptus biomass and volume estimation using interferometric and polarimetric SAR data. *Remote Sensing*, 2(4), 939–956. <https://doi.org/10.3390/rs2040939>.

Rossi, C., & Erten, E. (2015). Paddy-rice monitoring using TanDEM-X. *IEEE Transactions on Geoscience and Remote Sensing*, 53(2), 900–910. <https://doi.org/10.1109/TGRS.2014.2330377>.

Wang, H., Magagi, R., Goita, K. (2016). Polarimetric decomposition for monitoring crop growth status. *IEEE Geoscience and Remote Sensing Letters*, 13(6), 870–874. <https://doi.org/10.1109/LGRS.2016.2551377>.

Erten, E., Lopez-Sanchez, J., Yuzugullu, O., & Hajnsek, I. (2016). Retrieval of agricultural crop height from space: A comparison of SAR techniques. *Remote Sensing of Environment*, 187, 130–144. <https://doi.org/10.1016/j.rse.2016.10.007>.

Frey, O., Werner, C., & Coscione, R. (2019, July 28 – August 2). Car-borne and UAV-borne mobile mapping of surface displacements with a compact repeat-pass interferometric SAR system at L-band. *IGARSS, Yokohama, Japan*. <https://doi.org/10.1109/IGARSS.2019.8897827>.

Molijn, R., Iannini, L., Rocha, J., & Hanssen, R. (2019). Sugarcane productivity mapping through C-band and L-band SAR and optical satellite imagery. *Remote Sensing*, 11(9), 1–28. <https://doi.org/10.3390/rs11091109>.

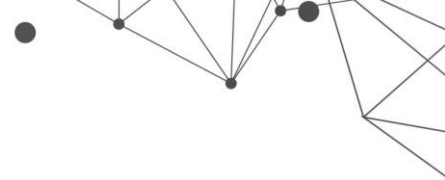
Baghdadi, N., Todoroff, P., & Zribi, M. (2011, July 24–29). Multitemporal observations of sugarcane by TerraSAR-X sensor. *IEEE International Geoscience and Remote Sensing Symposium, Vancouver, BC, Canada*. <https://doi.org/10.1109/IGARSS.2011.6049328>.

Chen, J., Li, H., & Han, Y. (2016, July 18–20). Potential of RADARSAT-2 data on identifying sugarcane lodging caused by typhoon. *Agro-Geoinformatics, Tianjin, China*. <https://doi.org/10.1109/Agro-Geoinformatics.2016.7577665>.

Li, H., Yuan, X., Han, Y., Chen, J., & Chen, X. (2019, August 5–6). Monitoring of sugarcane crop based on time series of Sentinel-1 data. *BIGSAR DATA, Beijing, China*. <https://doi.org/10.1109/BIGSAR DATA.2019.8858450>.

Stasolla, M., & Neyt, X. (2019, July 28 – August 2). Applying Sentinel-1 time series analysis to sugarcane harvest detection. *IGARSS, Yokohama, Japan*. <https://doi.org/10.1109/IGARSS.2019.8898706>.

Oliveira, G. (2015). Produtividade de biomassa de cana-de-açúcar em função dos índices de vegetação utilizando técnicas de sensoriamento remoto. Master's thesis, UNESP, Brazil. UNESP Institutional Repository. <https://repositorio.unesp.br/handle/11449/136733>.



Wang, J., Xiao, X., Liu, L., Qin, Y., Steiner, J., & Dong, J. (2020). Mapping sugarcane plantation dynamics in Guangxi, China, by time series Sentinel-1, Sentinel-2 and Landsat images. *Remote Sensing of Environment*, 247. <https://doi.org/10.1016/j.rse.2020.111951>.

Sambatti, J., & Luebeck, D. (2015). Sensing change underneath vegetation. GIM International. <https://www.gim-international.com/content/article/sensing-change-underneath-vegetation>.

Ludeno, G., Catapano, I., Renga, A., Rodi, A., Fasano, G., & Soldovieri, F. (2018). Assessment of a micro-UAV system for microwave tomography radar imaging. *Remote Sensing of Environment*, 212, 90–102. <https://doi.org/10.1016/j.rse.2018.04.040>.

Woodhouse, I. (2017). *Introduction to Microwave Remote Sensing* (1st edition). CRC Press. <https://doi.org/10.1201/9781315272573>.

Papathanassiou, K., Reigber, A., Sheiber, R., Horn, R., Moreira, A., & Cloude, S. (1998, July 6–10). Airborne polarimetric SAR interferometry. IGARSS, Seattle, WA, USA. <https://doi.org/10.1109/IGARSS.1998.703689>.

Moreira, L., Castro, F., Goes, J., Bins, L., Teruel, B., Fracarolli, J., Castro, V., Alcantara, M., Oré, G., Luebeck, D., Oliveira, L., Gabrielli, L., & Hernandez-Figueroa, H. (2019, April 22–26). A drone-borne multiband DInSAR: Results and applications. RadarConf, Boston, MA, USA. <https://doi.org/10.1109/RADAR.2019.8835653>.

Magro, F., Takao, G., Camargo, P., & Takamatsu, S. (2011). Biometria em cana-de-açúcar. USP, Brazil, Escola Superior de Agricultura Luiz de Queiroz. <https://edisciplinas.usp.br/mod/resource/view.php?id=3109627>.

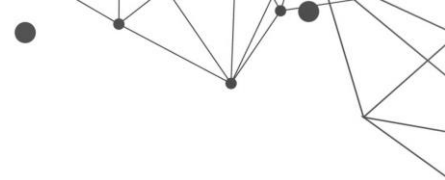
Molijn, R., Ianini, L., Rocha, J., & Hanssen, R. (2018). Ground reference data for sugarcane biomass estimation in Sao Paulo state, Brazil. *Scientific Data*, 5, 1–18. <https://doi.org/10.1038/sdata.2018.150>.

Moreira, A., Prats-Iraola, P., Younis, M., Krieger, G., Hajnsek, I., & Papathanassiou, K. (2013). A tutorial on synthetic aperture radar. *IEEE Geoscience and Remote Sensing Magazine*, 1(1), 6–43. <https://doi.org/10.1109/MGRS.2013.2248301>.

Castro, F. (2018). Antenas para radar de abertura sintética embarcado em drone. Master's thesis, University of Campinas, São Paulo, Brazil. Acervus UNICAMP. <https://doi.org/10.47749/T/UNICAMP.2018.1126375>.

Gray, A., Vachon, P., Livingstone, C., & Lukowski, T. (1990). Synthetic aperture radar calibration using reference reflectors. *IEEE Transactions on Geoscience and Remote Sensing*, 28(3), 374–383. <https://doi.org/10.1109/36.54363>.

Oré, G., Alcantara, M., Goes, J., Teruel, B., Oliveira, L., Yepes, J., Castro, V., Bins, L., Castro, F., Luebeck, D., Moreira, L., Cintra, R., Gabrielli, L., & Hernandez-Figueroa, H. (2022). Predicting Sugarcane Harvest Date and Productivity with a Drone-Borne Tri-Band SAR. *Remote Sensing*, 14(7), 1–24. <https://doi.org/10.3390/rs14071734>.



Nizalapur, V., Jha, C., & Madugundu, R. (2010). Estimation of above ground biomass in Indian tropical forested area using multi-frequency DLR-EASR data. *International Journal of Geomatics and Geosciences*, 1, 167 – 178.

Terr, D. (2020). Weighted mean. From MathWorld – a Wolfram web resource. <https://mathworld.wolfram.com/WeightedMean.html>.

Oré, G., Alcântara, M., Góes, J., Oliveira, L., Yepes, J., Teruel, B., Castro, V., Bins, L., Castro, F., Luebeck, D., Moreira, L., Gabrielli, L., & Hernandez-Figueroa, H. (2020). Crop Growth Monitoring with Drone-Borne DInSAR. *Remote Sensing*, 12(4), 705 1–18. <https://doi.org/10.3390/rs12040615>.

Lin, H., Chen, J., Pei, Z., Zhang, S., & Hu, X. (2009). Monitoring sugarcane growth using ENVISAT ASAR data. *IEEE Transactions on Geoscience and Remote Sensing*, 47(8), 2572–2580. <https://doi.org/10.1109/TGRS.2009.2015769>.

APPLICATION OF MULTICOMMODITY FLOW OPTIMIZATION FOR PROPAGATION LOSS MODEL FOR INDOOR ENVIRONMENTS

DOI: 10.51859/amplla.sst631.1122-10

Alexandre H. S. de Oliveira¹
Gustavo P. N. de Queiroz¹
Maria G. Rocha da Silva²
Humberto D. de Andrade³
Glauco Fontgalland¹

¹ Federal University of Campina Grande – UFCG, Applied Microwave and Electromagnetics Laboratory.

² Federal University of Campina Grande – UFCG, Petroleum Exploration Research Laboratory.

³ Federal Rural University of Semi-arid – UFERSA, Engineering Center.

ABSTRACT

Among a wide range of applications, the development of systems capable of harnessing the energy present in the environment itself is increasingly used. One of the technologies that have gained more and more notoriety in energy harvesting is the Simultaneous Wireless Information and Power Transfer (SWIPT), mainly in industrial applications focused on the sensing of the industrial environment. As SWIPT systems need to collect energy from the radio frequency signal for both rectification and energy harvesting as well as for information decoding, the use of models that can predict the received signal level is a critical factor, to analyze and ensure the reliability and applicability of the systems, especially in indoor industrial environments, commonly referred to by the English term indoor environment. Thus, in this research, we developed a propagation loss model based on multicommodity flow (MCF) modeling, an optimization tool capable of presenting a good response to optimization problems and a satisfactory computational performance due to its ability to decompose complex systems as a sum of simpler problems. The proposed MCF model presented a satisfactory performance for the prediction of propagation losses in indoor environments compared to other models commonly used in this type of situation. Frequencies of 915 MHz, 2.4 GHz; 3 GHz, and 3.5 GHz were analyzed for transmission powers of 0, 1, 10, 20, and 30 dBm.

Key words: Multicommodity flow. Internet of things. Propagation models. Simultaneous transmission of information and energy.

1. INTRODUCTION

In last years, concepts like the Internet of Things (IoT) and Embedded Systems become very common in industrial and commercial application scenarios. A preponderant feature of these applications is the heterogeneous applications with a diverse propagation environment (Da Silveira Farias & Borenstein, 2017; Park et al., 2016).

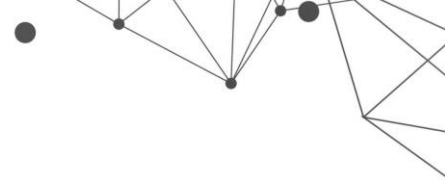
Industrial environments can present very specific characteristics and demands. In this situation the use of usual wireless channel propagation models cannot describe enough the application conditions, thus they are not able to apply directly to evaluate or describe the wireless communication condition, requiring a more detailed study of each situation or an adaptation of existents channel models (Silva & Hancke, 2016).

This occurs because the wireless channel characteristics of each application scenario can be differed from others considerably, even in the same environment. For example, throughout the workday in an industrial environment, the conditions can be changed by a specific operation, the manufacturing of a product may require one step on specific equipment or not (Silva & Hancke, 2016).

In this way, the site survey in the industrial environment can be a very important step to maximize the understanding of the wireless communications scenarios. Therefore, increasing the communication reliability by adjusting parameters for a better performance of the communication systems. For example, choosing the proper signal modulation for the signal-to-noise (SNR) presented in the environment, and choosing adequate antennas analyzing the right gain, bandwidth, polarization, and size, among other technical features (Zaidi et al., 2018).

The development of more accurate propagation models focused on these applications can generate greater reliability in the operation of this type of communication system (Kang et al., 2020). However, accurate systems that have a high computational demand may not meet the requirements that make their implementation feasible (Tavares et al., 2020).

Multicommodity flow problems are NP-hard numerical problems that have the objective of minimizing the transport costs of commodities between a source node and a destination node along the arcs of a network. One of the advantages of



using MCF modeling is that depending on the nature of the problem it can be decomposed as the sum of single-commodity problems, reducing computational complexity in many applications. This kind of approach is widely used in resource optimization problems, especially in the areas of logistics and operations research (Da Silveira Farias & Borenstein, 2017; Saritha & Vinod Chandra, 2019; Y. Zhang et al., 2020).

In this chapter, it is presented the MCF-based model, which is characterized as a semi-deterministic propagation loss model for the wireless communication channel for SWIPT IoT applications for indoor industrial environments. It is shown how the MCF-based model applied to propagation losses can circumvent situations under analysis in which these models usually present inferior performance for indoor environments.

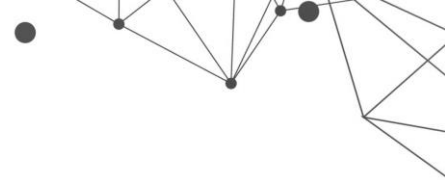
The measurements are made for frequencies 915 MHz, 2.4 GHz, 3 GHz, and 3.5 GHz, representing some of the mostly used Industrial, Scientific, and Medical (ISM) frequencies for mobile network applications. The experiments were made using various transmission power such as 0, 1, 10, 20, and 30 dBm.

2. PROPAGATION MODELS

In short, propagation in the wireless communication channel can be subject to several factors such as reflections, diffractions, refractions, multipath scattering, and shadowing. These phenomena directly affect how the transmitted signal will reach the receiver. Propagation models or communication channel models have emerged to predict signal levels more accurately between the transmitter and the receiver.

Reflection occurs when radio waves propagating in one medium collide with another medium with different electromagnetic properties. Radio waves can be absorbed by the reflecting medium, resulting in a reflected wave that is attenuated. The amplitude and phase of the reflected wave are strongly related to the intrinsic impedance of the medium, the angle of incidence, and the electric field polarization (Garg, 2007)

Diffraction is a phenomenon whereby propagating waves undergo deflections triggered by obstacles in their propagation path. Diffraction results from the propagation of waves in a shaded region caused by obstructions such as walls,



buildings, mountains, and so on (Farooq & Zhu, 2019; Kar et al., 2016). Scattering occurs when a radio signal hits a rough surface or an object with a size much smaller or on the order of the wavelength of the signal. This causes the signal energy to scatter in all directions. Scattering can be seen in the receiver as another source of radio waves. Typical scattering objects are furniture, lampposts, street signs, and foliage, this type of effect can be quite present in indoor propagation environments (Farooq & Zhu, 2019).

2.1. PROPAGATION MODELS FEATURES

For the design, simulation, and planning of wireless systems, models for the propagation channels are needed (Amorim et al., 2017). There are two main applications for channel models:

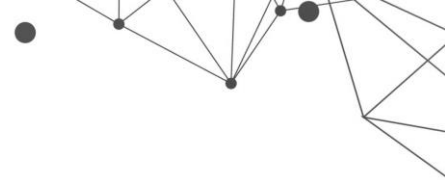
- Parametric design of wireless communication systems.
- Geometric or geographic models are developed considering the specific characteristics of a given location.

In general, communication channel models seek to determine the behavior of signal propagation, from parameters that influence the behavior of the transmitted signals. More complex channel models, in general, use a larger number of parameters, such as antenna height, carrier frequency, the presence of obstacles, the distance between transmitter and receiver, and weather, among several other factors (Joung et al., 2017).

However, a larger number of parameters analyzed increases the complexity of the channel model, which requires deep knowledge about the location where the system will be installed or even requires a higher computational demand to generate a result. Furthermore, they can be easily implemented by system designers for testing purposes (Song et al., 2018). Communication channel models can be divided into three main types:

1. Channel impulse response models.
2. Deterministic channel models.
3. Stochastic channel models.

In stored impulse response models, the main advantage is that the impulse responses are realistic. Furthermore, system simulations use the stored impulse responses that are reproducible because the data remains available and can be reused indefinitely, even for simulations of different systems (Silva & Hancke, 2016).



This is an important distinction from field tests of whole systems, where there can be no guarantee that the impulse response remains constant over time. The main disadvantages of using stored impulse responses are two (Maravić et al., 2003):

- The large effort in acquiring and storing the data.
- The fact that the data characterizes a certain area of a propagation environment.

In turn, deterministic models use the geographic and morphological information from a database for a deterministic solution of Maxwell's equations or some approximation of it (Shi et al., 2018). The main advantage is that computer simulations for the deterministic models are easier to perform than measurement campaigns. In addition, certain types of computational methods allow the effects of different propagation mechanisms to be separately treated (Amorim et al., 2017). The disadvantages of deterministic channel models compared to stored impulse responses are:

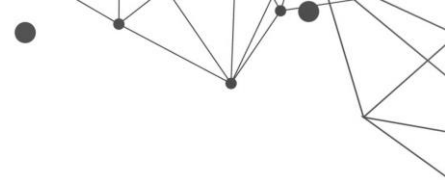
- the large computational effort.
- less accurate results, due to inaccuracies in the underlying databases and the approximate nature of the numerical computation methods.

Stochastic channel models are characterized by the probability density function (PDF) of the channel impulse response. These methods do not aim to predict the impulse response at a specific location (Shi et al., 2018).

In general, stochastic models are used more for system design and comparison, while site-specific models are preferable for network planning and system deployment (Kim et al., 2018). Furthermore, deterministic, and stochastic approaches can be combined to increase the efficiency of a model: for example, large-scale average power can be obtained from deterministic models, while variations within an average area are stochastically modeled.

2.2. PROPAGATION CHANNEL MODEL MAIN TYPES

There are different types of propagation models, which can be classified according to their characteristics and types of applications. Concerning to bandwidth, the propagation models can be divided between narrowband models and wideband models, as they consider the bandwidth of the transmitted signals of the communication channels (El Chall et al., 2019). Examples of narrowband models



are small-scale and large-scale fading models. For a non-frequency-selective narrowband channel, the impulse response can be represented by the expression $h(t, \tau) = \alpha(t)\delta(\tau)$.

The variations in signal strength over a small area are usually characterized by a random process, with an autocorrelation function that is determined by the Doppler spectrum. However, for the channel with Rayleigh fading, the complex gain $\alpha(t)$ is characterized by a complex Gaussian process. The complex amplitude is modeled as a zero-averaged and circularly symmetric complex Gaussian stochastic variable (Jo et al., 2020).

Another category of narrowband propagation models is Path Loss Models, which consider the received signal strength in terms of both small-scale and large-scale fading. There are several Path Loss models, ranging from deterministic models to empirical models developed to address more specific situations (Bertoldo et al., 2019).

The path loss models, or channel propagation models, are very meaningful in planning any wireless communication system. This application starts with outdoor communication systems for long or medium distances. One of the simplest and most initial models to consider is the free-space propagation model, which considers a direct line of sight, represented by the Friis free space propagation equation (Aldhaibani et al., 2020) as can be seen in Equation 1,

$$P_r = P_t \left(\frac{\lambda}{4\pi d} \right)^2 G_t G_r \quad (1)$$

Where, P_r is the received power, P_t is the transmitted power, λ is the wavelength, d is the distance between the transmitter and the receiver, G_t is the gain of the transmitting antenna, and G_r is the gain of the receiving antenna (Aldhaibani et al., 2020).

Among the propagation loss prediction models one of the most widely used is the Okumura-Hata model. This model has an empirical basis developed from measurements in high-density urban environments in Japan. Due to its character of using an empirical database, the Okumura-Hata model presents different equations for urban, suburban, and rural regions, where the carrier wave frequency predicted for this model varies between 150 MHz and 2.2 GHz, as exemplified in Equation 2 (Hoomod et al., 2018),

$$PL = 69,55 + 26,16 \log f_c + (44,9 - 6,55 \log h_b) \log d - 13,82 \log h_b - a(h_m) \quad (2)$$

$a(h_m)$ is the correction factor for the height of mobile device antennas relative to the base, this correction factor can be represented as shown in Equations 3 to 7. For areas of greater urban densification,

$$a(h_m) = 8,29[\log(1,54h_m)]^2 - 11 \quad f_c \leq 200 \text{ MHz} \quad (3)$$

$$a(h_m) = 3,2[\log(11,7h_m)]^2 - 4,97 \quad f_c \geq 200 \text{ MHz} \quad (4)$$

for smaller areas and therefore less urban densification,

$$a(h_m) = [1,1 \log(f_c) - 0,7]h_m - [1,56 \log(f_c) - 0,8] \quad (5)$$

suburban regions can be represented by,

$$L_s = L_{urbano} - 2 \left[\left(\log \left(\frac{f_c}{28} \right)^2 \right) - 5,4 \right] \quad (6)$$

and rural areas,

$$L_r = L_{urbano} - 4,78(\log f_c)^2 + 18,33 \log f_c - 40,94, \quad (7)$$

where, f_c , represents the carrier wave frequency in MHz. The distance between the base station and the device is given by d , which can vary between 1 and 20 km. h_b , represents the height of the base station (BS) antenna in meters, which can vary between 30 and 200 m. h_m , represents the height of the mobile device between 1 and 10 m (Silva & Hancke, 2016).

Another model that is an extension of the Okamura-Hata model is the COST-231 Hata model, which was developed based on empirical corrections to the initial model. It can be used for frequencies up to 2 GHz, the path signal in dB is represented by,

$$PL = 46.3 + 33.9 \log(f) - 13.82 \log(h_b) - a(h_r) + [44.9 - 6.55 \log(h_b)] \log(d) + c \quad (8)$$

In the COST-231 Hata, the term c is used to represent the population density, where 0 (zero) for suburban and rural areas and 3 (three) for urban regions. This

model has an extension called COST-231 Walfisch-Ikegami, this model was adapted for frequencies above 2 GHz, considering situations of LoS e NLoS. For LoS conditions the path loss is given by,

$$PL = 42.64 + 26 \log(d) + 20 \log(f) \quad (9)$$

For NLoS conditions the Walfisch-Ikegami model is represented by the summation of three terms, the attenuation in free space (L_0), diffraction from rooftop to street (L_{RTS}), and diffraction loss from multiple obstacles (L_{MSD}). This model is presented in Equations 10 to 13,

$$PL = L_0 + L_{RTS} + L_{MSD} \quad (10)$$

$$L_0 = 32.45 + 20 \log(d) + 20 \log(f) \quad (11)$$

$$L_{RTS} = -16.9 - 10 \log(w) + 10 \log(f) + 20 \log(h_b - h_r) + L_{ori} \quad (12)$$

$$L_{MSD} = L_{BSH} + k_A + k_d \log(d) + k_f \log(f) - 9 \log(s_b) \quad (13)$$

Where L_{BSH} is an empirical correction of propagation between receiver device and base station, k_A , k_d , and k_f are correction factors for population density, distance, and frequency respectively (Hoomod et al., 2018; Shabbir et al., 2011; Simmons et al., 2022).

The Okamura-Hata, COST-231 Hata, and COST-231 Walfish-Ikegami are focused on outdoor applications, mainly for mobile communications. Following its original proposition, it no longer represents many of the situations present in modern communications systems. Just as there are several propagation models focused on different situations for outdoor applications, there are also a plethora of models focused on or that can be applied to indoor applications. Such as the versatile Log-Distance model, ITU-R, and Motley-Keenan (Shabbir et al., 2011).

The Log-distance model is based on experimental results and presents high flexibility in its applications, as it can be used in both indoor and outdoor applications, it is independent of frequency and antenna gain, using distance and power as a basis, as shown in Equation 14,

$$P_r(d) = P_r(d_0) - 10n \log \frac{d}{d_0}, \quad (14)$$

where, $P_r(d)$ is the received power at a given distance d from the transmitting source. $P_r(d_0)$ is the power received at a reference point at a distance d_0 . n is the densification coefficient of the measurement site, which depends on the type of environment and the characteristics in which the communication system will be inserted, such as free space, LoS, and NLoS (J. Zhang et al., 2013).

A model focused on indoor environments is the ITU-R P.1238-1 model, developed by the International Telecommunication Union (ITU). One of its main features is to consider the influence of indoor environments with propagation through multiple floors of a building, as can be seen in Equation 15 (J. Zhang et al., 2013),

$$L = 20 \log f + N \log(d) + L_f(n_f) - 28, \quad (15)$$

where, L_f is a signal penetration factor on floors that depends directly on the value of n_f ; N is the loss coefficient factor concerning distance and is also provided in the description of the standard ITU-R P.1238-1, f is the frequency expressed in MHz usually, but this model foresees its use between 900 MHz and 100 GHz. The indoor environments predicted by the model definition standard consist of residential, commercial, and office environments (ITU, 2017).

The Motley-Keenan model was developed for indoor environments based on the Log-Distance model and was integrated into the COST 231 propagation model suite. Also known as COST-231 Motley-Keenan, this model is optimized mainly for the 1.8, 2.4, and 5.2 GHz frequencies Equation 16 (Kar et al., 2016)

$$L = L_0 + 10n \log(d) + \sum_{\{i=1\}}^I k_{f,i} L_{f,i} + \sum_{\{j=1\}}^J k_{w,i} L_{w,i}, \quad (16)$$

where, L_0 is the propagation loss at 1 m distance from the transmitting source, d is the distance traveled by the signal, n is the propagation coefficient, based on the environments to be traversed, $L_{f,i}$ is the propagation losses through floor i , $k_{f,i}$ is the number of floors traversed, $L_{w,i}$ are the propagation losses through walls j , $k_{w,i}$ is the number of walls crossed (Kar et al., 2016).

2.3. MULTICOMMODITY FLOW OPTIMIZATION IN PROPAGATION MODELS

The MCF problems can be modeled as a network, where a commodity must be transported between a source node and a destination node. These commodities can be modeled as telephone calls in a telecommunications network, and access

requests on a server. Signals containing information and energy, vehicles in a logistics fleet (Jia et al., 2018).

The MCF problems are quite flexible, depending on how you define each commodity. There are three main ways: a commodity can originate at a subset of nodes in the network and be destined to another subset of nodes, or it can originate at a single node and be destined to a subset of the node, or it can originate at a single node and be destined to a single node. Overall, MCF problems are considered NP-Hard, Numerical Problems. In Equations 16 to 19 a generalist way of representing MCF problems is shown (Jia et al., 2018)

$$\min \sum_{k \in K} \sum_{ij \in A} c_{ij}^k q^k x_{ij}^k \quad (16)$$

s. t.,

$$\sum_{ij \in A} x_{ij}^k - \sum_{ji \in A} x_{ji}^k = b_i^k, \quad \forall i \in N, \forall k \in K \quad (17)$$

$$\sum_{ij \in A} q^k x_{ij}^k \leq d_{ij}, \quad \forall ij \in A \quad (18)$$

$$x_{ij}^k \geq 0, \forall ij \in A, \quad \forall k \in K \quad (19)$$

where, A is the set of arcs in the network, $\forall ij \in A, N$ is the set of nodes in the network, $\forall i \in N, K$ is the set of commodities, k is a specific commodity, $\forall k \in K, x$ is representing the decision variable, x_{ij}^k is the fraction of commodity k , carried by arc $ij, \forall k \in K, \forall ij \in A, q^k$ is the total quantity of commodity $k, \forall k \in K, c_{ij}^k$ is represents the cost of ij on the flow of commodity k, d_{ij} is the capacity of the arc ij and b_i^k is the supply of node i of commodity k (Yan et al., 2021).

Equation 16 is the objective function that represents the minimization of the cost per arc to transport a quantity of the commodity through the set of arcs in the network. Equation 17 represents the flow conservation constraint on the arcs between the source(s) and destination(s), Equation 18 denotes the flow values of different commodities and Equation 19 is the non-negativity constraint (Yan et al., 2021).

The more complex the propagation loss prediction model, the more parameters will be taken into consideration and more complex is its representation. The MCF model proposed in this work, instead of representing it this way, it represents MCF model as a form of a set of equations for optimization of the

parameters. Although it seems more complex than other models, its implementation, especially at the algorithm level, can be done more objectively (Arif et al., 2020).

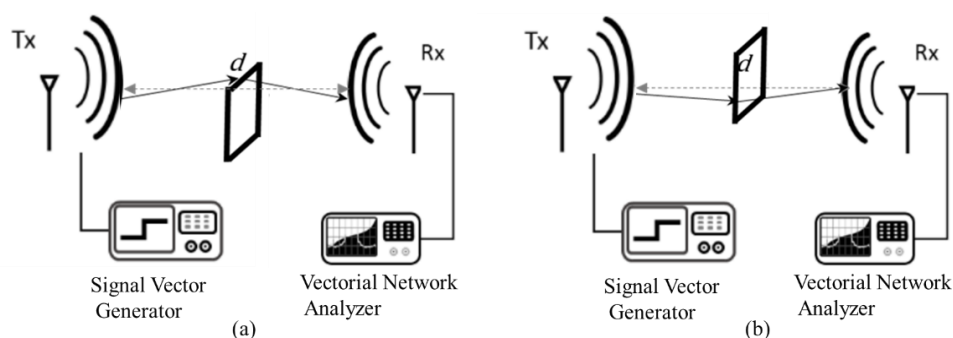
Modeling Equations 16 to 19 as components of a wireless communication channel, with links, carrier wave frequencies, fading, refraction, and diffraction, the presented model could be represented in a way that is closer to the traditional models analyzed (Yan et al., 2021).

3. RESULTS AND DISCUSSION

The site survey consists in analyzing the main characteristics of the environment where the communication system will be installed, for indoor and especially industrial indoor environments this is a critical analysis for the performance of the overall system. Some good practices are established for good parameters measurement in industrial indoor environments, for radio frequency (RF) applications, like measure in a closer possible of everyday operations, analyze the possible movements to interrupt LoS of the system, evaluate the results, and replicate the measurements (Aldhaibani et al., 2020; Shafique et al., 2018).

In some industrial activities the site survey for RF measurements can be very difficult, because the high-risk level of the activity, i.e., in the oil and gas industry, some indoor environments can be dangerous, presenting the risk of creating explosive atmospheres, or with chemical agents that are harmful to health. Thus, for this type of Application, the environments can be simulated in controlled locations such as laboratories or computation simulations. Simulating mainly sources of overlap, reflection, and refraction, knife-edge refraction of the RF signal (Aldhaibani et al., 2020).

Figure 7- measurement structure



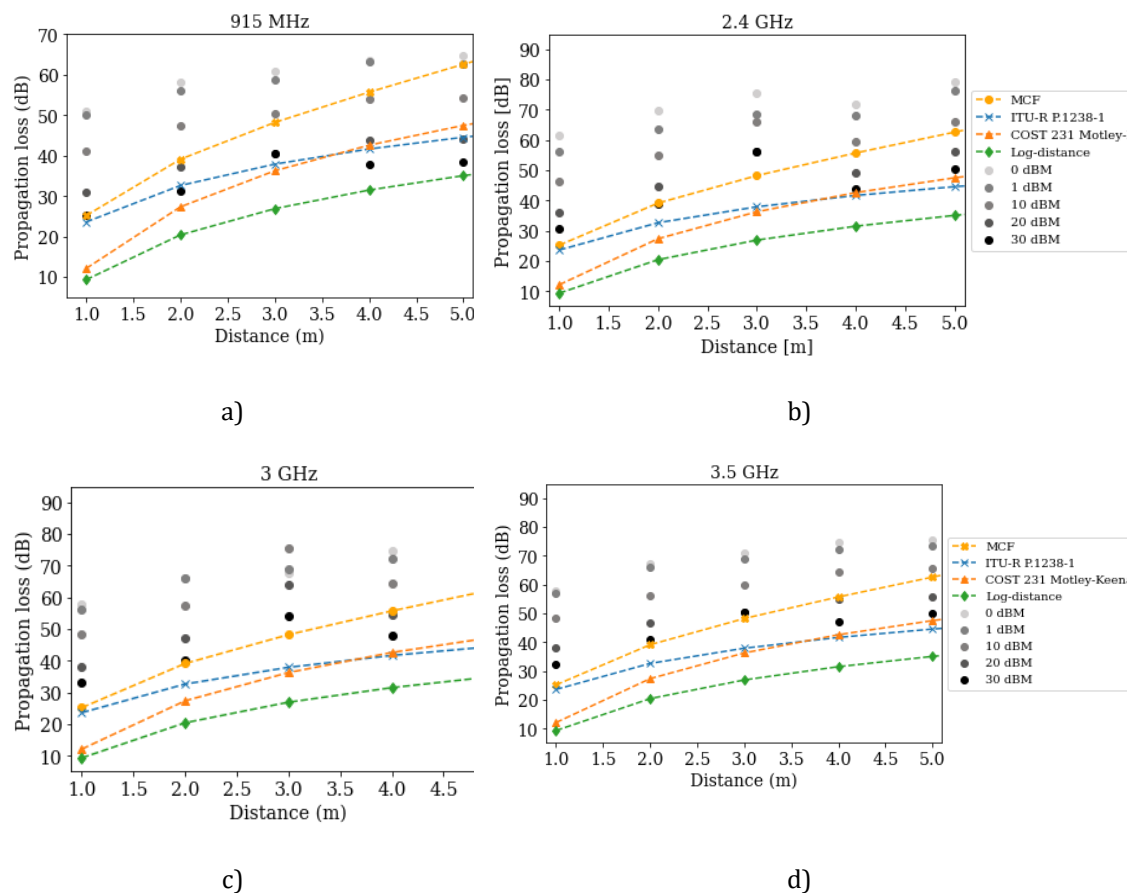
Source: The authors.

In Figure 1 we can see the structure of measurements using the object to simulate the RF signal effects like refraction or knife-edge refraction, shadowing, and NLoS also in the communication system between the transmitter and receiver.

In this setup the signal vector genitor represents the transmitter (Tx) and the vectorial network analyzer (VNA) the receiver (Rx), the object can be put at a distance d between the Tx and Rx . In the example shown in Figure 1a, the object was positioned to cause refraction while knife-edge refraction on the top of the objects is shown in Figure 1b. These cases also consider diffractions on the side of the object, which simulate the movement of cargos between Tx and Rx in an industrial indoor application.

The simulated and measured values were obtained and the comparison with made for in terms of Propagation Loss models for indoor environments. The models used to compare with MCF are the ITU-R P.1238, Motley-Keenan, and Log-distance. The results obtained are presented in Figure 2.

Figure 8 – measurements results



Source: The authors.

As can be seen in Figure 3, the items from (a) to (d) represent, respectively, the frequencies of 915 MHz, 2.4 GHz, 3 GHz, and 3.5 GHz. The proposed MCF Model shows greater proximity with the measured data items, i.e., the error between the predicted values by the models and the effects of measured values, for the MCF model for all analyzed situations, especially for the 915 MHz frequency.

There are several techniques to evaluate the errors between a series of predicted data those measured among them are the Mean Absolute Error (MAE), the Mean Squared Error (MSE), the Root Mean Squared Error (RMSE), and the Mean Squared Logarithmic Error (MSLE). Each of these forms of error analysis has a higher or lower sensitivity regarding the variation of values, as a result, when possible, it is interesting to use more than one form of evaluation. As shown in Equations 20 to 24, respectively, (Daliya et al., 2021).

$$MAE = \frac{1}{n} \sum_{i=1}^n |Y_i - \hat{Y}_i| \quad (20)$$

$$MSE = \frac{1}{n} \sum_{i=1}^n (Y_i - \hat{Y}_i)^2 \quad (21)$$

$$RMSE = \sqrt{\frac{\sum_{i=1}^n (Y_i - \hat{Y}_i)^2}{n}} \quad (22)$$

$$MSLE = \frac{1}{n} \sum_{i=1}^n (\log(Y_i + 1) - \log(\hat{Y}_i + 1))^2, \quad (24)$$

Table 1 - Error metric analysis

Model	Frequency (MHz)	Powe Tx (dBm)	MAE	MSE	RMSE	MSLE
MCF	915	0	23,08	24,11	4,91	0,24
ITU	915	0	33,18	33,20	5,76	0,45
Motley-Keenan	915	0	36,09	36,63	6,05	1,31
Log-Distance	915	0	44,61	44,70	6,69	1,31
MCF	915	1	21,34	22,57	4,75	0,22
ITU	915	1	31,44	31,48	5,61	0,42
Motley-Keenan	915	1	34,35	34,98	5,91	1,26
Log-Distance	915	1	42,87	42,99	6,56	1,26
MCF	915	10	12,70	14,45	3,80	0,12
ITU	915	10	22,80	22,83	4,78	0,26
Motley-Keenan	915	10	25,71	26,46	5,14	0,98
Log-Distance	915	10	34,23	34,35	5,86	0,98
MCF	915	20	6,07	7,41	2,72	0,04
ITU	915	20	12,99	13,05	3,61	0,11
Motley-Keenan	915	20	15,91	17,05	4,13	0,66
Log-Distance	915	20	24,42	24,58	4,96	0,66

Model	Frequency (MHz)	Powe Tx (dBm)	MAE	MSE	RMSE	MSLE
MCF	915	30	6,38	7,66	2,77	0,03
ITU	915	30	7,90	8,28	2,88	0,05
Motley-Keenan	915	30	10,81	12,64	3,55	0,49
Log-Distance	915	30	19,33	19,65	4,43	0,49

Source: The authors.

where, Y_i is the measured value, \hat{Y}_i is the value predicted by the models analyzed and n is the sample size. Table 1 shows the results for error analysis using the techniques of MAE, MSE, RMSE, and MSLE (Daliya et al., 2021).

As can be seen in Table 1, for all power situations applied for the 915 MHz frequency, using different error analysis techniques, the MCF method presented lower errors, so the values predicted by the model are the closest one compared to the values effectively measured. For the other frequencies analyzed the same behavior was maintained.

4. CONCLUSIONS

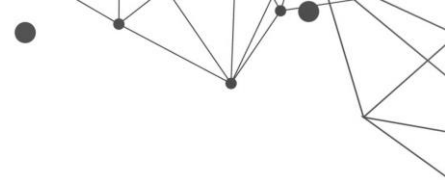
In this chapter, we present the application of multicommodity flow optimization to develop a propagation path loss model based on an industrial indoor environment. This type of problem modeling is not usually used for this kind of application, however, is flexible enough to use in this situation. For future works, we want to develop MCF prediction models for another situation where is will be integrated with machine learning prediction techniques.

ACKNOWLEDGMENT

We thank the National Council for Scientific and Technological Development - CNPq, Brazil, for all its support of this research.

REFERENCES

- Aldhaibani, A. O., Rahman, T. A., & Alwarafy, A. (2020). Radio-propagation measurements and modeling in indoor stairwells at millimeter-wave bands. *Physical Communication*, 38, 100955. <https://doi.org/10.1016/j.phycom.2019.100955>
- Alhassoun, M., & Durgin, G. D. (2019). Spatial Fading in Backscatter Channels: Theory and Models. *2019 16th IEEE Annual Consumer Communications and Networking Conference, CCNC 2019*, 1–6. <https://doi.org/10.1109/CCNC.2019.8651838>



Amorim, R., Nguyen, H., Mogensen, P., Kovács, I. Z., Wigard, J., & Sørensen, T. B. (2017). Radio Channel Modeling for UAV Communication over Cellular Networks. *IEEE Wireless Communications Letters*, 6(4), 514–517. <https://doi.org/10.1109/LWC.2017.2710045>

Arif, A., Wang, Z., Chen, C., & Chen, B. (2020). A Stochastic Multi-Commodity Logistic Model for Disaster Preparation in Distribution Systems. *IEEE Transactions on Smart Grid*, 11(1), 565–576. <https://doi.org/10.1109/TSG.2019.2925620>

Bertoldo, S., Paredes, M., Carosso, L., Allegretti, M., & Savi, P. (2019). Empirical indoor propagation models for LoRa radio link in an office environment. *13th European Conference on Antennas and Propagation, EuCAP 2019, EuCAP*, 1–5.

Da Silveira Farias, E., & Borenstein, D. (2017). Modeling the logistics design of a multi-commodity industry. *Gestao e Producao*, 24(1), 148–160. <https://doi.org/10.1590/0104-530X842-16>

Daliya, V. K., Ramesh, T. K., & Ko, S. B. (2021). An optimized multivariable regression model for predictive analysis of diabetic disease progression. *IEEE Access*, 9, 99768–99780. <https://doi.org/10.1109/ACCESS.2021.3096139>

El Chall, R., Lahoud, S., & El Helou, M. (2019). LoRaWAN network: Radio propagation models and performance evaluation in various environments in Lebanon. *IEEE Internet of Things Journal*, 6(2), 2366–2378. <https://doi.org/10.1109/JIOT.2019.2906838>

Farooq, M. J., & Zhu, Q. (2019). Modeling, Analysis, and Mitigation of Dynamic Botnet Formation in Wireless IoT Networks. *IEEE Transactions on Information Forensics and Security*, 14(9), 2412–2426. <https://doi.org/10.1109/TIFS.2019.2898817>

Garg, V. K. (2007). CHAPTER 3 Radio Propagation and Propagation Path-Loss Models. In *Wireless Communications & Networking* (pp. 47–84). Morgan Kaufmann Publishers, Elsevier. <https://doi.org/10.1016/B978-0-12-373580-5.50037-5>

Hoomod, H. K., Al-Mejibli, I., & Jabboory, A. I. (2018). Analyzing Study of Path loss Propagation Models in Wireless Communications at 0.8 GHz. *Journal of Physics: Conference Series*, 1003(1), 0–8. <https://doi.org/10.1088/1742-6596/1003/1/012028>

ITU. (2017). Propagation data and prediction methods for the planning of indoor radiocommunication systems and radio local area networks in the frequency range 900 MHz to 100 GHz. *Recommendation ITU-R P.1238-9*.

Jia, X., Cai, Y., Zhou, Q., & Yu, B. (2018). A Multicommodity flow-based detailed router with efficient acceleration techniques. *IEEE Transactions on Computer-Aided Design of Integrated Circuits and Systems*, 37(1), 217–230. <https://doi.org/10.1109/TCAD.2017.2693270>

Jo, H. S., Park, C., Lee, E., Choi, H. K., & Park, J. (2020). Path loss prediction based on machine learning techniques: Principal component analysis, artificial neural

network, and gaussian process. *Sensors (Switzerland)*, 20(7).
<https://doi.org/10.3390/s20071927>

Joung, J., Kurniawan, E., & Sun, S. (2017). Channel correlation modeling and its application to massive MIMO channel feedback reduction. *IEEE Transactions on Vehicular Technology*, 66(5), 3787–3797.
<https://doi.org/10.1109/TVT.2016.2598364>

Kang, J.-M., Chun, C.-J., Kim, I.-M., & Kim, D. I. (2020). Dynamic Power Splitting for SWIPT With Nonlinear Energy Harvesting in Ergodic Fading Channel. *IEEE Internet of Things Journal*, 4662(c), 1–1. <https://doi.org/10.1109/jiot.2020.2980328>

Kar, K., Datta, S., Pal, M., & Ghatak, R. (2016). Motley Keenan model of in-building coverage analysis of IEEE 802.11n WLAN signal in electronics and communication engineering department of National Institute of Technology Durgapur. *International Conference on Microelectronics, Computing and Communication, MicroCom 2016*, 2–7. <https://doi.org/10.1109/MicroCom.2016.7522577>

Kim, Y., Lee, T. J., & Kim, D. I. (2018). Joint Information and Power Transfer in SWIPT-Enabled CRFID Networks. *IEEE Wireless Communications Letters*, 7(2), 186–189. <https://doi.org/10.1109/LWC.2017.2763950>

Maravić, I., Kusuma, J., & Vetterli, M. (2003). Low-sampling rate UWB channel characterization and synchronization. *Journal of Communications and Networks*, 5(4), 319–326. <https://doi.org/10.1109/JCN.2003.6596614>

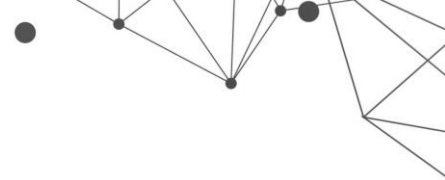
Park, C. M., Jang, H. Y., & Han, J. H. (2016). *What Characteristics Make an Enterprise More Proactive Toward Innovation? Case of Adopting RFID at Kumho Tire in Korea*. 309–312.

Saritha, R., & Vinod Chandra, S. S. (2019). Multimodal Foraging by Honey Bees Toward Optimizing Profits at Multiple Colonies. *IEEE Intelligent Systems*, 34(1), 14–22. <https://doi.org/10.1109/MIS.2018.111144149>

Shabbir, N., Sadiq, M. T., Kashif, H., & Rizwan Ullah. (2011). Comparison of Radio Propagation Models for Long Term Evolution (LTE) Network. *International Journal of Next-Generation Networks*, 3(3), 27–41. <https://doi.org/10.5121/ijngn.2011.3303>

Shafique, K., Khawaja, B. A., Khurram, M. D., Sibtain, S. M., Siddiqui, Y., Mustaqim, M., Chattha, H. T., & Yang, X. (2018). Energy Harvesting Using a Low-Cost Rectenna for Internet of Things (IoT) Applications. *IEEE Access*, 6, 30932–30941. <https://doi.org/10.1109/ACCESS.2018.2834392>

Shi, L., Ye, Y., Chu, X., Zhang, Y., & Zhang, H. (2018). Optimal Combining and Performance Analysis for Two-Way EH Relay Systems with TDBC Protocol. *IEEE Wireless Communications Letters*, 8(3), 713–716. <https://doi.org/10.1109/LWC.2018.2886895>



Silva, B., & Hancke, G. P. (2016). IR-UWB-Based Non-Line-of-Sight Identification in Harsh Environments: Principles and Challenges. *IEEE Transactions on Industrial Informatics*, 12(3), 1188–1195. <https://doi.org/10.1109/TII.2016.2554522>

Simmons, N., Gomes, S. B. F., Yacoub, M. D., Simeone, O., Cotton, S. L., & Simmons, D. E. (2022). *AI-Based Channel Prediction in D2D Links: An Empirical Validation*. 1–15. <http://arxiv.org/abs/2206.08346>

Song, Q., Guo, S., Liu, X., & Yang, Y. (2018). CSI Amplitude fingerprinting-based NB-IoT indoor localization. *IEEE Internet of Things Journal*, 5(3), 1494–1504. <https://doi.org/10.1109/JIOT.2017.2782479>

Tavares, C. H. A., Marinello, J. C., Proenca, M. L., & Abrao, T. (2020). Machine learning-based models for spectrum sensing in cooperative radio networks. *IET Communications*, 14(18), 3102–3109. <https://doi.org/10.1049/iet-com.2019.0941>

Uwaechia, A. N., & Mahyuddin, N. M. (2020). A comprehensive survey on millimeter wave communications for fifth-generation wireless networks: Feasibility and challenges. *IEEE Access*, 8, 62367–62414. <https://doi.org/10.1109/ACCESS.2020.2984204>

Yan, J., Xing, L., Li, C., & Zhang, Z. (2021). Multicommodity Flow Modeling for the Data Transmission Scheduling Problem in Navigation Satellite Systems. *Complex System Modeling and Simulation*, 1(3), 232–241. <https://doi.org/10.23919/csms.2021.0019>

Zaidi, A., Athley, F., Medbo, J., Gustavsson, U., Durisi, G., & Chen, X. (2018). Propagation and Channel Modeling. In *5G Physical Layer* (pp. 35–85). Elsevier. <https://doi.org/10.1016/B978-0-12-814578-4.00008-4>

Zhang, J., Xin, L., & Zhang, F. (2013). Propagation characteristics and modeling in indoor multi-floor environment. *Physical Communication*, 9, 246–256. <https://doi.org/10.1016/j.phycom.2012.05.008>

Zhang, Y., An, X., Yuan, M., Bu, X., & An, J. (2020). Concurrent Multipath Routing Optimization in Named Data Networks. *IEEE Internet of Things Journal*, 7(2), 1451–1463. <https://doi.org/10.1109/JIOT.2019.2955139>

MOBILE CHANNEL CHARACTERIZATION IN V2I SYSTEM INSIDE A TUNNEL IN 5.8 GHZ

DOI: [10.51859/amplla.sst631.1122-11](https://doi.org/10.51859/amplla.sst631.1122-11)

Andréa Lima¹
Leni Matos²
Pedro Castellanos³
Vitor Mota⁴

¹ M. Sc. in Electrical and Telecommunication Engineering. Universidade Federal Fluminense – UFF.

^{2,3} Professors at the Program of Post-graduation in Electrical and Telecommunication Engineering. Universidade Federal Fluminense – UFF. D.Sc. in Electrical Engineering – PUC/Rio.

⁴ Doctorate student of the Program of Post-graduation in Electrical and Telecommunication Engineering. Universidade Federal Fluminense – UFF.

ABSTRACT

Lately, with the arrival of 5G systems, the Vehicular Communication Systems have received substantial attention, mainly to help road safety and transport efficiency, both on roads and in urban traffic, with reliable communication. Among them, the Vehicle-to-Infrastructure communication system is analyzed in the propagation channel inside of a tunnel for understand better this kind of channel, and measurements were performed with the transmission of an unmodulated carrier, avoiding to determine the statistics and signal coverage, respectively, through small-scale fading signal and the fitting of some prediction models, in order to contribute to the characterization of channels in tunnel scenary.

Key words: Propagation in tunnels. Propagation models. Ray tracing. V2I propagation.

1. INTRODUCTION

With the growing demand for Internet of Things (IoT) as well as the arrival of the 5G technology, the characterization of radio communication channels in Vehicle-to-Infrastructure (V2I) and Vehicle-to-Vehicle (V2V) systems is essential because the channel is that limits as the capacity as the performance of the system. It leads, therefore, to the planning of reliable systems of communication and data traffic between autonomous vehicles.

One propagation environment where the mechanism of propagation of radio waves is peculiar, differing from the conditions of open environment, is the interior of tunnels. In this case, in addition to natural dependence of frequency, obstacles and their positions, radiation and antenna position, and polarization, they also have to consider: shape and transverse dimension of tunnel, curves inside the tunnel, surface roughness and electromagnetic properties of the walls [1]. Thereby, several articles deal with propagation models for tunnels: Hovrat et al., 2014 [2] describe numerical methods for solving Maxwell equations, waveguide or model approach, ray tracing methods and two-slope path loss modeling; Qureshi et al., 2018 [3] propose a lightweight radio propagation model for applying in vehicle communication in road tunnels, which utilizes a minimal set of parameters to estimate path loss in an acceptable range; Guan et al., 2018 [4] performed extensive measurements to provide the insight into the large-scale fading characteristics in real curved subway tunnels at various carrier frequencies (920, 2400 and 5705 MHz); Zhao et al., 2016 [5] simulated and analyzed the channel characteristics (path loss, Rician K-factor, RMS delay spread, and angular spread) in different carrier frequencies and tunnel cross-sections using ray tracing; Oliveira et al., 2015 [6] characterized, experimentally, in narrowband and wideband, the V2I propagation channel at 5.9 GHz in small distances in-tunnel and open-area.

As the carrier frequency of 5.8 GHz is one of the frequencies proposed by ANATEL (Telecommunications National Agency) in Brazil for vehicular systems, this chapter deals with the experimental analysis of the real coverage in a V2I communication in a tunnel. In addition, the statistics of small-scale variability signal (known as fast fading) is calculated and the most usual probability density functions

(p.d.f) are adjusted to it. Furthermore, adherence tests of propagation models are performed in order to verify the best model for this kind of channel.

In Section II, a literature review is presented and some prediction models are described. The measurement setup and environment are described in Section III. Section IV presents the results and analysis and Section V provides the conclusions.

2. LITERATURE REVIEW

Among the relevant propagation models found in the bibliography, which provide the loss of propagation in tunnels, are:

2.1 MULTI-RAYS

The multi-rays model based on ray tracing is commonly found [2]. In this case, the loss, in dB, for the propagation signal is calculated from:

$$L = -10 \cdot \log_{10} \left[\left(\frac{\lambda}{4\pi} \right)^2 * \left\| \frac{G_t}{d} + \frac{\sum_{i=1}^{\infty} G_i R_i(\theta_i) e^{j\frac{2\pi}{\lambda}(d_i-d)}}{d_i} \right\|^2 \right] \quad (1)$$

where G_t and G_i are the gains of transmitting (T_x) and receiving (R_x) antennas, respectively, which correspond to the path of the direct and the i -th reflected ray, respectively; d and d_i are the paths lengths of the direct and i -th reflected rays; R_i is the product of reflection coefficients of all walls from which the i -th ray is reflected; θ_i is the incidence angle of the i -th ray on obstacles; λ is the wavelength; R_0 is the direct ray; R_1 is the reflected ray in the soil; R_2 is the reflected ray on the left side while R_3 is the reflected ray on the right side; and so on.

A particular case of multi-rays channel is the two-rays model in which only the direct ray and that reflected on the ground are considered. In this article the multi-rays model was simulated for two, four, six and eight rays.

2.2 LIGHTWEIGHT RPM (RADIO PROPAGATION MODEL)

Another model, named Lightweight RPM [3], which considers the positive effects of tunnel geometry on radio propagation, establishes the basic loss, in dB, as:

$$P = k \log_{10} d \quad (2)$$

$$d = \begin{cases} r + w/(h \cdot \lambda), & w > h \\ r + h/(w \cdot \lambda), & w < h \end{cases} \quad (3)$$

where h and w represent the height and width of the tunnel, respectively, and r is the difference of height and width of the tunnel. The impact of moving radio obstacles on the radio propagation (vehicles, in general) can be estimated using the single knife-edge model [3], but it is not used here because there were not vehicles between T_x and R_x antennas when measurements were performed.

2.3. LOG-DISTANCE

The log-distance model (Lee, 1990) [7] is also used, however, it uses the loss coefficient (N) calculated from the data. Therefore, it always has a good fitting and, if no data is available, no coefficient can be calculated. Its equation is in (4), where d_0 is the distance from T_x to a reference point of the route, located nearest the transmission antenna; P_0 and P_r are the levels of the received signal at d_0 and d , respectively, in dBm; and N is the loss coefficient of the path loss.

$$P_r(d) = P_0 - 10.N.\log(d/d_0) \quad (4)$$

Therefore, in dB, the loss is calculated as:

$$L = 10.N.\log(d/d_0) \quad (5)$$

2.4. FREE SPACE

This model is also known as *Friis equation* (Lee, 1990) [7], and it is used as a reference since it takes account only the signal loss in an environment without multipath and obstructions. Its equation is:

$$L_0 = 32,4 + 20 .\log(d_{km}) + 20 .\log(f_{MHz}) \quad (6)$$

and d_{km} is the distance between the T_x and R_x antennas, in km, and f_{MHz} is the transmitted carrier frequency, in MHz.

3. TEST SETUP AND SOUNDED ENVIRONMENT

Measurements were performed inside the tunnel that links Jacarepaguá to Água Santa district in Rio de Janeiro city, Brazil. The tunnel is practically right with a soft curve at 1339.70 meters from the position of the transmitter system, whose installation is on the small circle depicted on the left in Figure 1. There was traffic, therefore, the speed could keep almost constant at 20 km/h, with the vehicle moving along the central line of the tunnel showed in Figure 1, on the right. Its extension is 1876.90 m.

Figure 1 -Sounded tunnel: aerial view (left) and sounded route (right)



Source: GoogleMaps and the authors

A power generator fed the transmission system. In this, the 5.8 GHz CW signal was generated and forwarded to T_x antenna, via coaxial cable, and Effective Isotropic Radiated Power (EIRP) of 24 dBm. In the R_x system, fed by battery and inverter, the antenna was fixed on the top of the vehicle, capturing and delivering the signal to the spectrum analyzer inside the car. All systems specifications are in Table 1.

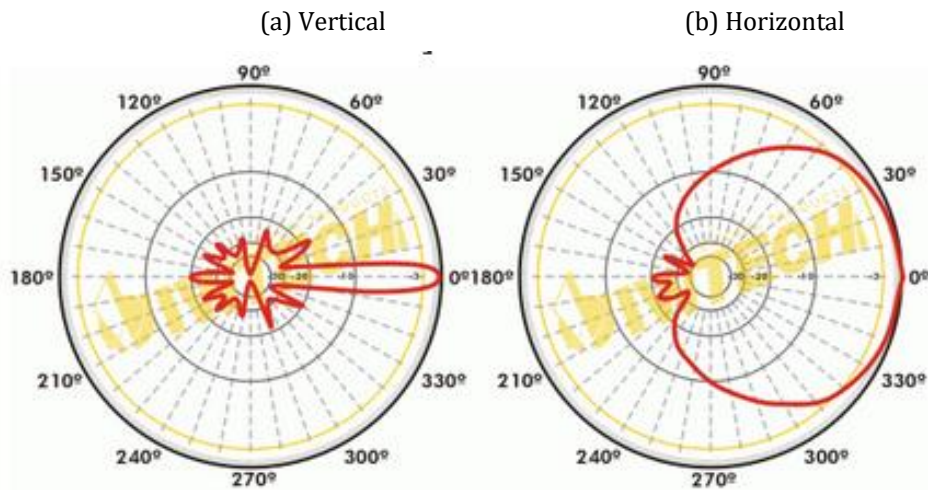
Table 1 -Technical specifications of the measurement setup

Transmission	
Device	Specifications
MG3700A Vector Signal Generator, ANRITSU	10 dBm (output Power)
OIW-5817P09 OIWTECH Antenna	Gain: 17 dBi, Z_{in} : 50 Ω , $P_{m\acute{a}x}$: 100W Aperture: $V = 7^\circ$, $H = 90^\circ$, Band: 5725 - 5850 MHz
Anritsu cable and adapters	Loss: 3 dB
Reception	
HP 8594E Spectrum Analyzer	10 kHz to 3 GHz
AIR-ANT2547V-N CISCO Antenna (dual band)	Band: 5150–5875 MHz, Z_{in} : 50 Ω Gain: 7 dBi, Aperture: $V = 13^\circ$ omnidirect.
Network Analyzer ¹ /Spectrum Analyzer ² MS2034A, ANRITSU	2 MHz a 4 GHz ¹ / 9 kHz a 4 GHz ²
Anritsu cable and adapters	Loss: 3 dB

Source: The Authors

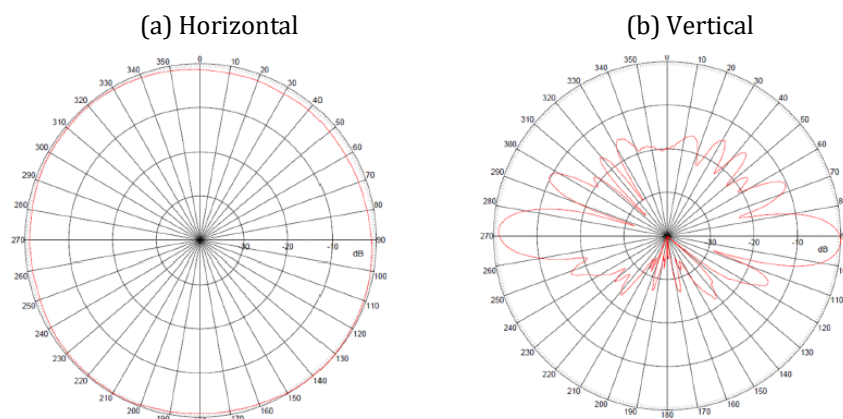
Figure 2 and Figure 3 show the radiation patterns of T_x and R_x antennas so that the results can be better interpreted. It is important to observe the high directivity of the T_x antenna.

Figure 2 - Radiation pattern of the transmitting antenna



Source: www.oiwtech.com

Figure 3 - Radiation pattern of the receiving antenna

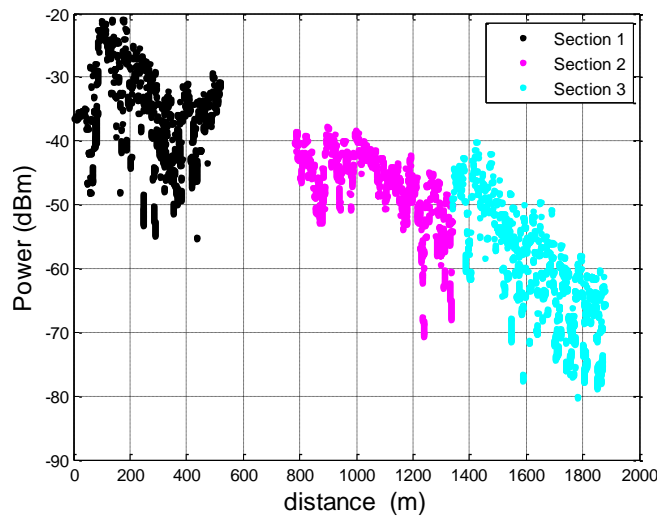


Source: www.cisco.com/c/en/us/td/docs/wireless/antenna/installation/guide/ant2547vn.html

4. PROCESSING AND RESULTS

Initially, the total path was divided into two sections due to a failure in the measures acquisition in the distances between 518.36 m to 781.71 m from the transmitter. Because the presence of a curvature in the route, verified in loco, the signal level has a more accentuated drop from 1339.65 meters, as depicted in Figure 4, so the total path was finally divided into three sections, with the last section practically without sight to the transmitter, dominating diffraction and reflections, and finishing in 1876.90 meters.

Figure 4 – Received power level measured along the sounded route showing three different regions



Source: The Authors

Figure 4 highlights, in different colors, the regions mentioned and the measured signal shows the small scale variability signal (or fast fading) over the path loss along the route in-tunnel. Due to the constant speed, the signal level, measured along the time, was easily plotted versus distance. There is a rapid initial decreasing of the signal until close to 55 meters. It is worth to observe that the narrow vertical aperture of the T_x (7°) and R_x (13°) antennas, as can be observed in Figure 2 and Figure 3, respectively, and the fact they were not at the same height, as seen in Figure 1, leads to 57.22 m as the minimum calculated distance from which the R_x antenna "sees" the main portion of the T_x antenna diagram (known as HPBW – Half Power Beam Width). Then, the signal level increases until 100 meters, from which decreases gradually.

Starting with the analysis of the signal variability in the sections, a study of the probability density function (p.d.f.) better adjusted to the data was performed for each section. Some more used p.d.f.'s (Nakagami, Rayleigh, normal and Rayleigh) (Parsons, 2000) [8] were adjusted to the data histogram, through the *dffitool* function of MATLAB® software [9]. Then, the histogram of the experimental data of small scale variability (or small scale fading), without the fall effect of the signal, was calculated and Table 2 presents the results of log likelihood between each fitted p.d.f. and the data histogram.

Table 2 –Log likelihood between each adjusted p.d.f. and the data of the small scale fading in the sections

P.D.F.	Section 1	Section 2	Section3
Nakagami	10676.2 ($m= 0.767168$)	81472.5($m = 1,87125$)	38068.4 ($m =1.08359$)
Rayleigh	7726.51	69327.3	37827.3
Rice	7726.51	83140.4	37866.4
Normal	-2996.21	82583.9	31297.7

Source: The Authors

It is observed that Nakagami was the best fit in both section 1 and section 3, respectively with $m \approx 0.8$ and $m \approx 1.1$. When this parameter is equal to 1, the Nakagami p.d.f. falls into the Rayleigh p.d.f., meaning that there are only multipath or, yet, a direct path, but its amplitude is near the level of the multipath. If, however, $0.5 \leq m < 1$, it means that the channel is worse than Rayleigh, with weaker multipath. When m is growing from 1, Rice p.d.f. can be a better fit than Nakagami p.d.f. mainly if there is a sight (LoS) to the T_x antenna, with strong direct ray. It occurred in the section 2, in which Rice was the best fit. In the section 3, however, there was not sight to the T_x antenna, and although m is slightly larger than 1, Nakagami predominated Rice distribution.

Like the measured signal was in dBm, it was necessary to calculate the loss associated to the signal, therefore, with the same basic conditions used in the experimental sounding:

$P_{tx} = 10$ dBm → output level of the vector signal generator;

$G_{tx} = 15$ dBi → gain of the transmission antenna;

$G_{rx} = 7$ dBi → gain of the reception antenna;

$h_{tx} = 5$ m → height of the transmission antenna;

$h_{rx} = 1,5$ m → height of the reception antenna;

$f = 5,8$ GHz → carrier frequency;

$L_{ctx} = 3$ dB → losses on cable and connections of the transmitter;

$L_{crx} = 3$ dB → losses on cable and connections of the receiver,

the measured signal levels were converted to the measured Path Loss (PL) though the following equation:

$$PL_{dB} = P_{tx,dBm} - L_{ctx} + G_{tx} - L_{crx} + G_{rx} - P_{rx,dBm} \quad (7)$$

where P_{rx} is the signal level measured along the tunnel, from 4 m to 1.876.90 m.

Some important remarks are:

1. the models were calculated for 3 sections due to the third one be in NLoS condition, in the shadow zone, differing from other two sections;

2. the multiple-rays model was calculated for: 2 rays (direct and reflected of the ground rays); 4 rays, adding more one reflection on the right wall and other on the left wall; 6 rays, adding more one reflection on the ground and on the right wall, other on the ground and the left wall; 8 rays, adding more one reflection on the right wall followed by another on the left wall and vice-versa.

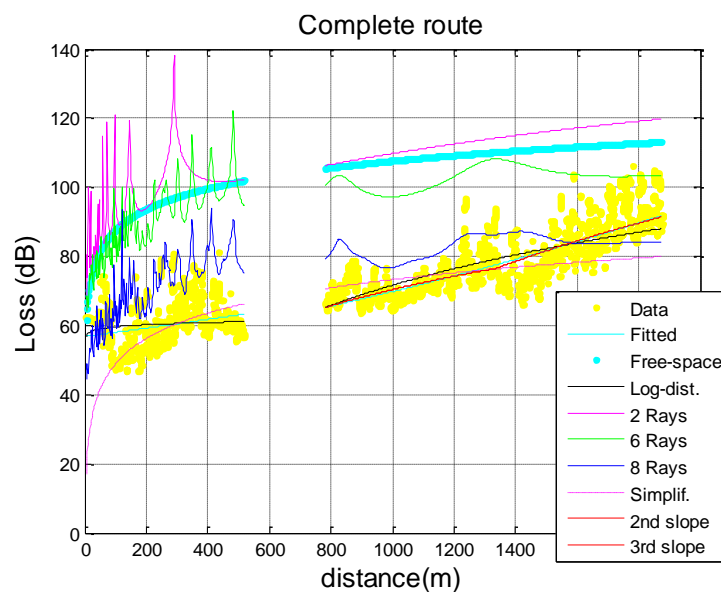
The graphics in Figure 5 shows all models simulated and the mean experimental path loss (named *Fitted* in the legend), obtained through the *cftool* function of MATLAB® [9]. It is observed that:

1. 4-rays model was not showed in order not to saturate the graphics, although its calcul has been performed and used. Its curve was near that of 6-rays model;

2. the name *Simplif* in the legend refers to the *RPM model* since it is a simple model;

3. *2nd slope* and *3rd slope*, respectively, refer to the *Log-distance* model applied to the second and third sectors, separately, because the third sector clearly presents higher loss coefficient than the second one, as seen in Figure 4. In this case, the adjustment is better than that with only two sectors.

Figure 5. Simulated models for propagation in-tunnel compared to empirical path loss



Source: The Authors

Table 3 and Table 4, respectively, provide the RMSE (Root Mean Square Error) calculated for the best models fitted to the path loss measured in the channel considering 2 and 3 sections and the smaller errors are highlighted.

Table 3. RMSE between models simulated and path loss considering 2 sectors

Model	Section 1 (LoS)	Section 2 (LoS + NLoS)
Log-Distance (2 slopes)	0.1369	0.1612
Simplified	0.1905	0.5131
8 Rays	0.7522	0.3413

Source: The Authors

Table 4. RMSE between simulated models and path loss considering 3 sectors

Model	Section 1 (LoS)	Section 2 (LoS)	Section 3 (NLoS)
Log-Distance (3 slopes)	0.1369	0.0652	0.0888
Simplified	0.1905	0.0747	0.1791
8 Rays	0.7522	0.5330	0.4265

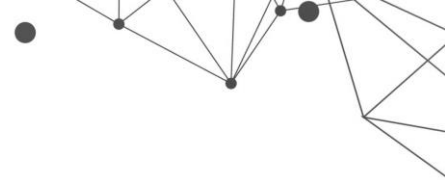
Source: The Authors

5. CONCLUSIONS

By analyzing results for fast fading in a sounded channel in the interior of a tunnel, it was observed that in the nearby region to the transmitter the signal did not contain a strong component in LoS, justified by the Nakagami p.d.f. adjusted to the data distribution with the parameter $m \cong 1$. Although Rice p.d.f. was hoped the best fit in section 1, where the direct wave is dominant, this did not occurred because of the narrow vertical aperture of the antennas and the fact they were not in the same height.

In the middle region, it observes that from 781.71 to 1339.65 meters, the signal variability is smaller and Rice p.d.f. best fitted, indicating a direct ray stronger than the mutipath. The antennas were in good sight, however, after 1339.65 meters the multipath confined by the walls of the tunnel predominated and Nakagami p.d.f. was the best fit with $m = 1$ practically.

Analyzing the RMSE errors, among the simulated models used to predict the signal, the log-distance model proved to have the better adherence to the measured path loss, as expected, since it works with the coefficient loss calculated from the



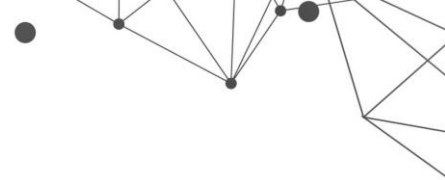
data obtained in the measurements. These coefficients calculated for the three sections (1, 2 and 3) were: 0.210, 4.863 and 10.17, indicating faster fall in section 3. Excepting that model, the Lightweight RPM, although simpler, showed very promising because it considers the effect of the tunnel geometry on the signal propagation. The multi-rays model showed, however, that eight rays is not sufficient to model the channel, and more than this is necessary if is required better adherence to the data measured in the tunnel. Therefore, much more processing is necessary in order to find the minimum number of rays such that the multi-rays model has, at least, an adherence equal to the log-distance model. For verifying that number, through the exponential curve adjusted to $RMSE \times N$ (number of rays), it was calculated that $N \geq 26$ in the first section and $N \geq 12$ in the second and third sections in order to get error (RMSE) beneath or equal to the error calculated for log-distance model, the best one. It is worth to observe that the variables G_i 's used in the multi-rays model are approximated because the values were obtained from the antennas radiation patterns. A smaller error certainly would be reached if we disposed of their exact values. Finishing, the simplified model showed a good starting point to calculate signal coverage in tunnels in V2I system, and if cars existing between T_x and R_x , the excess loss must be calculated by single knife-edge model [7] taking into account the number and size of them [3]. More measures in other tunnels must be obtained in order to confirm this simpler model (Lightweight RPM) for V2I communication, also including vehicles between T_x and R_x antennas.

ACKNOWLEDGEMENTS

The authors would like to thank CAPES (Coordenação de Aperfeiçoamento de Pessoal de Nível Superior) for granting a scholarship for the development of their studies and this research.

REFERENCES

- [1] Computer world. "Mercado de carros autônomos contribuirá com US\$ 13,7 milhões até 2030". 2020. Available: <<https://computerworld.com.br/2020/02/10/mercado-de-carros-autonomos-contribuira-com-us-137-bilhoes-ate-2030/>>.
- [2] Hrovat, A., Kandus, G., & Javavornic, T. (2014). A Lightweight Radio Propagation Model for Vehicular Communication in Road Tunnels, *Report*, NCBI, 2016.

- 
- [3] Qureshi, M. A., Noor, R. M., Shamim, A., Shamshirband, S., Zhao, J., Xiong, L., He, D. & Du, J. (2018). Channel Characteristics of Rail Traffic Tunnel Scenarios Based on Ray-Tracing Simulator, *Wireless Communications and Mobile Computing*, v. 2018, 9 pages, Wiley.
- [4] Guan, k., Ai, B., Zhong, Z., López, C. F., Zhang, L., Rodríguez, C. B., Hrovat, A., Zhang, B., He, R., & Tang, T. (2015). *Measurements and Analysis of Large-Scale Fading Characteristics in Curved Subway Tunnels at 920 MHz, 2400 MHz, and 5705 MHz*, *IEEE Trans. on Intelligent Transp. Systems*, v. 16, n. 5, 2393-2405.
- [5] Zhao, J., Xiong, L., He, D., & Du, J. (2018). Channel Characteristics of Rail Traffic Tunnel Scenarios Based on Ray-Tracing Simulator. *Wireless Communications and Mobile Computing*, 1-9.
- [6] Oliveira, F. J., Castellanos, P. V. G., Matos, L. J., Meza, W. D. T., & Silva Mello, L. A. R. (2018). Channel Characterization on Vehicle to Infrastructure Scenarios in 5.8 GHz, in *EEE MTT-S Latin America Microwave Conference - LAMC 2018*, Arequipa, Peru, 3 pages.
- [7] Lee, W. C. Y. (1990). *Mobile Cellular Telecommunications Systems*, McGraw-Hill.
- [8] Parsons, J. D.. *The Mobile Radio Propagation Channel*, John Wiley & Sons, 2nd. Ed., 2000.
- [9] Matrix Laboratory (Matlab) software, *MathWorks Inc.*, 2012.

NEW ANALYTICAL APPROACH TO ESTIMATE THE ELECTROMAGNETIC SPECTRUM FROM DEVICES SUBMITTED TO HIGH VOLTAGES

DOI: 10.51859/ampla.sst631.1122-12

Galba Falcão Aragão¹
Glauco Fontgalland²
Humberto Dionísio de Andrade³

¹ PhD, Instituto Federal do Rio Grande do Norte - IFRN – Campus Parelhas, Parelhas, RN, Brasil.

² PhD, Universidade Federal de Campina Grande – UFCG, CIEE – DEE, Campina Grande, PB, Brasil.

³ PhD, Universidade Federal Rural do Semi-Árido – UFERSA, DET, Mossoró, RN, Brasil.

ABSTRACT

A simplified physical model and an analytical equation to estimate the frequency range of the radiated spectrum from an ionized region using computational simulation are presented in this chapter. This phenomenon is frequently caused by the corona effect generated from high voltages sources. Mostly not seem, this ionization can damage over time the device and the radiated frequencies can cause electromagnetic interference (EMI). Based on particle radiation and the momentum equation, the velocity and frequency equations for accelerated charges in an electric field are presented. The proposed model presents compatible results according to the results widely found in the literature, from kHz frequencies to infrared and ultraviolet ranges. The model also explains why the corona effect spectrum for slowly changing electric fields is limited to the ultraviolet range and why rapidly changing fields can emit X-ray signals. The results can be used to guide in the evaluation of devices submitted to high voltage (HV) as well as to contribute to the development of devices that use HV electric fields to generate high frequencies, such as X-ray sources, and in the research field on harvest energy systems, corona discharges industrial processes, among others.

Key words: Corona effect. EMI. Electrostatic source. Electromagnetic spectrum. HV electric field.

1. INTRODUCTION

The corona effect has many industrial applications, but in transmission line engineering it was initially studied to understand the process of energy losses and to avoid electromagnetic interference (EMI). More recently, emissions have been studied to evaluate the conditions of equipment subjected to high voltage electric fields, where the characteristic of the measured spectrum indicates the status of the equipment. Many of these studies are based on the comparison between the spectrum radiated by equipment in good condition and the spectrum radiated by defective equipment. During the evaluation some of these studies, we realized that there was not much information about the radiated spectrum and its limits, which led us to research about the ionization process and the corona effect. This chapter presents a simplified model that allows to achieve an equation for radiated spectral range estimation generated by ionization and the corona effect. The equation is based on the intensity of the electric field and the distance that the electron can take between collisions and its acceleration.

2. THEORY

In the early 20th century, PEEK (1911, 1912) investigated that a loss occurs by dissipation of power into the air in alternating-current transmission lines at very high voltages and reported that this is accompanied by luminosity of the air surrounding the line conductor - the so-called corona.

To LOEB (1965), the expression corona is used to describe the general class of luminous phenomena appearing associated with the current jump to some microamperes at the highly stressed electrode preceding the ultimate spark breakdown of the gap.

According to GIAO & JORDAN (1968), corona discharges attract attention in power transmission engineering because of the breakdown phenomena and the mostly undesirable effects on insulation and because they produce radio noise and power loss. On the other hand, corona discharges are applied in many useful industrial processes. According to these authors, three conditions must be satisfied to initiate a corona discharge:

- 1) field intensity should be high enough.

2) the degree of field nonuniformity should be high enough.

3) free electrons should be available in the overstressed field region.

It is well-known that a gas can be considered as an almost perfect insulator at normal state. However, when a high voltage is applied between two electrodes immersed in a gaseous medium, the gas can become a conductor (by ionization) and the dielectric breakdown can occur (NAIDU & KAMARAJU, 1997; DATSIOS & MIKROPOULOS, 2016).

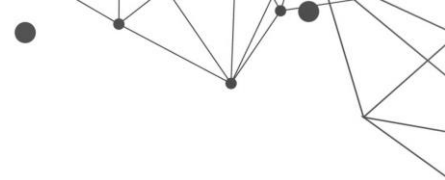
In this process, the air can be ionized mainly by photoionization and collision (NAIDU & KAMARAJU, 1997), and detailed explanation of the air ionization process is presented in CHACHEREAU & PANCHESHNYI (2014).

The air region where ionization processes occur is called the region of space charges. McMILLAN (1932) and LIM *et al.* (2019) present theories of formation of the regions of space charges and the corona effect in devices subjected to high alternating voltage (AC).

In the ionization process, there is a delay between the discharge voltage and the discharge current, named time-lag (OKANO, 2013). The use of voltage impulses shorter than the time-lag allows to reach very high discharge voltages and, therefore, obtain electric fields greater than the breakdown limit (3 MV/m), under atmospheric conditions.

X-ray emission has been detected occasionally during the streamer-corona propagation in a wire-plate corona reactor open to ambient air (NGUYEN *et al.*, 2009) using an impulse generator superimposed on a 20 kV DC bias. Because of the short pulse duration regarding the primary streamer transit time, no total gap breakdown occurred.

Electrical energy in the corona discharges is transformed into other forms of energy such as light, sound, electromagnetic energy, etc. However, the main part of energy is lost in the collisions of electrons and ions with neutral gas molecules. In other words, the main effect of corona loss is the gas heating (GIAO & JORDAN, 1968). Several measurement systems have been developed using the corona effect to identify the conservation status of elements subjected to high voltage (HV). The corona effect is detected indirectly based on measurement of conducted current (CHUN *et al.*, 2001), ultraviolet radiation (PINNANGUDI *et al.*, 2002; PINNANGUDI *et al.*, 2005), thermographic cameras, sound, and ultrasound (VAHIDI *et al.*, 2003),



and measurement of the radiated electromagnetic spectrum (FONTGALLAND *et al.*, 2004; ROCHA & FONTGALLAND, 2014).

In his study on the radio interference (RI) caused by air ionization and corona effect in high alternating voltages, McMILLAN (1932) attributes the RI to small ionizations or corona discharges due to the high electric field. According to ZAAZOU *et al.* (1964), RI can also be produced by elements subject to high direct voltage.

ADAMS (1956) proposed a method to calculate the RI Level from transmission line using laboratory results on conductor samples and knowledge of the geometry of the line.

From the above, HV devices can radiate EM waves (SARATHI & UMAMAHESWARI, 2013). The electromagnetic (EM) waves can cover the spectrum of radio waves, ranging from the infrared range to the ultraviolet range. And in special conditions, reaching the X-ray range (NGUYEN *et al.*, 2009). Several studies have been carried out to assess the state of electrical components subject to high electric fields based on changes in their electromagnetic emissions (FONTGALLAND *et al.*, 2004; ROCHA & FONTGALLAND, 2014; MOURA *et al.*, 2014; FONTGALLAND & PEDRO, 2015; SARATHI *et al.*, 2008). However, there is not much information about the spectral band emitted, which can be used to select the sensor's frequency band and the origin of electromagnetic interference (EMI) source as well.

When evaluating the problem of EMI emissions originated from devices submitted to HV, it was realized that the emissions occur because of the ionization of the air and by the movement of charges in the region. Therefore, the ionization effect can be obtained from electrostatic sources, as demonstrated in ARAGÃO *et al.* (2017). These important results and the lack of an expression to estimate the frequency range of the EMI field have encouraged our study on the determination of the spectrum radiated by the corona effect using analytical formulation.

The use of an electrostatic source, such as the Wimshurst electrostatic machine, greatly simplified the experiments and the experimental results can accurately be applied to HV components without loss of generality (ADAMS, 1956).

3. MODEL DEVELOPMENT

3.1. PARTICLE RADIATION

Electromagnetic emissions from a device subjected to high electric field are related to the air ionization (GIAO & JORDAN, 1968; McMILLAN, 1932; ZAAZOU et al., 1964, ADAMS, 1956). Therefore, the frequency range emitted by this type of source are proportional to the variation in the electrical charges speed in the region of space charges. This variation, in turn, depends on the distance between collisions and the intensity of the electric field.

Based on antenna theory (BALANIS, 2005), for an electromagnetic signal to radiate, there must be a variation in the conductor current.

In the region of space charges subjected to HV, the charges are basically electrons, positive ions, and negative ions. This consideration is in line with ADAMS (1956), which states that this movement of charge, both positive and negative, constitutes an electric current, $I = dQ/dt$. For simplicity, only electrons will be considered.

3.2. THE PROPOSED MODEL

The model is based in two charged electrodes (A and B). The electrode A is charged with $Q_A = +Q$ and B is charged with $Q_B = -Q$ (where $|Q_A| = |Q_B| = |Q|$). Considering that only a single electron subjected to the electric field between the electrodes, with rest mass m_0 , departs from the proximity of the negative electrode and it is accelerated towards the positive electrode (Fig. 1) in a straight line. According to GRIFFITHS (2013), when charges accelerate, their fields can transport energy irreversibly out to infinity – the electromagnetic radiation.

The electron undergoes several inelastic collisions with other atoms or ions and its energy is transferred to them. After each collision, the electron's velocity is considered to drop to zero. It must be highlighted that by the equation of momentum $p = m_0 v / \sqrt{1 - v^2/c^2}$ (DE BROGLIE, 1924), where c is the speed of light, if the velocity v drops to zero, the momentum will be zero, and this model will be invalidated. But, according to LANDAU & LIFSHITZ (1975), in relativistic mechanics, the energy (ϵ) of a free particle does not go to zero for $v = 0$. This can be seen in Eq. (1):

$$\varepsilon = \frac{m_0 c^2}{\sqrt{1 - \frac{v^2}{c^2}}} = m_0 c^2 |_{v=0} \quad (1)$$

As the momentum can be related to the energy by $p = \varepsilon/c$, it is verified that the momentum will not be 0 ($p = m_0 v$).

In this model, the electron does not recombine during its journey, and, after each collision, the electron resumes its movement since it remains subjected to the electric field. The acceleration of the electron, in the region of space charges, is responsible for electromagnetic emissions. This statement seems to violate the energy and momentum conservation laws, however, as will be seen, when the electron is accelerated, an electromagnetic field proportional to its acceleration appears in the opposite direction, causing its resulting acceleration to decrease with increasing velocity. And this deceleration effect is responsible for the electromagnetic emissions of accelerated loads and is in accordance with the energy and momentum conservation laws.

3.3. THE MODEL EQUATION

To define the equation that can determine the electromagnetic spectrum radiated by the proposed model, the momentum equation will be used as a starting point

$$p = \frac{m_0 v}{\sqrt{1 - \frac{v^2}{c^2}}} \quad (2)$$

The wavelength of a particle, λ , can be related to its momentum by the Eq. (3), as

$$\lambda = \frac{h}{p}, \quad (3)$$

where h is the Planck constant.

The wavelength can also be related to the particle oscillation frequency in free space by (in media, refractive index must be included)

$$\lambda = \frac{c}{f}, \quad (4)$$

where f is the frequency.

Combining Eq. (2), (3) and (4), is obtained

$$f = \frac{c m_0 v}{h \sqrt{1 - \frac{v^2}{c^2}}} \quad (5)$$

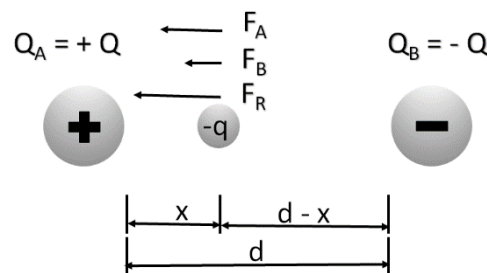
The frequency determined in Eq. (5) varies if the particle v varies, by the Lorentz factor.

3.3.1 THE ELECTRIC FIELD BEHAVIOR

Since the frequency of the applied voltage is relatively low, the distribution of the electric field can be calculated by the methods employed to electrostatic fields (ADAMS, 1956).

The problem in determining the particle acceleration can be modeled by an electric charge (electron, $-q$) subjected to an electric field between two electrodes as shown in Fig. 1.

Figure 1 - Representation of forces acting on an electrical charge between two electrodes.



Source: The authors.

Coulomb's Law shows that electrical force can be given by

$$F_R = F_A + F_B = k|Q||q| \left(\frac{1}{x^2} + \frac{1}{(d-x)^2} \right) \quad (6)$$

The resulting electric field can be obtained from

$$E = \frac{F_R}{|q|} \quad (7)$$

where F_R is the resultant force that the charge q undergoes when placed between the electrodes with charges Q_A and Q_B in relation to their position.

3.3.2 CHARGE ACCELERATION

The particle acceleration, considering the variation of mass with velocity, is given by Eq. (8), which corresponds to the x direction. In this study, the displacement was considered only in the x direction, according to the proposed model. The applied force corresponds to the electrical force that the electron is subjected to, which is given by

$$a_x = \frac{F_x}{m_0} \left(1 - \frac{v^2}{c^2}\right)^{3/2}. \quad (8)$$

From Eq. (7), the force in the x direction can be represented by $F_x = |q| E_x$, therefore, the acceleration as a function of the electric field can be written as

$$a_x = \frac{|q| E_x}{m_0} \left(1 - \frac{v^2}{c^2}\right)^{3/2}. \quad (9)$$

An important interpretation of the result presented in Eq. (9) is that the acceleration decreases as the particle speed increase. And this deceleration effect may explain why accelerated charges are able to radiate electromagnetic emissions without violating energy and momentum conservation laws.

3.3.3. CHARGE VELOCITY

To determine the velocity of the particle, an infinitesimal element of length, ds_0 , was considered, which corresponds to the distance traveled by a low-speed particle. The electric field will be considered constant in this element of length and, therefore, we can simplify the movement of the particle to the uniformly accelerated rectilinear movement (UARM). Because of space contraction at high speeds, the infinitesimal element of length, ds , can be determined by Eq. (10)

$$ds = \sqrt{1 - \frac{v^2}{c^2}} ds_0. \quad (10)$$

Hence, the Torricelli equation (Eq. (11)) is used to determine the velocity of particle in each element of length ds ,

$$v_{(s)} = \sqrt{v_0^2 + 2 a ds}. \quad (11)$$

Therefore, replacing Eq. (9) and Eq. (10) in Eq. (11), we have

$$v_{(s)} = \sqrt{v_0^2 + 2 \frac{|q| E_x}{m_0} \left(1 - \frac{v^2}{c^2}\right)^2 ds_0}. \quad (12)$$

Eq. (12) shows that the particle velocity increases with: the distance between collisions increases; the increase of the element electrical charge; the increase of the electric field.

3.3.4. FREQUENCY EMITTED BY AN ACCELERATED CHARGE

Substituting Eq. (12) in Eq. (5), we obtain:

$$f = \frac{c m_0}{h \sqrt{1 - \frac{v^2}{c^2}}} \sqrt{v_0^2 + 2 \frac{|q| E_x}{m_0} \left(1 - \frac{v^2}{c^2}\right)^2} ds_0. \quad (13)$$

In Eq. (13), it can be observed that the frequency increases with the increase of the particle velocity and with its mass. It must be pointed out here that Eq. (13) governs the behavior of the electron under BC considered in our model.

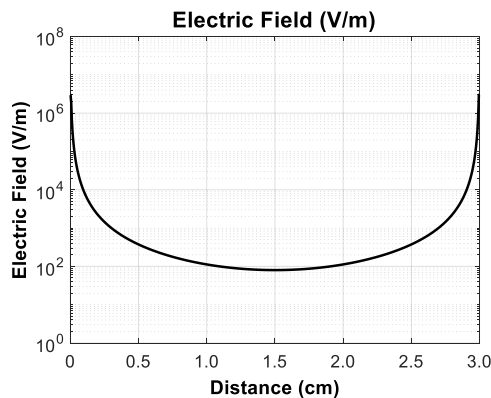
3.4. SIMULATED RESULTS

Computational routines were developed to implement the BC to the proposed equations providing simulated results and their graphical representations. These simulations were performed in MATLAB® to evaluate the behavior of the particle velocity (Eq. (12)) and the radiated frequency (Eq. (13)). Histograms of the occurrences of radiated frequencies were constructed to represent the radiated spectrum.

The profile of the resulting electric force was calculated from Eq. (6), where was considered: $|Q| = 1 \text{ pC}$, $|q| = 1.6021917 \times 10^{-19} \text{ C}$, and $d = 3 \text{ cm}$. These parameters correspond approximately to the configuration presented by a Wimshurst electrostatic machine with its electrodes separated by 3 cm.

The resulting electric field was calculated using Eq. (7) (Fig. 2). As expected, the electric field tends to have very high values in the vicinity of the electrodes, consequently, very high frequencies. However, the dielectric strength constant of the air must be considered, and the electric field has its maximum value limited to 3 MV/m in the vicinity of the electrodes.

Figure 2 – Simulated results for electric field between two electrodes 3 cm apart



Source: The authors.

For simulating the collisions occurred by the electron during the path between the electrodes, the interval between collision can be estimated by considering the Van der Waals radii for nitrogen and oxygen (Table 1), since these elements correspond to 78% and 21% of the atmosphere composition, respectively. This approach to the composition of the atmosphere is in accordance with CHACHEREAU & PANCHESHNYI (2014).

Table 1 – Radii of nitrogen and oxygen.

Element	Atomic Radius (pm)	Covalent Radius (pm)	Van der Waals Radius (pm)
Nitrogen (N ₂)	65	75	155
Oxygen (O ₂)	60	73	152

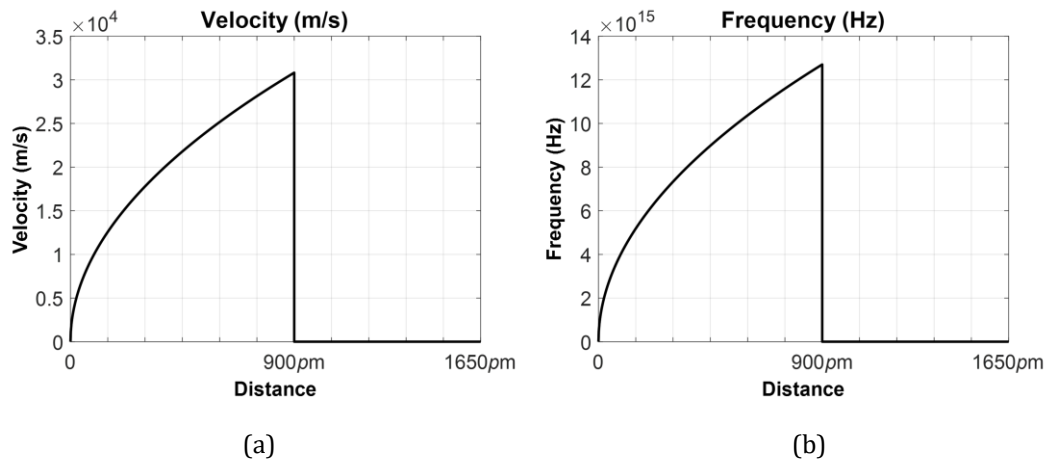
Source: The authors.

For proof of concept (PoC), we assume that the minimum distance between a collision is 150 pm , which corresponds approximately to the Van der Waals radii for nitrogen and oxygen. It was added to the minimum distance interval ten times its length ($10 \times 150 \text{ pm}$) to define the longest distance between a collision, which corresponds to $1,650 \text{ pm}$. Thus, the distances between the collisions were calculated using a normal distribution with an average of 900 pm and standard deviation of $\sigma = 300 \text{ pm}$, which should happen in the interval between 150 pm and $1,650 \text{ pm}$. The choice of collision distances was hypothetical.

Air density is related to the longest collision interval. If the air density increases, the collision interval decreases, and the maximum frequencies decrease. If the air density decreases, higher frequencies can be obtained.

Fig. 3 shows the simulated results for the electron velocity (Eq. (12)) and for the radiated frequency (Eq. (13)), in a linear scale, considering that a single collision occurs at 900 pm . Fig. 3a shows that the particle starts to move at a $v = 0 \text{ m/s}$ (initial condition). As the traveled distance increases the velocity grows and the acceleration reduces. The phenomenon continues until the collision occurs and the velocity drops back to 0 m/s . The radiated frequency variation has the same characteristic to the velocity, as can be seen in Fig. 3b.

Figure 3 – Simulated results for (a) velocity of electron and (b) radiated frequency considering the electric field limited to 3 MV/m for a single collision at 900 pm, in the interval between 0 pm and 1,650 pm

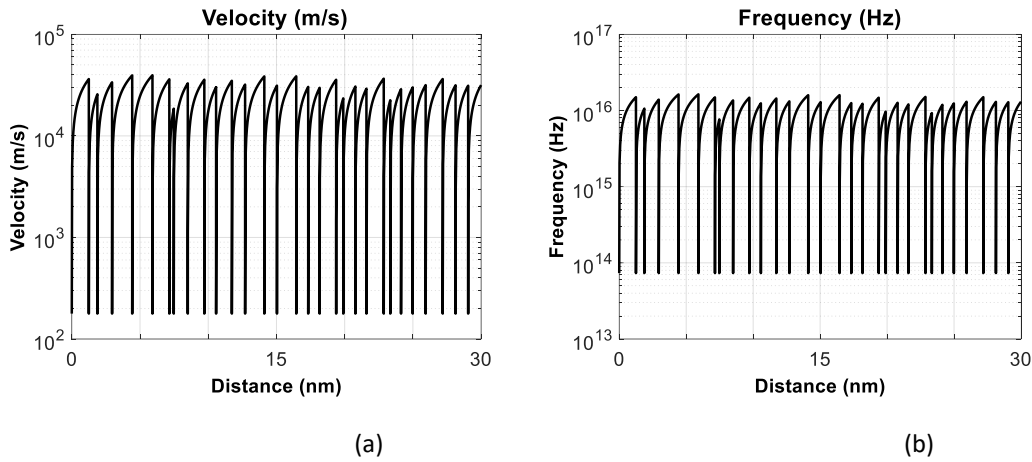


Source: The authors.

The graphs shown in Figs. 4, and 5 represent the solutions of Eq. (12) (for velocity) and Eq. (13) (for frequency). Three frames taken into the space variation of 30 nm located around the beginning (0 cm + 30 nm), middle (1.5 cm ±15 nm), and the end (3 cm – 30 nm) of the path between the electrodes were simulated for the electric field curve in Figure 2. The first and third frames show very similar results, as the electric field is limited to 3 MV/m. The third frame is not shown. As can be seen, 30 nm spatial variation was enough to represent the number of collisions (approximately 30 collisions). This space variation was further divided into 1×10^6 linear parts, which represent the infinitesimal elements in length ($ds_0 = 3 \times 10^{-14} \text{ m}$). The plots are presented in logarithmic scale and show the velocities and frequencies at the second interaction interval. For the electron, the infinitesimal element of length, ds_0 , is large enough to cause great acceleration. This effect hides lower velocities and frequencies in Figs. 4, and 5. Using linear scale plots, these smaller values become more evident (Fig.3). Therefore, there is no restriction on the use of Eqs. (12) and (13).

Fig. 4a shows that the initial variation in speed of electron is very intense. This intense velocity variation causes the frequency (Fig. 4b) to vary very quickly. This variation decreases when it tends to its maximum value, because of the Lorentz factor.

Figure 4 – Simulated results for (a) velocity of electron and (b) radiated frequency considering the electric field limited to 3 MV/m for distances between 0 nm and 30 nm.

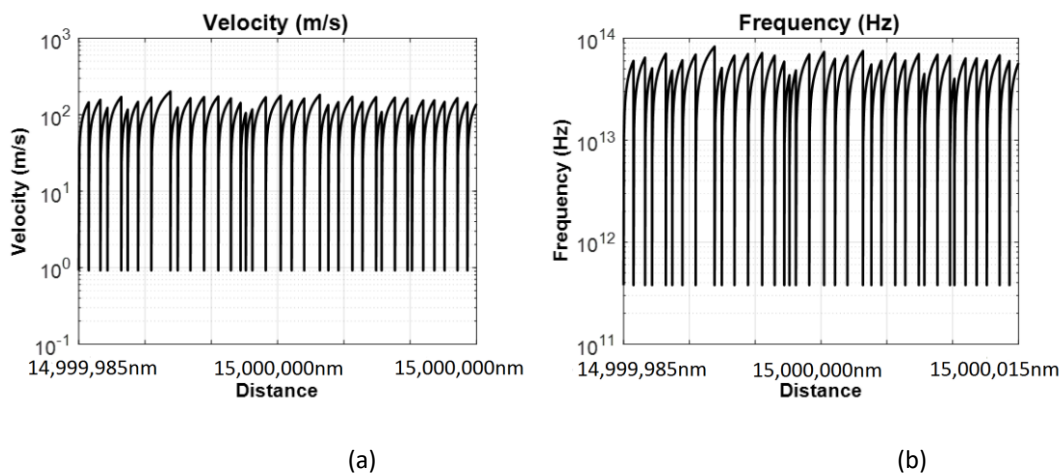


Source: The authors.

It is also observed that the maximum frequency emitted by the charge in each path depends on the electric field. In the case of free space, where the dielectric strength is 3 MV/m, the maximum frequencies will be in the ultraviolet range (10^{16} Hz). These emissions will occur near the electrodes (Fig. 4) since the electric field is stronger in these surroundings.

Due to the variation of the electric field with the distance, the maximum frequencies fall rapidly to values in the infrared region ($f < 10^{14}$ Hz) (Fig. 5).

Figure 5 – Simulated results for (a) velocity of electron and (b) radiated frequency considering the electric field limited to 3 MV/m for the 1.5 cm +/- 15 nm interval

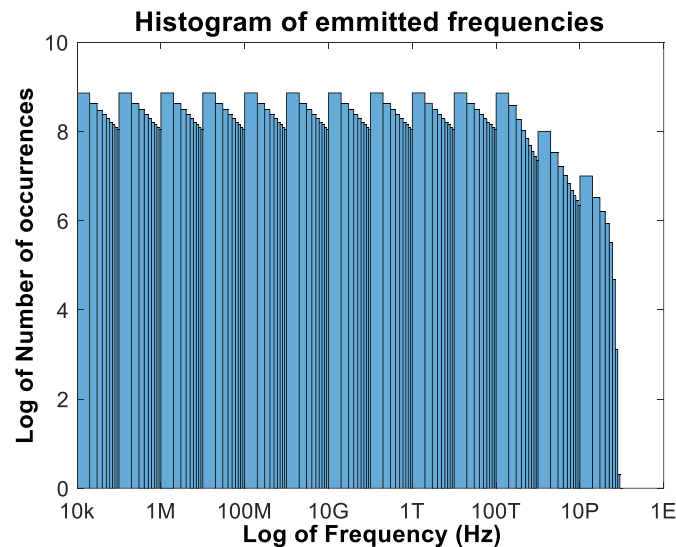


Source: The authors.

It can be seen from Eq. (13) that the frequency varies from values close to zero to values in the order of 10^{16} Hz.

Eq. (13) was calculated to demonstrate the frequency range emitted throughout the path between the electrodes. The occurrences of each frequency were counted to generating the histogram shown in Fig. 6. From the comments above, it must be highlighted that both scales are logarithmic. To perform this calculation, 1,000 points, logarithmically spaced, were used in the interval between each collision (approximately 33 million collisions between the electrodes were considered). The starting distance range is $ds_0 = 1 \times 10^{-34}$ m. The use of a linear scale would better represent the emissions profile, however, the limitation of the processing capacity of the used system did not allow its use. Fig. 6 shows the full spectrum, where the maximum frequencies are limited by the maximum electric field (3 MV/m). The same results were obtained with 100,000 points between collisions. The histogram was used to demonstrate that the frequencies are emitted in a wide range.

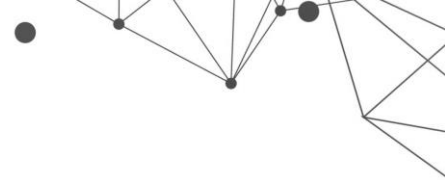
Figure 6 - Histogram representation of the radiated frequencies from 10 kHz up to 100 PHz(1×10^{17} Hz)



Source: The authors.

Fig. 6 shows the presence of radiated frequencies from 10 kHz to 100 PHz. The electric field is more intense near the electrodes and decreases when moving away from them. We can remark also that the occurrence of frequencies higher than 100 THz decreases in relation to the others.

The use of logarithmic scale to calculate the radiated frequencies produces the sawtooth shape-curve of the histogram, Fig. 6.



This result is compatible with the spectrum proposed by ADAMS (1956). However, this reference does not present the frequency spectral range.

The spectrum emitted by an element subjected to high voltage occurs during the ionization process of the medium and is influenced by the intensity of the electric field, the dielectric strength constant of the ionizable medium, and the distance between collisions of the charged particles in the region of space charges.

To obtain higher frequencies, such as x-ray signals, the interval between collisions or the intensity of the electric field must be increased. The interval between collisions can be increased, by decreasing the density of the air. High Voltage pulses with duration less than the time-lag between discharge voltage and discharge currents can be used to obtain electric fields greater than 3 MV/m in atmospheric conditions, as shown in NGUYEN et al. (2009).

The spectrum emitted by an element subjected to high voltage occurs during the ionization process of the medium and is influenced by the intensity of the electric field, the dielectric strength constant of the ionizable medium, and the distance between collisions of the charged particles in the region of space charges.

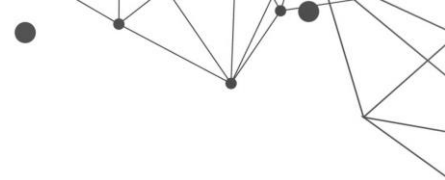
As the intensity of the electric field influences the velocity of particle, the higher frequencies (UV) will be emitted at the places of greater intensity of the electric field, making the source of emission to be close to the surface responsible for the electric field or at the concentration points, as quoted by GIAO & JORDAN (1968).

The developed equations and simulations showed that the radiated spectrum can start near to zero up to very high frequencies, which is limited by the dielectric strength of the medium, and for the air in atmospheric conditions, it reaches ultraviolet range.

The results obtained and the formulation presented demonstrate that the radiated spectrum is mainly due to the accelerated movement of electrons and an amount of emitted energy is available to be used.

4. CONCLUSIONS

The obtained results can make a valuable contribution to the study of air ionization and the corona effect. They contribute to the development of techniques



for the electrical components' characterization subject to HV, as well as guide the development of devices that use electric fields to generate high frequencies.

The proposed model for calculating the frequency spectrum generated by air ionization and the corona effect presents compatible results with the results widely found in the literature up to ultraviolet frequencies. The model also explains why the corona effect spectrum for slowly changing electric fields is limited to the ultraviolet range and why rapidly changing fields can emit X-ray signals.

The presented model contribution goes beyond the characterization of the spectrum radiated by devices and may contribute to research on X-ray generation, generators in the terahertz range, harvest energy systems, ISM band applications, corona discharges industrial processes, among others.

REFERENCES

Adams, G. E. (1956) *The Calculation of the Radio Interference Level of Transmission Lines Caused by Corona Discharges* [includes discussion]. Transactions of the American Institute of Electrical Engineers. Part III: Power Apparatus and Systems 75.3, pp. 411-419.

Aragão, G. F.; Fontgalland, G.; Andrade, H. D. (2017) *Measuring potential EMI fields from electrostatic sources*. 2017 IEEE International Symposium on Antennas and Propagation & USNC/URSI National Radio Science Meeting, San Diego, CA: pp. 2607-2608.

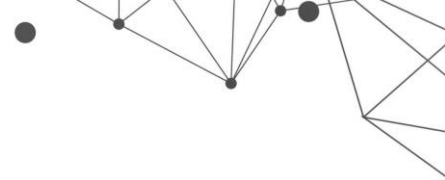
Balanis, C. A. (2005) *Antenna Theory: Analysis and Design*, 3rd Edition, John Wiley and Sons, New York.

Chachereau, A.; Pancheshnyi, S. (2014) *Calculation of the Effective Ionization Rate in Air by Considering Electron Detachment from Negative Ions*. IEEE Transactions on Plasma Science, 42(10), pp.3328-3338, 2014.

Chun, L.; Yuanfang, W.; Yixiong, N.; Munong, M.; Guofu, D.; Kecheng, L. (2001) *Investigation on characteristics of corona current to single insulator*. In *Electrical Insulating Materials, (ISEIM 2001)*. Proceedings of 2001 International Symposium on (pp. 286-289). IEEE.

Datsios, Z.G.; Mikropoulos, P.N. (2016). *Modeling of lightning impulse behavior of long air gaps and insulators including predischage current: implications on insulation coordination of overhead transmission lines and substations Lightning overvoltage performance of 110 kV air-insulated substation*, *Electr. Power Syst. Res.* 139, pp. 37-46.

de Broglie, L. -V. 1924 *Recherches sur la théorie des Quanta*. Physique [physics]. Migration - université en cours d'affectation, Français. tel-00006807.



Fontgalland, G.; Pedro, H. J. G. (2015) *Normality and Correlation Coefficient in Estimation of Insulators' Spectral Signature*. Signal Processing Letters, IEEE 22, no. 8: 1175-1179.

Fontgalland, G.; Vuong, T. P.; Bezerra, J. M. B.; Neri, M. G. G.; Baudrand, H.; Raveau, N. (2004) *Electromagnetic noise measured from glass insulator under discharge activity*. In 12^o Colloque International de Compatibilité Electromagnétique, pp. 00-001.

Giao, T. N.; Jordan, J. B. (1968) *Modes of corona discharges in air*. IEEE transactions on power apparatus and systems 5, 1207-1215.

Griffiths, D. J. (2013). *Introduction to Electrodynamics*. 4th Edition, Pearson Education, Inc.

Landau, L. D.; Lifshitz, E. M. (1975) *The Classical Theory of Fields: Volume 2*. Butterworth-Heinemann.

Lim, D. Y.; Jee, S. W.; Bae, S.; Choi, Y.K. (2019) *Analysis of the influence of a conductive particle on the surface flashover characteristics of epoxy dielectric in atmospheric air*. Journal of Electrostatics 99, pp. 31-40.

Loeb, L. B. (1965). "Electrical coronas, their basic physical mechanisms." Univ of California Press.

McMillan F. O. (1932) *Radio interference from insulator corona*. Transactions of the American Institute of Electrical Engineers. 2, no. 51: 385-391.

Moura, E. P.; Albert, B. B.; Fontgalland, G. (2014) *Statistical classification of contamination in glass insulators by reading its spectrum*. International Journal of Applied Electromagnetics and Mechanics 45, no. 1-4: 589-595.

Naidu, M. S.; Kamaraju, V. (1997) *High Voltage Engineering*, 2nd Edition, McGraw-Hill.

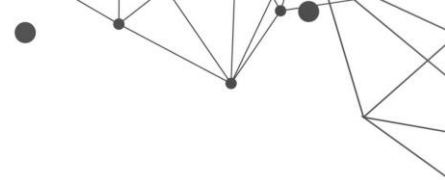
Nguyen, C. V. *et al.* (2009) *X-ray emission in streamer-corona plasma*. Journal of Physics D: Applied Physics 43.2, 025202.

Okano, D. (2013) *Time-lag properties of corona streamer discharges between impulse sphere and dc needle electrodes under atmospheric air conditions*. Review of Scientific Instruments 84.2, 024702.

Peek, F. W. (1911) *The law of corona and the dielectric strength of air*. Proceedings of the American Institute of Electrical Engineers 30.7: 1485-1561.

Peek, F. W. (1912) *The law of corona and dielectric strength of air—II*. Proceedings of the American Institute of Electrical Engineers 31.6 (1912): 1085-1126.

Pinnangudi, B. N.; Gorur, R. S.; Kroese, A. J. (2002) *Energy quantification of corona discharges on polymer insulators*. In Electrical Insulation and Dielectric Phenomena, Annual Report Conference on (pp. 315-318). IEEE.



Pinnangudi, B. N.; Gorur, R. S.; Kroese, A. J. (2005) *Quantification of corona discharges on nonceramic insulators*. IEEE Transactions on Dielectrics and Electrical Insulation, 12(3), pp.513-523.

Rocha, P. H. V.; Fontgalland, G. (2014) *Measuring the radiation bands of overhead power lines glass insulators*. In Antenna Measurements & Applications (CAMA), 2014 IEEE Conference on, pp. 1-3. IEEE.

Sarathi, R.; Reid, A. J.; Judd, M. D. (2008) *Partial discharge study in transformer oil due to particle movement under DC voltage using the UHF technique*. Electric Power Systems Research 78, no. 11, pp. 1819-1825.

Sarathi, R.; Umamaheswari. R. (2013) *Understanding the partial discharge activity generated due to particle movement in a composite insulation under AC voltages*. International Journal of Electrical Power & Energy Systems 48, pp. 1-9.

Vahidi, B.; Alborzi, M. J.; Aghaeinia, H.; Abedi, M. (2003) *Acoustic diagnoses of AC corona on the surfaces of insulators*. In Power Tech Conference Proceedings, IEEE Bologna (Vol. 2, pp. 5-pp). IEEE.

Zaazou, A.; Khalifa, M.; El-Debeiky, S. (1964) *Radio noise due to insulator corona*. Electrical Engineers, Proceedings of the Institution of, 111(5), pp.959-966.

PROPOSAL FOR MATCHING THE IMPEDANCE OF A BROADBAND AND HIGH BAND RF RECTIFIER EFFICIENCY FOR ENERGY HARVESTING

DOI: 10.51859/ampla.sst631.1122-13

Francisco Silva e Serpa¹
Hugo Daniel Hernandez Herrera²
Ricardo Luiz da Silva Adriano³

¹ MSc degree in Electrical Engineering and Professor at University of Minas Gerais (UFMG) and Professor at Federal Institute of Pará (IFPA), Parauapebas, PA, Brazil.

² Ph.D degree in Electrical Engineering from University of São Paulo.

³ Ph.D degree in Electrical Engineering and Professor at University of Minas Gerais (UFMG), Belo Horizonte, MG, Brazil.

ABSTRACT

The expansion of wireless devices, added to the diversity of communication standards using different frequency bands in urban environments, have boosted energy harvesting from RF. RF rectifiers for direct current are traditionally designed to operate in a narrow frequency range, but the harvesting of RF energy in a wide frequency band advantageously allows to have access to several RF sources simultaneously. However, the conversion efficiency and the impedance matching in a wide frequency band are profoundly affected by the non-linearity of the diodes and the input impedance variation as a function of the input RF power. Therefore, new topologies and techniques are needed for the design of broadband RF rectifiers. This work proposes a design of a RF rectifier with high efficiency in broadband frequencies for harvesting applications. The project includes a double topology rectifier, and a new impedance matching circuit composed of an inductor and a transmission line, correctly dimensioned using a new design methodology, thus obtaining resonance in a wide bandwidth. The proposed rectifier was manufactured and experimentally characterized, demonstrating an energy conversion efficiency greater than 50% for a bandwidth of 92.06% (0.68 – 1.84 GHz), 0 dBm of power from 1.5 $k\Omega$ input and load, with maximum efficiency of 67.6% at 1.03 GHz frequency.

Key words: Broadband. Efficiency. Energy Harvesting. Radio-frequency. Rectifier RF.

1. INTRODUCTION

The reuse of electromagnetic energy is increasingly space. This is mainly due to the increase in the number of Internet Things (IoT) that use different communication standards, such as Wireless Fidelity (Wi-Fi), Bluetooth, ZigBee, Sigfox, Radio Frequency Identification (RFID), Long Range (LoRa), 3G, 4G and Global System for Mobile Communications (GSM) 900 or 1800 MHz to communicate with other devices or people.

Most of the studies proposed in the literature of wireless sensor networks using Energy Harvesting, using a single band of frequencies (Mansour & Kanaya, (2019)). However, the strength of the RF signals presents in the environment is not stable, varying over time according to distance from the rectenna to the transmitter (Mansour & Kanaya, (2019)). Then, it can be concluded that energy from a wide frequency range, to a wide range of RF power levels, promises to be a more reliable approach for this kind of applications.

However, designing a high-efficiency RF-DC rectifier for a wide frequency band because the capability of this parameter at the input of the rectifier causes instability in the input impedance of the rectifier, consequently, mismatch with antenna impedance, drastically affecting the disaster do the power conversion system. The input impedance of the rectifier is based on in the diode impedance, which does not vary linearly with the operating frequency and the available RF signal strength (He & Liu, (2020)). This impedance mismatch input of the rectifier circuit with the antenna, it needs a correction through an impedance matching circuit. This circuit must be carefully designed for simultaneously high efficiency over a wide frequency band for a low input power.

The main objective of this study is to design, simulate and experimentally characterize a high RF rectifier operating in a wide frequency range for Energy Harvesting applications. In addition to reviewing the literature on quarter-wave transformer impedance matching circuits section, propose a new wideband rectifier input impedance matching circuit, as well as a suitable design methodology for the calculation and selection of components, implement the designed circuit layout and perform electromagnetic simulations and

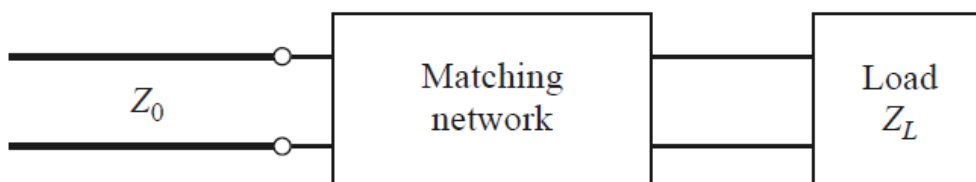
manufacture the prototype and validate the data through experimental measurements.

The chapter is divided into three parts. In the first part is the introduction and objectives. The second part will present a review of the literature on quarter-wave transformer impedance matching circuits single section. The third part describes a design methodology that includes an input impedance correction used in the rectifier for impedance matching and analysis tools and, finally, presents simulation and experimental results that illustrate and confirm the computational efficiency of the proposed system, and compares with other works consolidated in the literature.

2. IMPEDANCE MATCHING METHOD

Impedance matching is one of the most important parts of a process. Design of a microwave system. The basic concept of impedance matching is illustrated in Figure 1, which shows an impedance matching network inserted between a load impedance (Z_L) and a transmission line (Z_0) (Pozar, (2012)). Impedance matching happens when $Z_0 = Z_L$ which satisfies the maximum power given at this point. The matching network is ideally lossless, to achieve the power maximum provided in the circuit. When using a matching circuit, reflections on the line of transmission will be eliminated for the left side of the matching circuit, taking into consideration that there will be multiple reflections between the load and the match circuit. That impedance adjustment procedure for loss reduction and power optimization it's called tuning.

Figure 1 – An impedance matching network between an arbitrary impedance with a transmission line.



Source: Pozar, (2012).

There are various designs and methods of matching networks that can be used, the choice of a particular network will depend on the simplicity of the application,

the bandwidth, the type of transmission line or waveguide used and the adjustability in variable impedances.

2.1. MATCHING CIRCUIT WITH QUARTER WAVE TRANSFORMER SINGLE SECTION

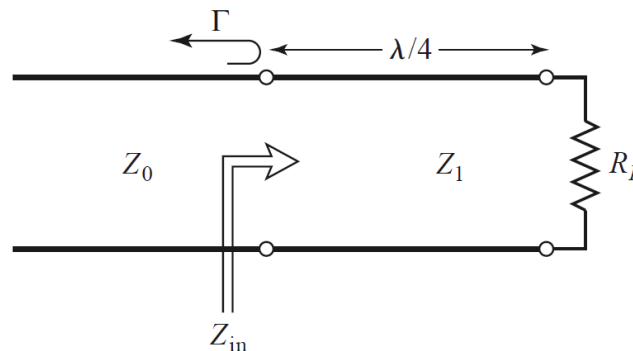
The method for matching the circuit to the quarter-wave transformer inserts a transmission line with a length of $\lambda/4$ and characteristic impedance unknown Z_1 that produces a combined system when placed between a resistance of load R_L and the transmission line characteristic impedance Z_0 which are known, as shown in figure 2.

$$Z_{in} = Z_1 \frac{R_L + jZ_1 \tan \beta l}{Z_1 + jR_L \tan \beta l} \quad (1)$$

But $\beta l = \left(\frac{2\pi}{\lambda}\right) \left(\frac{\lambda}{4}\right) = \frac{\pi}{2}$ then $\tan \beta l = \infty$ so $Z_{in} = \frac{Z_1^2}{R_L}$

$$Z_{in} = \frac{Z_1^2}{R_L} = Z_0 \rightarrow Z_1 = \sqrt{Z_0 R_L} \quad (2)$$

Figure 2 - Impedance matching method with quarter transformer wave.



Source: Pozar, (2012).

For $\Gamma = 0$, one should have $Z_{in} = Z_0$, which yields the characteristic impedance Z_1 as what is the geometric mean of the load and source impedances. Then there won't be standing waves in the supply line (Standing Wave Ratio (ROE) = 1), although there are standing waves in the corresponding section $\lambda/4$. Furthermore, the condition above applies only when the length of the corresponding section is $\lambda/4$ or an odd multiple of $\lambda/4$, long, so a perfect match can be achieved in one frequency, but the impedance mismatch will occur at other frequencies. At the design

frequency, f_0 , the electrical length of the corresponding section is $\lambda_0/4$, but at other frequencies the length is different, so a combination perfect is no longer obtainable. In order to generate an approximate expression for the resulting impedance versus frequency mismatch will be derived some expressions, the first of which is the input impedance seen for the match section is given by equation 3:

$$Z_{in} = Z_1 \frac{Z_L + jZ_1 t}{Z_1 + jZ_L t} \quad (3)$$

where $t = \tan \beta \ell = \tan \theta$, and $\beta \ell = \theta = \pi/2$ at design frequency f_0 .

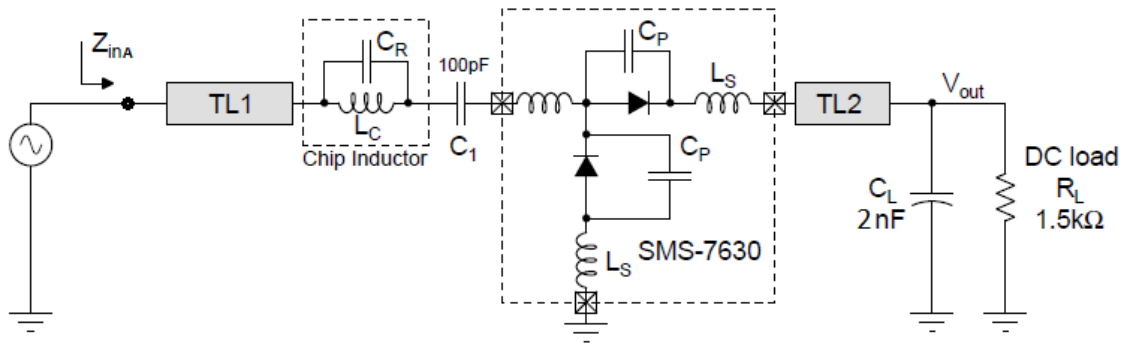
3. PROJECT METHODOLOGY AND RESULTS

In this part, the design methodology used will be presented and discussed for matching the input impedance of the rectifier. And then will be discussed the computational tools used for circuit modeling and simulation of calculations. And soon after, the manufacturing and measurement parameters of the prototype will be displayed. Finally, the validation of the experimental results of the performance parameters (PCE and S11) with the simulated values and with the related works.

3.1. RECTIFIER ARCHITECTURE

In figure 3 shows the schematic of the proposed rectifier circuit which is based on in a voltage doubler topology. The input impedance correction is performed by inserting an inductor and a transmission line called TL_1 in series with the rectifier, which will be analyzed later, the 100 pF series C_1 capacitor with the function to block the DC voltage of the source, two Schottky SMD diodes model SMS7630-005LF, a TL_2 transmission line of $\lambda/4$ in series with the load with the function of blocking the harmonics generated by the rectifier, a 2 nF charge capacitor C_L with the function of reducing the ripple effect of the voltage of output and also a charging accumulator. And finally, the charge called the R_L of 1.5 k Ω .

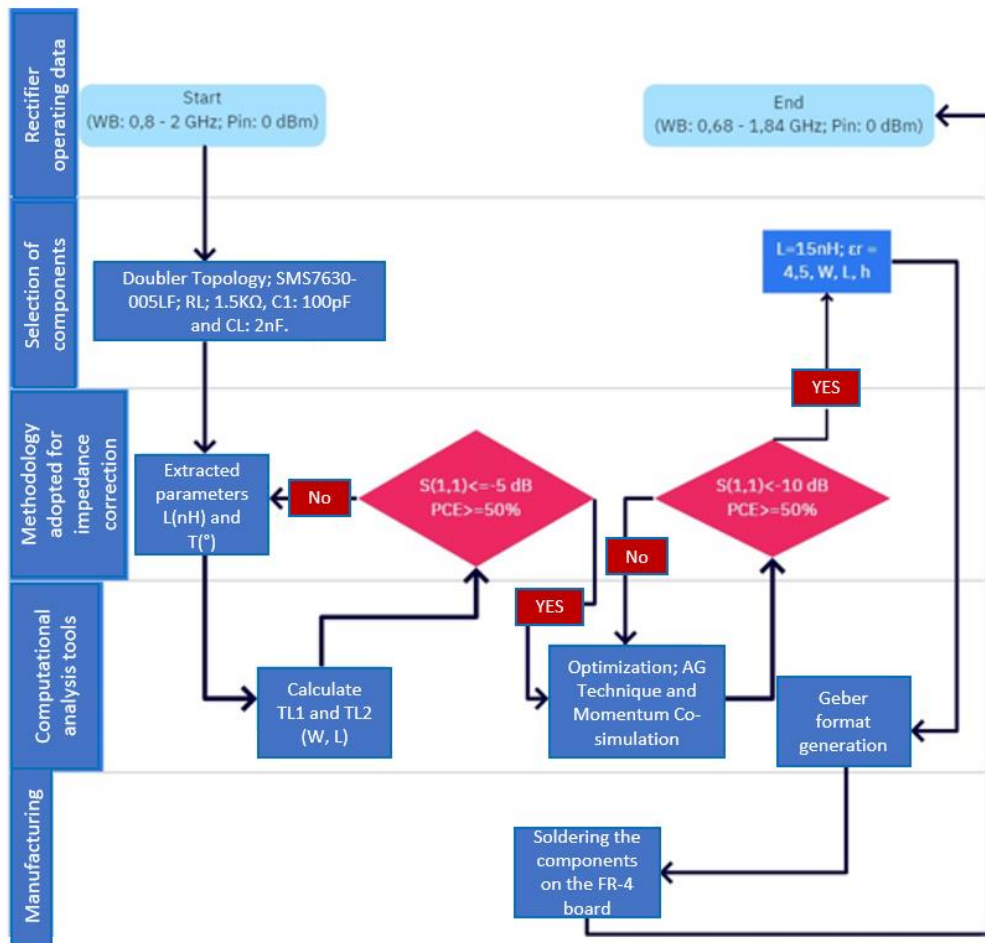
Figure 3 – Schematic of the proposed rectifier circuit.



Source: The author.

All stages of the project can be visualized in the flowchart in figure 4. According to the first stage, the operating data foreseen for the project were the width bandwidth (WB) of 0.8 to 2 GHz and an input power (P_{in}) of 0 dBm. Right after study presented in second part and based on bandwidth and (P_{in}), were also defined the topology, the Schottky diode model and some components such as the resistor (R_L), the blocking capacitor (C_1) and the charging capacitor (C_L). The choice of 1.5 kΩ resistor was based on correlated work presented in table 1. With the new methodology for correcting the input impedance of the rectifier, shown in the next subsections, it is possible to extract the values of the parameters values wavelength (θ or T), inductor (L_c) and characteristic impedance (Z_A or Z_c). In the fourth step, the width (W) and length (L) of the track (TL1) were dimensioned and then verified the first decision making with the prerequisites of performance $S_{11} < -5dBm$ and $PCE > 50\%$, how effectively met advanced use to the penultimate step called optimization, which computational tools are essential to achieve the efficiency of the prerequisites ($S_{11} < -10dBm$ and $PCE > 50\%$) and the scaling accuracy of the parameters L_c, er, h, L, W and TL2. At In the last step, the project was generated in Gerber format for manufacturing of the FR4 substrate and the soldering of the components. The prototype can be seen in Fig. 8.

Figure 4 – Flowchart with the project stages.



Source: The author.

3.2. METHODOLOGY FOR INPUT IMPEDANCE MATCHING

This work proposes a new design methodology for impedance matching rectifier input based on quarter transformer method single section waveform mentioned in subsection 2.1. As per the fractional bandwidth, a high percentage of bandwidth can be achieved. Band across load impedance (Z_L), transmission line characteristic impedance (Z_0), design frequency (f_0) and a given ROE. But to reach a track wide bandwidth, the equation does not meet, as only a frequency of project. So, the proposal to adapt the impedance matching method with quarter-wave transformer is to use equation 3 for two frequencies of design, defined as f_1 and f_2 , and insert in addition to a transmission line TL_1 with a predicted wavelength (θ) and characteristic impedance Z_A , also an inductor in series (L_c) that will produce a matched system when placed between the impedance of the rectifier circuit/load (Z_{rc}) and the characteristic impedance of the transmission line Z_0 that are known. TL_1 is employed to make Z_{inA} real almost constant and the part imaginary

symmetric (odd) with respect to the central frequency ($f_c = (f_1+f_2)/2$), according to with the following conditions:

$$\text{Real}\{Z_{inA}(f_1) = 50\} \quad (4)$$

$$\text{Real}\{Z_{inA}(f_2) = 50\} \quad (5)$$

$$\text{Imag}\{Z_{inA}(f_1)\} = -\text{Imag}\{Z_{inA}(f_2)\} \quad (6)$$

The reactance of the rectifier/load circuit impedance (Z_{rc}) will sum to the inductive reactance predicted for the two design frequencies, as shown in the equations 7 and 8.

$$X'_1 = X_{rc1} + 2\pi f_1 L \quad (7)$$

$$X'_2 = X_{rc2} + 2\pi f_2 L \quad (8)$$

The TL_1 transmission line has characteristic impedance Z_A and length electric θ_1 to f_1 and electric length θ_2 to f_2 . The input impedance point A in the proposed circuit can be seen in figure 3 and the expressions are given by:

$$Z_{inA}(f_1) = Z_A \frac{(R_1 + jX'_1) + jZ_A \tan\theta_1}{Z_A + j(R_1 + jX'_1)\tan\theta_1} \quad (9)$$

$$Z_{inA}(f_2) = Z_A \frac{(R_2 + jX'_2) + jZ_A \tan\theta_2}{Z_A + j(R_2 + jX'_2)\tan\theta_2} \quad (10)$$

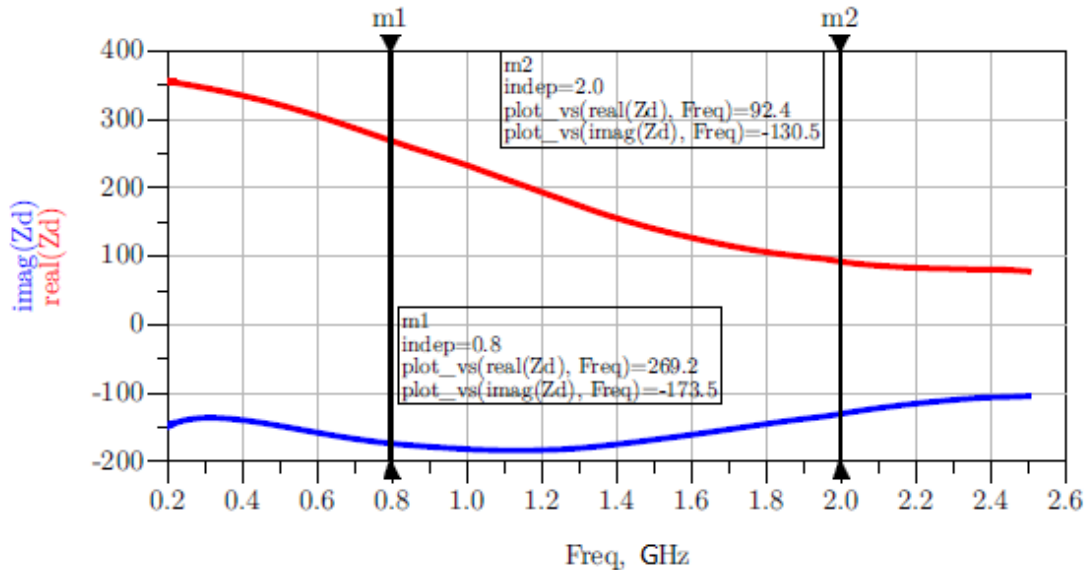
$$\theta_2 = k\theta_1 \quad (11)$$

3.3. COMPUTATIONAL ANALYSIS TOOLS

Figure 5 illustrates the real part (R) and the imaginary part (X) of the impedance of rectifier input in terms of frequency of the Large-Signal S-Schematic Simulation Parameter (LSSP), for an input power (P_{in}) of 0 dBm. To facilitate the analysis of the circuit, the lowest and highest frequencies of the frequency band of operation as f_1 and f_2 , respectively. In this work, nominally the frequencies $f_1 = 0.8$ GHz and $f_2 = 2$ GHz. A frequency relationship was also defined as $k = f_2/f_1 = 2, 5$. At f_1 and f_2 , the input impedance of the rectifier (Z_{inA}) was denoted as $R_1 + X_1j = 269 - 173, 5j$ and $R_2 + X_2j = 92 - 130j$. Through the inductor matched (L_c) in series with the DC

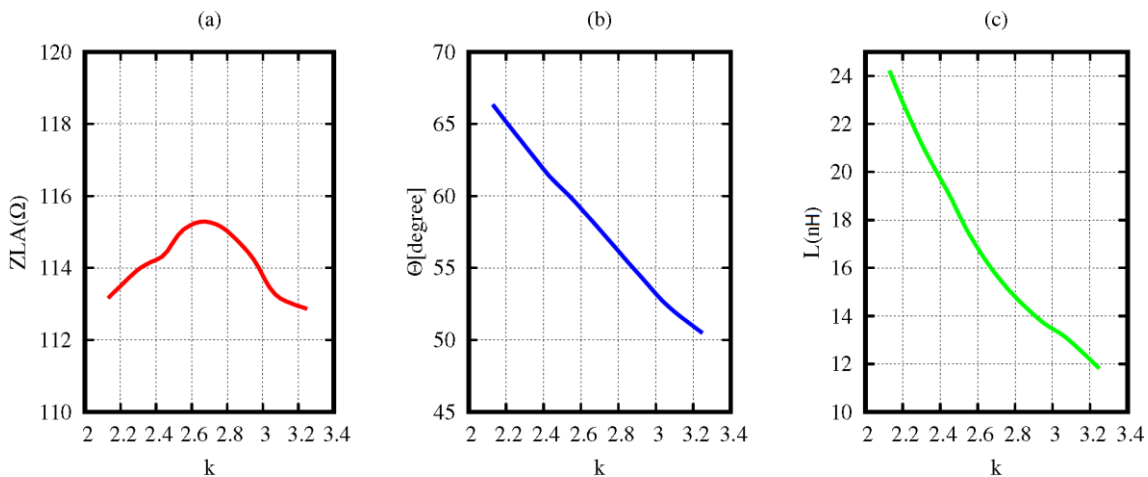
blocking capacitor (C_1) will allow to reduce the reactance capacitive input impedance. Equations 4 through 6 can be solved numerically, obtaining θ , L , and Z_A , from real and imaginary part of Z_{rc} in f_1 and f_2 . Figure 6 shows the calculated values of θ_1 , L and Z_A with respect to k .

Figure 5 – Real part (R) and imaginary part (X) of rectifier input impedance versus frequency for schematic simulation LSSP.



Source: The author.

Figure 6 – Calculated values of θ_1 , L , and Z_A with respect to k .

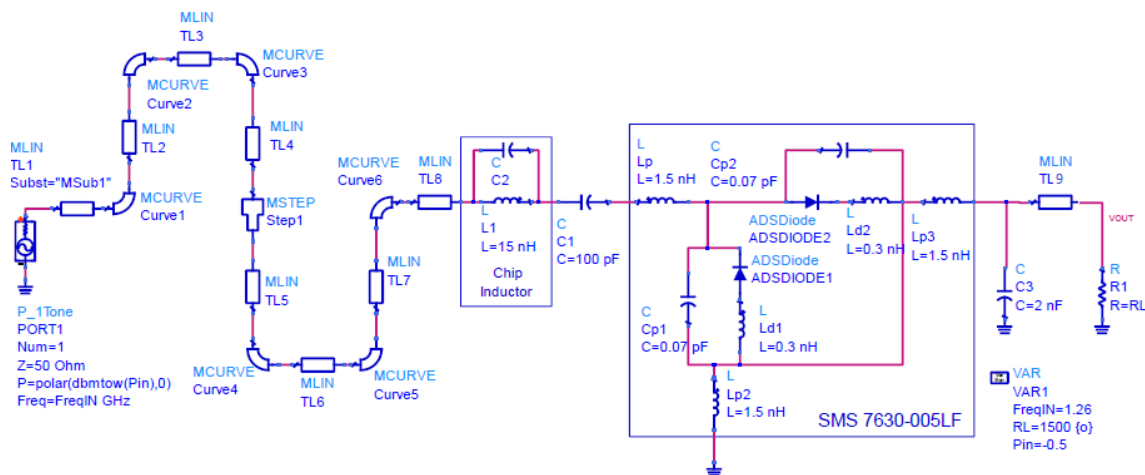


Source: The author.

However, in addition to the method used for impedance matching and the LSSP simulation tool of the Advanced Design System® (ADS®) software as a way of extracting the impedance of input, other support tools were used, such as the Harmonic Balance (HB) simulation mode used for simulation and analysis of power in analog circuits nonlinear operating on RF and impedance with power control.

Then it was used the optimization tool that uses the technique of Genetic Algorithm (GA), with 500 iterations depending on the condition of efficiency greater than 60%. Finally, the last optimization step is Electromagnetic Co-simulation, an electromagnetic simulator which transforms Maxwell's electromagnetic equations into integral equations and then applies numerical discretization, a process known as the method of moments. With this is possible a numerical approximation of the simulation with the measurements, because the calculation now considers the plane structures in substrates with layers and losses. In this way the Circuit layout has undergone minor adjustments, as shown in Figure 7.

Figure 7 – Final layout of the rectifier circuit.

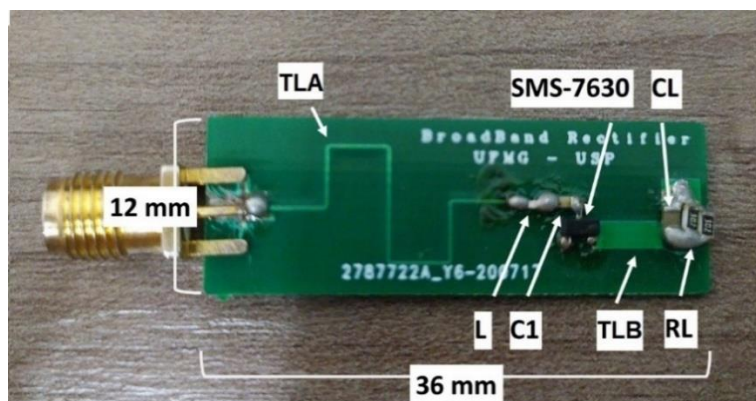


Source: The author.

3.4. EXPERIMENTAL RESULTS

The designed wideband rectifier is manufactured on FR4 substrate 0.8 mm ($\epsilon_r = 4.5$) as shown in figure 8.

Figure 8 – Photo of the manufactured rectifier circuit.



Source: The author.

S11 measurements were performed with a Vector network analyzer (VNA) ROHDE&SCHWARZ model ZVL6. The return loss indicates the proportion between the power incident and reflected, which corresponds to parameter S11 in the scattering matrix, so it is defined as:

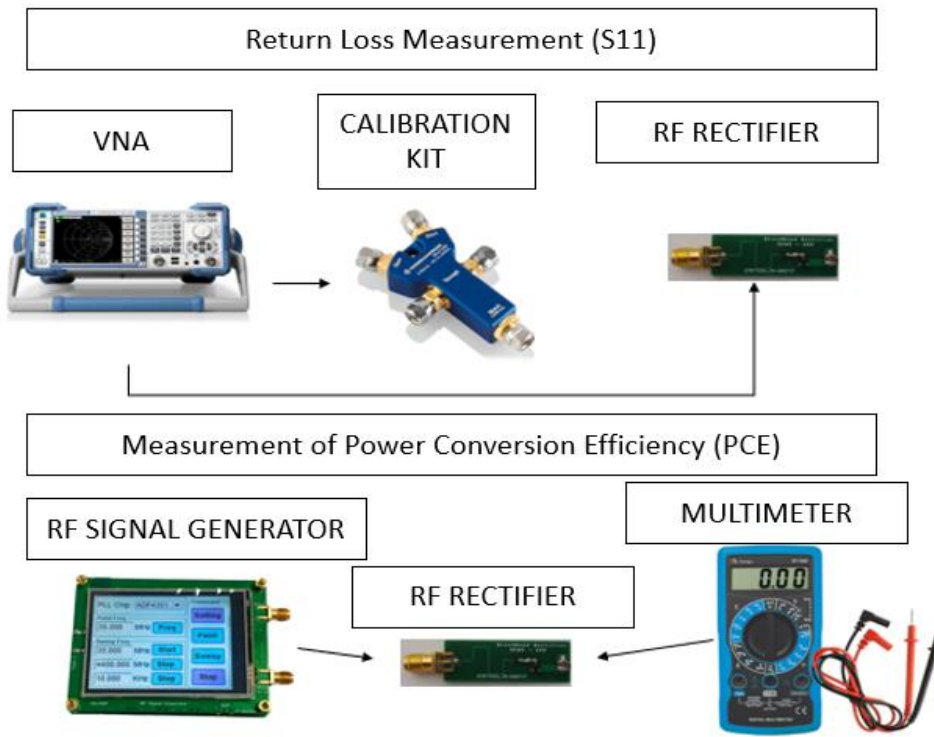
$$S_{11}(dB) = 20 \log \frac{|V_i^-|}{|V_i^+|} (dB) = 20 \log |\Gamma_i| (dB) \quad (12)$$

Being an excellent index for performance determination, in which it is accepted in the practice values smaller than $-10dB$. Before performing the S11 measurement, the VNA was calibrated to remove systematic errors that can alter the actual reading value, then used the calibration kit with known standards (open, short and load) and compared to the value that the VNA measured. And through a series of corrections error, the VNA port 1 reference point has moved to the calibration point, located at the end of the cable. And with that it removed all the propagation loss from the cable and the connector used. Figure 9 shows a schematic of the elements used in the S11 and PCE measurements.

Figure 10 shows the simulated and measured S11 in the same graph for 0 dB of input power. The results show good agreement between the simulated values. And measured, with slight difference in impedance bandwidth and location of the resonant sinkings. However, S11 is below -10 dB in the frequency range. Range from 0.4 to 1.8 GHz, as shown in figure 10. The discrepancies may have been generated by diode model inaccuracies and variations in the FR4 substrate parameters.

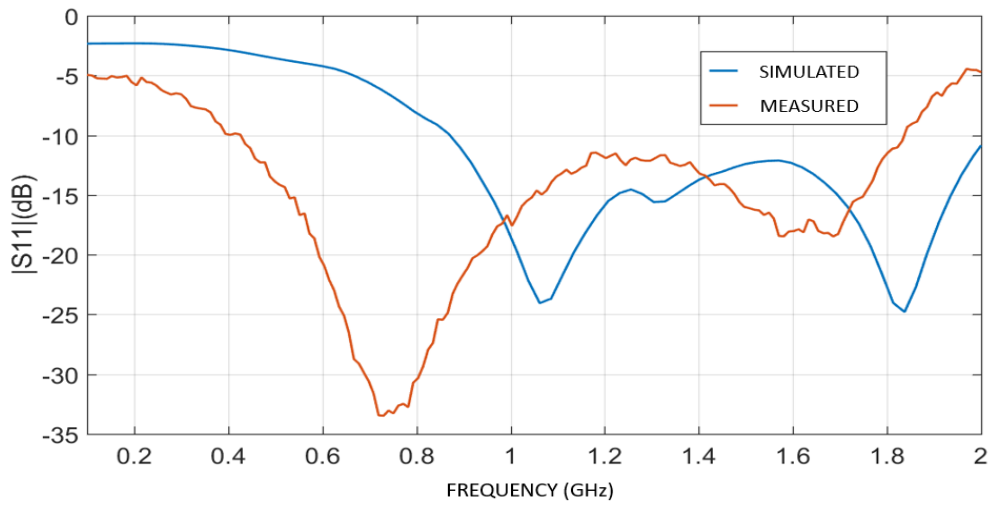
The power conversion efficiency (PCE) of the proposed rectifier was characterized through measurements made by an RF signal generator with fixed input power of 0 dBm and a multimeter to collect the DC output voltages at the load. This measure was performed on two prototypes for comparison and verification. Figure 11 shows the simulated and measured PCE, which shows a good agreement between the two results. An efficiency greater than 50% is achieved from 0.68 to 1.84 GHz, corresponding to a fractional bandwidth of 92%. With the proposed approach, complex circuits for marriage of impedance are not required, resulting in a significant reduction in loss of insertion and circuit dimensions, ensuring high efficiency over a wide range of frequency.

Figure 9 – Schematic of S11 and PCE measurements.



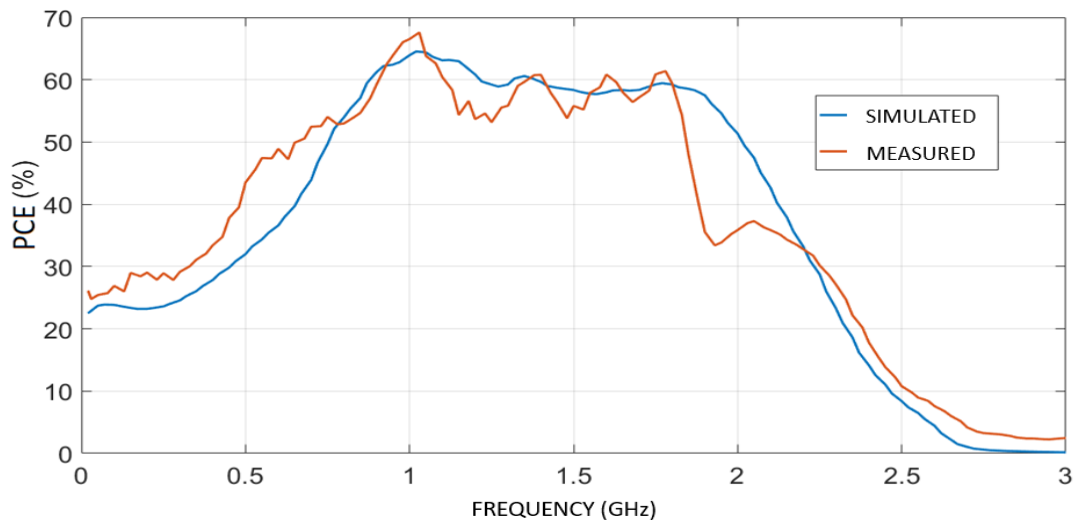
Source: The author.

Figure 10 – Measurement and simulation chart $|S_{11}|$ versus frequency at 0 dBm P_{IN} .



Source: The author.

Figure 11 – PCE measurement and simulation graph versus frequency at 0 dBm P_{IN} .



Source: The author.

A comparison was also made between the proposed rectifier of this work and the rectifiers presented, according to table 1. were chosen rectifiers sized for wide frequency band and with the same objective of maximum efficiency. It can be seen that the proposed rectifier has a competitive featuring a Wide-band (BW) with efficiency greater than 50% of 1.16 GHz (92% fractional bandwidth), even for lower input power than previous works. To make a fair comparison, the Figure of Metric (FoM) used by several works was calculated for each proposal. And this parameter has its expression given by:

$$FoM = \frac{PCE(F_{max} - F_{min})}{F_c} \quad (13)$$

Table 1 – Comparison with other reported broadband rectifiers.

References	[1]*	[2]*	This work
Freq. (GHz)	0.54 – 1.3	0.87 – 2.5	0.68 – 1.84
BW (GHz)	0.76	1.63	1.16
Pin(dBm)	5	0	0
PCE @ Máx. (%)	50 @ 80**	30 @ 63	50 @ 67.6
FoM	41.3	29	42.85
Size (mm²)	670	114	432

[*][1]=(PARK & HONG, (2020)) e [2]=(MANSOUR & KANAYA, (2018)); [**] para 10 dBm.

Source: The author.

4. FINAL CONSIDERATIONS

This work presented the matching method of impedance with quarter-wave transformer

single section. With this, it was possible to introduce a new topology of the input impedance matching circuit of the wideband rectifier. The new circuit consists of an inductor and a transmission line, sized correctly through a new design methodology.

This new simple methodology design for the proposed matching circuit was based on simulation results, where it was possible to have an initial model and finally an adjustment of the project through optimization tools.

The proposed rectifier was fabricated and experimentally characterized, the results have proven rectification efficiency greater than 50% for a bandwidth 92.06% (0.68 – 1.84 GHz), 0 dBm input power and 1.5 load $k\Omega$, with the maximum efficiency of 67.6% at the frequency of 1.03 GHz. And when compared with other related scientific works, it was competitive mainly due to low input power and FoM.

REFERENCES

e Serpa, F. S., Hernandez, H. D., & Adriano, R. L. D. S. (2021, October). A Compact High-Efficiency Broadband RF Rectifier for Energy Harvesting Applications. *In 2021 SBMO/IEEE MTT-S International Microwave and Optoelectronics Conference (IMOC)* (pp. 1-3). IEEE.

He, Z., & Liu, C. (2020). A compact high-efficiency broadband rectifier with a wide dynamic range of input power for energy harvesting. *IEEE Microwave and Wireless Components Letters*, 30(4), 433-436.

Mansour, M. M., & Kanaya, H. (2018). Compact and broadband RF rectifier with 1.5 octave bandwidth based on a simple pair of L-section matching network. *IEEE Microwave and Wireless Components Letters*, 28(4), 335-337.

Mansour, M. M., & Kanaya, H. (2019). High-efficient broadband CPW RF rectifier for wireless energy harvesting. *IEEE Microwave and Wireless Components Letters*, 29(4), 288-290.

Park, H. S., & Hong, S. K. (2019). Broadband RF-to-DC rectifier with uncomplicated matching network. *IEEE Microwave and Wireless Components Letters*, 30(1), 43-46.

Pozar, D. M. (2011). *Microwave engineering*. John wiley & sons.

TECHNIQUES TO OPTIMIZE RETURN LOSS OF HIGH-SPEED SERIAL LINKS ON A MULTILAYER PCB

DOI: 10.51859/ampla.sst631.1122-14

Bruno Machado Bernardi¹
Eduardo Endler²
Diego August Timm¹
Rodrigo Marques de Figueiredo³
Eduardo Luis Rhod⁴
Sandro Binsfeld Ferreira⁵

¹ MSc in Electrical Engineering from Unisinos School. R&D at Teracom Telemática S.A.

² BSc in Electrical Engineering from the Federal University of Rio Grande do Sul. R&D at Teracom Telemática S.A.

³ Dr. in Geology from Unisinos University. Professor at the Polytechnique School. Unisinos University.

⁴ Dr. in Microelectronics from the Federal University of Rio Grande do Sul. Illusense Inc.

⁵ Dr. in Microelectronics from the Federal University of Rio Grande do Sul. Professor at the Polytechnique School. Unisinos University.

ABSTRACT

Optimizing return loss for vias and high-density BGA (Ball Grid Array) areas is becoming important as signaling speed increases. Designing high speed PCB (Printed Circuit Board) without field solver simulations can cause severe signal integrity problems. In this paper, design and simulation methodologies are adopted to optimize 25 Gbps (Gigabits per second) high-speed serial links on a multilayer PCB. To improve signal integrity, return loss is lowered using two key strategies. Initially, a differential-via anti-pad impedance is optimized in a high-speed connector through a 3-D field solver approach. Then, advanced PCB layout techniques for BGA signals breakout (fan out) are employed from the ball to the outside of BGA area, and effectively demonstrated using field solver results. Therefore, an overall return loss improvement of approximately 8 dB is achieved between 5 to 7 GHz, enabling the design to pass 25GBASE-KR normative mask with a good margin.

Key words: Anti-pad optimization, High-speed, Return Loss, Signal Integrity, BGA Breakout.

1. INTRODUCTION

The constant increase in data demand on telecommunication networks caused by the evolution of several online services requires increasing equipment data rates. Consequently, it is necessary to increase the frequency of buses in network equipment progressively. Nevertheless, the evolution of serial buses brings additional difficulties to the development of printed circuit boards since the higher the frequency, the greater the number of factors that affect signal integrity. One of the main aggressors of high-speed signal integrity is energy loss due to the reflection effect caused by impedance discontinuities in the transmission lines.

Impedance discontinuities on a printed circuit board (PCB) are caused by transmission line changes, such as distance to the return path, line width, variations in the dielectric constant (D_k) of the PCB substrate, or by required vias (vertical interconnect access). When a signal encounters an impedance discontinuity, part of the signal energy is reflected to the source and while the rest proceeds in the forward direction. This lost energy is called return loss (RL) and is represented by the Scattering parameters S_{11} or S_{22} , for a two port network.

There are several studies on optimization of insertion loss and return loss of signals through vias. In (VASA *et al.*, 2018), common designer errors in the optimization of impedance of vias are discussed. In (ZHANG *et al.*, 2014), the addition of transition lines with slightly lower impedance in relation to the vias is proposed to compensate for the capacitive and inductive discontinuities generated by the vias. In (LEE; HIRSCH; BELL, 2018), the optimization of vias using the frequency domain reflected impedance (Z_{11}) is proposed instead of the time domain reflected impedance (TDR) optimization. In (DONG *et al.*, 2017), a method of design and analysis of transmission lines and anti-pads is presented.

In this chapter, we present techniques to reduce the return loss in signals originating from BGA (Ball Grid Array) integrated circuits (IC) and in signal transitions between PCB layers through vias. These techniques were applied in the development and optimization of a 16-layer PCB for 25 Gbps (Gigabit per second) lines. After this brief introduction, section II presents a review of the main return loss reduction techniques used here. Section III presents the problem

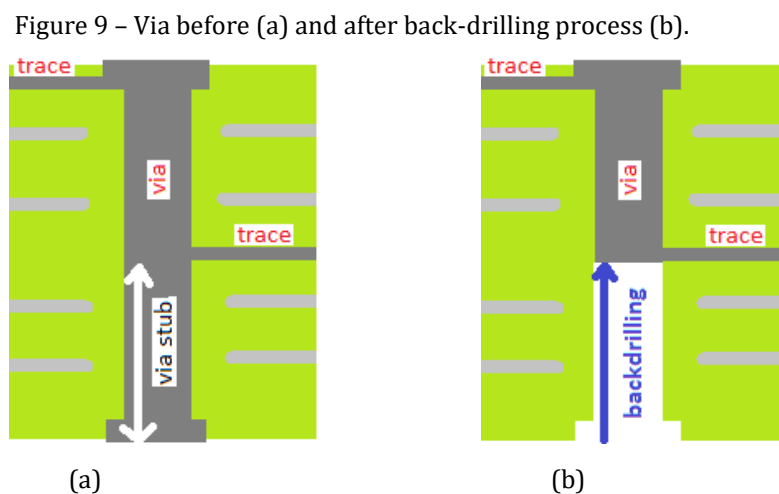
characterization and the target design to be optimized. Optimization results are discussed in section IV. Finally, conclusions are presented in section V.

2. TECHNIQUES TO MINIMIZE RETURN LOSS

Most signal reflections in a multi-layer PCB are caused by via impedance discontinuities. The impedance, as with any transmission line, is defined by the properties of the materials, such as the distance between signal path and return plane, as well as the associated dielectric constant.

2.1. BACK-DRILLING

The back-drilling was used to suppress reflection. In this process, part of the copper that has no signal transmission function in the via is removed, reducing the stub, and consequently the signal return loss. Figure 1a shows a via that carries a signal from the top layer to an inner layer. The portion of the via that goes from the inner layer to the bottom layer is named via stub. Figure 9b shows a via after the back-drilling technique was applied, thus eliminating the stub.



Source: (FEI, 2013).

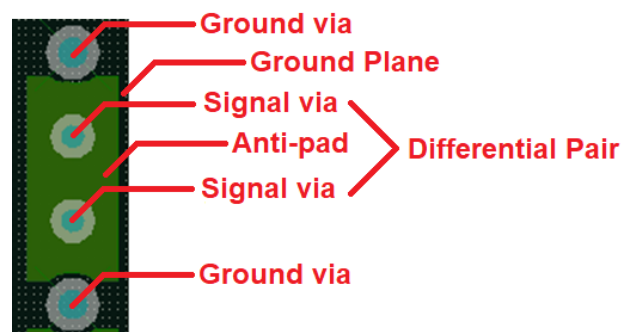
No simulations have been performed to demonstrate the advantages of back-drilling since the technique is widely covered by several studies. Fei concluded that “a higher channel bandwidth is realized by a transmission line with back-drilled vias” (FEI, 2013). The Insertion Loss (IL) of vias without back-drilling, microvias and back-drilled vias are compared in (JOHANSSON; MANEFJORD, 2017), and the paper concludes that “the measured loss of the microvia and back-drilled via showed almost the same performance regarding their signal loss”. The variations of link

performance depending on the line length and the number of PCB layers were studied in (HAN *et al.*, 2014), and it was observed that “for the cases where the layer number is equal or larger than six, the reflection loss from stub vias limits speeding up the signal velocity. For the stubless case (using back-drilling), the maximum allowable baud rate stays almost constant with the increase in the number of signal layers”.

2.2. CONNECTOR ANTI-PADS

In a connector via, the distance between signal via and return via is called anti-pad. It is identified in green in the component footprint of a differential via presented in Figure 10. In the footprint, other elements like ground vias and ground planes are also identified.

Figure 10 - Initial connector anti-pad.



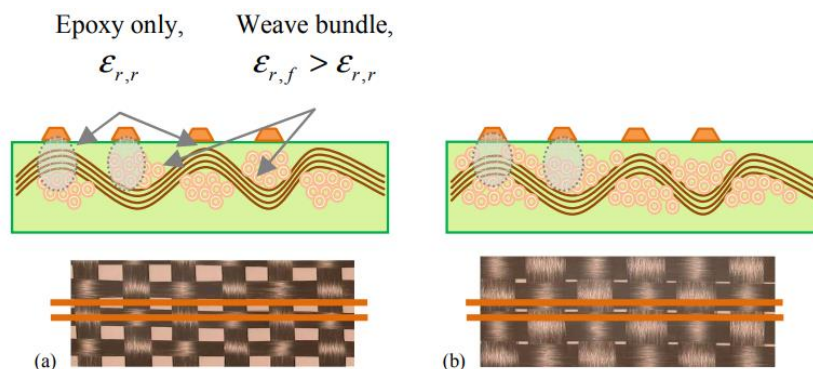
Source: The authors.

2.3. FIBER WEAVE EFFECT

Another source of small discontinuities along the PCB line is the fiber weave effect (FWE), caused by the difference in fiber weave ($\epsilon_{r,f}$) and resin dielectric constant ($\epsilon_{r,r}$). It is a constructive feature of multi-layer PCBs and cannot be eliminated. This difference in dielectric constant changes the signal speed in the dielectric material.

Figure 11 presents two different substrates with non-spreading and spreading glass cloth substrates, resulting in different dielectric properties.

Figure 11 – Traces with different substrates, different dielectric permittivities with non-spreading glass cloth (a) or spreading glass cloth (b).



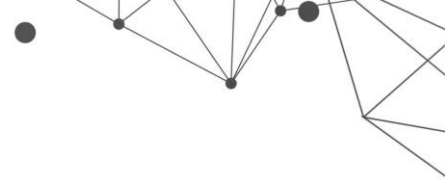
Source: (BUCUR, 2014).

For high-speed differential pairs, this effect could be critical, as one line of the pairs can run over the resin and the other over the fiber, which would cause different signal arrival times at the receiver, thus degrading the signal integrity. It was pointed out in (BUCUR, 2014) that the timing skew has to be carefully verified when design is moving towards data rates higher than 3 Gbps.

3. STRUCTURES, MATERIALS AND COMPONENTS DEFINITION

The study case design shows the optimization of the channels between the connectors and the BGA IC. The laminates used in the optimized PCB case were EM-891 and EM-891B from Very Low Loss Material line from Elite Material Co., Ltd. with dielectric constant (Dk) between 3.26 and 3.56 (values for 1 GHz) and dissipation factor (Df) between 0.0035 and 0.0037 (values for 1 GHz). HVLP (hyper very low profile) copper foils were used. Figure presents the stackup adopted in this design. All vias in the high-speed signals path (25 Gbps in this work) have been back-drilled. All simulations performed considered a stub of 8 mils on each lane, which is the PCB house tolerance for back-drilling.

The fiber weave effect was mitigated using glass weave style 1035, which is a spread fiberglass. As presented in (BUCUR, 2014), the use of spread fiberglass



improves the performance of a differential signal circuit. In addition, the “two-ply” technique was used, where two layers of dielectric material are stacked between signal layer and return path layer to reduce the probability of a differential pair with one line running over the fiber and another running over the resin. This effect was not simulated. The simulation tools used in this work do not consider the fiber weave effect either. As presented in (BOGATIN *et al.*, 2017), two-ply constructions should have lower intra-pair skew than single-ply.

3.1. CONNECTOR ANTI-PAD OPTIMIZATION

The optimization of connector anti-pads corresponds to the optimization of the signal impedance when running through the connector via. Both the connector and the PCB have a target impedance of 100Ω , so the differential pair vias through the connector will also have this target impedance. The goal is to minimize the impedance discontinuities across the entire signal path. For this work, we used a 3-D field solver to simulate the effects of discontinuities across the vias with the TDR (Time Domain Reflectometer) analysis, which calculates instantaneous impedance along the signal path, and used S parameter extraction for the Return Loss Analysis.

Figure 5 shows the default footprint defined by the connector manufacturer of the used part number. Since it is a press-fit connector, placement and dimensions of the vias cannot be changed. We can only optimize anti-pad dimensions (133.8 x 59 mils) to get the differential target impedance closer to 100Ω .

Figure 4 – PCB stackup.

Name	Thickness (mils)	Material	Dielectric constant	Loss tangent
DIELECTRIC-1	0.67	SolderMask_SCC	4	0.025
L1 - top	2	copper	4	0.025
Dielectric_1	3.34646	EM891_PP_1078_RC69	2.96	0.0036
L2 - GND	1.22047	copper	2.96	0.0036
Dielectric_2	5	EM891_Core_2x1078_RC57	3.26	0.0039
L3 - mid1	0.61	copper	2.92	0.0035
Dielectric_3	4.146	EM891_PP_2x1035_RC71	2.92	0.0035
L4 - GND	1.22047	copper	2.92	0.0035
Dielectric_4	5	EM891_Core_2x1078_RC57	3.26	0.0039
L5 - mid2	0.61	copper	2.92	0.0035
Dielectric_5	4.146	EM891_PP_2x1035_RC71	2.92	0.0035
L6 - GND	1.22047	copper	2.92	0.0035
Dielectric_6	4.01575	EM891_Core_1x3313_RC57	3.56	0.0039
L7 - mid4	1.22047	copper	2.96	0.0035
Dielectric_7	5.563	EM891_PP_2x1080_RC69	2.96	0.0035
L8 - GND 3oz	3.66141	copper	2.96	0.0035
Dielectric_8	5.90551	EM891_Core_2x1080_RC65	3.1	0.0037
L9 - GND 3oz	3.66141	copper	2.96	0.0035
Dielectric_9	5.563	EM891_PP_2x1080_RC69	2.96	0.0035
L10 - mid5	1.22047	copper	2.96	0.0035
Dielectric_10	4.01575	EM891_Core_1x3313_RC57	3.56	0.0039
L11 - GND	1.22047	copper	2.92	0.0035
Dielectric_11	4.146	EM891_PP_2x1035_RC71	2.92	0.0035
L12 - mid6	0.61	copper	2.92	0.0035
Dielectric_12	5	EM891_Core_2x1078_RC57	3.26	0.0039
L13 - GND	1.22047	copper	2.92	0.0035
Dielectric_13	4.146	EM891_PP_2x1035_RC71	2.92	0.0035
L14 - mid7	0.61	copper	2.92	0.0035
Dielectric_14	5	EM891_Core_2x1078_RC57	3.26	0.0039
L15 - GND	1.22047	copper	2.96	0.0036
Dielectric_15	3.34646	EM891_PP_1078_RC69	2.96	0.0036
L16 - bottom	2	copper	4	0.025
DIELECTRIC-2	0.67	SolderMask_SCC	4	0.025

Source: The authors.

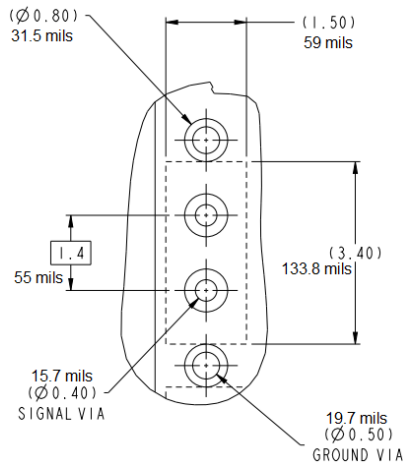
The anti-pad identified previously in Figure 10 is the only part to be optimized. PCB layout was designed in Altium Designer, exported in ODB++ and imported into Ansys SIwave. The 3-D model was generated using Ansys HFSS, as shown in Figure .

3.2. BGA BREAKOUT

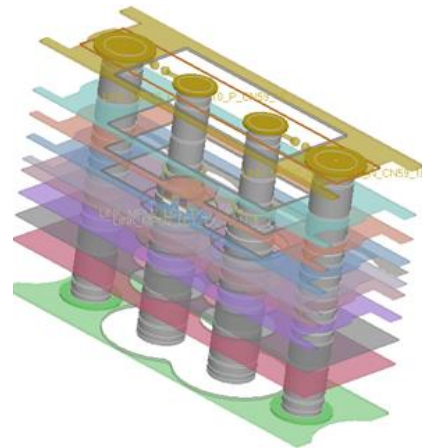
One of the biggest contributors to the reflections in a PCB design with BGA is the signal fan-out from the BGA area, also called signal breakout. Hence, improvements need to be implemented there to reduce reflections and signal return loss. The distribution of BGA balls demanded the signals fan-out distribution in two different layers, which contributed to the isolation of RX (receive) and TX (transmit) signals, thus minimizing crosstalk. To reduce the layer count, the signals were routed as differential pairs in the breakout area. Another option would be to route as single-ended signals and coupling them outside, which would be better for signal integrity, but it would add at least four layers to the PCB stackup.

Figure 5 – Footprint defined by the press-fit connector [10].

Figure 6 - HFSS 3-D connector via model.



Source: The authors.



Source: The authors.

The main difficulty of routing traces in the BGA area is the limited space. In this design, the smallest allowed via diameter due to PCB thickness is 8 mils in diameter, according to the maximum aspect ratio defined by the PCB house. Consequently, with 1 mm pitch for balls and vias and with the anti-pads width of 26 mils, the available space remaining for pairs routing is about 12.8 mils. The differential pair structure used was loosely coupled (except in the breakout area), in which the pair separation should be between 1.5 and 2 times the reference plane distance, as suggested by the IC manufacturer. The loosely coupled pair adopted here has 4.7-mil trace width, 7.2 mils of separation, approximately 5 mils for the reference plane and 100Ω impedance. The chosen trace width is not so thick that it makes difficult to route a high-density bus and is not so thin as to impose high insertion loss. This pair structure could not be used for breakout BGA signals, as the pair (4.7 mils / 7.2 mils / 4.7 mils) occupies 16.6 mils, and a consequent tightly coupled structure was used (in which the separation must be equal or smaller than the distance to the reference plan), with 3.7 mils for trace width and 3.5 mils separation. The thinner trace, despite imposing higher losses, reduces discontinuities, as it separates the pair from the edges of the anti-pads, as shown in Figure .

The outer layers (top and bottom) were not used to route high-speed signals, since these layers have less manufacturing control and greater variations, which makes signal integrity less repetitive and predictable. The top layer was used only for the signal output from the ball to the via.

The differential via anti-pads in BGA area (26 x 65 mils) cannot be optimized as they should be much larger to reach 100Ω , though being limited by the high-

density high-speed lines. Figure shows the initial breakout proposal, with tightly coupled lines and anti-pads defined.

Figure 7 – Tightly coupled pair under BGA area.

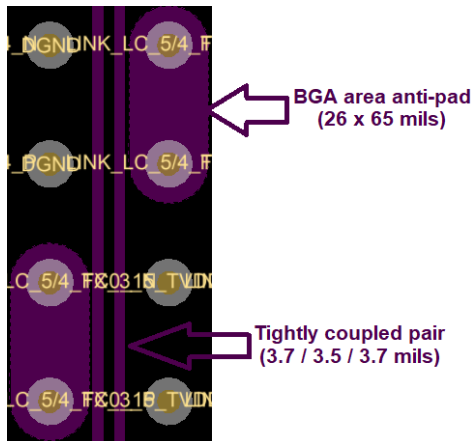


Figure 8 – Initial breakout proposal for high-speed lines.



Source: The authors.

Source: The authors.

4. OPTIMIZATION RESULTS

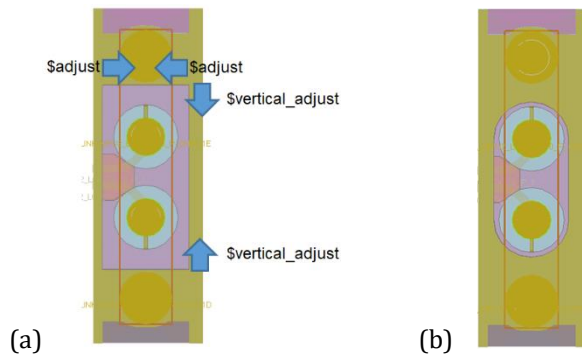
The optimization results are below into anti-pad, ground stub, and breakout area sections for better understanding.

4.1. CONNECTOR ANTI-PAD OPTIMIZATION

To find the most appropriate anti-pad for the connector differential vias, a parametric sweep of the width and height of the anti-pad was performed with Ansys HFSS and Ansys EDT. Because of the parametric sweep, we added (for comparison) the simulation of an oblong anti-pad with the same length and width dimensions as the rectangular anti-pad with the best results, as shown in Figure .

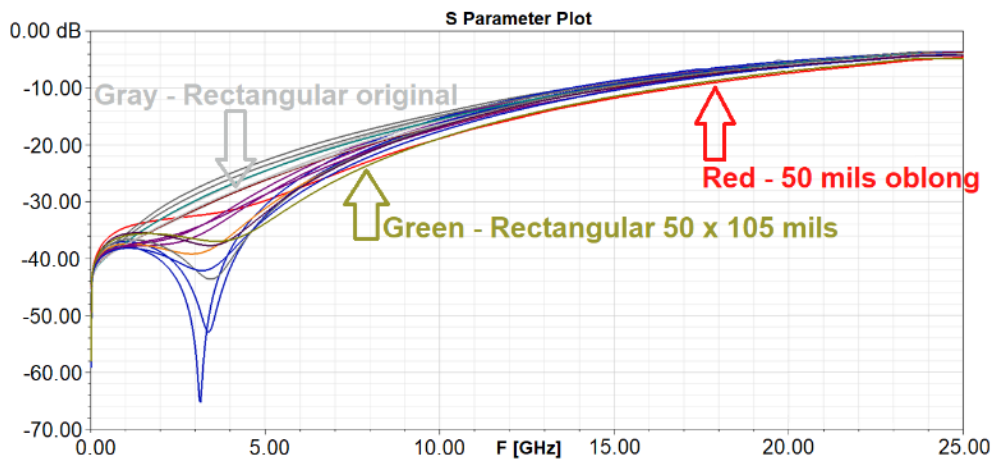
According to the results obtained in differential return loss, differential insertion loss, and TDR simulations, and presented in Figure , Figure and Figure , the best rectangular anti-pad dimensions were 50 x 105 mils, reducing impedance discontinuity from 9 Ω to 5 Ω . The oblong anti-pad with the same dimensions used for comparison showed similar return loss result but presented lower impedance variations in the TDR analysis and better insertion loss. Therefore, the oblong anti-pad format was chosen for the connector.

Figure 9 – Parametric sweep of rectangular anti-pad with Ansys EDT (a). Oblong anti-pad of 50 x 105 mils (b).



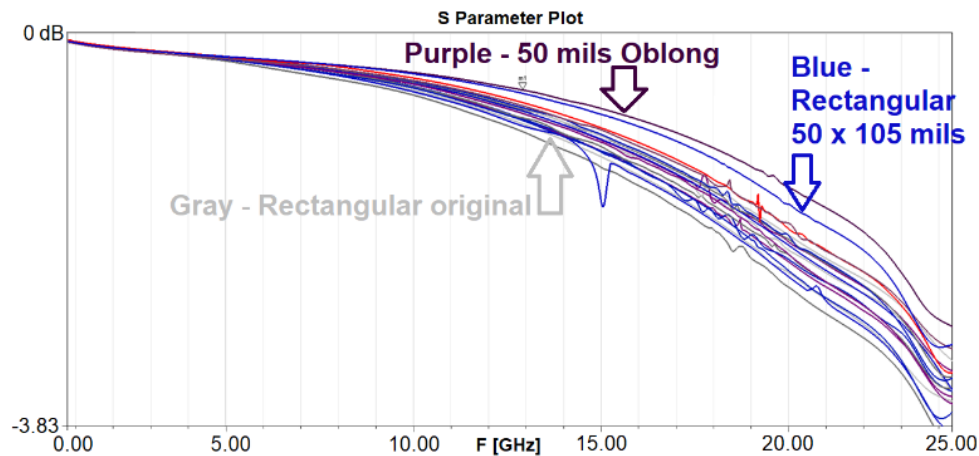
Source: The authors.

Figure 10 - Differential Return Loss (SDD11) resulting from the parametric sweep.



Source: The authors.

Figure 11 - Differential Insertion Loss (SDD12) resulting from the parametric sweep.

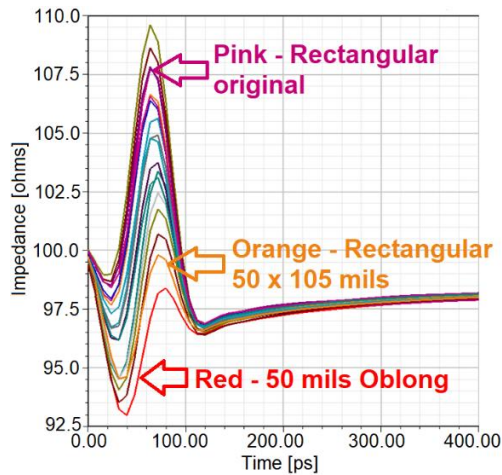


Source: The authors.

The parametric sweep was performed for a differential pair originating from the top layer and with destination at layer 5, with 23 mils of via length. The anti-pad defined for the connector is presented in Figure .

Figure 12 - TDR resulting from the parametric sweep.

Figure 13 - Anti-pad defined for the connector.



Source: The authors.



Source: The authors.

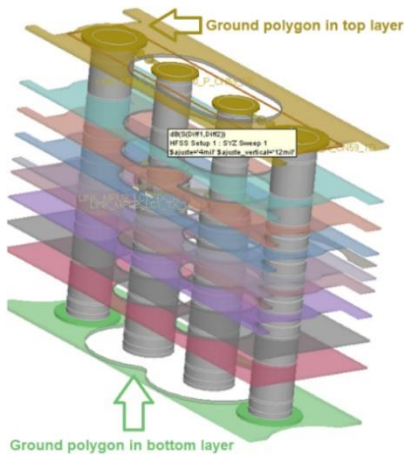
4.2. GROUND STUB ELIMINATION

Ground stub is analogous to the transmission line stub, which is an unwanted part of the line and should be removed whenever possible (with back drilling, for instance). The ground stub solution is much simpler, though. Ground stub occurs when part of the transmission line observes a higher impedance due to the reference plane distance. In the connector footprint, the absence of return planes in the top and bottom layers causes impedance discontinuity (ground stub) for signal vias. Addition of copper polygons connected to the ground plane in the top and bottom layers, as shown in

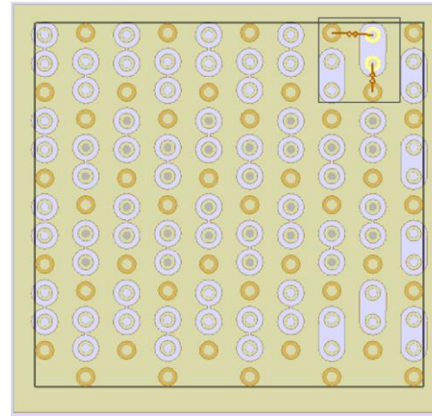
The parametric sweep performed in the previous section has already improved TDR results. To demonstrate the positive effect of ground stub elimination, some scenarios were simulated for a differential pair originating from the top layer to layer 12, as shown in Figure . The differential pair vias with original anti-pad (133 x 59 mils) and ground polygons on the top and bottom layers (green) show a significant improvement over the original anti-pad with the ground stub (blue). Additionally, the 50-mil oblong anti-pad appears as the best option for layer 12, since the discontinuity amplitude caused by the connector via is the smallest, ranging from 85 to 103 ohms. The overshoot above 100 Ω on the oblong anti-pad curve is due to the inductive effect caused by the length of the via (L1 - L12).

Figure 14 – Copper polygon in the connector area at the top and bottom layer.

Figure 15 - Copper polygon in the connector area (top view).



Source: The authors.



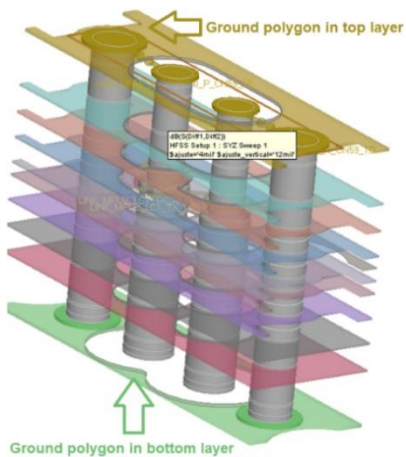
Source: The authors.

and Figure , considerably improve TDR results, as seen in Figure .

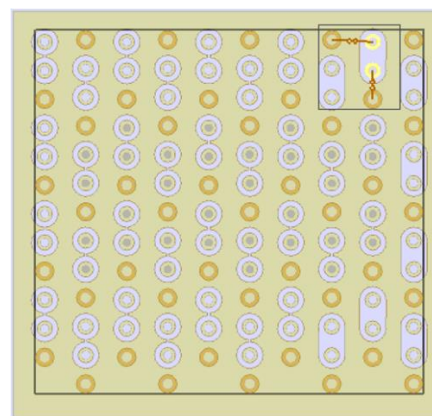
The parametric sweep performed in the previous section has already improved TDR results. To demonstrate the positive effect of ground stub elimination, some scenarios were simulated for a differential pair originating from the top layer to layer 12, as shown in Figure . The differential pair vias with original anti-pad (133 x 59 mils) and ground polygons on the top and bottom layers (green) show a significant improvement over the original anti-pad with the ground stub (blue). Additionally, the 50-mil oblong anti-pad appears as the best option for layer 12, since the discontinuity amplitude caused by the connector via is the smallest, ranging from 85 to 103 ohms. The overshoot above 100 Ω on the oblong anti-pad curve is due to the inductive effect caused by the length of the via (L1 - L12).

Figure 14 – Copper polygon in the connector area at the top and bottom layer.

Figure 15 - Copper polygon in the connector area (top view).

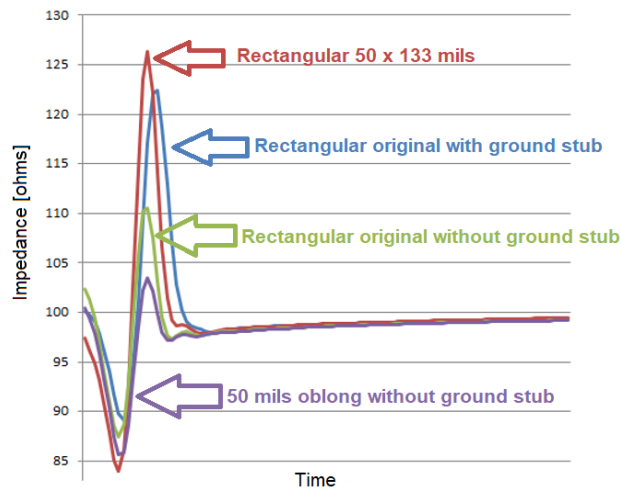


Source: The authors.



Source: The authors.

Figure 16 - TDR analysis for ground stub effect.



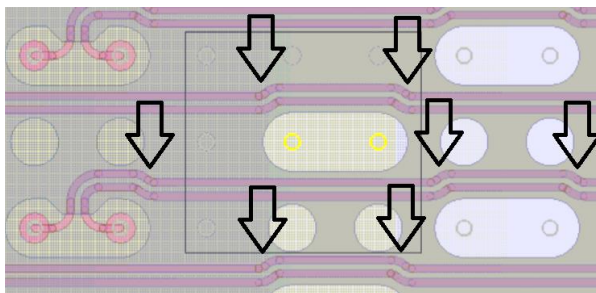
Source: The authors.

4.3. BGA BREAKOUT OPTIMIZATION

This section presents six different techniques to improve return loss in 25 Gbps serial links in the BGA breakout area:

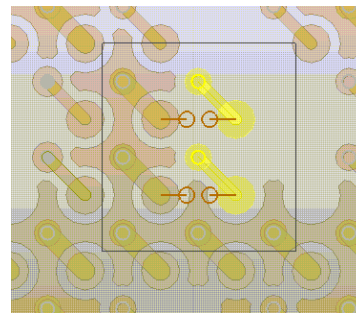
1. Differential pairs have been redesigned (in BGA area) to move them away from the return plane voids (anti-pads), reducing discontinuity regarding the reference plane (Figure);
2. Copper polygons connected to the ground plane were added at the top and bottom layers in the BGA area to eliminate ground stub from the reference vias (Figure);

Figure 17 - Differential pairs deviating from reference plane voids in BGA area.



Source: The authors.

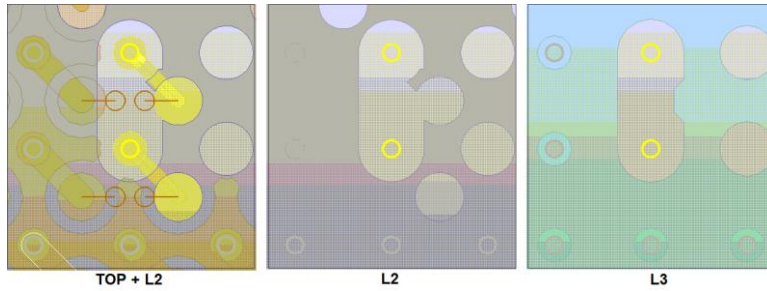
Figure 18 - Ground polygons in Top layer.



Source: The authors.

3. Cutouts were added to the layer L2 below the BGA balls, with layer L3 being the ground-plane return path, approaching ball pads impedance to 50 ohms (Figure);

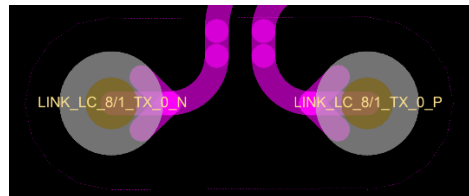
Figure 19 - BGA balls return path from ground plane at layer L3. Top and layer L2 (left), layer L2 (center) and layer L3 (right).



Source: The authors.

4. Teardrops were added to the high-speed signal vias. The goal in this case was to do a smooth transition between via and trace, thus reducing the effect of impedance discontinuity on return loss (Figure);

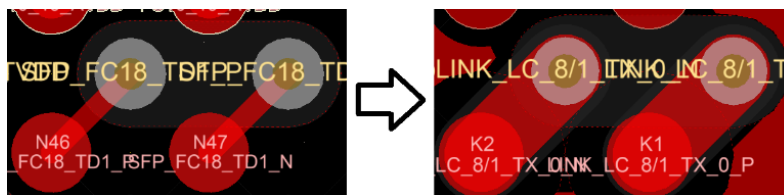
Figure 20 - Differential pair vias with teardrop.



Source: The authors.

5. The top layer trace between the BGA ball and the via has been redesigned to get closer to the desired 50-ohms impedance (Figure);

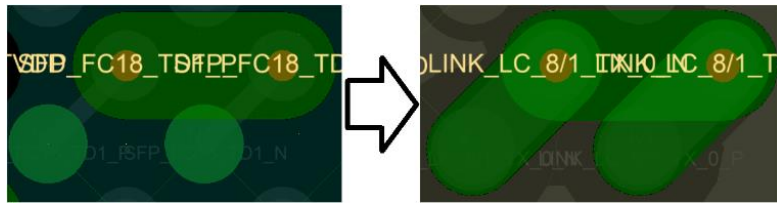
Figure 21 - Top layer trace with 50 ohms impedance.



Source: The authors.

6. Cutout on layer L2 was increased to cover the area below the traces on the top layer between the BGA ball and the via, with ground-plane return path at layer L3, thus reducing line discontinuity and approaching the trace impedance to 50 ohms (
7. Figure).

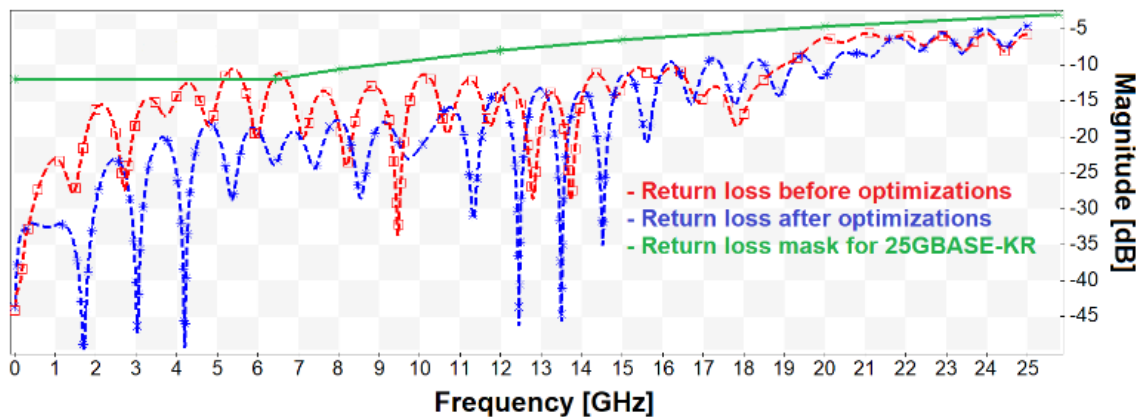
Figure 22 - Layer L2 cutout covering the top layer trace.



Source: The authors.

Figure shows the return loss results for a 7-inch differential pair transmission line between BGA and the high-speed connector, before (red line) and after (blue line) the proposed optimizations. Optimization results showed significant decrease in reflection losses in the simulated channel.

Figure 23 - Return loss simulated results before and after the optimizations.

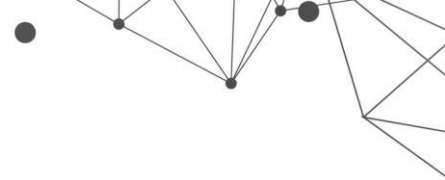


Source: The authors.

At the frequencies of major reflection in the original design between 5 and 7 GHz, there was an improvement of approximately 8 dB in the return loss. The original channel (without optimizations) was not complying with 25GBASE-KR normative mask, which could present practical operating problems.

5. CONCLUSIONS

This paper presents techniques for optimizing impedance of differential vias in high density BGA areas, thus reducing the return loss it imposes on high-speed



signals. Parametric sweep was used to improve anti-pad dimensions, reducing differential-via anti-pad impedance discontinuity from $9\ \Omega$ to $5\ \Omega$ for a via of 23 mils length (from PCB layer 1 to 5). The oblong shaped anti-pad showed lower impedance discontinuities and insertion loss when compared to the rectangular anti-pad under the same circuit application and simulation conditions.

Simulation results show that ground stub should be eliminated in high-speed differential vias. For a differential via with 70 mils length (from PCB layer 1 to 12), ground stub elimination reduced the impedance discontinuity from $33\ \Omega$ to $23\ \Omega$, prior to any anti-pad optimization.

The techniques presented for optimization of return loss in breakouts (or fan-outs) of BGA-type integrated circuit signals proved effective in reducing return loss, consequently improving the integrity of high-speed signals. With the techniques applied in the BGA area, the return loss in a 25 Gbps differential link was improved by approximately 8 dB between 5 and 7 GHz, consequently passing 25GBASE-KR normative mask with a good margin.

REFERENCES

BOGATIN, E. *et al.* A New Characterization Technique for Glass Weave Skew Sensitivity. **Signal Integrity Journal**, [S. l.], p. 27, 2017.

BUCUR, D. Fiber weave effect - A performance-limiting factor. **IEEE International Conference on Communications**, [S. l.], 2014. Available at: <https://doi.org/10.1109/ICCOMM.2014.6866737>

DONG, G. *et al.* Research on the influence of vias on signal transmission in multi-layer PCB. **ICEMI 2017 - Proceedings of IEEE 13th International Conference on Electronic Measurement and Instruments**, [S. l.], v. 2018- January, p. 406–409, 2017. Available at: <https://doi.org/10.1109/ICEMI.2017.8265976>

FEI, Y. C. Methods of optimized via design for higher channel bandwidth. **Proceedings of the 5th Asia Symposium on Quality Electronic Design, ASQED 2013**, [S. l.], p. 170–177, 2013. Available at: <https://doi.org/10.1109/ASQED.2013.6643582>

HAN, K. J. *et al.* Modeling on-board via stubs and traces in high-speed channels for achieving higher data bandwidth. **IEEE Transactions on Components, Packaging and Manufacturing Technology**, [S. l.], v. 4, n. 2, p. 268–278, 2014. Available at: <https://doi.org/10.1109/TCPMT.2013.2277291>

JOHANSSON, C.; MANEFJORD, T. Analysis of a high-speed PCB design. *In*: 2017, **2017 IEEE Nordic Circuits and Systems Conference, NORCAS 2017: NORCHIP and**



International Symposium of System-on-Chip, SoC 2017, Proceedings. : Institute of Electrical and Electronics Engineers Inc., 2017. p. 1–4. Available at: <https://doi.org/10.1109/NORCHIP.2017.8124982>

LEE, H.; HIRSCH, N.; BELL, O. **Via Characterization and Modeling By Z Input Impedance | 2018-06-12 | Signal Integrity Journal.** [s. l.], 2018. Available at: <https://www.signalintegrityjournal.com/articles/864-via-characterization-and-modeling-by-z-input-impedance>. Accessed on: 12 mar. 2022.

VASA, M. *et al.* Demystifying Via impedance optimization for high speed channels. **15th International Conference on Electromagnetic Interference and Compatibility, INCEMIC 2018,** [S. l.], 2018.

ZHANG, J. *et al.* PCB via to trace return loss optimization for >25Gbps serial links. **IEEE International Symposium on Electromagnetic Compatibility,** [S. l.], v. 2014-September, n. September, p. 619–624, 2014. Available at: <https://doi.org/10.1109/ISEMC.2014.6899045>

